Mechanisms controlling the recycling of nutrient silicon in freshwater sediments: An experimental study of the interactions between silicon, iron and phosphorus

by

Lu Huang

A thesis
presented to the University of Waterloo
in fulfilment of the
thesis requirement for the degree of
Doctor of Philosophy
in
Earth Science (Water)

Waterloo, Ontario, Canada, 2020

Examining Committee Membership

The following served on the Examining Committee for this thesis. The decision of the Examining Committee is by majority vote.

External examiner	Dr. Maria Dittrich Associate Professor Department of Physical and Environmental Sciences University of Toronto Scarborough
Supervisor	Dr. Philippe Van Cappellen Professor, Canada Excellence Research Chair Laureate Department of Earth and Environmental Sciences University of Waterloo
Co-supervisor	Dr. Christopher T. Parsons Assistant Professor Department of Earth and Environmental Sciences University of Waterloo
Committee Member	Dr. Raoul-Marie Couture Professeur agrégé, Chaire de recherche Sentinelle Nord en géochimie des milieux aquatiques Department of Chemistry University of Laval
Committee Member	Dr. Fereidoun Rezanezhad Research Associate Professor Department of Earth and Environmental Sciences University of Waterloo
Internal-external Member	Dr. Helen Jarvie Professor and University Chair Department of Geography and Environmental management University of Waterloo

Author's declaration

This thesis consists of material all of which I authored or co-authored: see Statement of Contributions included in the thesis. This is a true copy of the thesis, including any required final revisions, as accepted by my examiners.

I understand that my thesis may be made electronically available to the public.

Statement of Contributions

This thesis consists of a series of co-authored papers. As a first author of each chapter, I was primarily responsible for experimental design and execution. The contributions of co-authors for each chapter are outlined below.

Chapter 2: Philippe Van Cappellen (PVC), Christopher T. Parsons (CTP) and I defined the scope of the research. I designed the experiment with assistance from PVC and CTP. I conducted laboratory experiments, analyzed the data, and executed the model. I wrote the chapter with feedback from PVC.

Chapter 3: I designed the study with input from PVC and CTP. I performed the laboratory experiments and data analysis. PVC helped to come up with the model, and I implemented it. I wrote the chapter with feedback from CTP.

Chapter 4: I designed the study with input from PVC and CTP. I performed the laboratory experiments, data analysis, model simulation and chapter writing with input from PVC and CTP.

Chapter 5: PVC, CTP and I designed the study. I performed the laboratory experiments and analyzed the data. I wrote the chapter with inputs from PVC and CTP.

Abstract

Dissolved silicon (DSi) is an essential nutrient for numerous terrestrial and aquatic organisms. In freshwater systems, including streams, rivers and lakes, an important class of siliceous algae are diatoms. Human activities, including land use changes, nitrogen (N) and phosphorus (P) enrichment, and hydrological alterations, have caused a decrease of DSi availability relative to N and P. In turn, these changes in macronutrient availability may contribute to shifts in phytoplankton communities that increase the likelihood of nuisance and harmful algal blooms. Internal loading of nutrient silicon (Si) from bottom sediments is one key process regulating the availability of DSi in the overlying water column. The magnitude and timing of internal DSi loading in freshwater bodies are controlled by biogeochemical reactions in sediments whose mechanisms and kinetics remain to be fully understood. In this thesis, I use controlled laboratory experiments to unravel the roles of different reaction pathways in the immobilization and release of DSi in freshwater sediments. Starting with initially very simple synthetic reaction systems, I progressively include additional components, specifically iron (Fe) and P, in order to mimic more realistic biogeochemical reaction networks, and ultimately, perform experiments with real freshwater sediments.

After an introduction of the Si biogeochemical cycle, a review of the literature, and an outline of my thesis (Chapter 1), I present a study on the dissolution kinetics of amorphous silica (ASi) as a function of pH and salinity across the ranges typically found in natural freshwater (Chapter 2). The surface properties of ASi of various synthetic and natural sources are characterized with potentiometric titrations whose results are interpreted with the help of a constant capacitance model. Next the dissolution kinetics of ASi are measured in batch experiments, and the observed dissolution kinetics of ASi are fitted to a surface reaction model. The results confirm the previously reported non-linear relationship between the dissolution rate of ASi and the degree of undersaturation, implying that at least two dissolution rate constants are needed to describe the dissolution kinetics at high (typically, >0.4) and low (typically, <0.4) degree of undersaturation. In addition, the lack of correlation between the total measured electrical charge and dissolution rate constants provide a way to estimate the fraction of internal silanol groups in porous ASi materials. The quantitative relationships between the dissolution rate constant of ASi and environmental variables, including pH, degree of undersaturation, and salinity obtained in Chapter

2 contribute to the general framework for predicting dissolution rates of ASi in freshwater environments. The dissolution of ASi is the first step to recycling ASi back to bioavailable DSi in surface water.

Based on the findings in Chapter 2, the effects of Fe(II) adsorption on the dissolution kinetics of ASi are assessed in Chapter 3. A series of batch reactor experiments with variable amounts of aqueous Fe(II) added to ASi suspensions are conducted under anoxic conditions. Experimental results show that the presence of Fe(II) under anoxic conditions retards the release of DSi, with the magnitude of the retardation dependent on the initial Fe(II) concentration. Trace amounts of Fe(II) slow down the release of DSi probably by forming bidentate surface complexes which block reactive sites on ASi, rather than through the formation of new ferrous iron silicate phases. A Langmuir adsorption model that incorporates two types of surface groups (silicate groups bonded to the silica lattice via two bridging oxygens, Q_2 groups, and silicate groups bonded to the silica lattice via three bridging oxygens, Q_3 groups) is used to describe the effect of Fe(II) on the dissolution kinetics of ASi. The modeling results suggest that Fe(II) preferentially adsorbs to the Q_2 groups. In addition, Fe(II) ions adsorbed to the two types of surface sites have contrasting effects on the dissolution kinetics of ASi, inhibiting dissolution by stabilizing Q_2 sites, and enhancing dissolution by catalyzing the detachment of Q_3 groups. Thus, the redox cycling of Fe can induce an apparent redox dependence of ASi dissolution, which consequently affects the recycling rate of ASi and the timing of DSi release in freshwater systems.

In Chapter 4, I investigate the effects of the oxidative precipitation of Fe(II) on the immobilization of DSi in the absence of ASi. I present kinetic data on the concurrent consumption of aqueous Fe(II) and DSi during their co-precipitation in batch experiments, at different pH values and in the presence of variable initial dissolved phosphate (DP) concentrations. The data, combined with kinetic modeling, indicate that the consumption of DSi during Fe(II) oxidation proceeds along two pathways. At the beginning of the experiments, the oxidation of Fe(II)-DSi complexes induces the fast removal of DSi. Upon complete oxidation of Fe(II), further DSi removal is due to adsorption to surface sites of the Fe(III) oxyhydroxides. The presence of DP effectively competes with DSi via both of these pathways during the initial and later stages of the experiments, with as a result more limited removal of DSi during Fe(II) oxidation. Additionally, results from heterogeneous column experiments show that in porous media the transport of dissolved reactants imposes further

controls on the oxidation kinetics of Fe(II) and, therefore, on the removal kinetic of DSi. Overall, I conclude that the oxidation of Fe(II) can immobilize DSi, but that DSi immobilization is strongly diminished in the presence of DP.

In Chapter 5, I present the results of experiments using a natural sediment collected from a pond in Cootes Paradise marsh, Ontario. Flow-through experiments with sediment columns are carried out by flowing anoxic solutions containing variable concentrations of Fe(II), DSi and DP via the lower inlet. The outflow side of each columns is exposed to aerated water, hence creating an oxic upper layer of sediment in the columns. The inflow of Fe(II) causes the retention of DP in the sediment as a result of the precipitation of Fe(III) in the uppermost sediment. However, the Fe(III)-enriched surface layer is unable to completely retain all the DP supplied to, as well as produced within, the sediment columns, resulting in considerable DP flux across the sediment water interface. In contrast to Fe(II) and DP, there is little evidence of DSi retention within surficial Fe(III) rich precipitates when the column surface is exposed to oxic conditions. When anoxia is induced in the overlying water, the release of Fe(II) and DP from the columns is enhanced significantly. However, no corresponding changes to DSi efflux are observed upon switching to anoxic overlying water. The constant net production of DSi in the sediment is likely due to the dissolution of naturally occurring biogenic silica. Overall, the results with the natural sediment confirm that, at near-neutral pH, the presence of high DP concentrations inhibit the co-precipitation and adsorption of DSi with Fe(III) oxyhydroxides, hence preventing DSi retention in sediments at the interface with oxic overlying water. Therefore, I conclude that the speciation and stability of legacy P pools in sediment, as well as recent P inputs exert a control on the capacity of sediment to release or retain Si by decoupling Fe and Si cycling.

In the final chapter of my thesis (Chapter 6), I summarize the main findings of my research, as well as their implications for the recycling of nutrient Si in freshwater environments. I further present possible future research directions into the biogeochemical cycle of this often overlooked nutrient element.

摘要

溶解硅（DSi）是许多陆生和水生生物的必需营养元素。在淡水系统（包括溪流，河流和湖泊）中，硅藻是一类重要的硅质藻类。人类活动，包括土地利用类型的变化、氮（N）和磷（P）的富集以及改变河流的水文特征，已导致 DSi，相对于 N 和 P，的可利用率下降。DSi 的相对匮乏可能导致浮游植物群落发生变化，从而增加了无益和有害藻类的滋生的可能性。从水底沉积物释放的 DSi 称为硅的内源输入，是调节水体中 DSi 可获得性的关键过程。淡水中 DSi 内援输入量的大小的输入的时间是由沉积物中的生物地球化学反应控制的，而这些反应的机理和动力学特征需要更全面的学习和了解。在本论文中，我使用实验室控制实验来揭示淡水沉积物中不同反应途径对 DSi 固化和释放的作用。从最初非常简单的人工合成反应系统开始，我逐渐加入了其他成分，特别是铁（Fe）和 P，以模拟更现实的生物地球化学反应网络，并最终用淡水沉积物进行实验。

在做了硅的生物地球化学循环相关的文献综述并且介绍了论文结构内容后（第一章），我在论文的第二章研究了在自然淡水范围内 pH 和盐度对 ASi 溶解动力学的影响。首先，我用电位滴定的方法表征各种人工合成和天然来源的 ASi 的表面特性，并用恒定电容模型来解释实验结果。接下来，我用均一批量实验研究 ASi 的溶解动力学，并将观察到的 ASi 溶解动力学拟合到表面反应模型中。本章研究的结果证实了先前文献中记录的 ASi 溶解速率与不饱和度之间的非线性关系，这意味着为了描述完整的 ASi 的溶解动力学，至少需要两个溶出速率常数：高不饱和度（通常> 0.4）和低不饱和度（通常<0.4）。此外，多孔 ASi 材料实验测得的表面总电荷数与溶解速率常数之间缺乏统一的相关性，这种不相关性可以用来估算 ASi 材料孔隙内部硅烷醇基团的比例。由于 ASi 的溶解是将 ASi 循环回可生物利

用的 DSi 的第一步，本章获得的 ASi 溶解速率常数与环境变量（包括 pH 值，不饱和度和盐度）之间的定量关系为预测淡水环境中 ASi 溶解速率的一般框架。

基于第二章中的发现，我在第三章中研究了 Fe（II）吸附对 ASi 溶解动力学的影响。通过向 ASi 悬浮液中添加了不同浓度的 Fe（II），在无氧条件的条件下进行了一系列分批均一反应器实验。实验结果表明，在无氧条件下 Fe（II）的存在会延迟 DSi 的释放，且延迟的大小取决于初始 Fe（II）的浓度。痕量的 Fe（II）可能通过在 ASi 上形成二齿络合物从而阻断反应位点来减慢 DSi 的释放，而不是通过形成新的硅酸亚铁相。结合了两种类型的表面基团（通过两个桥连的氧键合至二氧化硅晶格的硅酸盐基团 Q_2 基团和通过三个桥连的氧键合至二氧化硅晶格的硅酸盐基团 Q_3 基团）的 Langmuir 吸附模型被用来表征 Fe（II）吸附对 ASi 的溶解动力学的影响。模型结果表明 Fe（II）优先吸附到 Q_2 基团，并且吸附到两种类型表面位点的 Fe（II）离子对 ASi 的溶解动力学具有相反的影响：通过稳定 Q_2 位点来抑制溶解和通过催化 Q_3 基团的分离来加速溶解。因此，Fe 的氧化还原循环可以引起 ASi 溶解的氧化还原依赖性，因此影响 ASi 的循环速率和 DSi 在淡水系统中释放的时间。

在第四章中，我研究了在没有 ASi 的情况下 Fe（II）的氧化沉淀对 DSi 固定的影响。我展示了在均一批处理实验中、不同的 pH 值和不同的初始溶解磷酸盐（DP）浓度的情况下，溶解态 Fe（II）和 DSi 在共沉淀过程中移除的动力学数据。通过结合实验数据与动力学建模，本章研究的结果显示在 Fe（II）氧化过程中 DSi 的移除通过两个途径进行：在实验开始时，DSi 和 Fe（II）形成配合物，这些配合物的氧化导致氧化反应开始时 DSi 的快速移除； Fe（II）完全氧化后，DSi 吸附到 Fe（III）的氧化物和氢氧化物表面，从而导致 DSi 的进一步移除。无论在实验的初始阶段还是后期阶段，DP 的存在都会与 DSi 产生有效竞

争，从而限制 DSi 在 Fe（II）氧化过程中的移除。此外，异质柱实验的结果表明，在多孔介质中，溶解的反应物的扩散性运输会进一步限制 Fe（II）的氧化动力学和 DSi 的去除动力学。总的来说，我得出的结论是，Fe（II）的氧化可以固定 DSi，但在 DP 的存在使得这个过程中 DSi 的移除大大降低。

在第 5 章中，我介绍了从安大略省 Cootes Paradise 采集的天然沉积物的实验结果。通过将含有不同浓度组合的 Fe（II），DSi 和 DP 的无氧溶液从填满相同沉积物的柱子下端入口处泵入，我进行了一系列的流通柱实验。沉积物柱子的上端的出口处会暴露在充空气的水中，从而在沉积物柱形成一个氧化层。泵入沉积物柱的 Fe（II）在氧化层被氧化形成 Fe（III）沉淀并将 DP 固定在沉积物中，但是这个过程无法固定包括外源泵入和沉积物中产生的全部的 DP。与 Fe（II）和 DP 相比，我们没有观测到氧化条件下 DSi 的固定。当上层水变成无氧条件时，Fe（II）和 DP 从沉积物柱的释放显着增强。但是，切换到缺氧的上层水后 DSi 的释放没有明显变化，这稳定的 DSi 净产量可能来是自 ASi 的溶解。总体而言，天然沉积物的实验结果证实，在接近中性的 pH 值下，高 DP 浓度的存在会抑制 DSi 的共沉淀和吸附，从而防止 DSi 在氧化沉积物中保留固定。我们得出的结论是，孔隙水 DP 和 DSi 的相对生产率可能代表着淡水系统内源 Si 通量对氧化还原依赖性的主要控制。因此，沉积物中历史遗留和最近的输入的 P 的形态和稳定性都会控制沉积物释放或保留 Si 的能力。

在论文的最后一章（第 6 章）中，我总结了我论文研究的主要发现以及它们对淡水环境中营养硅的循环的影响。此外，我还介绍了硅这种经常被忽视的营养元素在生物地球化学循环中可能的未来研究方向。

Acknowledgment

Firstly, I would like to thank my supervisor, Philippe Van Cappellen. I thank you for giving me the opportunity to work with you, as well as a great deal of freedom to pursue projects in my own way as I chose. I may not have always been going in the right direction, but you were always able to guide me in building on the work I have done. The ways that you think about scientific questions and your enthusiasm for research will always inspire me. For that, I am deeply grateful to you.

Secondly, I would like to thank my co-supervisor, Chris Parsons, for all the valuable suggestions, help, and encouragement. I learned something from every talk we have had during the past five years. All the fancy software you recommended helped me to finish my thesis more effectively.

Thirdly, I thank my advisory committee members Raoul-Marie Couture, William Taylor and Fereidoun Rezanezhad for committing your time and advice to help me with this research. I wish to also thank Maria Dittrich and Helen Jarvie for agreeing to be part of my examination committee.

I also thank Marianne Vandergriendt for helping me to start my life in Canada and to start my work in the lab. I thank Stephanie Slowinski, who assisted me in many ways throughout my years here, especially the feedbacks and comments on my thesis. I thank Shuhuan for helping me with my research progress and guiding me on my life. I thank Erin, Sue, Tatjana, Linden, Amanda and Bhaleka for keeping things running smoothly. Thank you to Igor for helping me with model development and implementation, and to Kunfu for his feedback on my research chapters. I thank all past and current graduate students in the Ecohydrology Research Group who helped me in different ways at different times: Sabur, Christine, Bingjie, Peng, Saru, Yao, Qingqing, Taylor, Hellen, Adrian, Bijen, Zahra, and Tariq.

Special thanks go to Micheal Krom for guiding me to this great platform. I want to thank Xiaodan who initiated my research journey and have been supporting me for the past ten years. Thank you to Fan for encouraging me to take on this challenge and always being supportive.

Without the support of my family, I will not be able to make it here. Thank you for being considerate and for being there for me.

Finally, I wish to thank the Canada Excellence Research Chairs Program and the China Scholarship Council for funding my research.

Dedication

To my mother, Zhenling Wang, thank you for everything I had, have, and will have.

献给我的母亲王振岭，谢谢您，为我曾经经历的，现在拥有的，和将来可能获得的一切。

Table of Contents

List of Figures

List of Tables

List of Acronyms

On an alphabetical order

APW	Artificial porewater
ASi	Amorphous silica
BAC	Buffered ascorbic-citrate
BET	Brunauer-Emmett-Teller
CCM	Constant capacitance model
DO	Dissolved oxygen
DP	Dissolved phosphate
DSi	Dissolved silicon
Fe(III)	Ferric iron
Fe(II)	Ferrous iron
Fe	Iron
ICP-OES	Inductively coupled plasma-optical emission spectrometry
Si	Silicon
K	Equilibrium constant
k	Rate constant
N	Nitrogen
P	Phosphorus
PZC	Point of zero charge
Q_2	Silicate groups bonded to the silica lattice via two bridging oxygens
Q_3	Silicate groups bonded to the silica lattice via three bridging oxygens
RPSi	Reactive particulate silicon
SEM	Scanning electron microscope
WSOS/DF	Weighted sum of squares divided by degree of freedom

Chapter 1
Introduction

1.1 Silicon and the silicon cycle

Silicon (Si) is a globally important macronutrient for phytoplankton communities in freshwater and seawater. Its recycling within and through these systems is thus coupled to the recycling of other macronutrients including phosphorus, nitrogen and carbon, some of which have been enriched in natural waters as a result of human activities. In sediments, its recycling is coupled to the recycling of elements that it tends to form bonds with, including iron and aluminum, as well as competing oxyanion-forming elements such as phosphorus. Lentic systems connect the biogeochemical processes occurring in sediments to the biogeochemical processes occurring in the water column, and Si can be actively cycled between its sediment and water column pools. Thus, understanding the biogeochemical processes in sediments that can mobilize or immobilize Si is a key step for understanding the recycling of Si in lentic systems and the contribution of internal Si cycling in these systems to phytoplankton primary productivity, and is the focus of this thesis.

As the second most abundant element in the earth's crust, Si occurs almost invariably in combination with oxygen (as in the minerals quartz and cristobalite), and often with aluminium, potassium and hydrogen (as in feldspars, micas, and clay minerals) in solid phases. Although they are not very soluble, these minerals can dissolve during chemical weathering on geological timescales, releasing Si into aqueous solution. Aqueous Si occurs primarily in the form of monosilicic acid (H_4SiO_4), although it can also be found in multinuclear species under specific pH and concentration ranges (Davis et al., 2002; Lagerstrom, 1959; Stumm et al., 1967). Dissolved silicon (DSi) is often used as the general term to describe all the Si species in solution.

1.1.1 The biological significance of Si

DSi concentrations in natural waters vary from 1 µM in rainwater to 1000 µM in groundwater (Kristiansen and Hoell, 2002; Pradeep et al., 2016; Zhang et al., 2005). DSi is taken up by living organisms and used for different functions (Simpson and Volcani, 1981). For example, DSi taken up by plants can be deposited as amorphous silica inside the plant's tissues. These deposits, known

as phytoliths, have been shown to increase the resistance of plants to abiotic (*e.g.*, drought, water logging, UV light, salinity, heavy metals) and biotic (*e.g.*, viral and bacterial pathogens, fungi, herbivores) stressors (Farooq and Dietz, 2015; Simpson and Volcani, 1981). Additionally, DSi is essential for various siliceous organisms living in water, including diatoms, radiolarians, silicoflagellates and siliceous sponges (Figure 1.1) (Simpson and Volcani, 1981). Most of DSi uptake by these siliceous organisms is used to build their cell walls or skeletons, resulting in the deposition of a cryptocrystalline polymer of silica ($(SiO_2)_n$) (Nelson et al., 1995; Simpson and Volcani, 1981; Volcani, 1981), which is referred to as biogenic or amorphous silica (ASi). These rigid siliceous deposits can support soft protoplasmic bodies and protect them from injury and to some extent from predators (Boltovskoy, 1998; Ehrlich et al., 2010; Greenwood et al., 2001; Lipps, 1993; Maldonado et al., 2005; Rickert, 2000; Simpson and Volcani, 1981).

1.1.2 The environmental significance of Si

Diatoms, the most conspicuous and abundant algal groups in marine and freshwater environments, contribute around 20% of global primary productivity (Malviya et al., 2016). Because of their large cell size relative to other phytoplankton, diatoms are effective food sources for higher trophic levels, from zooplankton to aquatic insects to fish (Finkel et al., 2010). Diatoms produce long-chain fatty acids that are favorable energy sources for these predators, which consequently makes diatoms the basis of some of the most productive food chains (Yi et al., 2017). Diatoms tend to dominate the species composition of phytoplankton due to their rapid growth rates. However, environmental conditions including, but not limited to nutrient concentrations, can shift the species composition to non-diatom algae dominance (Conley et al., 1993; Egge and Aksnes, 1992; Makulla and Sommer, 1993; Officer and Ryther, 1980).

The major nutrients, nitrogen (N), phosphorus (P) and silicon (Si), are required for diatoms' photosynthetic growth in atomic ratios of approximately 16:1:16 (Officer and Ryther, 1980; Redfield et al., 1963). It should be noted these values are the mean values for marine diatoms (Brzezinski, 1985), the atomic ratios in fact vary with diatom species, nutrient availability, and other environmental variables (Lomas et al., 2019; Turner, 2002). Because DSi is not an essential nutrient for non-siliceous algae, the dominant species of phytoplankton may shift from diatoms to non-siliceous algae when DSi is limiting nutrient relative to N and P, which consequently may

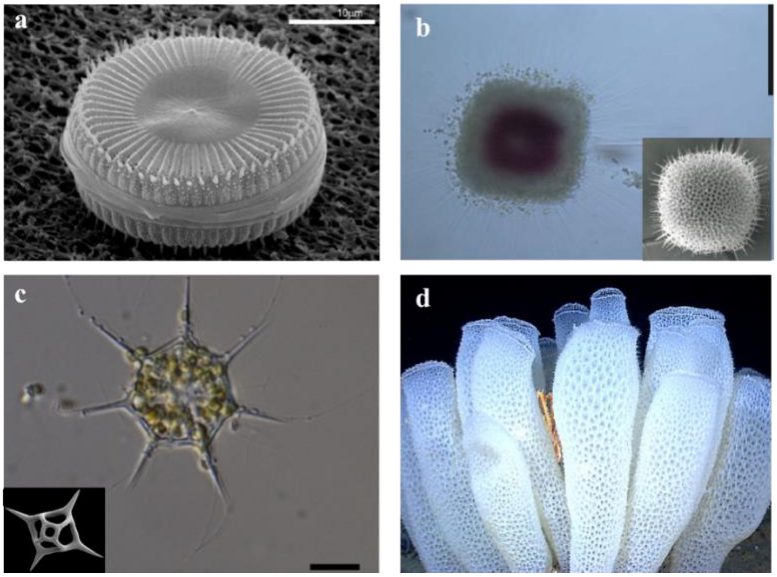

Figure 1.1. Images of siliceous organisms. A. Scanning electron microscope (SEM) image of live diatom *Cycletella meneghiniana* (Scale bar: 10 µm). Image taken from Marshall (2009). B. Photomicrograph of live radiolarian *Spongaster tetras tetras* Ehrenberg (Scale bar: 0.1 mm, small window shows its siliceous frustule whose scale bar is not known). Images taken from Matsuoka (2017). C. Light micrograph of live silicoflagellate *Distephanus speculum* (scale bar: 10 µm, small window shows its siliceous frustule whose scale bar is not known). Images taken from McCartney et al. (2014). D. Photo of siliceous sponge *Euplectella aspergillum*. Photo source: National Oceanic and Atmospheric Administration (NOAA) Okeanos Explorer Program, Gulf of Mexico 2012 Expedition.

Figure 1.2. Harmful algal blooms on Lake Erie. A. Satellite image of harmful algal bloom on Lake Erie in 2018 (Credit: NOAA), b. Photo of harmful algal bloom in Lake Erie (Credit: NOAA GLERL).

increase the likelihood of harmful algal blooms (Egge and Aksnes, 1992; Makulla and Sommer, 1993; Officer and Ryther, 1980; Turner, 2002). Harmful algal blooms may damage the health of ecosystems by producing toxins that can harm fish, wild life or human consumers, and shading submerged organisms from light, and depleting oxygen in water columns (Figure 1.2) (Anderson et al., 2002).

1.1.3 The global Si cycle

Decomposition of silicate minerals by chemical, physical, and biological processes initiates the global biogeochemical Si cycle by releasing DSi. The released DSi may be cycled within terrestrial ecosystems (mostly by plants) and transformed to particulate silica, which buffers the export of DSi to the ocean. Reactive Si, including DSi and reactive particulate Si (RPSi) is delivered by rivers to the oceans where Si is recycled until, ultimately, a small fraction is permanently buried (Figure 1.3).

Over the past several decades, there has been a significant increase in the study of the Si cycle (Berner et al., 1983; Bootsma et al., 2003; Duerr et al., 2011; Frings et al., 2014; Ittekkot et al., 2006; Johnson and Eisenreich, 1979; Laruelle et al., 2009; Ragueneau et al., 2000; Schelske, 1985; Tréguer et al., 1995). However, most of the research has been restricted to the role of Si in marine biogeochemical cycling. DSi in seawater is also more likely to be the limiting nutrient due to the restricted external sources and intensive consumption by siliceous organisms (Ittekkot et al., 2006; Tréguer et al., 1995; Tréguer and De La Rocha, 2013). Despite large uncertainties, the fluxes of Si inputs and internal cycling in the world ocean were summarized by Tréguer et al. (1995), and implemented by Tréguer and De La Roxha (2013). As Figure 1.3 shows, transport of both DSi and reactive particulate Si (RPSi) by rivers constitute about 67% of the external flux to the ocean. Estuaries, which are known for their high biogeochemical cycling rates, retain more than 20% of total riverine input and 1.3% of biogenic silica produced in the ocean. The open ocean is effective in recycling biogenic silica. More than 97% of biogenic silica produced is recycled in the water column and at the sediment-water interface, leaving 2.5% permanently buried in deep ocean sea sediments (Figure 1.3).

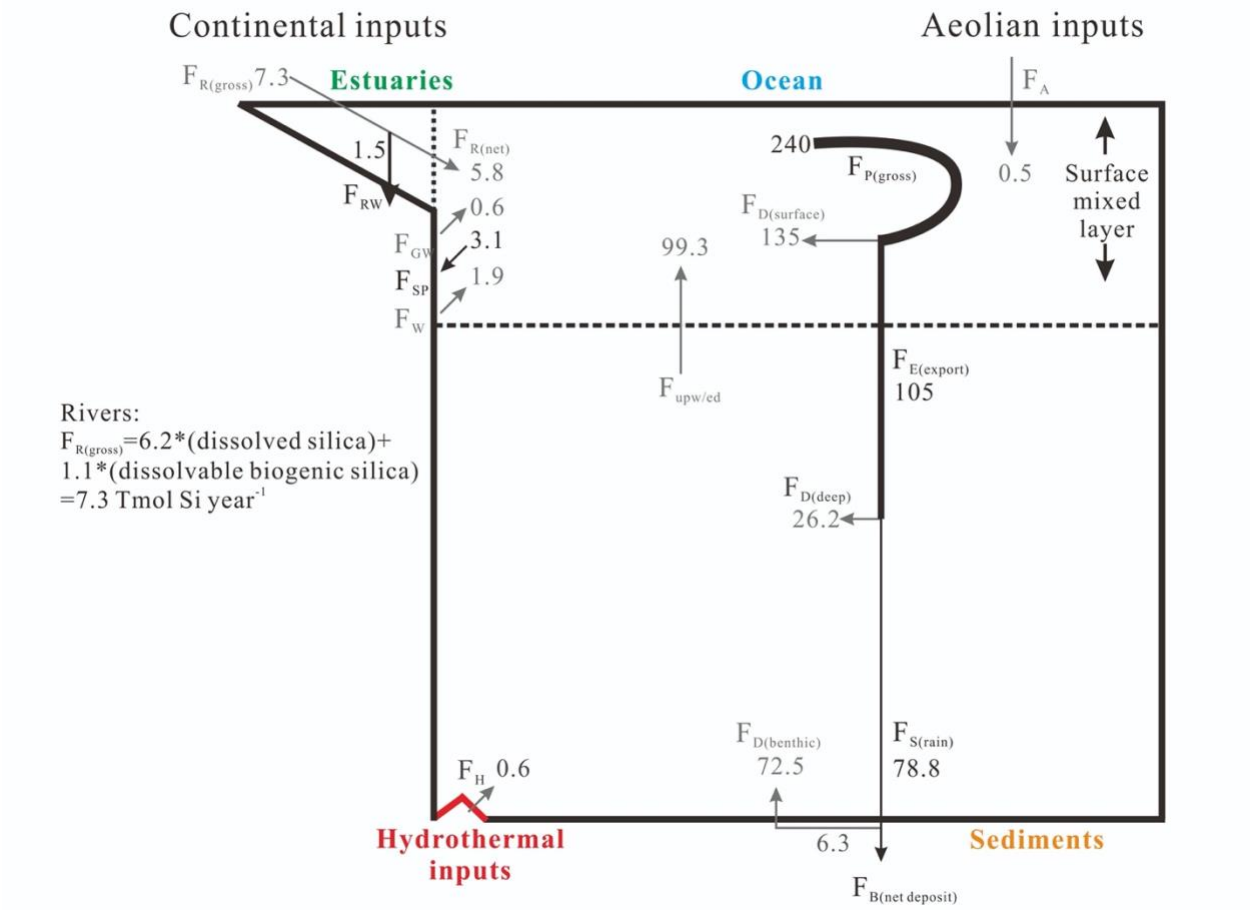

Figure 1.3. Silicon cycle in the world's oceans at steady state (Tréguer and De La Roxha, 2013). Grey arrows represent fluxes of dissolved silicon (DSi) ($F_{R(net)}$, net riverine inputs; F_{GW}, groundwater flux; F_W, seafloor weathering inputs; F_H, hydrothermal inputs; $F_{D(benthic)}$, flux of DSi recycled at the sediment-water interface; $F_{D(deep)}$, flux of DSi recycled in deep water; $F_{upw/ed}$, flux of DSi transferred from the deep reservoir to the surface mixed layer; $F_{D(surface)}$, flux of DSi recycled in the surface reservoir; F_A, aeolian inputs), and black arrows represent fluxes of particulate biogenic silica (F_{RW}, deposits of biogenic silica and reverse weathering in estuaries; F_{SP}, the net sink of biogenic silica in sponges on continental shelves; $F_{B(net\ deposit)}$, net deposit of biogenic silica in coastal and abyssal sediments; $F_{S(rain)}$, flux of biogenic silica that reaches sediment-water interface; $F_{E(export)}$, flux of biogenic silicas exported toward the deep reservoir; $F_{P(gross)}$, biogenic silica gross production). All fluxes are in 10^{12} or teramoles of Si per year.

1.1.4 Anthropogenic alternations of the freshwater Si cycle

Less research has been conducted on the Si cycle in freshwater systems. The world average DSi concentration in freshwater is more than twice that in the oceans (Maavara et al., 2014; Tréguer et al., 1995; Tréguer and De La Rocha, 2013), and DSi should thus be less limiting to biological activity in freshwater. However, freshwater systems, especially lentic systems, have been increasingly recognized as sinks for the DSi that is supplied to these systems (Nriagu, 1978; Ridenour, 2017; Schelske, 1985; Schelske et al., 1983). Many studies have shown decreases in DSi concentrations in surface freshwaters relative to historical concentrations, which has also been matched by decreased loads of reactive Si delivered to the oceans (Maavara et al., 2014; Nriagu, 1978; Schelske and Stoermer, 1971).

In general, human activities have increased N and P, but not Si, loads to water bodies. N and P enrichment of surface waters relative to Si via excess nutrient loading facilitates the sustained growth of diatoms to the point of depleting DSi from the water column (Anderson et al., 2002; Garnier et al., 2010; Officer and Ryther, 1980; Triplett et al., 2012). The burial of the diatom frustules as particulate reactive Si in sediments following these large diatom blooms may eventually lead to the decrease of DSi concentrations in freshwaters over time (Harrison et al., 2012; Schelske and Stoermer, 1971). For example, depletion of DSi in the water column over time has been observed in the Greats Lakes. This, according to the increased diatoms frustules retained in sediments, is ascribed to the increased loads of nutrient P from human activities, including land use changes and the use of P-containing fertilizers and detergents, to these lakes since the 1970s (Nriagu, 1978; Schelske, 1985; Schelske et al., 1983).

Another important anthropogenic perturbation are hydrological alterations by dam construction, which has significantly altered the total amount of reactive Si delivered to the oceans (Humborg et al., 2000; Triplett et al., 2012). Maavara et al. (2014) estimated that river damming retains 5.3% of global reactive Si loading to rivers in the sediments of reservoirs. Additionally, land use changes have been recognized as an important controlling factor on the amount of Si exported from terrestrial systems (Street-Perrott and Barker, 2008; Struyf et al., 2010). In summary, human activities affect not only the fluxes into and out of, but also the internal Si cycling in aquatic environments (Humborg et al., 2000; Triplett et al., 2012). Therefore, to better understand and

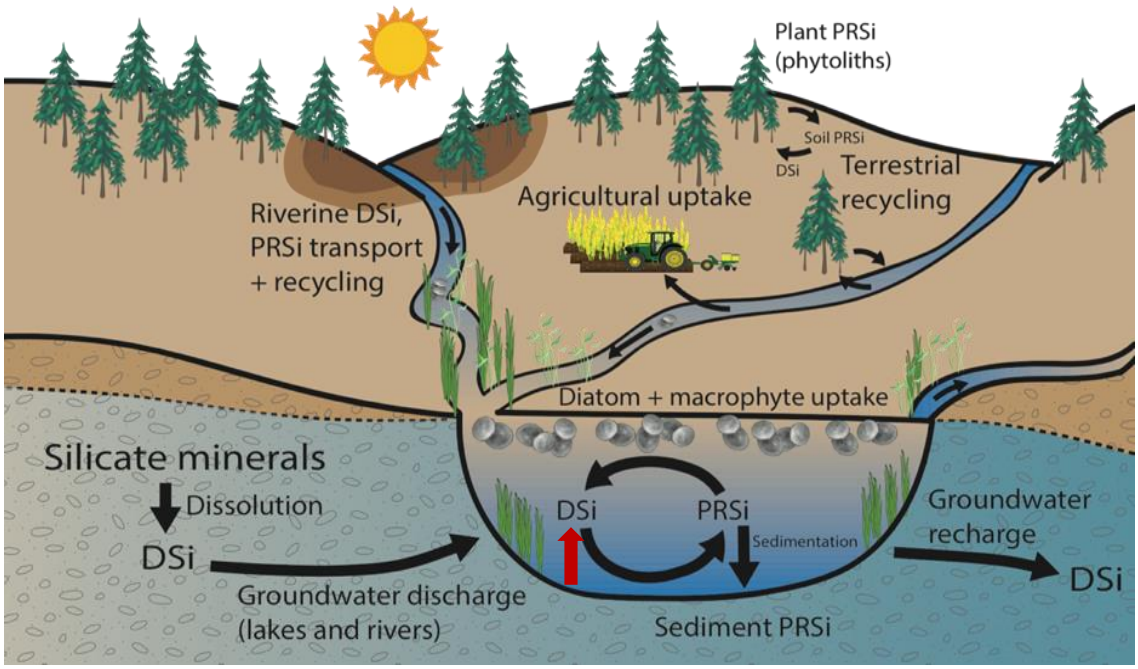

Figure 1.4. Silicon cycle in terrestrial systems (Figure source: Taylor Maavara). Black arrows represent fluxes of dissolved silicon (DSi) or reactive particulate Si (RPSi), the main biogeochemical processes that drive the fluxes are shown in the figure. The red arrow represents internal DSi loading from sediments. (Figure: courtesy of Taylor Maavara).

predict the impacts of human activities on Si cycling in these freshwater systems, the modifications to both the external loading to and the internal reactive Si cycling in these systems need to be studied (Maavara, 2017; Schelske, 1985; Street-Perrott and Barker, 2008; Struyf et al., 2010; Triplett et al., 2012).

1.2 On the importance of internal Si loading

Recycling in the water column, in the sediment and at the sediment-water interface constitute the internal sources of DSi (Ragueneau et al., 2006). Attempts to quantify internal Si loading have generally been motivated by two objectives. Firstly, quantifying the burial flux of Si to sediments which is coupled to the flux of carbon is vital to understanding the effects of the paleoclimate (*e.g.*, atmospheric CO_2) on paleoproductivity in aquatic systems (Barker et al., 1994a; Conley and Schelske, 2002; Mortlock et al., 1991; Ragueneau et al., 2000). Biogenic silica concentrations in lake sediments, in combination with other proxies, *e.g*., Ge/Si (Mortlock et al., 1991), diatom community composition (Moser et al., 2002) and carbon isotopes (Stager and Johnson, 2000), can be used to reconstruct paleolimnological and paleoclimate conditions, which provide insight into the change of trophic dynamics in lakes over time (Bootsma et al., 2003; Randsalu-Wendrup et al., 2016; Stager and Johnson, 2000).

Secondly, quantifying the fraction of Si reaching the sediment-water interface which is subsequently recycled back into water columns to participate again in biological cycling is vital to understanding the Si cycle in both local and global aquatic systems. Globally, internal Si loading from marine sediments is about 4 times that of the riverine inputs to the oceans (Figure 1.3) (Tréguer et al., 1995; Tréguer and De La Rocha, 2013). The contributions of internal loading to the Si cycle in freshwater systems however are highly variable (Afonso and Stumm, 1992; Aston, 1983; Maavara, 2017; Mortimer, 1941). For example, the internal Si loading in Lake Superior, characterized by a low upwelling rate, is of the same magnitude as atmospheric inputs and represents approximately 20% of the input by external sources (Johnson and Eisenreich, 1979; Schelske, 1985). In contrast, the internal loading is only 1% of DSi input into the Lake Pepin, a highly perturbed eutrophic shallow lake (Triplett, 2008). The existing body of research demonstrates that it is not only the physical, chemical, and biological conditions that impact the internal Si loading, but that meteorological and hydrological conditions also play important roles

(Afonso and Stumm, 1992; Aston, 1983; Bootsma et al., 2003; Johnson and Eisenreich, 1979; Laruelle et al., 2009; Maavara, 2017; Mortimer, 1941; Ridenour, 2017; Schelske, 1985).

1.3 Reactive forms of Si in sediments

The internal loading of P and Fe and mechanisms controlling their release from aquatic sediments have been thoroughly studied (Couture et al., 2010; Katsev et al., 2006; Markelov, 2019; Mortimer, 1941; Nriagu and Dell, 1974). Meanwhile, the internal Si loading has drawn less attention, and the mechanisms controlling Si release from sediments are not well understood. Most Si in sediments is bound in the form of quartz and other recalcitrant silicate minerals, and is unavailable on a biological timescale. The forms of Si relevant to its biogeochemical cycle are therefore the reactive forms that are likely to be bioavailable on a biological, rather than geological timescale. These reactive forms of Si are dissolved Si (DSi) and reactive particulate Si (RPSi). Sediment RPSi consists mainly of amorphous silica (ASi) deposited abiotically from supersaturated solution in natural waters, ASi in living biomass and in biogenic detritus (Daval et al., 2013; Iler, 1979b; Ragueneau et al., 2000), as well as different pedogenic Si forms, including amorphous aluminosilicates, and Si bound to metal oxyhydroxides (Aston, 1983; Ragueneau et al., 2000). The ASi deposited as biogenic detritus and Si bound to metal oxides are the two major pools of RPSi in sediments, and thus they are the two major pools contributing to the internal DSi loading.

1.3.1 Amorphous silica

As the major pool of reactive Si in sediments, the dissolution rate of amorphous silica (ASi) is a key control on the magnitude of internal DSi loading. The concentration of ASi in sediments is controlled by many factors, such as the primary production rate, algal community composition and hydraulic residence time, and as a result, ASi concentrations in sediments vary from 0.04% in sandy sediments (Koning et al., 2002) to 92% in aged diatomaceous earth deposits (in weight%). Laruelle et al. (2009) used a value of 5% as the world average concentration of ASi in freshwater sediments. All the moles of ASi present in a lake sediment is not equally soluble, however. ASi that is still within the organisms in which it was formed is resistant to dissolution due to the protective effect of the organic matrix. After death of these organisms, bacterial assemblages colonize and breakdown the organic matrix via the production of specific enzymes, including ectoprotease, exposing the ASi surface to the surrounding solution. Following the degradation of

the organic matrix, the ASi dissolution rate is highly variable and depends on the intrinsic physiochemical properties of ASi, and those of the solvent, in particular the temperature and pH, and the concentrations of chemical constituents in the solution that may interact with the ASi surface.

ASi has the same silicon-oxygen tetrahedron unit as quartz (Figure 1.5). However, the chemical units in ASi do not exhibit long-range ordered: lengths and angles of Si-O-Si bonds (siloxane) show large variations (Dove et al., 2008; Iler, 1979b). Once exposed to water, two different types of groups are present on the ASi surface: surface siloxane groups (>Si-O-Si<) and surface hydroxyl groups (*i.e.*, silanol groups, >SiOH) as a result of hydroxylation (Stumm, 1992; Zhuravlev, 2000). The nucleophilic attack of water molecules weakens and break siloxane bonds, which initiates the dissolution process of ASi. Surface silanol groups can protonate and deprotonate depending on the pH of the solution.

$$> \mathrm{Si} - \mathrm{O} - \mathrm{Si} < + H_2O \leftrightarrow 2 > SiOH^0 \quad (1.1)$$

$$> \mathrm{SiO}H^0 + H^+ \leftrightarrow > \mathrm{Si}OH_2{}^+ \quad (1.2)$$

$$> \mathrm{SiO}H^0 \leftrightarrow > \mathrm{Si}O^- + H^+ \quad (1.3)$$

where > represents a surface species. Because of the very low point of zero surface charge of ASi ($pH_{zpc} \approx$ 2-3.5) (Dixit and Van Cappellen, 2002; Stumm, 1992), the deprotonated surface silanol groups (Reaction (1.3)) dominate in natural waters (pH>3.5). The presence of these negatively charged surface species $>SiO^-$ can polarize and weaken the siloxane bounds, which in turn enhances the dissolution of ASi (Stumm, 1992).

The mechanisms of silica dissolution include either the direct attack on a charged surface site by H_2O or catalysis by OH^- on a neutral site. Thus, because of the differences in the reactivity of the different surface group species, pH exerts a large control on the dissolution rate by controlling the distribution of surface group species (>SiOH, $>SiO^-$, $SiOH_2^+$), that each may dominate the dissolution process over a given pH range (Dove and Elston, 1992; Xiao and Lasaga, 1996). Except for the protonation/deprotonation processes, other processes that modify the surface characteristics, such as surface complexation reactions will also affect the dissolution rate of ASi (Dove and Nix, 1997). One well known example is that the presence of Na^+ which enhances the dissolution of ASi significantly (Dove and Crerar, 1990; Dove and Elston, 1992).

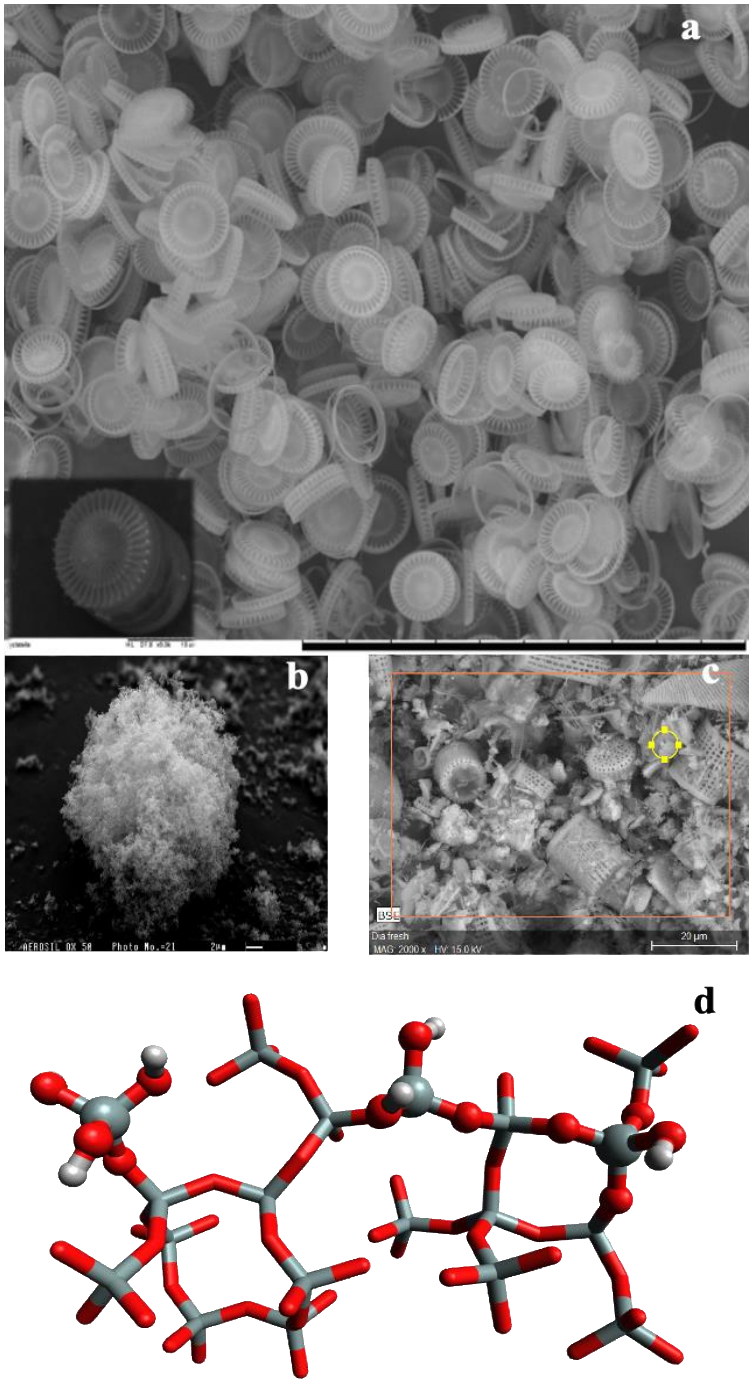

Figure 1.5. The morphology and structure of amorphous silica (ASi). a. SEM image of freshwater diatom *Cyclotella meneghiniana* (this study); b. SEM image of Aerosil OX 50 (Source: http://www.icare.univ-lille1.fr/progra2/database/index.html); c. SEM image of freshwater diatomaceous earth (this study); d. Illustration of ASi showing different surface species. Grey balls from left to right correspond to singly, doubly, and triply coordinated surface sites. Red and white balls represent oxygen and hydrogen atoms that are bound to surface silicon atoms. The sticks represent Si (grey) and O (red) in the bulk solid. Molecular model produced using Avogadro V1.2 (Hanwell et al., 2012).

1.3.2 Binding of Si to metal oxyhydroxide minerals

Metal oxyhydroxides, especially those of aluminum (Al) and iron (Fe), are abundant components of freshwater sediments. They are generally covered with surface hydroxyl groups when in aqueous solution due to the hydroxylation of the surface metal atoms (Schoen and Roberson, 1970; Stumm, 1992). Previous studies have shown that DSi exhibits a high affinity for hydroxylated Al and Fe oxides and hydroxides in neutral or slightly alkaline pH (Davis et al., 2002; Iler, 1979b). Adsorption and desorption of DSi to those metal oxyhydroxides in sediments have been recognized as important mechanisms controlling the internal DSi loading (Aduwusu and Wilcox, 1991; Bien et al., 1958; Hingston and Raupach, 1967; Mortimer, 1941; Nteziryayo and Danielsson, 2018a; Ridenour, 2017; Testa et al., 2013).

Iron (Fe) oxyhydroxides, such as magnetite, hematite, goethite, ferrihydrite and lepidocrocite are ubiquitous in sediments. They are characterized by their high surface areas and high densities of surface hydroxyl groups (Hiemstra, 2013; Stumm, 1992; Wang et al., 2013a). These hydroxyl groups attached to Fe atoms can protonate and deprotonate depending on the pH of solution (similar to reactions 1.2 and 1.3). The charged surface groups confer the ability to sorb different anions, cations, and even molecular species through electrostatic interactions and surface complexation reactions (Stumm, 1992). The magnitude of the electrostatic interactions is controlled by the charge of sorbate and sorbent, both of which are pH dependent. Because of its relatively high dissociation constant (9.8), DSi exists almost entirely as monomeric silicic acid (H_4SiO_4) at neutral pH. At a pH value below the point of zero charge (*i.e.*, pH_{PZC}, the pH value at which net surface charge is zero) of a given Fe oxyhydroxides (Fe oxyhydroxides typically have pH_{PZC} values ranging between 4.2 and 10.0, but usually below 9.0). the electrostatic interaction between DSi and Fe oxyhydroxides is limited by the neutral charge of H_4SiO_4. At pH values above the dissociation constant of silicic acid (pK_a = 9.8), deprotonated negatively charged silicic acid is attracted by the positively charged surface sites. However, with an increase in pH, the negatively charged surface sites on the Fe oxyhydroxides become dominant which may lead to the desorption of silicic acid.

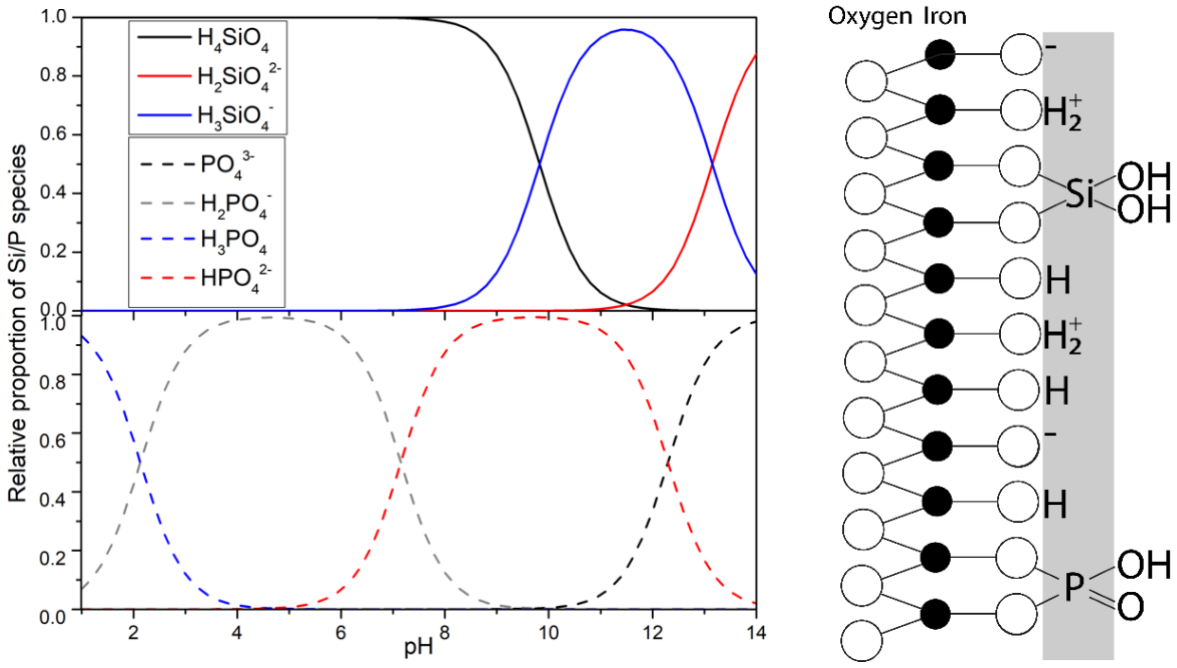

Figure 1.6. Speciation of silicic acid and phosphoric acid as a function of pH (left) and surface complexation formation of DSi and DP on the Fe oxyhydroxide surface (right)

Although DSi is faced with these unfavorable electrostatic conditions, it forms monomeric and polymeric surface complexes on the surface of Fe oxyhydroxides via covalent bonds (Aduwusu and Wilcox, 1991; Davis et al., 2002; Sabur, 2019). The extent of this specific adsorption interaction depends on the concentration of DSi, and the physiochemical properties of both the Fe oxyhydroxides mineral phase and the aqueous solution. For example, infrared spectroscopic studies have shown that H_4SiO_4 at low concentration can replace surface hydroxyl ligands of ferrihydrite and form monomeric species with Fe-O-Si linkages (Hiemstra et al., 2007), while at high concentration, H_4SiO_4 can form oligomeric surface silicates on ferrihydrite (Swedlund et al., 2010). Theoretically, H_4SiO_4 can be adsorbed by forming bidentate surface complexes (Figure 1.6). However, a Fourier transform infrared spectroscopic study by (Kanematsu et al., 2018) showed that monodentate silicate species are predominant on goethite and lepidocrocite surfaces.

Similar to iron, the oxyhydroxides of Al, such as gibbsite and boehmite, are ubiquitous in freshwater sediments (Barron and Torrent, 2013). One important difference between iron and aluminum is that aluminum does not have different oxidation states. Dissolved aluminum released from the dissolution of terrigenous aluminosilicate minerals precipitates as different kinds of Al oxyhydroxides (Schoen and Roberson, 1970). With high surface areas and high surface hydroxyl group densities, Al oxyhydroxides are capable of adsorbing DSi through ligand exchange (Aduwusu and Wilcox, 1991; Bien et al., 1958; Hingston and Raupach, 1967). In addition, because of the abundance DSi in many natural waters, the formation of aluminum oxides may be inhibited and aluminosilicate mineral formation prevails instead (Schoen and Roberson, 1970).

1.3.3 Aluminosilicate minerals

The formation of authigenic amorphous silicate minerals is generally accepted to be responsible for the far-from-saturation DSi concentrations in natural waters that are far below the equilibrium saturation of ASi (Iler, 1979b). The solubility of ASi in pure water can reach more than 1800 μM, but in the presence of polyvalent metal cations, especially aluminum, amorphous silicates are formed, which have a much lower solubility than ASi (Iler, 1979b)

Although Al is the third most abundant element in the Earth's crust, it exists in natural waters in very low concentrations, because Al released from chemical weathering will precipitate as aluminum hydroxides (Schoen and Roberson, 1970). In the presence of abundant DSi, which is

typical in natural freshwaters, H_4SiO_4 will compete with further hydroxylation or autocondensation of aluminum hydroxides, which leads to the formation of hydroxyaluminosilicates instead of gibbsite (Beardmore et al., 2016). This process is suggested to play an important role in keeping the inimical element Al from being incorporated by biological organisms (Exley, 1998). More importantly, this process may be a sink for Si that limits the availability of nutrient DSi to diatoms (Exley, 1998).

1.4 Environmental factors controlling internal DSi loading

Many environmental factors can modify the reactivity of the RPSi species present in sediments, which are ultimately the sources of the DSi released during internal loading. These factors include oxygen concentration, interactions with other naturally occurring ions, temperature, pH, and a variety of other factors. How these factors may impact internal DSi loading and influence the reactivity of sediment RPSi species are outlined below.

1.4.1 Oxygenation

The concentration of oxygen in surface sediments is one of the dominant variables controlling the chemical interactions between water and sediment. In the case of DSi, the presence of oxygen is important because the redox-controlled speciation of Fe at the sediment-water interface exerts a large control on the mobility of nutrients and contaminants, including DSi (Couture et al., 2010; Katsev et al., 2006; Li et al., 2012; Roberts et al., 2004; Sahai et al., 2007; Smolders et al., 2017).

Under oxic conditions, because of upward transport and mixing, anoxic porewater constituents, including Fe(II), will be oxidized near the sediment-water interface. In the case of Fe(II) oxidation, insoluble Fe(III) oxyhydroxides are then produced. During Fe(II) oxidation, DSi can bind to the Fe(III) oxyhydroxides through ligand exchange, both during the precipitation of the Fe(III) precipitates and after their formation. At high DSi concentrations, mixed minerals of ferric silicate, ferrous silicate, iron oxide and hydroxides can form (Costine and Thurgate, 2007). These mineral phases are thus another pathway for the co-precipitation of DSi and Fe (Kolthoff, 1932). While DSi is immobilized during oxic periods via these aforementioned pathways, under anoxic conditions, and in the presence of sufficient amounts of electron donors, the reduction and subsequent dissolution (which is also called reductive dissolution) of Fe(III) oxyhydroxides

releases Fe(II) and any DSi that was adsorbed to or co-precipitated with the Fe(III) oxyhydroxides (Smolders et al., 2017).Ferric iron oxyhydroxides will also age from amorphous to crystalline iron minerals with time (Cornell et al., 1987), which will decrease their surface reactivity and surface areas (Cismasu et al., 2014; Hiemstra et al., 2019).

Bottom water oxygenation also affects the activities and community composition of the microbial populations that are responsible for the decomposition of the organic matrix surrounding biogenic ASi, with higher oxygen concentrations being expected to be more energetically favourable and to thus confer higher rates of organic matrix decomposition compared to anoxic conditions (Ekeroth et al., 2016; Mortimer, 1941; Nteziryayo and Danielsson, 2018a). With these relatively higher rates of organic matrix decomposition, ASi dissolution rates would also be higher, because of the increasing surface area of ASi that is being exposed to solution. The published studies that have investigated the influences of oxygen concentrations on internal DSi loading are summarized and listed in Table 1.1.

Table 1.1. Summary of studies on the redox-dependent release of dissolved silicon (DSi) from sediments. The studies are grouped according to whether the authors reported an enhancement, inhibition or no effect of anoxic conditions on the release of DSi.

Study	Study site	Anoxic conditions on DSi release	Role of Fe	Role of P	Role of ASi
1	Esthwaite Water	Enhance	✓	✓	✗
2	Windermere		✓	✓	✗
3	Lake Kizaki		✓	✗	✗
4	Western Baltic Sea		✗	✗	✓
5	Lake Malaren and Baltic Sea		✓	✓	✗
6	Northern Baltic Sea		✗	✓	✗
7	South Ionian Sea		✓	✓	✓
8	South Atlantic Ocean		✗	✗	✓
9	South Atlantic Ocean		✗	✗	✓
10	Chesapeake Bay		✓	✓	✓
11	Baltic Sea		✓	✗	✓
12	Baltic sea		✓	✓	✗
13	Coastal Gulf of Finland		✗	✗	✓
14	Cootes Paradise		✓	✓	✗
15	Gulf of Finland		✗	✗	✗
16	Baltic sea	Inhibit	✓	✓	✓
17	Baltic sea		✓	✓	✓
18	Hamilton Harbor	No effect	✓	✓	✓

1 Measurement of water samples from Esthwaite Water, 2 Incubation of Windermere mud (Mortimer, 1941), 3 Measurement of vertical distribution of chemicals in Lake Kizaki (Kato, 1969). 4 In situ fluxes measurement at Kiel Bight (Bodungen, 1986), 5 Incubation of sediment cores from lake Malaren and Baltic Sea (Gunnars, 1990), 6 Measurement of chemical composition of water samples from northern Baltic Sea (Kuparinen and Tuominen, 2001), 7 Incubation of undisturbed sediments from South Ionian Sea (Belias et al., 2007), 8 Dataset analysis of porewater and sediment samples from South Atlantic Ocean (Seiter et al., 2010), 9 Porewater profiles from the South Atlantic (Holstein and Hensen, 2010), 10 Incubation of sediment cores from Chesapeake Bay (Testa et al., 2013), 11 Statistical analysis of the relationship between DSi concentration and oxygen conditions in the Baltic Sea (Danielsson, 2014), 12 In situ fluxes measurement in Kanholmsfjärden, Baltic proper (Ekeroth et al., 2016), 13 Incubation of mixture of natural sediments from and diatoms in batch reactors (Lehtimaki et al., 2016), 14 Batch experiment with surface sediments from Cootes Paradise (Parsons et al., 2017), 15 In vitro incubations of intact sediment cores, in situ measurement with a benthic lander, and measurement of porewater from Gulf of Finland (Tallberg et al., 2017), 16 Sediment cores collected from Baltic sea (Nteziryayo and Danielsson, 2018), 17 Sequential extraction of sediments from Baltic sea (Siipola et al., 2016), 18 Incubation of sediment cores collected from Hamilton Harbor (Ridenour, 2017).

Note: Fe-bound Si and amorphous silica (ASi) are the two main reactive particulate silica endmembers in sediments, that are usually proposed to account for the release of DSi. Phosphorus (P) is another nutrient often studied at the same time, however, its role on the release of DSi from sediments is barely discussed. "✓" indicates that the role was studied. "✗" indicates the role was not studied. Studies listed here may not be exhaustive.

1.4.2 Electrolyte composition

The presence of cations has been shown to affect the dissolution rate of ASi into different directions and with different magnitudes. Alkali cations, including Na^+ and K^+ that are abundant in natural waters, have been shown to increase the dissolution rate of ASi significantly by lowering the activation energy of dissolution at near neutral pH (Dove and Crerar, 1990; Icenhower and Dove, 2000). The role of alkaline earth cations, including Ca^{2+} and Mg^{2+}, on the dissolution kinetic of ASi have not been directly studied. But alkaline earth cations have been shown to enhance the dissolution of quartz by increasing the reactivity of siloxane groups at near neutral pH (Dove and Crerar, 1990; Dove and Nix, 1997). In contrast, multi-valent cations such as including Al and Fe, have been shown to retard the dissolution of ASi by producing a coating of insoluble silicates (Koning et al., 2007; Lewin, 1961; Van Cappellen et al., 2002). Thus, the presence of naturally occurring cations can either enhance or retard the dissolution of ASi, which consequently affect the internal DSi loading.

Naturally occurring anions, including Cl^-, HCO_3^- and HPO_4^{2-}, may affect DSi sorption to metal oxyhydroxides, e.g., Fe(III) oxyhydroxides. The effects of the redox transformations of Fe on the mobilization of DSi are briefly summarized in section 1.4.1 above. Under oxic conditions, the anions can compete directly with DSi for sorption sites of Fe(III) oxyhydroxides (Gao et al., 2013; Geelhoed et al., 1997; Gehlen and Van Raaphorst, 2002; Hansen et al., 1994; Sabur, 2019; Sibanda and Young, 1986; Zhang and Huang, 2007). However, anions can also affect the oxidation kinetics of Fe(II) by forming aqueous complexes with Fe(II) during a transition from anoxic to oxic conditions (Buamah et al., 2009; Kaegi et al., 2010; King, 1998; Kinsela et al., 2016; Mao et al., 2011; Mitra and Matthews, 1985a; Tamura et al., 1976; Wolthoorn et al., 2004). In turn, this may affect the uptake of DSi by the Fe(III) precipitates that are forming.

Among all the naturally occurring anions in natural waters, dissolved phosphate (DP) is an essential nutrient that often (co-)limits primary production in freshwater environments (Conley, 2002; Ekeroth et al., 2016; Hartikainen et al., 1996; Joshi et al., 2015; Mortimer, 1941; Parsons et al., 2017; Sabur, 2019; Schindler, 1977; Tuominen et al., 1998). Table 1.1 summarizes the studies in which the effects of DP on DSi release from sediments have been considered. At a pH value below the pH_{PZC} of an adsorbent, e.g., Fe oxyhydroxides, deprotonated phosphoric acid will be

attracted by the positively charged surface through electrostatic interaction, which subsequently facilitates chemical adsorption of DP via ligand exchange (Figure 1.6) (Li et al., 2016; Sabur, 2019). At that same pH value, the electrostatic interaction between DSi and Fe(III) oxyhydroxides is limited by the neutral charge of H_4SiO_4 (See details in 1.3.2). Not surprisingly, studies have shown that DP effectively outcompetes with DSi for the sorption sites of Fe oxyhydroxides at near neutral pH (Gächter and Mülle, 2003; Gachter and Muller, 2003; Jensen et al., 1992; Mortimer, 1941; Parsons et al., 2017; Ridenour, 2017; Sabur, 2019; Zhang and Huang, 2007). The presence of DP has also been shown to increase the homogeneous oxidation rate of Fe(II) at different pH values (Mao et al., 2011; Tamura et al., 1976). However, how this affects the mobility of DSi has not yet been studied.

1.4.3 Temperature

Temperature can alter nutrient fluxes across the water-sediment interface by altering the rates of the physico-biogeochemical processes in sediments (Duan and Kaushal, 2013; Ridenour, 2017; Srithongouthai et al., 2003; Zhou et al., 2016).

Firstly, vertical temperature gradients (*i.e.*, thermal stratification) drive the vertical and horizontal movement of water, which in turn exerts an important control on the chemical exchanges between the water column and the underlying sediments in large water systems (Mortimer, 1941, 1942).

Secondly, the breakdown of the organic matrix surrounding biogenic silica that enables the dissolution of ASi is a biologically mediated process whose rate has been long recognized to be temperature dependent (LaRowe and Van Cappellen, 2011; Vicente et al., 2016; White et al., 1991). Additionally, the growth rate of siliceous organisms that can inhabit surface sediment increases with temperature (Elvin, 1971). The release of DSi to the water column is retarded by the accumulation of these siliceous organisms that actively take up DSi.

Thirdly, temperature affects the rate of chemical processes in sediments. For example, the dissolution rate of ASi increases with increasing temparture (Kamatani, 1982; Loucaides et al., 2012b; Van Cappellen et al., 2002). In natural water systems, unraveling the individual effect of temperature on these different processes affecting DSi fluxes may be challenging, but a regression

analysis of incubation results had revealed that water temperature can account for 24% of the seasonal variability of DSi fluxes (Srithongouthai et al., 2003).

1.4.4 pH

When buffered by dissolved carbonate and bicarbonate dissolved in water, the pH of many natural waters do not vary greatly. However, in sediment porewaters, the pH can vary significantly over short distance (Hurd, 1973; Jourabchi et al., 2005). Jourabchi et al. (2005) showed that pH can vary up to one unit within the upper 5 cm. The effect of pH on the release of DSi can result from Si speciation changes in sediments. The common reactive Si endmembers in the sediment are amorphous silica (ASi), Si bound to metal oxides (Fe, Al, Mn oxyhydroxides), and amorphous aluminosilicates. The reactivities of all these reactive Si phases are sensitive to pH. Firstly, OH^- has been proposed to catalyze the dissolution of ASi. At pH higher than the PZC pH (1.4 to 4) of ASi, the dissolution rate of ASi increases with increasing pH (Fraysse et al., 2006). Secondly, the amount of Si bound to metal oxides is also pH dependent. For example, Sabur (2019) showed that the maximum adsorption of DSi on goethite was observed at around the PZC of goethite (pH = 10.0). The proposed mechanism is that the adsorption is limited by the neutral charge of silicic acid at pH below its deprotonation constant (pK_a = 9.8). At pH above 10.0, the negatively charged surface of goethite repulse the deprotonated silicic acid. This mechanism is applicable to the adsorption of DSi to other metal oxides. Finally, the solubilities of amorphous silicates depend on the pH of solution. For example, the solubility of aluminosilicates is proposed to be high at high and low pH values because of the inhibition of polymerization (Moller et al., 2006).

1.4.5 Other environmental factors

Other factors including the physical processes of resuspension and bioturbation, and chemical processes such as mineralization and microbial processes, also affect the internal DSi loading. For example, about 96% of gross sedimentation may be resuspended in Hamilton Harbour, which as a result increases the concentration of suspended matter in the overlying water and increases the recycling of reactive Si between sediments and water columns (Ridenour, 2017). Bioturbation by benthic invertebrates typically enhances the transport of dissolved O_2 as well as other dissolved chemicals, including DSi, and thus may enhance internal DSi loading (Hoelker et al., 2015; Matisoff and Wang, 1998; Parsons et al., 2017).

1.5 Thesis structure

1.5.1 Aims

Given the environmental significance of nutrient silicon, the aim of this thesis is to contribute to the understanding of the mechanisms responsible for internal DSi loading in lentic freshwater systems. The scope of the research is to investigate the contribution of abiotic chemical interactions between ASi, DSi, dissolved Fe(II), DP, and Fe(III) oxyhydroxides to DSi mobilization and immobilization in sediments. I accomplish these objectives using controlled lab experiments and pure chemicals that are meant to simulate the specific interactions between reactive particulate Si endmembers present in sediments, plus DSi, dissolved Fe(II), Fe(III) oxyhydroxides and DP. The kinetic parameters obtained in these experiments and the information about the mechanisms underlying the processes that lead to DSi production in sediments can then be applied to predict reactive Si, DP and Fe cycling in heterogeneous systems including more complex experiments involving more co-occurring reactions and processes, and real sediments *in situ*. The specific aims of this thesis are as follows:

- Using a coupled experimental and modeling approach, relate ASi surface processes and ASi surface interactions with dissolved chemicals in solution, including protons (pH), salts (salinity), and complexation agent Fe(II) to the ASi dissolution rate constant to consolidate the general framework for understanding Si recycling of ASi in freshwater systems;
- Develop a chemical reaction model to establish the mechanisms responsible for DSi co-precipitation with Fe(III) oxides during Fe(II) oxidation and the competitive role of DP in both homogeneous and heterogeneous aqueous systems;
- Investigate the contributions of surface adsorption by Fe(III) oxyhydroxides and co-precipitation during Fe(II) oxidation co-precipitation to the magnitude and timing of DSi release observed in a flow-through column system using natural sediments collected from Cootes Paradise marsh.

1.5.2 Research chapters

The primary research portion of this thesis is organized into four chapters (Chapters 2-5). proceeded by a general introduction (Chapter 1) to introduce the environmental significance of nutrient silicon (Si) and the Si cycle. Chapter 1 focuses on internal DSi loading, summarizing the dominant reactive particulate Si (RPSi) endmembers in sediments, and evaluating the factors that control the mechanisms responsible for DSi mobilization and immobilization in sediments, and thus the net internal DSi loading fluxes from the sediments to the water column.

In Chapter 2, *Amorphous silica: surface processes and dissolution kinetics,* I study the dissolution kinetics of various forms of amorphous silica (ASi) in artificial porewater solutions with different pHs and salinities that fall within the typical ranges of pH and salinity values observed in freshwater. I then apply a surface reaction model to predict the dissolution rate constants, which I calculate by fitting the experimental data using the first-order kinetic rate law, as a function of pH and salinity, reinforcing and consolidating the framework for predicting the ASi dissolution rate constant as a function of chemical interactions occurring at the ASi surface-aqueous solution interface.

In Chapter 3, *Influence of Fe(II) adsorption on the dissolution kinetics of amorphous silica*, I study the effects of Fe(II) adsorption on the dissolution rate constant of ASi. Such reactions commonly occur in natural sediments due to oscillating redox conditions and are simulated here using a series of ASi suspension batch experiments to which I add variable amounts of Fe(II) under anoxic conditions. I then demonstrate the application of a Langmuir adsorption model which accounts for two types of ASi surface groups for predicting the ASi dissolution rate constant as a function of Fe(II) concentrations. Chapter 3 highlights that the surface reaction model that is used to assess the effects of surface processes on the dissolution rate of ASi in Chapter 2 cannot be applied to the interactions of Fe(II) and ASi. Instead, the Langmuir adsorption model that incorporates two types of surface groups (silicate groups bonded to the silica lattice via two bridging oxygens, Q_2 groups, and silicate groups bonded to the silica lattice via three bridging oxygens, Q_3 groups) is used to predict the ASi dissolution rate constant as a function of the Fe(II) concentration.

In Chapter 4, *Co-precipitation of iron and silicon: Reaction kinetics, elemental ratios and the influence of phosphorus*, I study the effects of the oxidative precipitation of Fe(II) on the

immobilization of DSi. I measure the concurrent consumption of aqueous Fe(II) and DSi during their co-precipitation in batch experiments, at different pH values and in the presence of variable initial DP concentrations. A kinetic model that incorporates homogeneous oxidation, heterogeneous oxidation, surface precipitation, and adsorption/desorption reactions allows me to assess the relative contribution of each reaction to the removal of DSi in a homogeneous system. I then study the effect of diffusive transport on DSi immobilization during Fe(II) oxidation under conditions that are more representative of sediments than the batch systems, where Fe(II) oxidation is controlled by the diffusive transport of oxygen through the column reactors. I therefore add a diffusion term to the chemical reaction model to fit the column reactors' experimental data. The oxidation of Fe(II) can immobilize DSi, but that the latter is strongly diminished in the presence of DP and limited by diffusive transport.

In Chapter 5, *Controls on dissolved silicon release from natural sediments: Roles of oxygen and iron*, I collect surficial sediments from the open water area of a freshwater marsh to conduct a series of flow-through column experiments to elucidate the roles of different reaction pathways in the immobilization and release of DSi. I supply anoxic solutions containing variable concentrations of Fe(II), DSi and DP to 10 cm of the sediment columns and collect samples from 1 cm layer of overlying water that is initially kept aerated. The results show that the release of DSi from sediment does not necessarily depend on oxygen conditions, although dissolved Fe(II) is supplied to the columns. The dominant mechanisms proposed is that, at near-neutral pH, the presence of high DP levels (including DP supplied to and produced within the sediment columns) inhibit the co-precipitation and adsorption of DSi, hence preventing DSi retention in sediments under oxic overlying water. I conclude that the relative production rates of porewater DP and DSi likely represents the major control on the redox dependence of internal Si loading in freshwater systems.

Chapter 2

Amorphous silica: surface processes and dissolution kinetics

2.1 Summary

The availability of dissolved silicon (DSi) exerts an important control on the structure and activity of plankton communities in aquatic environments: DSi limitation can shift species dominance from diatoms to non-siliceous algae and increase the likelihood of harmful algal blooms. The availability of DSi in the water column in turn depends on the dissolution kinetics of amorphous silica (ASi), which are controlled by the surface properties of ASi and reactions occurring at the silica-solution interface. In this study, the surface properties of ASi of various origins were characterized using potentiometric titrations and modelled with a constant capacitance surface complexation model. The dissolution kinetics were measured in batch experiments under controlled conditions. The kinetic results agree with the non-linear relationship between the dissolution rate of ASi and the degree of undersaturation of the aqueous solution observed in earlier studies. This implies that at least two dissolution rate constants are needed to describe the reaction kinetics at high (typically, >0.4) and low (typically, <0.4) degrees of undersaturation. The results also confirm the accelerating effects of pH and Na^+ ions on the dissolution rates of ASi. The quantitative relationships between the dissolution kinetics of ASi and the key environmental variables pH, degree of undersaturation, and salinity obtained in this study, consolidate the general framework for understanding and quantifying reactive Si recycling in freshwater systems.

2.2 Introduction

As one of the main primary producers and a basis for some of the most productive food chains in aquatic systems, diatoms play a fundamental role in exporting carbon to higher trophic levels and in maintaining the health of ecosystems (Reynolds, 2006). Dissolved silicon (DSi) is an essential nutrient for diatoms who use it to produce siliceous frustules. As a result, the Si content of diatoms ranges between 5% and 37% of dry weight (Nelson et al., 1995; Simpson and Volcani, 1981; Volcani, 1981). Human activities, including nutrient enrichment, land use changes and river flow management, have often led to a depletion of DSi relative to other macronutrients, especially nitrogen (N) and phosphorus (P), in water bodies (Conley et al., 2008; Danielsson, 2014; Maavara

et al., 2014; Nteziryayo and Danielsson, 2018b; Rocha et al., 2002; Schelske, 1985; Schelske and Stoermer, 1971; Schelske et al., 1983). The depletion of DSi may shift the species composition of phytoplankton from diatoms to non-siliceous algae dominant (Conley et al., 1993; Egge and Aksnes, 1992; Makulla and Sommer, 1993; Officer and Ryther, 1980), which may further increase the risk of harmful algal blooms

Diatoms, plants and other siliceous organisms deposit DSi in their tissues as a hydrated, cryptocrystalline polymer of silica usually called amorphous silica, or ASi (Simpson and Volcani, 1981). The dissolution of ASi supplies DSi to the water column, and modulates the amount of ASi preserved in aquatic sediments (Bootsma et al., 2003). For example, 97% of the ASi produced by marine diatoms is recycled in the water column and the underlying sediments. Recycling of ASi by dissolution by far exceeds the external input of DSi to the oceans (Tréguer et al., 1995). The recycling of ASi, however, exhibits large temporal and spatial variations in both marine and freshwater systems (Aston, 1983), posing a challenge to the quantitative understanding of Si cycling.

Starting with simple batch experiments, laboratory studies have been widely used to investigate the dissolution rate of ASi under well-controlled conditions. These experimental studies show that the dissolution rate of ASi depends on the physicochemical properties of both the ASi, including the specific surface area (Lasaga, 1995; Oconnor and Greenberg, 1958), impurity content (Van Bennekom et al., 1991; Van Cappellen et al., 2002), and age of the silica (Loucaides et al., 2012b; Van Cappellen et al., 2002; Van Cappellen and Qiu, 1997a, b), and those of the aqueous medium, including temperature (Hurd, 1972, 1973; Kamatani, 1982; Kamatani and Riley, 1979), pH (Fraysse et al., 2006; Hurd, 1972), electrolyte composition (Icenhower and Dove, 2000; Lewin, 1961), and microbial activity (Alfredsson et al., 2016; Bidle and Azam, 1999, 2001).

To quantify the effect of individual environmental variable on the ASi dissolution rate, the first-order kinetic law has been widely used (Hurd, 1972, 1973; Kamatani, 1982; Kamatani and Riley, 1979; Loucaides et al., 2012b; Van Cappellen et al., 2002). Assuming that the net dissolution rate is the balance between reversible detachment and attachment of DSi at specific surface sites of the silica, linear relationships between the reaction rate and the degree of undersaturation would be expected (Dixit et al., 2001; Hurd, 1973; Kamatani and Riley, 1979; Van Cappellen et al., 2002;

Van Cappellen and Qiu, 1997b). However, the surface of ASi, and the corresponding surface sites, are not constant during dissolution. Bulk specific surface areas, as measured for instance by the N_2 adsorption method, may not account for changes in the surface area fraction (Falaize et al., 1999; Fraysse et al., 2009; Hubbard and Riley, 1984; Kamatani et al., 1980; Van Cappellen et al., 2002). Furthermore, detailed studies using flow-through reactors have yielded non-linear dependence of the dissolution rate and degree of undersaturation (Dove et al., 2008; Van Cappellen and Qiu, 1997b). In particular, the strong acceleration of the dissolution rate under high degrees of undersaturation points to different reaction mechanisms and silica surface structures at different degrees of undersaturation.

Much of the previous work on ASi dissolution has focused on mimicking marine environmental conditions (Bidle and Azam, 1999; Dixit and Van Cappellen, 2002; Hurd, 1972, 1973; Kamatani and Riley, 1979; Koning et al., 1997; Lehtimaki et al., 2016; Loucaides et al., 2012a; Loucaides et al., 2010b; Rickert et al., 2002; Van Cappellen et al., 2004; Van Cappellen and Qiu, 1997a, b). As shown by Loucaides et al. (2008), at a given temperature, the several-fold faster dissolution rates of ASi in seawater, compared to low-salinity freshwater can in large part be explained by the higher pH and salinity of seawater compared to a typical freshwater.

In this chapter, the dissolution kinetics of ASi, including synthetic and natural materials, are measured in simple NaCl solutions using batch experiments. The effects of pH and NaCl concentration are systematically assessed. In addition, potentiometric titrations are carried out to determine the surface charging properties of the various silicas. The results of the experiments provide baseline data in support of the use of Aerosil OX 50 as a synthetic analog of sediment ASi in the experiments described in the next chapter.

2.3 Materials and Methods

2.3.1 Materials

Dissolution experiments were carried out with Aerosil OX 50 and Aerosil 300 (Evonik Resource Efficiency GmbH), freshly cultured diatom frustules, and an aged freshwater diatomaceous earth (Perma-Guard Inc.) (Table 2.1). Aerosil OX 50 and Aerosil 300 are fumed silicas of high chemical purity. The specific surface area of Aerosil OX 50 (50 $m^{-2}g^{-1}$) falls within the typical range of

biogenic silicas. The diatomaceous earth are deposits of *Aulacoseria* diatom frustules (92 weight % SiO_2) formed during the Miocene in southern Nevada. The diatomaceous earth was suspended in a 50% (w/w) solution of HNO_3 to remove impurities. The suspension was then repeatedly centrifuged at 5000 rpm and resuspended in water until the pH stabilized at a near-neutral value.

The fresh diatoms, *Cyclotella sp., Navicula Pelliculosa, and Cyclotella meneghiniana*, were cultured in CHU-10 medium at room temperature (20±3 °C) under a 16/8 light-dark cycle with a light intensity of 50-65 mE m^{-2} s^{-1}. Twice a week, the diatoms were harvested on 0.2 μm pore-size polypropylene membrane filters. The collected cells were rinsed 3 times with Milli-Q water, frozen immediately and subsequently freeze-dried. After the freeze-drying cycle, the organic matrix of diatoms was removed by incubating the cells in concentrated nitric acid at 100 °C for 20 min. Cultured frustules were repeatedly centrifuged at 11000 rpm for 20 min and resuspended in Milli-Q water until the suspension pH returned to neutral conditions. The suspension was then freeze-dried. The harvest and cleaning processes were repeated until sufficient diatom frustules were collected to carry out the experiments.

Table 2.1. Amorphous silica (ASi) used in the experiments

ASi type	Specific surface area (s) [1]	Surface site density [2]	Capacitance [3]	Bulk solubility [4]	Dissolution rate constant (k) [5]	Deprotonation constant ($-\log K_{-}^{int}$) [6]
	$m^2\ g^{-1}$	$OH\ nm^{-2}$	$F\ m^{-2}$	$\mu mol\ L^{-1}$	$\mu mol\ m^{-2}\ h^{-1}$	
Aerosil OX 50	50	2.25	1.3	1480	0.28	7.7
Aerosil 300	300	2.25	1.3	2000	--	8.4
Cyclotella sp.	102	4.60	5.0	1351	0.39	7.2
Cyclotella meneghiniana	79	4.60	5.0	1156	0.22	7.1
Navicula pelliculosa	100	--	--	1300	0.33	--
Diatomaceous earth	35	0.50	5.0	--	--	7.1

[1]Measured by N_2 BET on a Gemini VII instrument; [2, 3] From previous studies (Charlet et al., 1993; Evonik Industries AG, 2015; Zhuravlev, 1987); [4, 5] "Fast" dissolution rate constants at pH 7.5 and 25±1 °C in this study. [6] Derived from constant capacitance model fits in this study, with initial values selected from previous studies (Dixit and Van Cappellen, 2002; Fraysse et al., 2009; Loucaides et al., 2010a; Osthols, 1995).

2.3.2 Potentiometric titrations

The surface charge of the different ASi materials were measured by potentiometric titrations in the pH range of 4.0 to 8.5. The surface site densities and site compositions were determined by fitting the experimental titration data with a surface complexation model (see below). The titration experiments were conducted at 25±1 °C in a 0.01 M NaCl matrix solution using a Metrohm 907 Titrando equipped with a high-resolution pH meter. The ASi suspensions of 1 g L^{-1} were continuously stirred for 3 days to equilibrate with the electrolyte solution, and then sparged with N_2 gas for 3 hours to degas CO_2. Before each titration, the pH value of the suspension was adjusted to 3 by stepwise additions of 0.02 M HCl. Titration started with the automatic injection of 0.1-15 µL of 0.02 M NaOH with a pH step of 0.2 units. A signal drift of less than 0.5 mV per minute or a maximum waiting time of 1 hour was used as the equilibrium criterium. The background solution, obtained by filtering the suspension of ASi through a 0.2 µm pore-size filter, was titrated in exactly the same manner as the ASi suspension described above. Humidified N_2 gas was continuously sparged during the titrations to keep the suspension CO_2 free, and the experimental reactor was covered with punctured Parafilm to minimize evaporation.

2.3.3 Surface charge calculations

In titrating a suspension of ASi, the silanol groups (>SiOH) formed by the hydration of the silica surface can protonate and deprotonate:

$$> \mathrm{SiOH} + \mathrm{H^+} \leftrightarrow \mathrm{SiOH_2}^+ \quad (2.1)$$

$$> \mathrm{SiOH} \leftrightarrow \mathrm{SiO^-} + \mathrm{H^+} \quad (2.2)$$

These reactions are responsible for the pH-dependent evolution of the surface charge of the ASi in the absence of specifically adsorbing ions other than H^+ and OH^-. According to charge balance, any point on the titration curve can be expressed by:

$$C_\mathrm{A} + [> \mathrm{SiO^-}] + [\mathrm{OH^-}] + [\mathrm{H_3SiO_4}^-] = C_\mathrm{B} + [> \mathrm{SiOH_2}^+] + [\mathrm{H^+}] \quad (2.3)$$

where [ ] indicates the molar concentration of a solute or surface species, expressed per unit volume solution, and C_A and C_B are the concentrations of acid (HCl) and base (NaOH) added, respectively.

The net surface charge Q can be calculated as a function of pH from the difference between the total amount of added base or acid and the equilibrium OH^- and H^+ ion concentrations, normalized to the ASi concentration a (g L^{-1}) (Stumm, 1992):

$$Q = \frac{C_A - C_B - 10^{-pH}(\gamma_{H^+})^- + 10^{(-pK_w+pH)}(\gamma_{OH^-})^- + [H_3SiO_4^-]}{a} \quad (2.4)$$

where γ_{H^+} and γ_{OH^-} are the activity coefficients of H^+ and OH^-, respectively, and pK_w is the negative logarithm of the water dissociation constant. The concentration of $H_3SiO_4^-$ as a function of pH was estimated by titrating the background solution. Consequently, the net surface charge Q of ASi can be alternatively calculated with:

$$Q = \frac{C_{Ai}(\text{suspension}) - C_{Ai}(\text{electrolyte}) - C_{Bi}(\text{suspension}) + C_{Bi}(\text{electrolyte})}{a} \quad (2.5)$$

where C_{Ai} and C_{Bi} correspond to the concentrations of acid and base, respectively, for the i^{th} addition of titrant to the ASi suspension and electrolyte solution, respectively. The surface charge density σ of ASi (C m^{-2}) is then given by:

$$\sigma = \frac{Q \cdot F}{s} \quad (2.6)$$

where F is the Faraday's constant (96485 C mol^{-1}), and s the specific surface area (m^2 g^{-1}).

The acid-base titration data were fitted with the constant capacitance model in FITEQL and deriving the intrinsic dissociation constant (-log K^{int}) of the surface silanol groups (Herbelin and Westall, 1999). The protonation reaction for ASi was ignored when fitting the titration data because of the very low point of zero charge of ASi ($pH_{zpc} \approx 2.0$-3.5) (Dixit and Van Cappellen, 2002; Stumm, 1992).

2.3.4 Dissolution experiments

Preliminary experiments were done with Aerosil OX 50 to test the effects of variable HEPES (4-(2-hydroxyethyl)-1-piperazineethanesulfonic acid) concentrations on the suspensions' pH stability and ASi dissolution rate. The results indicated that the addition of different amounts of HEPES barely affected the dissolution rate of ASi, and that 0.01 M HEPES was sufficient to keep pH stable during the experiments with solid to solution ratios of 1 g L^{-1} or 0.2 g L^{-1}.

Table 2.2. Experimental design for dissolution kinetics of amorphous silica (ASi).

Exp. No.	ASi	Solution	Solid:solution ratio	pH
1	Aerosil OX 50	0.001, 0.005, 0.007, 0.01, 0.05, 0.1, 0.3, 0.7 M NaCl + 0.01 M HEPES	1 g L^{-1}	6.8, 8.2
2	Aerosil OX 50	0.01 M NaCl + 0.01 M HEPES	1 g L^{-1}, 0.2 g L^{-1}	6.8, 7.5, 8.2
3	Aerosil 300		1 g L^{-1}	7.5
4	Freshwater diatomaceous earth		1 g L^{-1}, 0.2 g L^{-1}	6.8, 7.5, 8.2
5	*Cyclotella sp.*		0.2 g L^{-1}	6.8, 7.5, 8.2
6	*Navicula pelliculosa*		0.2 g L^{-1}	7.5
7	*Cyclotella meneghiniana*		0.2 g L^{-1}	7.5

The different dissolution experiments are summarized in Table 2.2. In experiment series 1, the effect of varying the NaCl concentration from 0.001 to 0.7 M NaCl on the dissolution of Aerosil OX 50 was tested. All other experiment series were run in 0.01 M NaCl. The dissolution experiments were carried out in 12 mL cleaned polypropylene tubes containing 10 mL of NaCl solution, whose pH value had been pre-adjusted with NaOH and HCl. The tubes were kept at 25± 1 °C on a rotating shaker at 18 rpm. In the case of the cultured diatom frustules, a solid concentration of 0.2 g ASi L^{-1} was used and aliquots of 2 mL suspension were collected at designated intervals because of the limited amounts of biogenic ASi available.

2.3.5 Analytical methods

All samples and solid reagents were weighed on an analytical balance with a precision of 0.1 mg and all solutions were prepared by dissolving analytical-grade reagents in Milli-Q water, unless otherwise stated. Samples collected from the dissolution experiments were filtered with 0.45 µm pore-size polypropylene syringe filters (EMD Millipore Corporation), acidified with ultra-pure nitric acid to pH < 2, and analyzed using Inductively Coupled Plasma-Optical Emission Spectroscopy (ICP-OES, Thermo Scientific iCAP 6300) for the concentrations of total dissolved Na, Si, and Fe with the US EPA Method 200.7. Matrix-matched standards were prepared from Fisher Scientific stock standards (Thermo Fisher Scientific) to eliminate matrix interferences on the analytical results. Reference samples prepared with multi-element standards (Delta Scientific Laboratory Products Ltd.) were analyzed along with all samples for data quality control. The precision of the reference sample measurements across the sample run was better than 10%, and the relative standard deviations were within 5%. For samples with a volume smaller than that required for ICP-OES analysis and the DSi concentration was below the ICP-OES detection limit after dilution, the molybdenum blue method (U.S. EPA., 1978) was used on a UV-Vis Spectrophotometer (Thermo Evolution 260) to measure the DSi concentration, with the precision better than 10%.

2.4 Results

2.4.1 Potentiometric titrations

From the data of the titration experiments, the pH-dependent surface charges of the different ASi materials were calculated with Equations (2.5) and (2.6). The results are shown in Figure 2.1. All ASi materials carried negative surface charge in the pH range of 4.0 to 8.5. They also showed increasing electrical charge build-up with increasing pH. However, large differences in the magnitudes of the charge per unit area were observed. The freshly harvested frustules had higher negative surfaces than Aerosil OX 50. For example, at pH 8.5, the absolute surface charges of fresh diatom frustules were more than three times than that of the Aerosil OX 50.

The surface charge of diatomaceous earth versus pH deviated significantly from the observed pH trends of the other ASi. In particular, between pH 4 and 5.5 the diatomaceous earth exhibited much larger negative surface charges than the other ASi. The trend for the diatomaceous earth, with the distinct break at pH 5.5, also could not be captured by the constant capacitance model. Possibly, the high negative surface charging at pH < 5.5 is due to a non-silica constituent within the earth mixture (Dixit and Van Cappellen, 2002). In what follows, only the data at pH ≥ 5.5 were modeled after correcting the surface charges assuming the pH 5 charge is entirely due to non-ASi constituents (the corrected data are shown by the black squares on Figure 2.1).

2.4.2 Surface complexation model

To fit the surface charge data with the constant capacitance model in FITEQL, five sets of simulations were carried out for various ASi materials. These sets of simulations and the results are illustrated Table 2.3 for Aerosil Ox 50. In each simulation, a value of the capacitance was imposed and initial values were assigned to the intrinsic proton dissociation constant, the total silanol site concentration and the aqueous silicic acid (or DSi) concentration. Note that the latter accounts for the fact that during the titration some dissolution of the solid takes place. The five sets of the simulations differed by the parameters that were optimized for. That is, the latter parameters were allowed to deviate from their initial values, while the values of the other parameters were hold constant. Goodness of fit was estimated using the weighed sum of squares

divided by the number of degree of freedom, WSOS/DF, where DF is equal to the number of parameters being optimized.

Simulation 1 yielded the best fits to the Aerosil OX 50 experimental data judging from the WSOS/DF values (Table 2.3). However, the optimized silanol site densities were much lower than those obtained in previous studies that assessed ASi surface site densities via titration and/or adsorption experiments (Dixit and Van Cappellen, 2002; Fraysse et al., 2009; Loucaides et al., 2010a; Osthols, 1995). Moreover, some of the optimized DSi concentrations in Simulation 1 exceeded the solubility of ASi under the experimental conditions. Simulation 3 yielded reasonable intrinsic dissociation constants of reaction (2-2) when imposing surface site densities close to those previously reported: 2.25 >SiOH nm^{-2} for Aerosil OX 50, 4.60 >SiOH nm^{-2} for the freshly harvested diatom frustules, and 0.5 >SiOH nm^{-2} for diatomaceous earth.

Given that, overall, the simulation 3 results produced good fit to the data, they guided the selection of the parameter values for the surface complexation modeling. The selected parameter values are summarized in Table 2.1 and the model fits of the surface charge data are shown in Figure 2.1. The interdependence of the surface site density and the proton dissociation constants, typically expressed in negative logarithmic form, -log K_{-}^{int}, is illustrated in Table 2.4, which provides the ranges of -log K_{-}^{int} corresponding to plausible ranges in site densities for the different ASi materials.

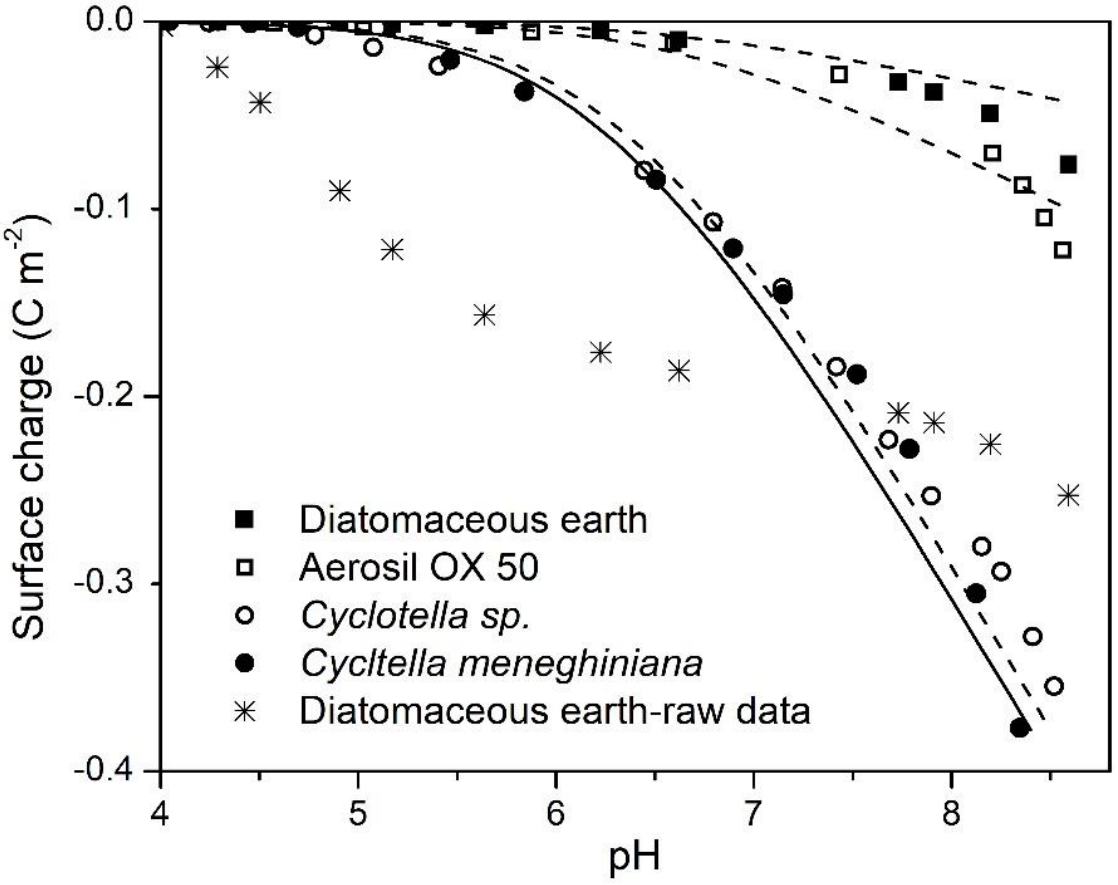

Figure 2.1. Surface charge density of various amorphous silica (ASi) as a function of pH. The data points are calculated with Equations (2.5) and (2.6) using the results of the potentiometric titrations; the solid squares are obtained by subtracting the charges of the diatomaceous earth measure at pH 5.5 from the charges measured at pH $\geq$ 5.5. This correction assumed that the charges measure at pH $\leq$ 5.5 are associated with non-siliceous detrital constituent in the diatomaceous earth. The lines are pH-dependent surface charges calculated the constant capacitance model.

Table 2.3. Simulation scenarios for fitting the constant capacitance model to the potentiometric titration data for Aerosil OX 50 with FITEQL.

Simulation No.[1]	Capacitance[2]	Parameters to be optimized	Initial -log K[3]	Initial silanol density α[4]	Initial H_4SiO_4[5]	Final -log K	Final silanol density α	Final H_4SiO_4	WSOS/DF[6]
	F m^{-2}	-	-	SiOH nm^{-2}	µM	-	>SiOH nm^{-2}	µM	-
1	0.4	K, α, H_4SiO_4	7.5	2.25	400	--	--	--	--
	0.5	K, α, H_4SiO_4	7.5	2.25	400	6.8	1.37	1809	3.23
	1.3	K, α, H_4SiO_4	7.5	2.25	400	6.4	0.33	2005	3.51
	2.0	K, α, H_4SiO_4	7.5	2.25	400	6.4	0.30	2048	3.65
	6.0	K, α, H_4SiO_4	7.5	2.25	400	6.5	0.29	2094	3.86
2	1.3	K, α	7.5	2.25	400	--	--	--	--
	1.3	K, α	7.5	2.25	1200	7.3	1.32	1200	4.90
	1.3	K, α	7.5	2.25	1800	6.6	0.40	1800	3.50
	1.3	K, α	7.5	2.25	2000	6.4	0.33	2000	3.39
	0.5	K, α	7.5	2.25	1200	--	--	--	--
	0.5	K, α	7.5	2.25	1800	6.9	1.57	1800	3.12
	0.5	K, α	7.5	2.25	2000	6.2	0.44	2000	3.24
3	0.5	K	7.5	1.00	1800	6.7	1.00	1800	3.04
	0.5	K	7.5	2.25	1800	7.1	2.25	1800	3.03
	0.5	K	7.5	4.60	1800	7.4	4.60	1800	3.04
	0.5	K	7.5	5.50	1800	7.5	5.50	1800	3.04
	0.5	K	7.5	10.00	1800	7.8	10.00	1800	3.05
	1.3	K	7.5	1.00	1800	7.5	1.00	1800	6.75
	1.3	K	7.5	2.25	1800	8.0	2.25	1800	8.20
	1.3	K	7.5	4.60	1800	8.3	4.60	1800	8.75
	1.3	K	7.5	10.00	1800	8.7	10.00	1800	9.00
4	0.5	α, H_4SiO_4	6.2	2.25	1800	6.2	0.47	1948	3.21
	0.5	α, H_4SiO_4	7.5	2.25	1800	7.5	5.57	1773	3.13
	0.5	α, H_4SiO_4	7.9	2.25	1800	7.9	13.77	1767	3.13
	0.5	α, H_4SiO_4	8.5	2.25	1500	8.5	54.36	1764	3.14
	1.3	α, H_4SiO_4	6.2	2.25	1800	6.2	0.28	2129	3.55
	1.3	α, H_4SiO_4	7.5	2.25	1800	7.5	1.50	1300	4.80
	1.3	α, H_4SiO_4	7.9	2.25	1800	7.9	3.47	1212	5.12
	1.3	α, H_4SiO_4	8.5	2.25	1500	8.5	13.2	1169	5.3
5	0.5	K, H_4SiO_4	8.5	2.25	1800	7.1	2.25	1789	3.12
	1.3	K, H_4SiO_4	8.5	2.25	1800	7.7	2.25	1233	5.00

[1]For each of the scenario series the shaded cells identify which parameter sensitivity is being tested. The corresponding parameter value was adjusted manually to determine its effect on the goodness-of-fit.
[2]The value of capacitance cannot be optimized in FITEQL, the values listed are based on previous studies (Dixit and Van Cappellen, 2002; Fraysse et al., 2006, 2009; Loucaides et al., 2010; Osthols, 1995).
[3]Values of initial -log K were selected from previous studies (Dixit and Van Cappellen, 2002; Loucaides et al., 2010a; Osthols, 1995; Fraysse et al., 2006).
[4]Values of initial H_4SiO_4 concentrations were assigned based on concentrations measured in the filtered electrolyte solutions of the titration experiments, based on the solubility of ASi measured in the dissolution experiments.
[5]Initial surface silanol densities α from previous studies (Armistead et al., 1969; Osthols, 1995).
[6]WSOS/DF: Weighted sum of squares divided by degree of freedom.

The baseline -log K_{-}^{int} values for *Cyclotella sp.* and *Cyclotella meneghiniana* were 7.2 and 7.1, respectively. Synthetic Aerosil OX 50 and Aerosil 300 had somewhat higher -log K_{-}^{int} values, 7.7 and 8.4, respectively. These values are very close to those obtained by Loucaides et al. (2010a) for fresh biogenic silica (6.8) and Aerosil OX 50 (7.8). While the model calculations converged for the diatomaceous earth, the fit to the corrected experimental data was not as good as for the other ASi materials (Figure 2.1), as also reflected by the almost 50 times larger WSOS/DF value than for Aerosil OX 50. With the model parameters in Table 2.1, the constant capacitance model predicts that at pH 8.5 26%, 51% and 50% of the silanol groups were deprotonated for Aerosil OX 50, the *Cyclotella sp*. and diatomaceous earth, respectively.

Table 2.4. Best guesstimates of silanol densities and ionization constants of the ASi materials.

Amorphous silica	Surface silanol density >SiOH nm^{-2}	-log K_{-}^{int}
Aerosil OX 50	2.25 (1.00 - 5.50)	7.7 (6.5 - 7.5)
Aerosil 300	2.25 (1.00 - 5.50)	8.4 (7.7 - 8.4)
Cyclotella sp.	4.60 (1.00 - 5.50)	7.2 (6.3 - 7.3)
Cyclotella meneghiniana	4.60 (2.25 - 4.60)	7.1 (6.7 - 7.1)
Diatomaceous earth	0.50 (0.40 – 1.00)	7.1 (7.0 - 7.5)

2.4.3 Dissolution kinetics of amorphous silica

2.4.3.1 Dissolution of different ASi at pH 7.5

The relative dissolution kinetics of the different ASi materials are illustrated in Figure 2.2. As expected, the dissolution of Aerosil 300 was fastest and reached equilibrium with the aqueous phase within the first 24 hours. In comparison, the dissolution of diatomaceous earth was so slow that the DSi concentration remained near zero after 140 hours at a solid to solution ratio of 1 g L^{-1}. The dissolution kinetics of Aerosil OX 50 fell between those of Aerosil 300 and the diatomaceous earth, releasing about 800 µM DSi to the aqueous phase after 150 hours (Figure 2.2, panel a). For the cultured diatoms frustules, at 0.2 g L^{-1} solid to solution ratio, steady DSi concentrations were reached after about 900 hours (Figure 2.2, panel b). For the same 0.2 g L^{-1} solid to solution ratio, it took Aerosil OX 50 about 1500 hours to reach equilibrium. Note that the solubility of Aerosil OX 50 and *Cyclotella sp*. were quite close to one other.

The first-order kinetic law has been widely used to analyze ASi dissolution data in batch experiments (Barker et al., 1994b; Hurd, 1972, 1973; Loucaides et al., 2012a; Van Cappellen et al., 2002):

$$R_{aq} = dC/dt = k^* \cdot (C_{\mathrm{eq}} - C) \qquad (2.7)$$

where R_{aq} is the dissolution rate in units of DSi produced per unit time (µmol L^{-1} h^{-1}), C is the concentration of DSi (µmol L^{-1}), C_{eq} is the equilibrium concentration of DSi (µmol L^{-1}), t is the reaction time (h), and k^* is the dissolution rate constant (h^{-1}). Given that the initial concentration of DSi at t = 0 is zero, integration of Equation (2.7) gives:

$$\ln\left[(C_{\mathrm{eq}} - C)/\,C_{\mathrm{eq}}\right] = -k^* \cdot t \qquad (2.8)$$

where the slope of ln [(C_{eq} - C)/C_{eq}] versus t is equal to -k^*. The term [(C_{eq} - C)/C_{eq}] is referred to as the degree of undersaturation. It is a nondimensional value that varies from 1 (highest undersaturation) to 0 (equilibrium). Thus, the value of k^* can be derived from a log-linear plot of the degree of undersaturation against time.

As the dissolution of solid phase takes place at the solid-aqueous solution interface, in order to compare the dissolution kinetics of different ASi materials, the rate is often normalized to the

amount of exposed surface area. For a specific surface area s ($m^2\ g^{-1}$) and a solid to solution ratio m ($g\ L^{-1}$) of ASi (m = 1 or 0.2 $g\ L^{-1}$ in this study), the rate per unit of exposed surface area, R, is given by:

$$R = R_{aq}/(m \cdot s) \tag{2.9}$$

where R is in unit of $\mu mol\ m^{-2}\ h^{-1}$. The rate R is then expressed as:

$$R = k \cdot [(C_{eq} - C)/C_{eq})] \tag{2.10}$$

where k, the surface area normalized dissolution rate constant of ASi in units of $\mu mol\ m^{-2}\ h^{-1}$, is derived from the observed rate constant k^*:

$$k = k^* \cdot [C_{eq}/(m \cdot s)] \tag{2.11}$$

A typical dissolution curve for *Navicula pelliculosa* frustules is shown in panel a of Figure 2.3. Plotting the data in a log-linear plot according to with Equation (2.8) reveals that the dissolution process can be broken down in three phases (Figure 2.3, panel b): (1) a very rapid initial build-up of DSi, likely due to fast release of adsorbed H_4SiO_4, followed by (2) fast ASi dissolution at high degree of undersaturation, and lastly, (3) a slower dissolution as the ASi-aqueous solution system approaches equilibrium. Each of the three stages, can be assign its own apparent (k^*) and surface normalized (k) rate constants. To compare the dissolution kinetics of the different ASi materials, in what follows, I use the rate constants k of the fast dissolution stage (*i.e.*, the second stage). These dissolution rate constants are summarized in Table 2.1. As can be seen, the values are all of similar order of magnitude. Note that the values of the rate constants for all three stages of the dissolution experiments can be found in the supplementary information (Table A.2).

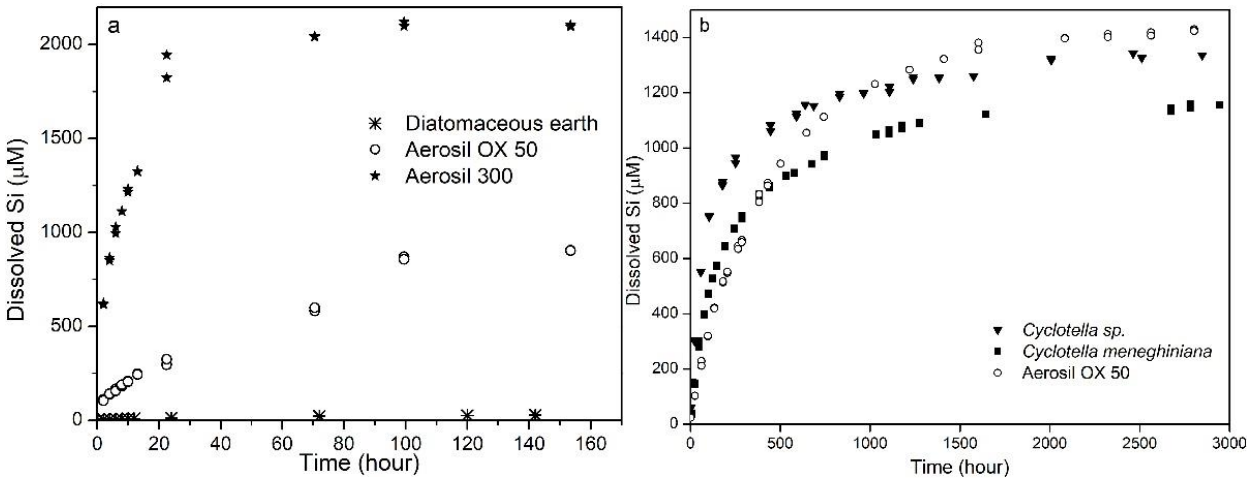

Figure 2.2. Dissolution kinetics of the different ASi in 0.01 M NaCl, pH 7.5 suspensions with (a) 1 g L^{-1} solid to solution ratio at room temperature (20±3 °C), and (b) 0.2 g L^{-1} solid to solution ratio at 25±1 °C.

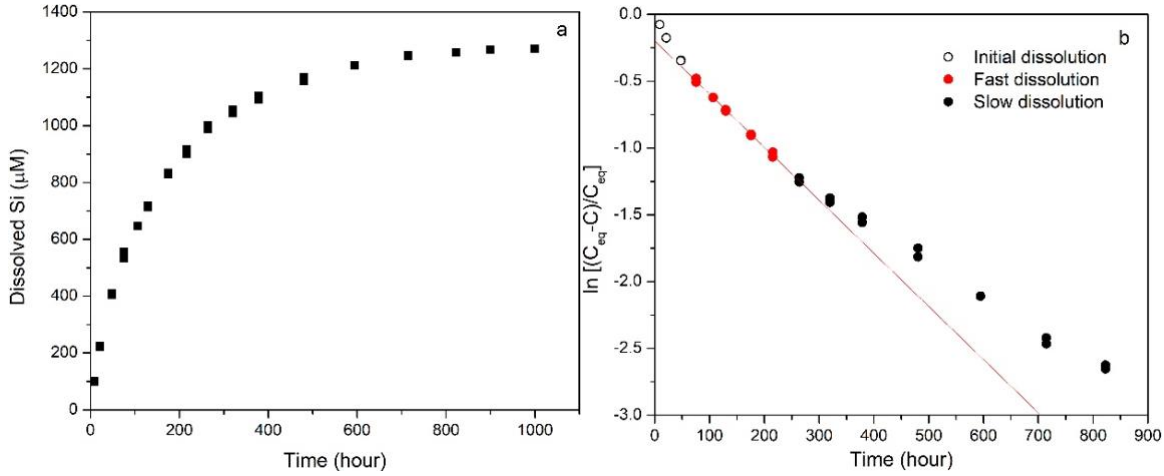

Figure 2.3. The dissolution kinetics of *Navicula pelliculosa* frustules in a batch experiment (0.2 g ASi in 1 L matrix solution with 0.01 M NaCl and pH 7.5, 25±1 °C). (a) DSi concentration versus time; (b) log-linear plot of [(C_{eq} - C)/C_{eq}] versus time (Equation (2.8). The slopes of the red line in panel (b) correspond to the "fast" dissolution rate constant k.

2.4.3.2 Dissolution kinetics: effect of pH

Aerosil OX 50 and acid-cleaned *Cyclotella sp.* frustules were suspended in 0.01 M NaCl plus 0.01 M HEPES solutions at pH values 6.8, 7.5 and 8.2 (Experiments 2 to 7, Table 2.2). The pH-dependent dissolution rate constants (k) calculated for the fast dissolution stage of ASi are shown in Figure 2.4. As can be seen, the logarithms of the dissolution rate constants increased linearly with pH. The dissolution rate constant of *Cyclotella sp.* at pH 8.2 was about 4.5 times larger than that at pH 6.8, whereas for Aerosil OX 50 it was about 3 times higher.

The effect of pH on the kinetics of silica dissolution has been widely studied, including for quartz (Brady and Walther, 1990; Knauss and Wolery, 1988), vitreous silica (Wirth and Gieskes, 1979), and biogenic silica (Fraysse et al., 2006; Lewin, 1961; Loucaides et al., 2008; Van Cappellen et al., 2002). The positive correlation between the dissolution rate constant and pH is explained by the increasing surface charge as pH increases, because of deprotonation of the surface silanol groups. Charged surface sites are inherently less stable and therefore dissolved faster.

The following surface reaction model (Dove, 1992, Fraysse, 2006) has been used to express the dissolution kinetics of ASi at different pH:

$$k = k_0 \cdot \theta_{>\mathrm{SiOH_2^+}} + k_1 \cdot \theta_{>\mathrm{SiOH}} + k_2 \cdot (\theta_{>\mathrm{SiO^-}})^n \qquad (2.12)$$

where $\theta_{>\mathrm{SiOHi}}$ is the fraction of the i-th surface species, k_0, k_1 and k_2 are the rate constants associated with the different surface species (units: μmol m^2 h^{-1}) and n is the order of the hydroxyl-promoted dissolution.

For pH ≥ 6.8, the protonated silanol groups are negligible, and the first term on the RHS of Equation (2.12) can be ignored. Fitting of the Aerosil OX 50 data then yielded the following rate parameters (R^2 = 0.99): k_1 = 0.04±0.01 (μmol m^2 h^{-1}), k_2 = 3.44±0.37 (μmol m^2 h^{-1}) and n = 1.28 ±0.07. In the pH range 6.0 to 8.5, the pH-dependent dissolution rate constant of Aerosil OX 50 could also be described by:

$$logk = 0.3832 \cdot pH - 3.4277 \qquad (2.13)$$

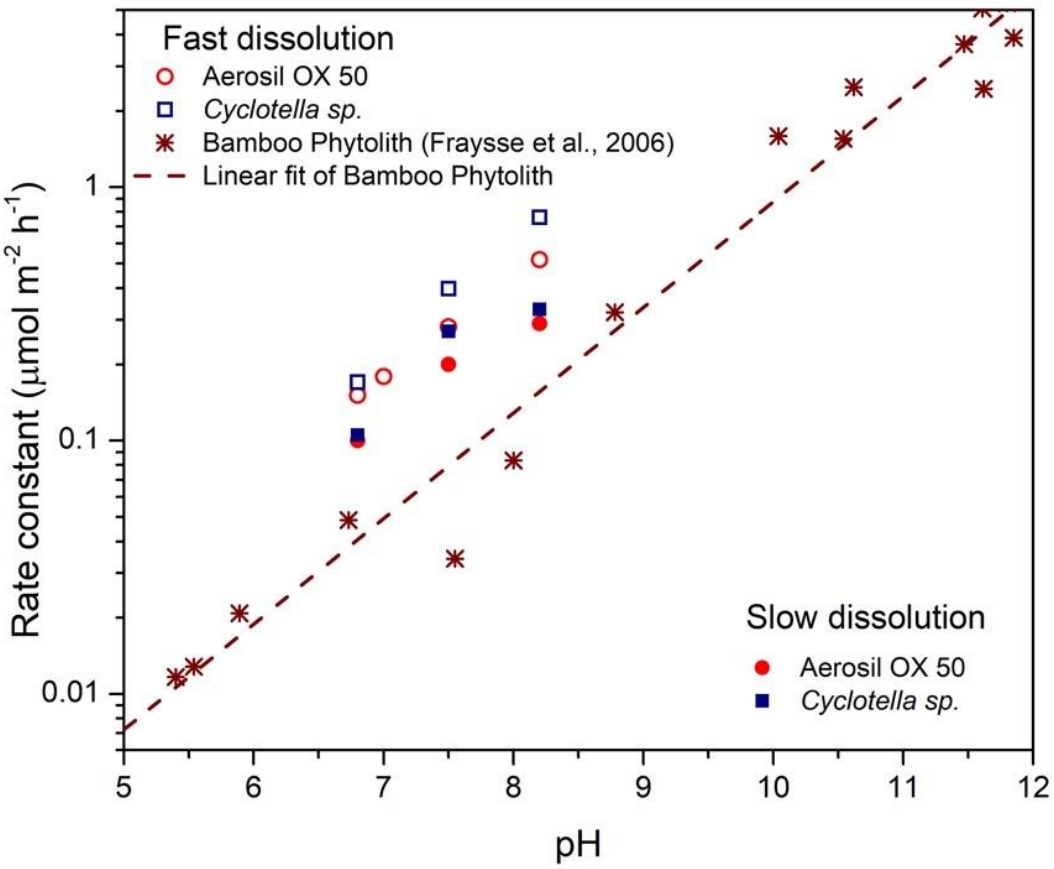

Figure 2.4. Dependence on pH of the surface area normalized dissolution rate constant (*k*) of various ASi materials. Note that the *y* axis is logarithmic. Data for bamboo phytoliths are from Fraysse et al. (2006) who used mixed flow reactors instead of batch experiments. Fast dissolution is the dissolution of ASi under high degree of undersaturation. Slow dissolution is the dissolution of ASi under low degree of undersaturation.

2.4.3.3 Dissolution kinetics: ionic strength dependence

The concentration of NaCl strongly impacted the ASi dissolution kinetics of Aerosil OX 50 at pH 6.8, as shown in Figure 2.5. The largest increase in the rate constant *k* occurred between NaCl concentrations from 0 to 0.1M. At higher NaCl concentrations, the rate constant asymptotically approached its maximum value. Thus, within the ionic strength range for natural fresh waters, the dissolution rate constant of ASi would be expected to be highly sensitive to salinity variations.

The rate-enhancing effect of NaCl on the dissolution kinetics of silica is well-known (Icenhower and Dove, 2000; S. Plettinck, 1994; Seidel et al., 1997). The enhancement effect is generally accepted to be linked to the formation of reactive surface complexes. The formation of these complexes can be described by a Langmuir isotherm, and the rate constant of dissolution is then given by (Icenhower and Dove, 2000; S. Plettinck, 1994):

$$k = k_{\max,\,\mathrm{Na^+}}\left(\frac{K_{\mathrm{abs,Na^+}}\,[m_{\mathrm{Na^+}}]}{1 + K_{\mathrm{abs,Na^+}}[m_{\mathrm{Na^+}}]}\right) + k_{Na,0} \qquad (2.14)$$

where $k_{Na,0}$ is the dissolution rate constant in the absence of NaCl, $k_{max,Na}$ is the maximum dissolution rate in NaCl solution corrected for $k_{Na,0}$, $[m_{Na^+}]$ is the molar concentration of sodium, and K_{abs,Na^+} is the equilibrium constant describing reversible Na^+ adsorption (dimensionless). Least square fitting of the data in Figure 2.5 to Equation (2.14) yielded ($R^2 = 0.99$): 0.07±0.01 and 0.46 ±0.02 µmol m^{-2} h^{-1} for $k_{Na,0}$ and k_{max,Na^+}, respectively, and 25.6±3.1 for K_{abs,Na^+}.

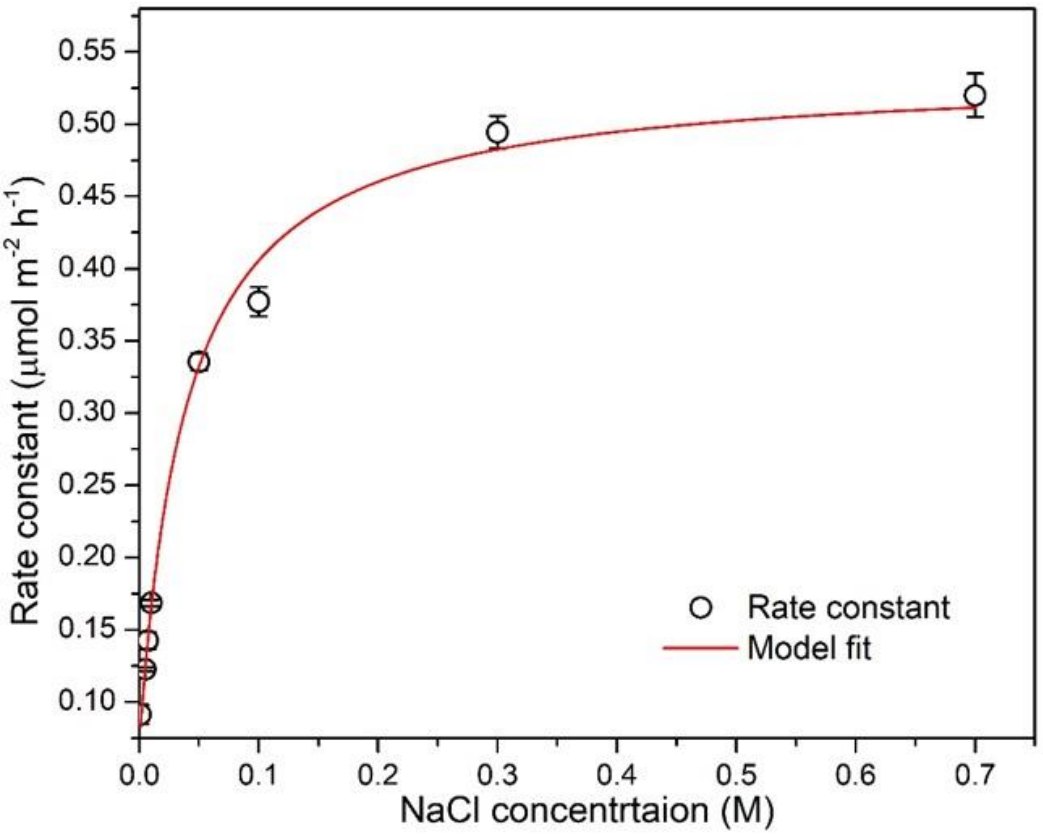

Figure 2.5. Effect of NaCl concentration on the dissolution rate of Aerosil OX 50 at pH 6.8 and 25± 1 °C and at a solid to solution ratio of 1 g L^{-1}. The solid line is the fit of the date to Equation (2.14).

2.5 Discussion

2.5.1 Electrical charging properties

Potentiometric titrations and surface complexation modeling have been widely used to characterize the aqueous surface chemistry of ASi (Dixit and Van Cappellen, 2002; Fraysse et al., 2009; Loucaides et al., 2010a; Osthols, 1995; Stumm, 1992). Because of the very low point of zero charge of ASi ($pH_{zpc} \approx 2.0$-3.5, Dixit and Van Cappellen, 2002), in natural waters the deprotonation of silanol groups is responsible for the negative surface charge of ASi materials (Figure 2.1). The surface charge is therefore mainly controlled by the surface silanol density (α), the intrinsic deprotonation constant ($-\log K^{int}$) and the electrostatic interactions that are accounted for by the capacitance values in surface complexation models.

Values of the surface silanol density and the intrinsic deprotonation constant can, in principle, be obtained by fitting acid-base titration data with constant capacitance model. However, the various model simulation scenarios illustrated in Table 2.3 for Aerosil OX 50, show that similar goodness of fits can be obtained with markedly different parameter values, because the parameters are highly correlated. Thus, a decrease in α can be compensated by a lower value of $-\log K^{int}$ and still yield the same surface charge. In addition, in the constant capacitance model the capacitance value has to be imposed, and the DSi concentration is an unknown parameter. Although I use relatively "fast" titration (about 10 hours for one titration), ASi dissolution can lead to a significant drift in the estimated surface charge, especially at high pH (Loucaides et al., 2010a). This can be corrected by allowing for a high DSi concentration, but this in turn may affect the quality of the model fit at low pH. Here, the best results were obtained with relatively high DSi concentration, close to solubility equilibrium (1000-2000 µM).

Because capacitance cannot be optimized with FITEQL, imposed values were manually varied. While the Simulation 1 results show that the capacitance value does not affect the goodness of fit of the model for Aerosil OX 50 and Aerosil OX 300, it impacts the fits to ASi materials with high charge densities, in particular the fresh cultured diatom frustules. In the model fits shown in Figure 2.1, a capacitance value of 5 F m^{-2} is imposed for *Cyclotella sp.*, *Cyclotella meneghiniana* and diatomaceous earth, and 1.3 F m^{-2} for Aerosil OX 50.

Highly variable surface silanol densities are obtained from the model fits as illustrated in Table 2.3 for Aerosil OX 50 (from 0.3 to ≥ 50 >SiOH nm^{-2}), implying that a high degree of uncertainty associated with these estimates. Similar broad ranges have been reported in previous studies, *e.g.*, Armistead et al. (1969) and Osthols (1995). In part this is due to the different methods used to measure surface site densities of oxide minerals. Zhuravlev (1987, 2000) used the deutrio-exchange method and concluded that the surface site densities of ASi materials varied within the range 4.20 to 5.70 >SiOH nm^{-2} for fully hydroxylated surfaces. The surface silanol density for Aerosil silica materials measured by the lithium alanate method, however, yields smaller values, 2.20 to 2.50 SiOH nm^{-2} (Evonik Industries AG, 2015).

In line with previous work, average total silanol densities of 2.25 and 4.60 >SiOH nm^{-2} are assigned to Aerosil OX 50 and fresh cultured diatoms frustules, respectively (Table 2.4), and 0.50 >SiOH nm^{-2} to the diatomaceous earth. The larger value for fresh frustules, compared to the Aerosil materials accounts for the presence of ionizable silanol groups located within the silica structure. The existence of these internal silanol groups was demonstrated by Loucaides et al. (2010a) and explains the high apparent surface charges on fresh diatom frustules (see also section 2.5.3). The low value for the diatomaceous earth accounts for aging processes that progressively eliminate the microporosity (internal silanol groups) and surface roughness (external silanol groups).

2.5.2 Dissolution kinetics: rate equation

The first-order kinetic law (Equation (2.7) can be derived from transition state theory (TST) when the dissolution of ASi can be treated as an elementary reaction, or when the activation energy of the detachment to solution of the reactive surface sites is much higher than those of other steps. However, the experimental results in this study, as well as previous work, show that a single linear dissolution rate equation does not hold across the entire domain of undersaturation as shown in panel b of Figure 2.3 (see also in Dove et al (2008) and Van Cappellen and Qiu (1997b)). Dove et al. (2008) proposed that the non-linear dissolution kinetics can be explained based on the classical theory of polynuclear nucleation kinetics. According to this theory, the availability of reactive Q_2 surface groups (*i.e.*, silicate groups bonded to the silica lattice via two bridging oxygens) increases

exponentially with increasing degree of undersaturation, as does the dissolution rate. The rate is then controlled by the detachment of Q_2 units at the surface.

The three phases observed during the dissolution batch experiments (Figure 2.3, panel b) can be attributed to the following succession of processes. (1) When ASi is first exposed to a DSi-free aqueous solution, loosely sorbed silicic acid molecules are immediately released to solution. (2) Polynuclear dissolution kinetics at high degree of undersaturation are responsible for the fast dissolution, which can be approximated by the linear rate law together with a relative high rate constant. (3) Below a critical degree of undersaturation, detachment of less reactive Q_3 surface groups (*i.e.*, silicate groups bonded to the silica lattice via three bridging oxygens) becomes the rate-controlling processes. The rate in the third phase can also be represented by the linear law, but with a slower value for the rate constant. The three rate constants describing the three phases of the dissolution processes as listed in Table A.2 for the different ASi materials used in the experiments.

To determine the degree of undersaturation separating the fast (stage 2) from the slow (stage 3) dissolution kinetics, all the existing studies that measured silica dissolution rates across the entire range of degree of undersaturation were assembled, that is, for values of $[(C_{\mathrm{eq}} - C)/\, C_{\mathrm{eq}}]$ from 1 to 0 (Table A.1, Supplementary Information). These include studies on biogenic ASi, synthetic ASi, and quartz (Berger et al., 1994; Dove et al., 2008; Gallinari et al., 2008; Rickert, 2000; Seeberg-Elverfeldt et al., 2005; Van Cappellen and Qiu, 1997b; Wu et al., 2017; Wu et al., 2015; Zhang et al., 2015). For each experimental data set the boundary between fast and slow dissolution is estimated from the intersection of the two corresponding linear trends. The values of the undersaturation boundaries are listed in Table A.1 and plotted as a frequency diagram in Figure 2.6: most values of $[(C_{\mathrm{eq}} - C)/\, C_{\mathrm{eq}}]$ are higher than 0.4, with a mean value around 0.55. Thus, in natural environments when the degree of undersaturation with respect to the dissolving ASi phase rises above 0.55, I can expect a significant acceleration of the dissolution rate (and vice versa).

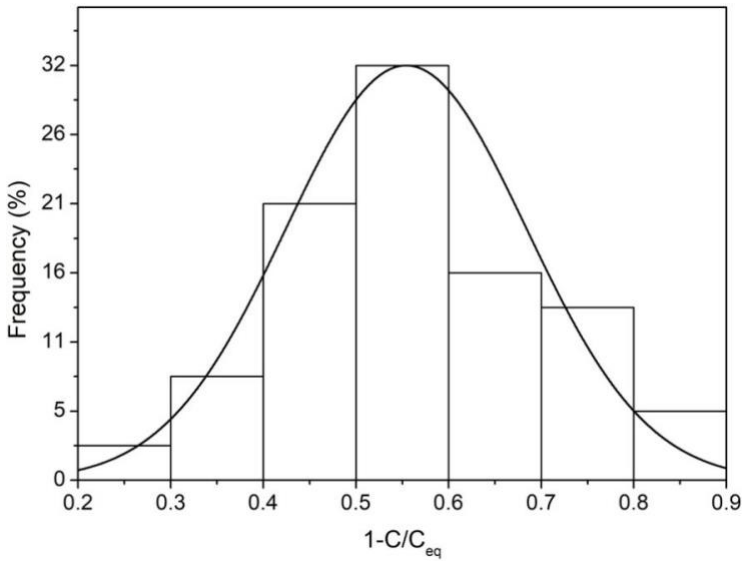

Figure 2.6. Probability distribution of degree of undersaturation at which the transition of "fast" and "slow" ASi dissolution has been observed (n = 39). Data are from previous studies: Berger et al., 1994; Dove et al., 2008; Gallinari et al., 2008; Rickert, 2000; Seeberg-Elverfeldt et al., 2005; Van Cappellen and Qiu, 1997b; Wu et al., 2017; Wu et al., 2015; Zhang et al., 2015. The studies were conducted with cultured biogenic ASi, recent sediments, diatomaceous earth and quartz. For the numerical values of the degree of undersaturation, see Table A.1.

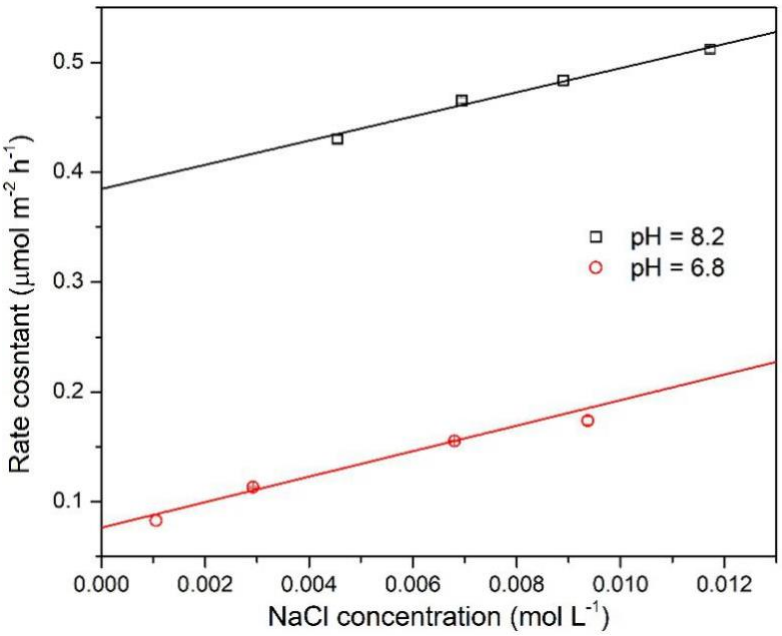

Figure 2.7. Effect of NaCl concentration on the "fast" dissolution rate constant of Aerosil OX 50 at pH 6.8 and 8.2, and at 1 g L^{-1} and 25±1 °C).

2.5.3 Dissolution kinetics: external versus internal silanol groups

The much higher electrical charging of the freshly harvested diatom frustules compared to Aerosil OX 50 (Figure 2.1) is not accompanied by a correspondingly higher dissolution rate (Figure 2.4), as would be expected from the surface complexation model of dissolution (Equation 2.12). This is consistent with the work of Loucaides et al. (2010a) who showed that the electrical charge of nanoporous biogenic silicas measured with potentiometric titrations reflects the ionization of both external and internal silanol groups, but the dissolution kinetics are controlled by the detachment of the external groups only (i.e., the silanol groups that are located on the outer surface of the frustules). This is because the internal groups are accessible to protons, but not to the relatively larger reactants involved in silica dissolution, such as H_2O and Na^+. For non-porous Aerosil OX 50, the absence of internal silanol groups results in a direct correlation between electrical charging and the dissolution kinetics, as embodied by Equation (2.12).

While Aerosil OX 50 provides a useful (and easily available) reference material to study surface-controlled dissolution processes of ASi (Dixit and Van Cappellen, 2002; Loucaides et al., 2010a; Osthols, 1995), it is important to acknowledge the variable fractions of internal and external silanols in biogenic silicas. For example, when using the parameters obtained by fitting Equation (2.12) to the Aerosil OX 50 data (see section 2.4.3.2), the pH-dependent dissolution rate constants of *Cyclotella sp.* are overpredicted. This apparent discrepancy can be resolved by taking into account the presence of (non-reactive) internal silanol groups: the kinetic data then imply that about 67% of the total silanol sites of the fresh *Cyclotella sp.* frustules are accessible to dissolution.

2.5.4 Dissolution kinetic: pH and Na^+

The pH trends of the fast dissolution rate constants of Aerosil OX 50 and *Cyclotella sp.* obtained here are consistent with those of other biogenic ASi, as shown in Figure 2.4. The pH-dependent ionization of silanol groups explains the correlation between the dissolution rate constants of ASi materials and the pH of the bulk solution (Fraysse et al., 2006, and references therein). The accelerating effect of Na^+ provides another example of a solution-driven change in the surface reactivity of silicas (Dove, 1995). As a major cation in fresh and marine waters, Na^+ is adsorbed on silica surfaces as an outer-sphere complex where it enhances the deshielding of >SiOH groups. The resulting change in the electron distribution of the Si atoms weakens the siloxane bond, hence

catalyzing the detachment to solution (Dove and Crerar, 1990; Icenhower and Dove, 2000; S. Plettinck, 1994; Seidel et al., 1997).

The maximum enhancement factor of the dissolution rate constant of Aerosil OX 50 at 0.7 M Na^+ is about 9 (Figure 2.5), which falls within the range of 3 to 21 in previous studies (Dove et al., 2008; Icenhower and Dove, 2000; Plettinck, 1994). The large variation in enhancement factors is likely be due to variable accessibility of surface sites for Na^+ adsorption and differences in experimental conditions. The $K_{abs,Na+}$ constant obtained by fitting Equation (2.14) to the data in Figure 2.5 (25.6±3.1) is close to the value of 22 reported by Icenhower and Dove (2000). Most fresh waters, however, have salinities that correspond to the extreme left side of Figure 2.5. As shown in Figure 2.7, at low Na^+ concentrations, the dependence of the dissolution rate constant of Aerosil OX 50 on the Na^+ concentration can be approximated by a linear relationship. For the pH extremes tested in this study (pH 6.8 and 8.2), the following equation accounts for variations in the Na^+ concentration:

$$k_{25°C} = 11 \cdot (C_{Na^+} - 0.01) + k_{0.01} \qquad (2\text{-}15)$$

where $k_{25°C}$ and $k_{0.01}$ are the rate constants (μmol m^{-2} h^{-1}) at the given Na^+ concentration and in 0.01 M NaCl, respectively, and C_{Na+} is the concentration of Na^+ in units of mol L^{-1}. Note that the rate constants in Equation (2.15) are the values at 25± 1°C. The rate constants can be corrected for temperature using the Arrhenius equation with an activation energy in the range 57-74 kJ mol^{-1} (see Loucaides et al., 2012b, and references therein).

2.6 Conclusions

Several ASi materials, including biogenic and synthetic ASi, were analyzed by potentiometric titrations and batch dissolution experiments. The titrations show major differences in the charging behavior of the ASi materials. While the data can be fitted with the constant capacitance model, the results also show that there are no unique solutions for the model parameters. In addition, the lack of correlation between measured electrical charge and dissolution rate constants confirms the existence of an internal pool of silanol groups in the freshly cultured diatom frustules. These internal groups, which contribute to the electrical charging of the frustules but not to their dissolution rate, are not explicitly taken into account in the constant capacitance model. However,

by comparing the charging and dissolution rate constants of porous (biogenic) and non-porous (Aerosil OX 50) silicas, it becomes possible to estimate the fraction of internal silanol groups in porous ASi materials. The dissolution batch experiments also show that a single linear rate law does not represent the dissolution kinetics of ASi over the entire range of degrees of undersaturation. At high degrees of undersaturation (on average ≥ 0.55), the larger value of the rate constant possibly reflects a polynuclear nucleation mechanism. In line with earlier work, our results further show a strong effect of changes in pH on the dissolution kinetics, because of the pH-dependent ionization of surface silanol groups. We also confirm the accelerating effects of Na^+ ions on the dissolution rates of ASi.

Chapter 3
Influence of Fe(II) adsorption on the dissolution kinetics of amorphous silica

3.1 Summary

The dissolution of amorphous silica (ASi) is the first step in the recycling of reactive Si back into solution where it can be used again by siliceous organisms, including diatom communities in aquatic environments. While the effects of environmental variables, such as temperature, pH and the degree of undersaturation, have been thoroughly investigated, the role of redox-sensitive variables on the dissolution of ASi remain largely unexplored. This is the case of iron (Fe) cycling along redox gradients in freshwater environments. The present study focuses on the mechanisms by which interactions between ASi and aqueous Fe(II) affect the dissolution rate of ASi. A series of batch reactor experiments were conducted by adding variable amounts of aqueous Fe(II) to ASi suspensions under anoxic conditions. Fitting of the adsorption data of Fe(II) with a constant capacitance model indicates that Fe(II) adsorbs mainly via the formation of bidentate complexes at the surface of ASi. In addition, our results suggest that increasing concentrations of Fe(II) adsorbed to Q_2 groups (*i.e.*, surface silicate groups bonded to the silica lattice via two bridging oxygens) inhibit ASi dissolution, likely by stabilizing the Q_2 sites. However, after reaching a maximum inhibition effect, further increasing the Fe(II) concentration actually slightly accelerates the dissolution rate. We interpret the opposing effects on ASi dissolution kinetics by additional binding of Fe(II) to Q_3 groups (*i.e.*, silicate groups bonded to the silica lattice via three bridging oxygens). The latter sites have a lower affinity for Fe(II) and, therefore, only become abundant at the highest aqueous Fe(II) concentrations. In contrast to the Q_2 groups, however, the detachment of Q_3 surface sites appears to be catalyzed by the binding of Fe(II).

3.2 Introduction

As amorphous silica (ASi) is one of the dominant reactive particulate Si endmembers in sediments, the dissolution of ASi exerts a strong influence on the magnitude of DSi internal loading and therefore the availability of DSi for siliceous phytoplankton in the water column. Although studies on this topic are limited, oxygen conditions have been shown to affect the dissolution rate of ASi

(Bauerfeind and von Bodungen, 2006; Holstein and Hensen, 2010; Lehtimaki et al., 2016), whose mechanisms, however, remain unclear. A change in oxygen conditions in sediments may be accompanied by changes in pH, reactive oxygen species, and redox transformation of redox sensitive elements such as iron (Fe). Redox potential and pH are usually negatively related (Grybos et al., 2009; Parsons, 2017): the production of CO_2 and the consumption of OH^- under oxic conditions can result in the decrease of pH. Previous studies have shown that the logarithm of ASi dissolution rate constants increase linearly with pH, and even a small change of pH at near neutral range can have a significant effect on ASi dissolution rates (Dove and Elston, 1992; Fraysse et al., 2009; Lewin, 1961; Loucaides et al., 2008). Additionally, the production of reactive oxygen species, such as hydroxyl free radicals, during redox reactions may lower the energy barrier of activated complexes (Konecny, 2001). This mechanism was posited based on model calculation, but has not been confirmed by experimental results. Oxygen conditions have also been shown to affect the dissolution of ASi due to changes in the composition of the microbial community controlling the degradation of the organic protective coating surrounding ASi (Bauerfeind and von Bodungen, 2006; Holstein and Hensen, 2010; Lehtimaki et al., 2016), which are beyond the scope of this study focused on the surface chemistry of ASi.

Dissolved ferrous iron (Fe(II) produced by the reductive dissolution of Fe(III) oxyhydroxides under anoxic conditions can adsorb to the ASi surface (Milonjic et al., 2006), which may consequently affect the dissolution rate of ASi under different oxygen conditions. However, the effects of Fe(II) on ASi dissolution are still under debate (Costine and Thurgate, 2007; Iler, 1979a; Mayer et al., 1991; Morris and Fletcher, 1987). Fe(II) has been shown to retard the dissolution of ASi probably by forming a coating of insoluble silicates (Lewin, 1961), while the change from anoxic to oxic conditions in the presence of Fe(II) has been shown to accelerate quartz dissolution by increasing its solubility (Morris and Fletcher, 1987). A thorough study is therefore required to better understand the mechanisms influencing ASi dissolution during Fe(II) adsorption under anoxic conditions, and to better understand the pathways and magnitudes of Fe and Si released as a result of these interactions.

Herein, I used a series of batch laboratory experiments to study the effects of Fe(II) adsorption on ASi dissolution kinetics at constant pH by systematically varying Fe(II) concentrations in solution. I coupled these experiments with a surface reaction model to represent and provide insight into

potential interactions between the ASi surface and aqueous Fe(II) and their impacts on the ASi dissolution rate constant.

3.3 Materials and Methods

3.3.1 Materials

A synthetic form of pure ASi Aerosil OX 50 (Evonik) was chosen for this study due to its availability as a commercial product. Further, Aerosil OX 50 is characterized as having no significant microporosity. This makes it an ideal material for the study of surface reactivity, as it has been shown in Chapter 2 that micropores in ASi can limit the accessibility of surface sites, which causes a deviation to the relationship between surface sites and rate constants. The physicochemical properties of Aerosil OX 50 were studied in Chapter 2, and are summarized in Table 3.1.

Table 3.1. The physicochemical properties of Aerosil OX 50.

Specific Surface Area[1]	Surface site density[2]	Capacitance[3]	Dissociation constant log $K\_^{int4}$
m^2g^{-1}	OH nm^{-2}	F m^{-2}	
50	2.25	1.3	-7.8

[1]Measured by N_2 BET method using a Gemini VII instrument; [2, 3] Charlet et al., 1993; Evonik Industries AG, 2015; Zhuravlev, 1987; [4] Derived from constant capacitance model fit in this study, using initial values sorted from previous studies (Dixit and Van Cappellen, 2002; Fraysse et al., 2009; Loucaides et al., 2010a; Osthols, 1995).

3.3.2 Methods

All solutions used were prepared with analytical grade reagents and 18.2 MΩ cm^{-1} (Millipore) unless otherwise stated. The pH values of solution and suspension were measured with Orion Versa Star electrochemistry meter (Thermo Scientific) equipped with a pH probe that was calibrated against pH 4.0, 7.0, and 10.0 standard buffer prior to each use. Samples were filtered with 0.2 µm pore-size polypropylene syringe filters, acidified with trace-metal hydrochloric acid to pH < 2, and analyzed with Inductively Coupled Plasma-Optical Emission Spectrophotometry (ICP-OES, Thermo Scientific iCAP 6300) for the concentration of total DSi and Fe with the US EPA Method 200.7 (U.S. EPA., 1994). Matrix-matched standards were prepared from Fisher Scientific stock standards (Thermo Fisher Scientific) to eliminate the interference of matrix. Reference samples prepared with multi element standards (Delta Scientific Laboratory Products Ltd.) were analyzed along with all samples for quality control. Fe(II) concentration was determined by the ferrozine method (Viollier et al., 2000). The precision of reference samples measurement across sample run was better than 10% and the relative standard deviation was well within 5%.

3.3.2.1 Preliminary batch experiments

A series of preliminary batch experiments combining ASi and Fe(II) in $NaHCO_3$ background solution were conducted to test which aspects of the iron redox cycle would affect the dissolution of ASi in a pure system. Fenton's reactions which occur naturally during iron cycling in sediments (White et al., 2003):

$$Fe^{2+} + H_2O_2 \rightarrow Fe^{3+} + HO\cdot + OH^-$$
$$Fe^{3+} + H_2O_2 \rightarrow Fe^{2+} + HOO\cdot + H^+$$

For each preliminary experiment, 10.0±0.2 mg of ASi, weighed using an analytical balance with a precision of 0.1 mg, was suspended into 10 mL of 10 mM NaH_2CO_3 solution that contained different initial H_2O_2 concentrations (0, 1, or 10 mM). Dissolved Fe(II), prepared from $FeCl_2$ salt, was added to the $NaHCO_3$ solution in experiments D-F (Table 3.2) to achieve a concentration of 0.01 mM Fe(II). The Fe(II) solution was added either under oxic conditions before the addition of ASi (Exp. D-F, Table 3.2) or under anoxic conditions after the addition of ASi (Exp. G-I, Table 3.2). The polypropylene vials containing the ASi suspension were then agitated on a rotating

Table 3.2. Structural design of preliminary experiments which target three different reaction pathways and mechanisms of DSi retention or release. The background starting solution for all experiment was 10 mM $NaHCO_3$; Step 1 involves the addition of varying amounts of H_2O_2 to a 10 mM $NaHCO_3$ background solution; Steps 2 and 3 involve targeting different reaction pathways between Fe and amorphous silica (ASi), *i.e.*, the dissolution of ASi in the presence of variable H_2O_2 concentration and in the absence of Fe(II) (A - C), the dissolution of ASi with varying H_2O_2 and in the presence of Fe(III) oxyhydroxides formed by the oxidative precipitation of 0.1 mM Fe(II) (D - F), and the dissolution of ASi in the presence of variable H_2O_2 concentrations and in the presence of Fe(II) with an initial concentration of 0.1 mM (H - G).

Exp No.	Reaction pathways targeted by experiment	Step 1	Step 2	Step 3
A	The effect of H_2O_2	0 mM H_2O_2		
B		1 mM H_2O_2	1 g L^{-1} ASi	0 mM Fe(II)
C		10 mM H_2O_2		
D	The effect of Fe-oxyhydroxides	0 mM H_2O_2		
E		1 mM H_2O_2	0.01 mM Fe(II) in oxic solution	1 g L^{-1} ASi
F		10 mM H_2O_2		
G	The effect of Fe(II)	0 mM H_2O_2		
H		1 mM H_2O_2	1 g L^{-1} ASi in anoxic solution	0.01 mM Fe(II)
I		10 mM H_2O_2		

shaker at 30 rpm (Glass-Col, 099A RD4512) for 5 days. The temperature was maintained at 20±3 °C for the duration of the experiment. 10 mM $NaHCO_3$ was used as a background electrolyte and pH to maintain a pH of 8.5±0.2 during the experiment. After 5 days, the suspensions were syringe filtered (0.45 µm pore-size polypropylene filters) for DSi analysis. All experiments were quadruplicated.

3.3.2.2 The adsorption of Fe(II) on amorphous silica

Following the preliminary experiments, the adsorption behavior of Fe(II) was studied across a range of pH. 1 g of ASi was suspended in 1 L of 10 mM NaCl background solution. The suspensions were continuously stirred for 1 day at 25±1°C for equilibration. After being sparged with N_2 gas for 3 hours, the suspension was transferred to the anaerobic chamber, where 0.2 mL of 100 mM $FeCl_2$ stock solution was added to the suspension to give a final concentration of 20 µM Fe(II). 100 mL of the suspensions were then separated into 120 mL glass serum bottles and adjusted to target pH values between 4.0 to 8.0 using concentrated NaOH and HCl. Relatively low Fe(II) concentration and low pH were used here to avoid the precipitation of ferrous hydroxide and ferrous silicates (Figure B.1), and concentrated acid/base was used to avoid excess volume and dilution effects. Before being brought out of the anaerobic chamber, serum bottles were sealed with butyl rubber stoppers and aluminum caps to eliminate O_2 contamination. Duplicates were run to evaluate experimental reproducibility. After equilibrating at 25±1°C for 12 hours, the suspensions were returned to the anaerobic chamber, where 10 mL of samples were filtered with a 0.2 µm pore-size polypropylene membrane filters and acidified with 0.3 mL of 6 N HCl.

3.3.2.3 Evaluating the effects of Fe(II) adsorption on the dissolution rate of amorphous silica

A series of kinetic dissolution experiments were subsequently performed with larger batch reactors. 1.00 g of ASi (weighed with an analytical balance) was suspended in a 100 mL solution of 10 mM NaCl and 10 mM HEPES (4-(2-hydroxyethyl)-1-piperazineethanesulfonic acid) adjusted to pH 7.0±0.1 with NaOH and HCl. The suspension was kept at 25±1 °C and continuously stirred for three days. It was then de-oxygenated by vigorously sparging with N_2 for at least 3 hours before being brought into an anaerobic chamber (atmospheric composition: 97-98% N_2, 2-3% H_2 and < 1 ppmv of O_2).

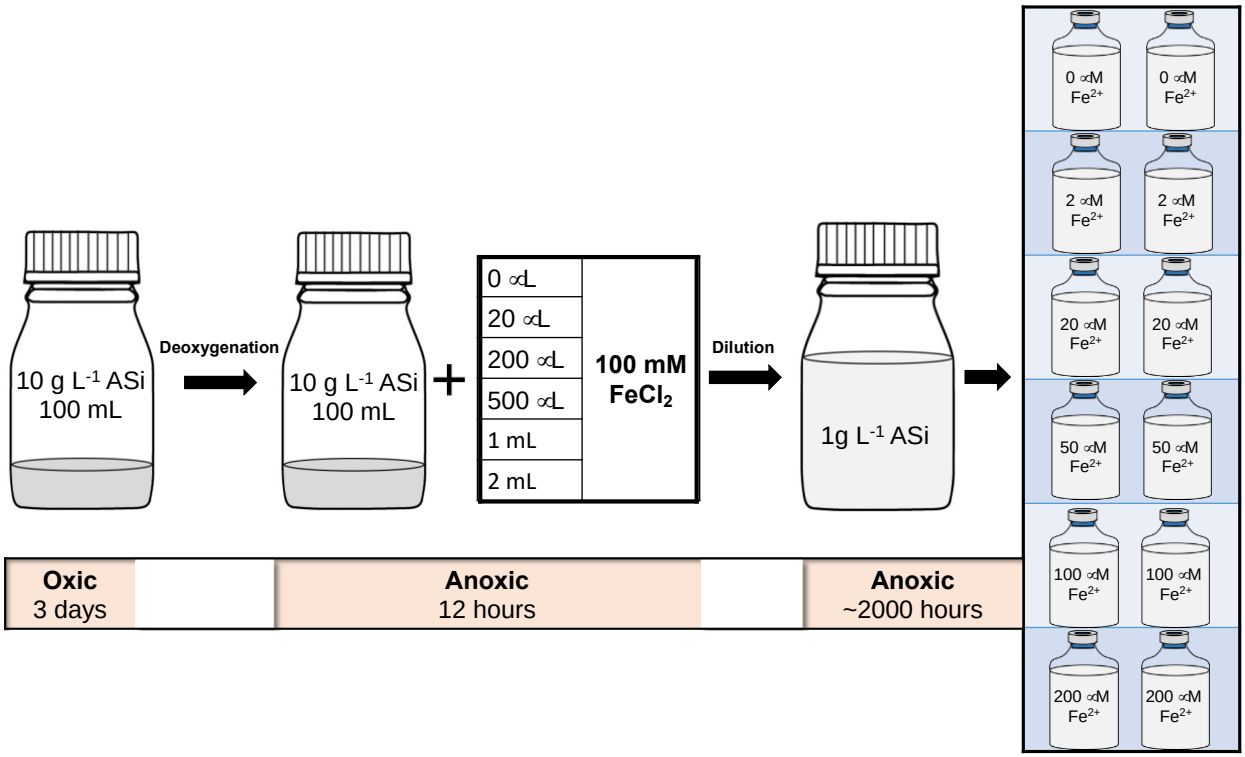

Figure 3.1. Overall design of dissolution experiment. 1.00 g amorphous silica (Aerosil OX 50) was suspended into 100 mL oxic solution and the suspension was continuously stirred for three days. 100 mM $FeCl_2$ solution was added to the suspension to achieve Fe(II) concentrations of 0, 20, 200, 500, 1000, 2000 µM Fe(II) in the anaerobic chamber. After equilibrating for 12 hours, the suspensions were diluted 10 times, *i.e.*, 1.00 g ASi L^{-1} with 0, 2, 20, 50, 100, 200 µM Fe(II). The anoxic condition was maintained by sealing with rubber stoppers and aluminum caps to keep O_2 free. pH of the suspensions was maintained at 7.0±0.1 during the experiment. Temperature was kept at 25±1 °C. Samples from anoxic bottles were collected in the anaerobic chamber to avoid the contamination of oxygen.

In the anaerobic chamber, varying amounts of a 100 mM $FeCl_2$ stock solution were added to ASi suspensions, to achieve Fe(II) concentrations of 0 µM, 20 µM, 200 µM, 500 µM, 1000 µM, and 2000 µM. This resulted in approximate initial Fe(II) to total surface groups ratio of 0, 0.01, 0.1, 0.25, 0.5 and 1 respectively. The total concentration of silanol (>SiOH) surface groups in the suspension was estimated to be 1868.8 µM based on the surface site density and surface area of Aerosil OX 50 (Table 3.1).

By keeping the suspensions in the anaerobic chamber overnight, effects of surface adsorbed silicic acid (H_4SiO_4) on ASi dissolution kinetics were excluded. Additionally, the adsorption of Fe(II) on surface of ASi presumably reached equilibrium after 12 hours. To study the dissolution kinetics of ASi with adsorbed Fe(II), the suspensions were diluted to 1.00 g L^{-1} of ASi and then divided into a group of serum bottles. The anoxic condition was maintained by sealing the serum bottles with rubber stoppers and aluminum caps to keep the solution O_2 free when removal from the anaerobic chamber.

Duplicates of experimental conditions were conducted to evaluate experimental reproducibility. All serum bottles were kept in a dark environmental chamber at 25±1°C during incubation. Samples were collected at designated intervals (see Figure 3.5 for time intervals and duration) by using needles through the butyl rubber stoppers to achieve a concentration time series. Anoxic samples were collected in the anaerobic chamber. All samples were filtered with 0.2 µm pore-size polypropylene syringe filters, acidified with HCl, and then stored at 4 °C for the analysis of dissolved Si and Fe. The details of environmental design are shown in Figure 3.1. A series of control experiments without Fe(II) were also conducted. The release of DSi from the glass serum bottle in the control experiments was measured as background.

3.4 Results

3.4.1 Effect of Fenton's reactions on ASi dissolution

A series of preliminary experiments were performed to assess the effects of different aspects of the iron redox cycle on ASi dissolution by adding H_2O_2 and Fe(II) into suspension (Figure 3.2). In the absence of aqueous Fe(II) (Exp. A-C, Table 3.2, black boxes in Figure 3.2), about 16% of the

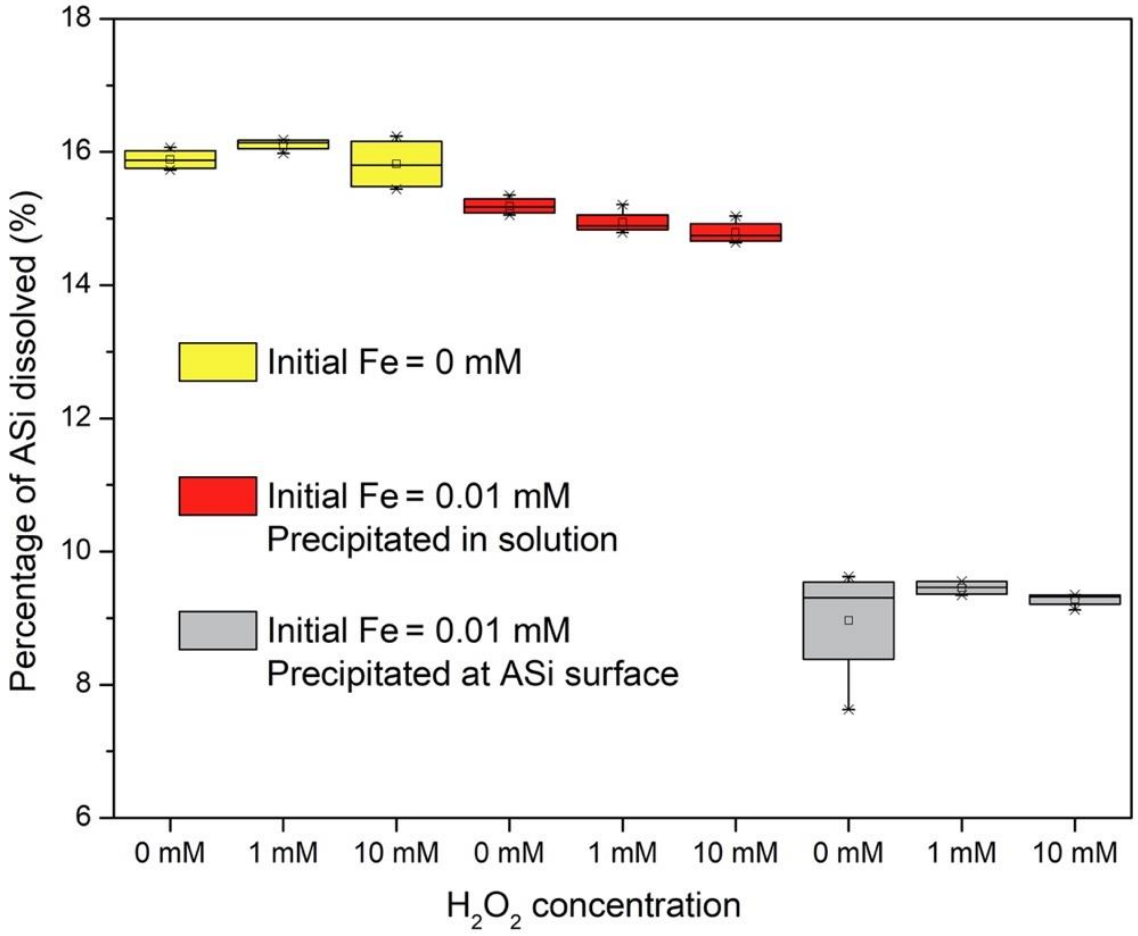

Figure 3.2. The effect of ferrous-ferric iron reactions on the dissolution of ASi. The *x* axis indicates the amount of H_2O_2 added into the ASi suspension; the *y* axis indicates the concentration of DSi after 5 days of dissolution. The data were collected after 5 days of dissolution at room temperature and in a 10 mM NaH_2CO_3 solution with a pH of 8.5. Boxes and whiskers in the figure show minimum, first quartile, median, third quartile, and maximum values of six groups of numbers (n = 4).

initial ASi dissolved during the 5 days incubation. Similar levels of dissolution occurred at varying H_2O_2 concentrations. With the addition of Fe(II) to oxic solutions before the addition of ASi (Exp. D-F, Table 3.2, blue boxes in Figure 3.2), slightly less DSi (about 15%) was released than was observed in the absence of Fe(II). In contrast, the release of Si decreased substantially with the addition of Fe(II) to the ASi suspension (Exp. G-I, Table 3.2, red boxes in Figure 3.2). This resulted in dissolution of less than 10% of the initial ASi.

3.4.2 Fe(II) adsorption on ASi

3.4.2.1 Effect of pH

The Fe(II) adsorption edge was determined by plotting the percentage of total dissolved Fe(II) removed from solution as a function of pH (Figure 3.3). The adsorption of Fe(II) did not show obvious pH dependence at low pH values (4.0 to 5.0), and only about 5% of the initial 20 µM Fe(II) was removed within this pH range. When pH was higher than 6.5, Fe(II) adsorption was highly pH dependent, and the fraction of Fe(II) adsorbed increased from 10% to nearly 100% within one pH unit (pH 6.5 to 7.5).

3.4.2.2 Effect of Fe(II) concentration

To mimic the broad range of conditions found in nature, a wide range of initial Fe(II) concentrations (0 to 2000 µM) were used in this study. After equilibrating experimental solutions (10 mM NaCl, 10 mM HEPES and varying Fe(II) concentration at pH 7.0±0.1) in an anaerobic chamber for 12 hours with a 1 g ASi per 100 mL solution, the suspensions were diluted to 1 g ASi per litre (thus diluting the initial Fe(II) concentrations to a range of 0 to 200 µM). By doing this, adsorption process was separated from the dissolution kinetics of ASi with adsorbed Fe(II). The amount of Fe(II) adsorbed increased with increasing initial Fe(II) concentration (Figure 3.4). As dissolved Fe(II) did not decrease over time during the dissolution experiment, the adsorption data with different initial Fe(II) concentrations at pH 7.0±0.1 were used to validate the results from surface complexation model.

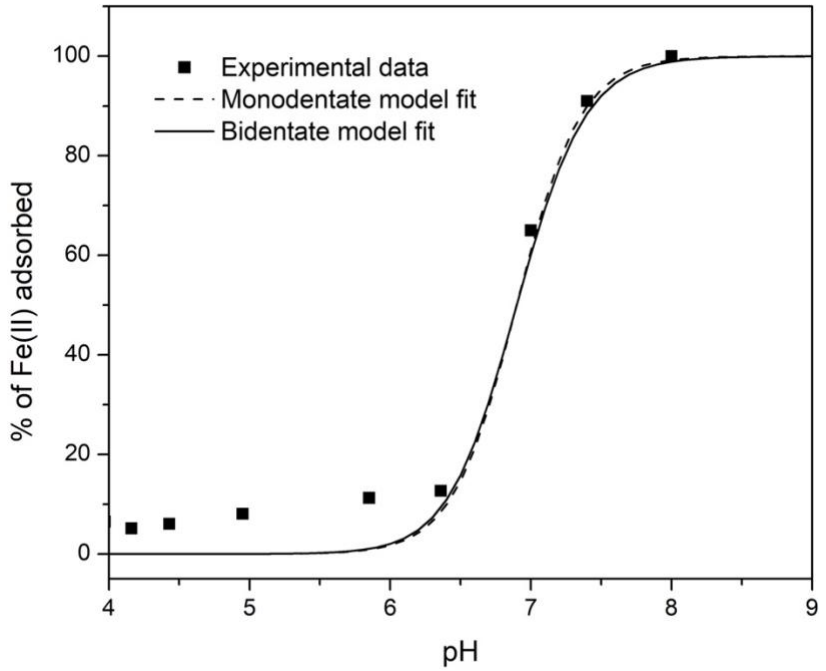

Figure 3.3. Fe(II) adsorption edge on Aerosil OX 50. The adsorption experiments were conducted by adding 20 µM Fe(II) into 1g L^{-1} of ASi suspension at 25±1 °C. Concentrated NaOH and HCl were used to adjusted pH, and the total volume changed by less than 1%. Black squares represent the average values of duplicate experiments (difference between duplicates is less than 3%). Dashed line is the result of a monodentate mononuclear surface complex reaction (Table 3.3), and solid line corresponds to a bidentate binuclear surface complex reaction (Table 3.3).

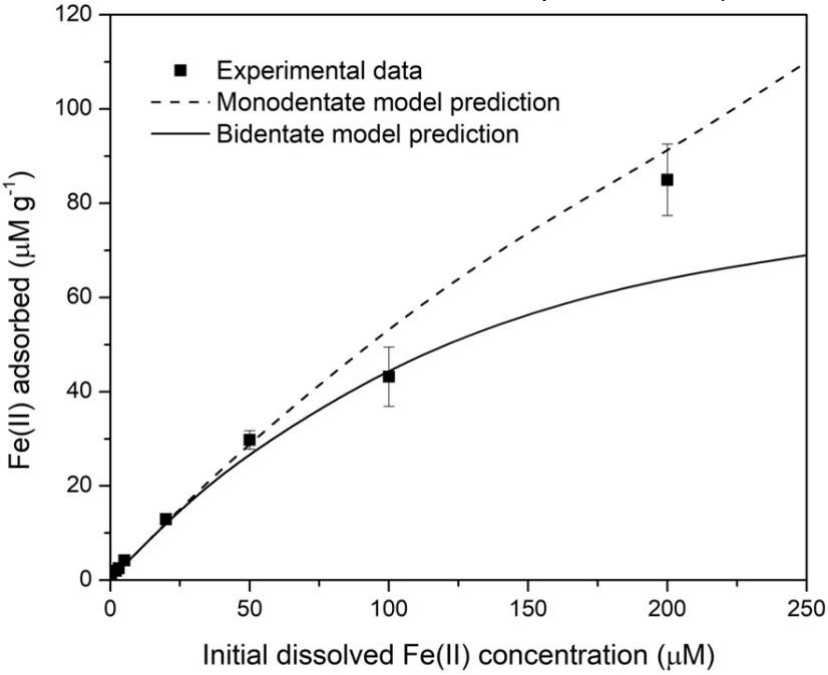

Figure 3.4. Fe(II) adsorption data and model prediction at constant pH 7.0±0.1 and constant silica suspension concentration (1 g L^{-1} Aerosil OX 50) for varying initial Fe(II) concentrations (n = 6). The dashed and solid lines are the result of monodentate and bidentate model predictions.

3.4.2.3 Surface complexation model

The constant capacitance model (CCM) was used to interpret the Fe(II) adsorption data at different pH values. Aerosil OX 50 was assumed to contain one type of amphoteric surface site which had a 1:1 stoichiometric ratio of Si and OH. Fe(II) can be adsorbed by forming monodentate mononuclear and/or bidentate binuclear surface complexes:

$$> \mathrm{SiOH} + Fe^{2+} \leftrightarrow > \mathrm{SiOF}e^{+} + H^{+} \quad (3.1)$$

$$> \mathrm{SiOH} + Fe^{2+} + H_2O \leftrightarrow > \mathrm{SiOFeOH} + 2H^{+} \quad (3.2)$$

$$(> \mathrm{SiOH})_2 + Fe^{2+} \leftrightarrow (> \mathrm{SiO})_2\mathrm{Fe} + 2H^{+} \quad (3.3)$$

where >SiOH denotes a surface site on silica, $(>\mathrm{SiOH})_2$ denotes a bidentate surface site that is the combination of two specific surface sites (Wang and Giammar, 2013). The experimentally observed proton stoichiometry factor for Fe(II) adsorption was 1.9 which was close to that of other divalent metal ions (Kosmulski, 2000). Therefore, Fe(II) adsorption data was interpreted primarily as a result of Reaction (3.2) or (3.3).

The deprotonation constant of monodentate surface sites were obtained by fitting potentiometric titration data (*i.e.*, in the absence of specifically adsorbed ions) of Aerosil OX 50 to the CCM (see more details in Chapter 2). With a surface site density of silanol groups of 2.25 >SiOH nm^{-2} and a specific capacitance of 1.3 F m^{-2}, the deprotonation constant for Aerosil OX 50 is 7.7 (Table 3.1). These parameters were used as input to a computer program Visual MINTEQ (Gustafsson, 2000) for Fe(II) adsorption equilibrium constants optimization with the CCM. The concentration of available silanol groups on the surface of 1g L^{-1} Aerosil OX 50 for Fe(II) adsorption is 186.9 µM. The best model fit yielded a value for the Fe(II) adsorption intrinsic equilibrium constant (-log *K*) of 9.83 ± 0.10. Solving Reaction (3.3) to determine the equilibrium constant of Fe adsorption requires the concentration of bidentate sites. Since bidentate sites are the combination of two adjacent surface sites that can react with Fe(II) simultaneously, their initial concentration was assumed to be half of the total surface site concentration, *i.e.*, 93.5 µM. This change to the initial surface sites concentration resulted in a revised dissociation constant of 7.2 for the first deprotonation of bidentate surface sites. Consequently, the best model fit yielded a value of Fe(II) adsorption intrinsic equilibrium constant (-log K) of 9.45 ± 0.10 for Reaction (3.3) (Table 3.3).

Table 3.3. Test of surface complexation model using different surface reactions.

No.	Reaction	[>SiOH]	[(>SiOH)$_2$]	-log K^{int}	Total sum of squares
		μM	μM		
1 Monodentate mononuclear	>SiOH + Fe^{2+} → >SiOFeOH + $2H^+$	186.9	0	9.83 ± 0.10	45.38
2 Bidentate binuclear	(>SiOH)$_2$ + Fe^{2+} → (>SiO)$_2$Fe + $2H^+$	0	93.5	9.45 ± 0.10	49.16

The equilibrium constants obtained from fitting Reaction (3.2) and Reaction (3.3) to Fe(II) sorption to Aerosil OX 50 were used to predict the adsorption of Fe(II) at different initial concentrations. Considering only monodentate mononuclear surface complexes (Reaction (3.2), Figure 3.4), with an intrinsic equilibrium constant of 9.83, the model was able to adequately reproduce the experimental Fe(II) adsorption data as a function of the initial Fe(II) concentration (Figure 3.4). Considering only bidentate binuclear surface complexes (Reaction (3.3), Figure 3.3), the model failed to reproduce the experimental Fe adsorption data at high initial Fe(II) concentration (200 µM), although the reproducibility at low initial Fe(II) was good (between 0 and 100 µM) (Figure 3.4).

CCM simulations that incorporate a combination of surface Reaction (3.1) and either Reaction (3.2) or (3.3) were also considered to fit Fe(II) adsorption data. A simulation combining Reactions (3.1) and (3.2), which considers the pH dependence of Fe(II) speciation (e.g., Fe(II) vs $Fe(OH)^{+}$), successfully reproduced the adsorption edge. However, these two reactions effectively described the same monodentate mononuclear adsorption mechanism and incorporating them both increased the complexity of the model. The combination of Reactions (3.1) and (3.3) however described different mechanisms of Fe(II) adsorption. As the relative abundance of available monodentate and bidentate sites could not readily be quantified, different ratios of [>SiOH] and [$(>SiOH)_2$] were assigned and tested. Varying the relative abundance of monodentate vs bidentate sites did not obviously improve the quality of the model fit. Therefore, in this study, Fe(II) was assumed to be adsorbed either by monodentate mononuclear (Reaction (3.2)) or bidentate binuclear surface complexes (Reaction (3.3)) on the surface of ASi in this study.

3.4.3 Effect of Fe(II) adsorption on ASi dissolution kinetics

3.4.3.1 Dissolution rate constants of ASi with varying initial Fe(II)

The effects of varying Fe(II) concentrations on ASi dissolution kinetics under anoxic conditions are shown in Figure 3.5. Although the kinetics of ASi dissolution after 2000 hours were not recorded, data points collected six months later showed that the solubility of ASi decreased with increasing Fe(II) (Table B.1). Specifically, trace Fe(II) (less than 2 µM) did not affect the solubility of ASi, which is in consistent with a previous study (Iler, 1979a). The solubility decreased from 1712 µM to 1575 µM when initial Fe increased from 2 to 200 µM.

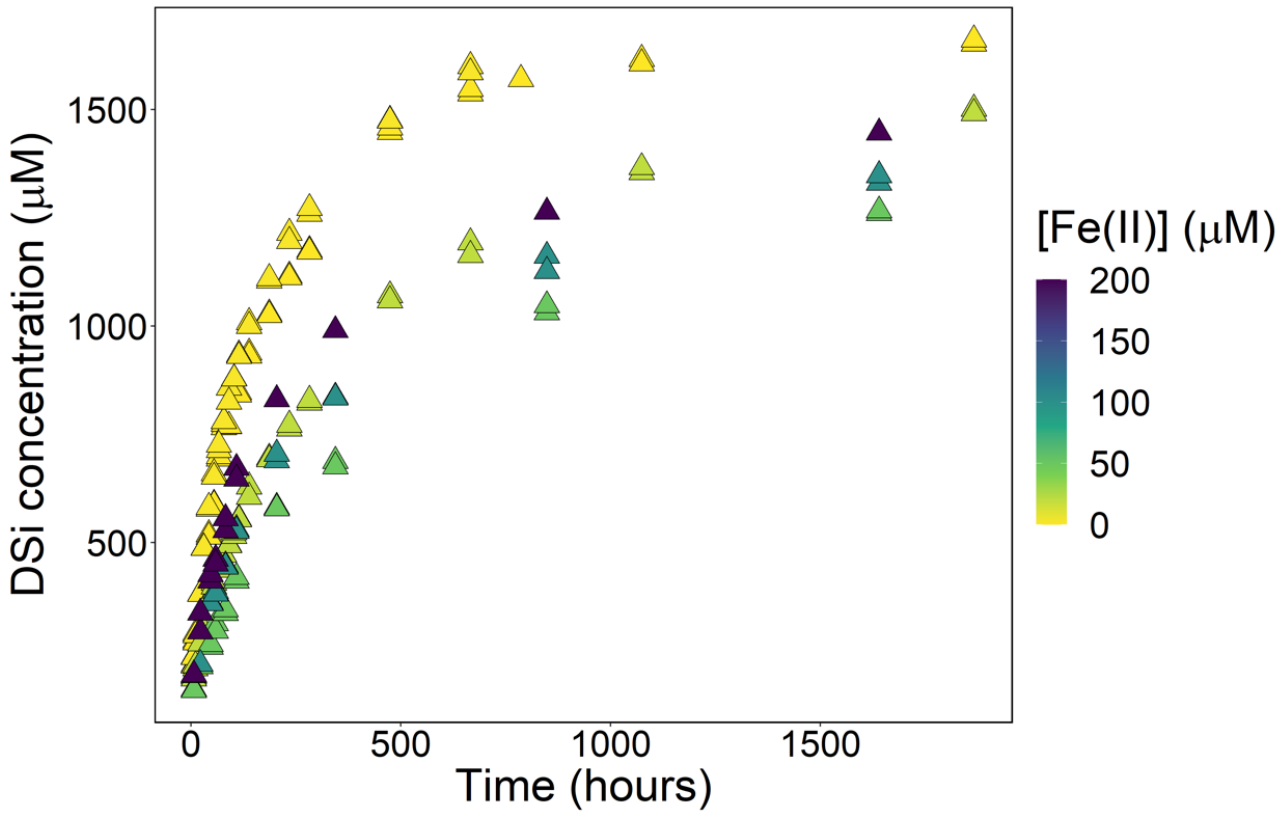

Figure 3.5. The effect of varying initial Fe(II) concentrations on the dissolution kinetics of Aerosil OX 50 under anoxic conditions. The dissolution experiments were conducted by suspending 1.0 g ASi in 1 L solution of varying concentration of initial Fe(II) at pH 7.0±0.1 and 25±1 °C. Anoxic conditions were created by vigorously sparging with N_2 for at least 3 hours and maintained by sealing the serum bottles with rubber stoppers and aluminum caps.

To quantify the inhibition effect of Fe(II) on ASi dissolution kinetics, the first-order kinetic law was used to quantify the rate constant. As is shown in Figure 3.6, the effect of Fe(II) on the dissolution rate could be categorized into two stages. The rate constant showed a sharp decrease with increasing initial Fe(II) concentration until the inhibition effect reached its maximum at 50 μM initial Fe(II). Above 50 μM of initial Fe(II), the dissolution rate constant increased slightly between 50 and 200 μM. Therefore, the greatest effect on the dissolution rate constant for ASi occurred at 50 μM initial Fe(II), where the rate constant reached 0.05 μmol m^{-2} h^{-1}. This was less than one third of the value obtained in the control solution (without the addition of Fe(II)) at pH 7.0±0.1 (0.17 μmol m^{-2} h^{-1}).

3.4.3.2 Surface reaction model

To interpret the inhibition effects of Fe(II) on the dissolution kinetics of ASi, I firstly tried to use a surface reaction model that accounted for the concentration and species composition of surface sites. Both monodentate mononuclear and bidentate binuclear surface complexes were tested. The results of bidentate binuclear were specified below:

$$k = k_0 \cdot \theta_{>SiOH} + k_1 \cdot (\theta_{>SiO^-})^n + k' \cdot (\theta_{(>SiO)_2Fe})^a \quad (3.4)$$

where $\theta_{>SiOi}$ is the fraction of surface species, k is the dissolution rate constant (μmol m^2 h^{-1}), k_0 and k_1 are rate constants of different surface species that have the same unit as k, n is the order of hydroxyl-promoted dissolution reaction, k' is the rate constants of Fe(II)-adsorbed surface sites that have the same unit as k (μmol m^2 h^{-1}), and a is the order of the Fe-affected dissolution reaction. Values of k_0 (0.04±0.01), k_1(3.44±0.37), and n (1.28±0.07) have been obtained in Chapter 2. The relative abundance of different surface species at pH 7.0±0.1 with varying initial Fe(II) concentrations was predicted using the CCM. The percentage of $(>SiO)_2Fe$ surface complexes increased with increasing initial Fe(II) concentration (Figure 3.6, small panel). Equation (3.4) was fitted to experimental rate constant data (Figure 3.6) to estimate the unknown parameters k' and a (with the assumption that k' and a should not be negative). However, surface reaction model using Equation (3.4) and the surface species composition shown in Figure 3.6 predicts much higher rate constants than those calculated for the experimental data, regardless of how small k' is (the dashed line in Figure 3.6 was produced from simulations where k' was equal to 0).

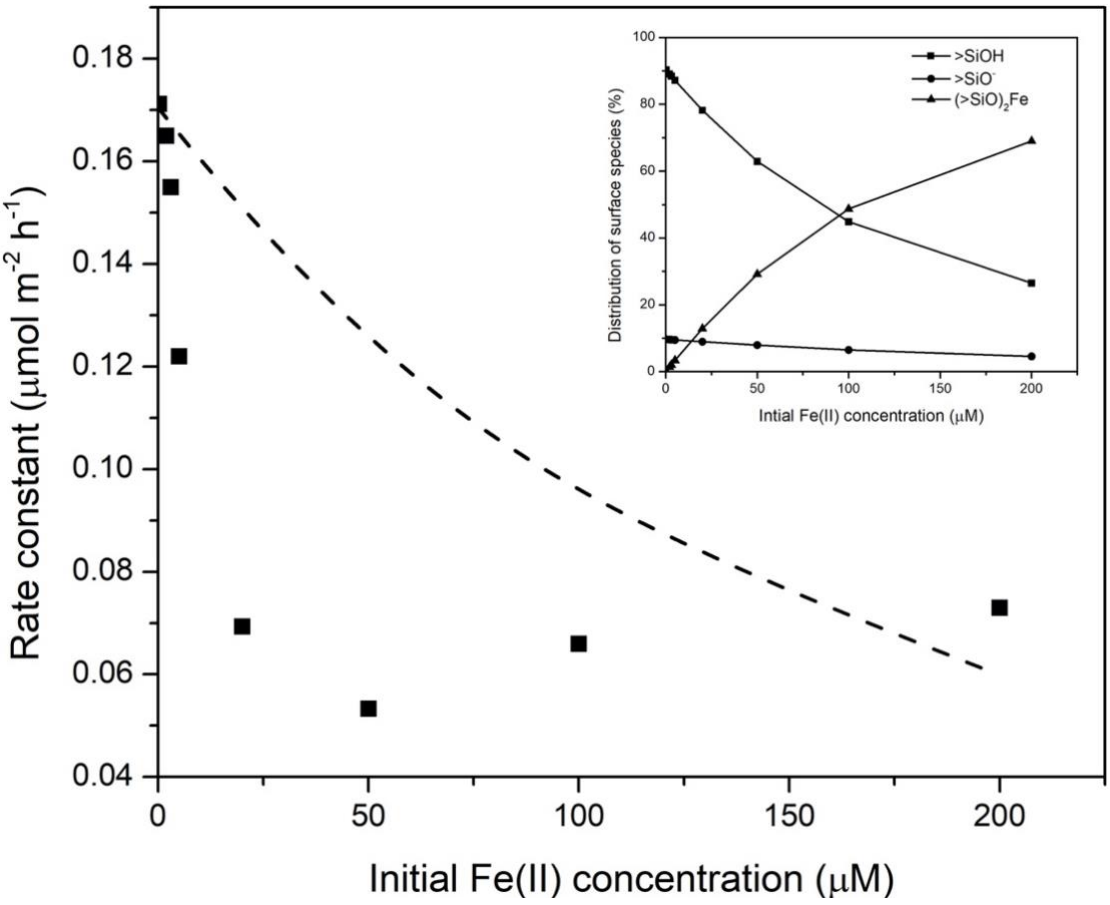

Figure 3.6. The dissolution rate constant of Aerosil OX 50 (ASi) in the presence of variable initial Fe(II) at pH 7.0±0.1. The rate constants were calculated using the first-order kinetic law: $R = k \cdot \left(1 - \frac{C}{C_{eq}}\right)$, where R is the reaction rate (μmol m^{-2} h^{-1}), C is the concentration of DSi (μmol L^{-1}), C_{eq} is the solubility of the reacting amorphous silica sample (μmol L^{-1}), and k is the reaction rate constant scaled by the specific surface area of ASi (μmol m^{-2} h^{-1}). Squares represent the results of duplicate experiments; and the dashed line corresponds to rate constants predicted by the surface reaction model (Equation (3.4)) with a minimum k' value of 0. The inset panel (top right) shows the distribution of Aerosil OX 50 surface species at pH 7.0±0.1 with varying initial Fe(II) concentrations.

3.4.3.3 Langmuir adsorption model

The poor fit of surface reaction model to the dissolution rate constants data of ASi in the presence of Fe(II) led to the assumption that the geometric coordinative arrangement of surface groups, other than concentration and species distribution of surface groups, also affect the dissolution rate of ASi. The inhibition effect of Fe(II) was then described by a Langmuir adsorption model that was presented by Christoffersen and Christoffersen (Christoffersen and Christoffersen, 1981, 1984) and has been widely used (Koutsopoulos and Dalas, 2000; Takasaki et al., 1994; Van Cappellen and Berner, 1991). The overall dissolution rate constant was assumed to be the sum of the rate constants of free Q_2 groups (germinal silanols that are bonded to the silica lattice via two bridging oxygens) and Fe(II) adsorbed Q_3 groups (isolated silanols that are bonded to the silica lattice via three bridging oxygens):

$$k = k_2 \cdot x_{Q_2}^{free} + k_3 \cdot x_{Q_3}^{ads} \tag{3.5}$$

where k is the rate constant observed (μmol m^2 h^{-1}), k_2 and k_3 are rate constants of active surface Q_2 and Q_3 groups that have the same unit as k, x_{Q2}^{free} is the fraction of Q_2 group that is not occupied by Fe(II), and x_{Q3}^{ads} is the fraction of Q_3 groups that is catalyzed by the adsorption of Fe(II):

$$x_{Q_2}^{free} = 1 - \frac{K_2 \cdot [Fe^{II}]}{1 + K_2 \cdot [Fe^{II}]} \tag{3.5a}$$

$$x_{Q_3}^{ads} = \frac{K_3 \cdot [Fe^{II}]}{1 + K_3 \cdot [Fe^{II}]} \tag{3.5b}$$

K_2 and K_3 are the Langmuir adsorption constants of Q_2 and Q_3 groups and, [Fe(II)] is the concentration of dissolved Fe(II) remaining. In the absence of Fe(II), the fraction of free Q_2 groups was therefore 1, and the fraction of Fe(II) adsorbed Q_3 groups was 0, therefore $k = k_2 = 0.17$.

The inhibition effect of Fe(II) on ASi dissolution was classified into two stages (Figure 3.7). When initial Fe(II) concentration was low (lower than 50 μM), detachment of Q_2 groups dominated the dissolution process. The dissolution rate constant in this case was approximated by:

$$k = k_2 \cdot (1 - \frac{K_2 \cdot [Fe^{II}]}{1 + K_2 \cdot [Fe^{II}]}) \tag{3.5c}$$

Re-arranging Equation (3.5c) gave:

$$\frac{k_2}{k} = 1 + K_2 \cdot [Fe^{II}] \quad (3.5d)$$

Equation (3.5d) demonstrated that the ratio of k_2/k is linearly dependent on the concentration of Fe(II), and slope of this linear relationship is $K_2 = 0.22 \pm 0.01$. With the known values of k_2 and K_2, the dissolution rate constant of Q_2 groups in the presence of different amounts of Fe(II) (the first term on the right side of Equation (3.5)) was able to be quantified.

When initial Fe(II) concentration was high (higher than 50 μM), fewer free Q_2 sites were available for further sorption and therefore the contribution of Fe(II)-catalyzed detachment of Q_3 groups to the overall dissolution rate became increasingly important. Therefore, the dissolution rate constant was calculated using:

$$k = k_2 \cdot x_{Q_2}^{free} + k_3 \cdot \frac{K_3 \cdot [Fe^{II}]}{1 + K_3 \cdot [Fe^{II}]} \quad (3.5e)$$

The first term on the right hand of Equation (3.5e, (k_2)) is known. The unknown parameters k_3 and K_3 were obtained by least square fitting of experimental data to Equation (3.5e). Following this approach, the values of k_3 and K_3 were determined to be 0.11 ± 0.06 μmol m^2 h^{-1} and 0.01 ± 0.01, respectively.

The concentrations of dissolved Fe(II) remaining in solution were predicted using the CCM assuming bidentate sorption (Reaction (3.3), and the values of k_2, k_3, K_2, and K_3 were obtained by fitting experimental data with a Langmuir adsorption model. Therefore, the fraction of free Q_2 groups and Fe(II) adsorbed Q_3 groups was able to be predicted with Equations (3.5a) and (3.5b). With the increase of initial Fe(II) concentration from 0 to 20 μM, the fraction of free Q_2 group x_{Q2}^{free} decreased from 100% to 40.5% and the fraction of Fe(II) adsorbed Q_3 groups increased from 0 to 7.7%. The contribution of the enhanced detachment of Q_3 groups to the overall rate constant was therefore minor, and the drastic decrease of the dissolution rate constant at low initial Fe(II) (Figure 3.8, initial Fe(II) lower than 50 μM) was attributed to the stabilization of Q_2 groups by the preferential adsorption of Fe(II). When the initial Fe(II) concentration increased to 50 μM, the fraction of free Q_2 groups and Fe(II) adsorbed Q_3 groups were 19.1% and 19.5% respectively, corresponding to the minimum rate constant illustrated in Figure 3.8. With the increase of initial Fe(II) concentration from 50 to 200 μM, the fraction of free Q_2 groups decreased to 3.9% and that of Fe(II) adsorbed Q_3 groups increased to 58.0%. The dissolution of Fe(II) adsorbed Q_3 groups

therefore dominates the release of DSi, and the combination of these two mechanisms leads to the slight increase of the rate constant at high initial Fe(II) shown in Figure 3.8. Thus, Equation (3.5), a Langmuir adsorption model, effectively predicted the effect of changing initial Fe(II) concentrations on the dissolution rate constant of ASi at pH 7.0±0.1 (Figure 3.8).

3.5 Discussion

3.5.1 Effect of Fenton's reactions on ASi dissolution

Hydroxyl free radicals produced by the Fe-catalyzed decomposition of H_2O_2 (Fenton's reactions) have been suggested to enhance the dissolution of silica by lowering the energy barrier (Konecny, 2001). However, enhancement of ASi dissolution was not observed in this experiment. One possible reason is that the pH of the $NaHCO_3$ buffered solution is sufficiently high (8.5) such that Fe (III) precipitated as iron oxyhydroxides, preventing the persistent production of hydroxyl free radicals that can diffuse into the bulk solution (Kwan and Voelker, 2002). In this case, only 0.01 mM hydroxyl free radicals are produced stoichiometrically. Hydroxyl free radicals are so active that they may be consumed by other redox active elements, notably Fe on solid surfaces, which means the amounts of free radicals that could actually react with ASi may be too small to generate an observable effect on ASi dissolution.

The much lower DSi concentration in ASi suspensions with the addition of Fe(II) (Exp. G-I, Table 3.2, grey boxes in Figure 3.2) could be due to: (1) adsorption of DSi to Fe(III) oxyhydroxides, (2) the precipitation of Fe and Si, including coprecipitates and precipitation of Fe silicate (Cismasu et al., 2014; Dyer et al., 2010; Jones et al., 2009; Kaegi et al., 2010; Wolthoorn et al., 2004), and/or (3) the formation of surface complexes and surface precipitates of Fe on ASi (Lewin, 1961; Milonjic et al., 2006; Morris and Fletcher, 1987). Adsorption of DSi to ferric oxyhydroxides has been widely reported (Hansen et al., 1994; Mortimer, 1941; Ridenour, 2017). However, with such low Fe(II) concentration of 0.01 mM used here, adsorption can account for 0.2% of the decrease assuming that 60% of Fe atoms form surface sites (Hiemstra, 2013) and trimeric silicate complexes form between two surface sites (Swedlund et al., 2010). The precipitation process, however, would rapidly lower DSi concentration in aqueous, thus promoting further released of DSi from ASi surfaces by increasing the degree of undersaturation of the solution with respect to ASi. This, as a result, lead us to the last plausible mechanism that trace amount of dissolved Fe exist in the

suspension may adsorb on the surface of ASi and prevent the attack of water, which would inhibit further dissolution of ASi.

3.5.2 Mechanisms of Fe(II) adsorption to Aerosil OX 50

Before studying their effects on the dissolution kinetics, the mechanism of Fe(II) adsorption to ASi need to be addressed. Although few studies focus on the adsorption of Fe(II) to ASi, one existing study (Milonjic et al., 2006) showed similar adsorption edge: about 7% of initial Fe(II) was removed at pH lower than 6.0 and the percentage adsorbed was independent of pH in this low pH range. The surface site density of ASi used in their study, however, is not known, and the adsorption edges they report are not comparable with the results in this study. The adsorption of other metal cations (Dixit and Van Cappellen, 2002; Osthols, 1995) have also been shown to deviate from model predictions at low pH. According to previous studies, this could be due to the existence of strong-binding surface species which are not pH sensitive (Nano and Strathmann, 2006; Tonkin et al., 2004).

Since the experimentally observed proton stoichiometry factor for Fe(II) adsorption on ASi was slightly smaller than 2 (1.9), Fe(II) is likely to adsorb to ASi by forming monodentate mononuclear complexes (Reaction (3.2)) or bidentate binuclear complexes (Reaction (3.3)). This is again supported by the good fit of CCM and measured data except for those at low pH values (Figure 3.3).

The CCM that considered only monodentate mononuclear surface complexes (Reaction (3.2), Figure 3.3) reproduced the adsorption data at different Fe(II) initial concentrations better than which considered only bidentate binuclear surface complexes (Reaction (3.3), Figure 3.3). However, this cannot lead to the conclusion that Reaction (3.2) describes the mechanisms of Fe(II) adsorption. According to the solubility diagram given by Tosca et al. (2016), the equilibrium constant of ferrous silicate identified as greenalite, is 27.6 at 25±1 °C, which indicates that ferrous silicate precipitation is not thermodynamically favorable at pH 7.0±0.1 below Fe(II) concentrations of 1600 µM with constant DSi concentration of 1500 µM. Thus, model predictions which assume that Fe(II) is only removed by forming surface complexes with ASi should reproduce most of the experimental adsorption data shown in Figure 3.4. However, the experimental incubation with an initial Fe(II) concentration of 200 µM, was diluted from an initial

solution with an Fe(II) concentration of 2000 µM, indicated that the formation of greenalite was thermodynamically favorable in this case. Therefore, the discrepancy between bidentate model prediction and experimental data (Figure 3.3) is likely due to the precipitation of greenalite, which is not considered by the surface complexation model, and not due to a failure of the model to adequately describe the surface complexation model. Although the bidentate model prediction fails to reproduce the experimental sorption results at 200 µM (Figure 3.4), Fe(II) is more likely adsorbed by forming bidentate binuclear surface complexes on ASi surface (Reaction 3.3).

3.5.3 Effect of Fe(II) adsorption on ASi dissolution kinetics

It is clear from the observed data that Fe(II) does inhibit the release of DSi under anoxic conditions (Figure 3.5). This inhibition seems mainly due to the formation of Fe(II) complexes on silanol surface groups, as supported by the good surface complexation model fits at low initial Fe(II) concentrations shown in Figure 3.4, rather than the retention of DSi in fresh iron silicate precipitates. The surface reaction model based on the formation of bidentate binuclear surface complexes, described with Reaction (3.3), cannot reproduce the experimentally observed decrease in the ASi dissolution rate constant caused by such small amounts of Fe(II) adsorbing to the ASi surface (Figure 3.6). This leads to the assumption that the geometric coordinative arrangement of surface groups affects the dissolution kinetics of ASi, in addition to concentration and charge. Germinal silanols (Q_2 groups) and isolated silanols (Q_3 groups) bonded to the silica lattice via two and three bridging oxygens, respectively, are the dominant surface groups on ASi (Figure 3.5). Previous studies have shown that Q_2 groups are more reactive, and the detachment of Q_2 groups thus determines the dissolution rate of ASi in the absence of Fe(II) (Dove and Crerar, 1990; Dove et al., 2008; Dove et al., 2005; Hiemstra and Van Riemsdijk, 1990).

However, in the presence of adsorbed Fe(II), the reactivity of surface groups may be changed by Fe(II) adsorption. The adsorption of Fe(II) can neutralize the surface charge produced by deprotonation of silanol groups, decreasing the probability of water attachment, and thus discouraging dissolution. On the other hand, Fe(II) may weaken the bridging Si-O bonds as other cations do (*e.g.*, Na^+, K^+, Ca^{2+}) (Dove and Nix, 1997), which can lower the energy required for the detachment of surface SiO_4 tetrahedra, enhancing dissolution. A multi-site complexation model that assumes two types of activated surface sites (Q_2 and Q_3 groups) with different affinities for

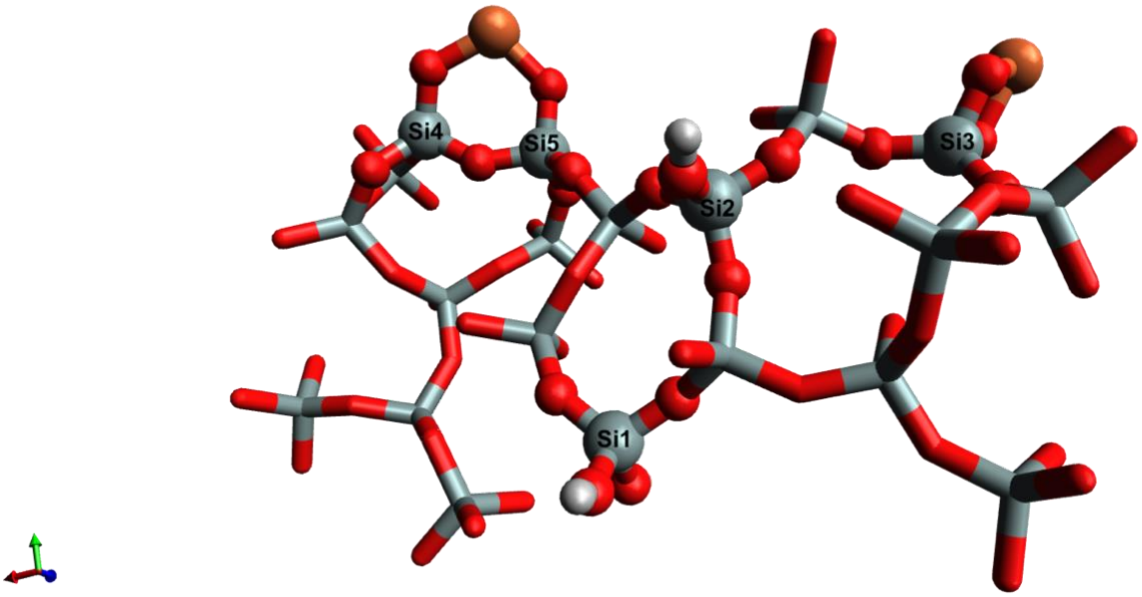

Figure 3.7. Illustration of amorphous silica showing different surface species in the presence of Fe. Si atoms are shown in grey, O in red, H in white and Fe in orange. Si1corresponds to a free doubly coordinated surface site (free Q_2 group); Si2 corresponds to a free triply coordinated surface site (free Q_3 group); Si3 corresponds to a Q_2 group that is occupied by Fe(II) forming a bidentate mononuclear surface complex; and Si4 and Si5 correspond to two Q_3 groups that are both occupied by Fe(II) forming a bidentate binuclear surface complex. Balls represent surface atoms; sticks represent atoms in the bulk solid (Constructed with Avogadro software).

Fe(II) was used to quantitatively understand the influence of these two opposing effects on ASi dissolution rate. This multi-site complexation model requires initial concentrations of Q_2 and Q_3 groups. Although there are many studies on the distribution of Q_2 and Q_3 groups on ASi (Evonik Industries AG, 2015; Liu and Maciel, 1996; Lutz et al., 2009), the densities of Q_2 and Q_3 are unknown because they will change during dissolution. For example, the detachment of Q_2 groups (Si1) in Figure 3.7 can lead to the production of two Q_3 groups. Therefore, traditional surface complexation models cannot be used to explain the effect of Fe(II) on the reactivity of surface sites.

The agreement between the rate constants derived experimentally and those predicted by the Langmuir adsorption model (Figure 3.8) suggests that Fe(II) is preferentially adsorbed to Q_2 groups. The adsorption of Fe(II) also has opposing effects on the reactivity of Q_2 and Q_3 groups. The dominance of the inhibition effect of Fe(II) on ASi dissolution is the result of the protective effect of Fe(II) adsorbed to Q_2 groups. But the catalytic effect of Fe(II) adsorbed to Q_3 groups becomes increasingly important with increasing Fe(II) concentration. The opposing effects of Fe(II) on the reactivity of surface groups provide a new mechanistic understanding that couples the Si and Fe cycles in nature (Ingall et al., 2013). However, the microscopic interactions that control the surface groups' reactivity require further study. For example, insight into how the adsorption of Fe(II) on Q_2 and Q_3 groups affects the electron distribution of their center Si atoms would be useful to more completely understand the nature of these interactions.

The inhibition effects of Fe(II) on the dissolution of quartz and biogenic ASi have been recognised and examined in previous studies (Lewin, 1961; Morris and Fletcher, 1987). In these studies, the inhibition of ASi dissolution is attributed to the formation of an Fe(II) surface complex. The results presented in this study, for the first time, show that the inhibition effect of Fe(II) on ASi dissolution does not increase continuously with increasing dissolved Fe(II) concentration. This is contrast to Al^{3+} (Iler, 1973; Koning et al., 2007), because Fe(II) does not substitute for Si in silica tetrahedra (Iler, 1979a) as Al^{3+} does.

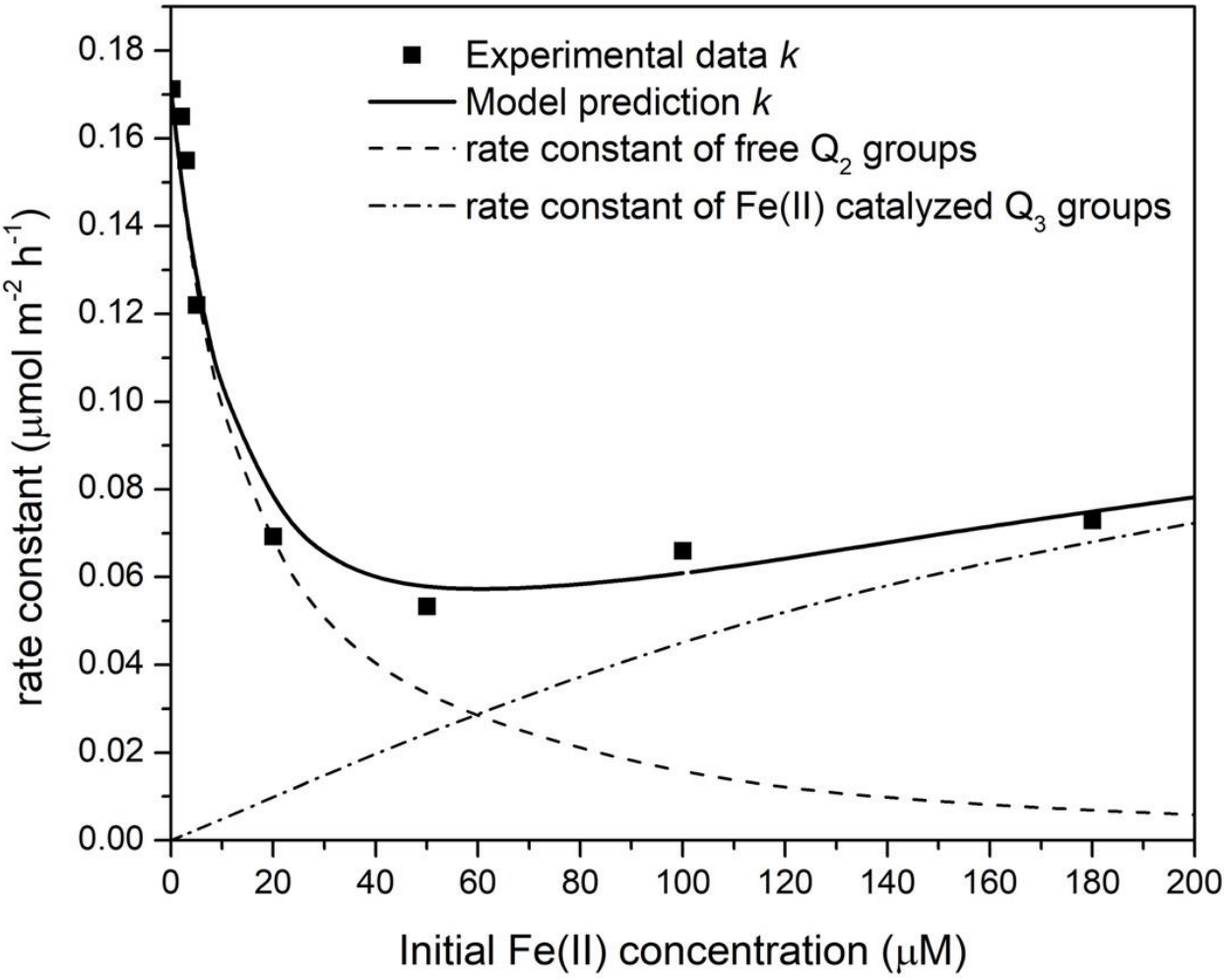

Figure 3.8. The effect of Fe(II) concentration on the dissolution rate constant of Aerosil OX 50. The rate constants were calculated using the first-order kinetic law: $R = k \cdot \left(1 - \frac{C}{C_{eq}}\right)$, where R is the reaction rate (μmol m^{-2} h^{-1}), C is the concentration of DSi (μmol L^{-1}), C_{eq} is the solubility of the reacting amorphous silica sample (μmol L^{-1}), and k is the reaction rate constant scaled by the specific surface area of ASi (μmol m^{-2} h^{-1}). The solid line is the overall rate constant predicted with Equation (3.5), the dashed line is the predicted rate constant of free Q_2 groups (free Q_2 groups decrease in abundance with increasing Fe(II) concentration), and the dash-dotted line is the predicted rate constant of Fe(II) Q_3 groups occupied by Fe(II).

Other than the initial concentrations, many other factors can affect the inhibition effect of Fe(II) on ASi dissolution. For example, pH, fixed at 7.0±0.1 in this study, determines the dominant species of both aqueous Fe(II) and surface silanol species. Therefore, variation in pH could affect the affinity of Fe(II) to surface groups. The pH dependence of the Aerosil OX 50 dissolution rate was studied in Chapter 2, from which k_2 at different pH values can be deduced. The Fe(II) adsorption intrinsic equilibrium constant obtained in this study can be used as an input parameter to the CCM to predict the concentration of dissolved Fe(II) at different pHs. K_2 and K_3 at different pH values can be easily quantified with mass law equations that incorporate the concentration of free H^+. A quantitative relationship between pH and k_3 is required to used Equation (3.5) to predict the pH dependence of the Fe(II) inhibition effect on ASi dissolution.

3.6 Conclusions

By adding a variable amount of Fe(II) to anoxic amorphous silica (ASi) suspensions and conducting kinetic dissolution experiments under anoxic conditions, the effects of Fe(II) adsorption on the dissolution rate of ASi were assessed. Observed experimental data show that the presence of Fe(II) under anoxic conditions inhibits the dissolution kinetics of ASi. By combining with different models, the results suggest that Fe(II) is adsorbed to ASi by forming bidentate surface complexes, and shows distinct affinity to different of surface groups. Fe(II) is preferentially adsorbed by Q_2 groups (*i.e.*, silicate groups bonded to the silica lattice via two bridging oxygens) of ASi, which lead to the stabilization Q_2 groups. Although Q_3 groups (*i.e.*, silicate groups bonded to the silica lattice via two bridging oxygens) have a much lower affinity to Fe(II), their detachment is catalyzed by the adsorption of Fe(II). The contradictory effects of Fe(II) lead to which enhances the dissolution of ASi after the maximum inhibition point. In combination with earlier work in Chapter 2, ours results suggest that, in addition to ASi surface groups' concentrations, charge and accessibility, their coordinative arrangement is an important control on ASi dissolution kinetics in the presence of complexation agent Fe(II).

This study demonstrates that Fe(II) adsorption has contradictory effects on the reactivity of surface Q_2 and Q_3 groups, which is a new mechanism that couples the Fe and Si cycles in nature. This interaction between Fe(II) and ASi, which are both abundant in freshwater sediments, has

implications for understanding and predicting the cycling of both species in sediments, sediment porewaters, and the overlying water column.

Chapter 4

Co-precipitation of iron and silicon: Reaction kinetics, elemental ratios and the influence of phosphorus

4.1 Summary

Oxidative precipitation of Fe(II) at oxic-anoxic interfaces may contribute to the immobilization of dissolved silicon (DSi). The efficiency of DSi immobilization, however, depends on solution variables, in particular pH and the presence and abundance of dissolved phosphate (DP). To investigate the behavior of DSi during Fe(II) oxidation, anoxic solutions containing mixtures of aqueous Fe(II), DSi, and DP were exposed to dissolved oxygen (O_2) in both batch and agarose column systems. In the batch experiments, O_2 was added by sparging initially homogeneous solutions with air. In the agarose columns the top was left open to the atmosphere, thus allowing O_2 to diffuse into the agarose gel and producing a downward moving oxidation front.

In the batch reactor experiments, when DP was absent, the final Si:Fe molar ratio of the co-precipitates ranged from 0.09 at pH 6.5 to 0.33 at pH 7.5. The pH effect is attributed to higher incorporation of DSi during faster oxidative precipitation of Fe(II) at higher pH. When DP was present in the initial solutions, the Si:Fe molar ratios of the resultant precipitates were much lower. The experimental data, combined with kinetic reaction modeling, show that DSi removal during Fe(II) oxidation occurs via two pathways: (1) co-precipitation with Fe(II) during the oxidation of Fe(II)-DSi complexes, and (2) subsequent adsorption to the newly formed Fe(III) oxyhydroxide phases. In the presence of DP, phosphate ions successfully outcompete silicate for complexation with aqueous Fe(II) and for sorption sites on the Fe(III) oxyhydroxides.

In the column experiment, the Si:Fe molar ratio of the co-precipitates formed at pH 7 in the absence of DP was below 0.03. The limited Si incorporation reflects the slow, diffusion-limited Fe(II) oxidation rates, compared to the batch experiments. A diffusion-reaction model yielded time- and depth-dependent pore water profiles of Fe(II), DSi and DP that were in general agreement with the observed distributions. Together, the experimental and modeling results indicate that DSi co-precipitation with Fe(II) strongly depends on the Fe(II) oxidation rate. The diffusion-controlled Fe(II) oxidation rates in the column experiments more closely resemble the transport-reaction

regimes encountered in natural sediments and stratified water columns. In other words, the efficient co-precipitation of DSi observed in the batch experiments, particularly in the absence of DP, may not provide a good analog for most natural settings where oxidative Fe(II) precipitation occurs.

4.2 Introduction

The availability of dissolved silicon (DSi) relative to that of dissolved phosphate (DP) in aquatic systems regulates the phytoplankton community composition. A sufficient supply of DSi relative to DP decreases the likelihood of harmful algal blooms in eutrophic waters (Egge and Aksnes, 1992; Makulla and Sommer, 1993; Officer and Ryther, 1980; Redfield et al., 1963). Internal fluxes of DSi from sediments to the overlying water (*i.e.*, "internal DSi loading") can be an important source of DSi to freshwater systems. Although data is sparse, internal DSi loading shows a dependence on redox conditions at many sites (Conley, 2002; Ekeroth et al., 2016; Mortimer, 1941; Ridenour, 2017). The reductive dissolution of Fe(III) oxyhydroxides, which have a high capacity to adsorb and/or incorporate a variety of anions including DSi and DP into their structures, is proposed to be the key process contributing to the increased DSi release during the transition from oxic to anoxic conditions (Kaegi et al., 2010; Mayer and Jarrell, 2000; Sung and Morgan, 1980; van der Grift et al., 2014; Voegelin et al., 2010).

Fe(III) oxyhydroxides are ubiquitous in sediments and are characterized by their high surface areas and high affinity for DP adsorption, and are therefore often considered to control the availability of DP in natural waters (Gächter and Mülle, 2003; Gachter and Muller, 2003; Jensen et al., 1992; Mortimer, 1941; Parsons et al., 2017; Ridenour, 2017; Sabur, 2019; Zhang and Huang, 2007). Unlike DP, the affinity of DSi for sorption to Fe(III) oxyhydroxide surface sites is limited by its speciation as monomeric silicic acid (H_4SiO_4) at neutral pH, which has a low affinity for the surface sites (Davis et al., 2002; Hiemstra et al., 2007; Sabur, 2019). In addition to surface adsorption (Figure 4.1A), the co-precipitation of dissolved Fe(II) and DSi, which are both commonly found in high concentrations in anoxic porewater, is another mechanism of DSi retention in sediments (Figure 4.1B). The oxidation of Fe(II) in the absence of complexation agents proceeds along two reaction pathways simultaneously: homogeneous oxidation, which occurs in solution, and heterogeneous oxidation, which takes place on the surface of Fe(III) oxyhydroxides

(*i.e*. the autocatalytic oxidation of Fe (II) by surface adsorption) (Pham and Waite, 2008; Tamura et al., 1976; Wolthoorn et al., 2004). The rates of both Fe(II) oxidation pathways depend on pH and the dissolved oxygen (DO) concentration (Millero, 1985; Morgan and Lahav, 2007; Stumm and Morgan, 1996). The presence of DSi can also affect the rates of both oxidation pathways as well as the stability of the Fe(III) oxyhydroxides produced (Cismasu et al., 2014; Davis, 2000; Dyer et al., 2010; Jones et al., 2009; Kaegi et al., 2010; Voegelin et al., 2010; Wolthoorn et al., 2004), which can affect the reactivity of the Fe(III) oxyhydroxides toward reductive dissolution (Sabur, 2019). However, a comprehensive understanding of the interactions between DSi and Fe(II) during the co-precipitation process is still lacking.

Dissolved inorganic ions other than DSi can also influence Fe(II) oxidation rates (Buamah et al., 2009; Kaegi et al., 2010; King, 1998; Kinsela et al., 2016; Mao et al., 2011; Mitra and Matthews, 1985a; Tamura et al., 1976; Wolthoorn et al., 2004). For example, the presence of DP increases the homogeneous oxidation rate of Fe(II). The proposed mechanism for this enhancement effect is that aqueous complexes of DP and Fe(II) constitute the oxidation reaction species, and that these complexes are more reactive towards oxidation than free Fe^{2+} (Mao et al., 2011; Tamura et al., 1976). At the same time, DP may retard the heterogeneous Fe(II) oxidation by competing with Fe(II) for adsorption to surface sites (Wolthoorn et al., 2004). Since the industrial revolution, large amounts of P have been loaded to water bodies by the use of P-containing fertilizers and detergents, which has led to substantial increases of P concentration in fresh waters (Filippelli, 2008). Although studies have shown that DP concentrations affect the precipitation rate of Fe and the properties of the precipitates (Mao et al., 2011; Tamura et al., 1976; Wolthoorn et al., 2004; Zhang and Huang, 2007), there are no studies that investigate how DP may compete with and influence the mobility of DSi in solution during the oxidative precipitation of Fe(II).

While batch experiments are typically used to study the kinetics of the reactions such as Fe(II) oxidation (or ASi dissolution kinetics, as in Chapter 2 and 3 of this thesis), column experiments can be used to study the interactive effects of reaction and transport, including, in the case of this study, the transport of dissolved O_2 (DO), dissolved Fe(II), DSi and DP. Sediment columns are typically used to study the interactions between reactions and transport processes and to best simulate the *in situ* conditions in natural sediments in the lab such that environmental conditions such as the inflow solution's chemical concentrations, temperature, and oxygenation are controlled

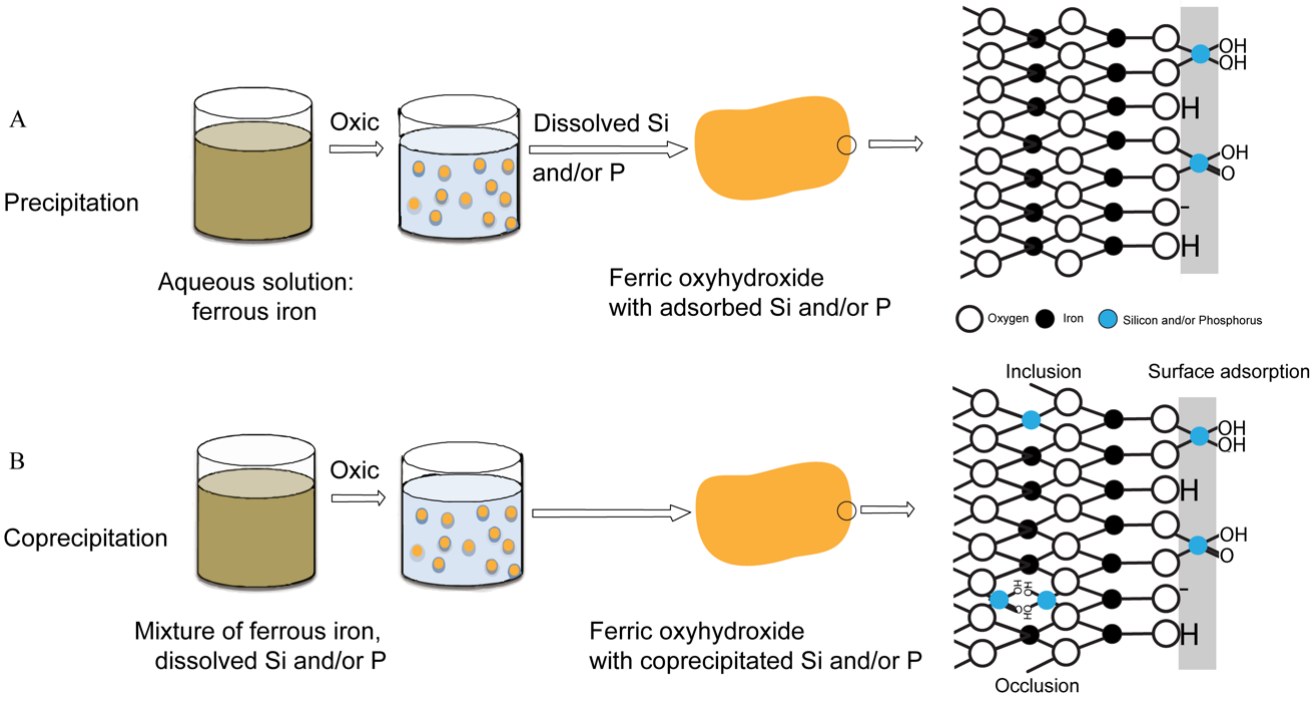

Figure 4.1. Illustration of surface adsorption and co-precipitation interactions. A. The oxidation and precipitation of Fe(III) oxyhydroxides and the subsequent adsorption of DSi and/or DP. B. The co-precipitation of Fe, Si and/or P during Fe(II) oxidation, DSi and/or DP can be incorporated by surface adsorption, lattice replacement (inclusion, also known as isomorphic substitutions, a previous study has shown that Si may not substitute for Fe in the goethite structure (Gomez et al., 2011)), and adsorption inside (occlusion, also known as the imperfection in the crystal).

(Couture et al., 2010; Couture et al., 2016; Ridenour, 2017). However, the complex processes occurring in natural sediments, where more than one reactive particulate Si endmember may be contributing to DSi (im)mobilization, multiple geochemical interactions are occurring simultaneously, the effect of co-precipitation of Fe and Si on the (im)mobilization of DSi may not be distinguished.

In this chapter, I use experimental data collected in batch and agarose column incubations coupled with chemical reaction modeling to investigate the interactions between DSi, dissolved Fe(II) and DP during oxygenation. I use the agarose columns to introduce and consider the role of diffusive transport of DO and the other chemical reactants and products, and to compare the results in the columns with those in the batch system. The chemical reaction model represents all of the relevant chemical interactions that would occur between DSi, DP, and dissolved Fe(II) during the transition from anoxic to oxic conditions. This chapter aims to use the coupled experimental and modeling approach to increase our understanding of these interactions and to demonstrate the ability to predict DSi removal rates as a function of pH, DP and Fe(II) concentrations, and molecular diffusion.

4.3 Methods

4.3.1 Reagents

HEPES (4-(2-hydroxyethyl)-1-piperazineethanesulfonic acid, Fisher Scientific, useful pH range: 6.8 to 8.2) and MOPS (3-(N-morpholino) propanesulfonic acid, Fisher Scientific, useful pH range: 6.5 to 7.9) were used as pH buffer. 100 mM DP and DSi stock solutions were prepared with sodium phosphate monobasic (NaH_2PO_4, Sigma Aldrich, ≥ 99.0%) and sodium metasilicate ($Na_2SiO_3.9H_2O$, Sigma Aldrich, ≥ 98.0%) respectively. 100 mM Fe(II) stock solution was prepared with ferrous chloride tetrahydrate ($FeCl_2.4H_2O$, Sigma Aldrich, ≥ 99.0%) in an anaerobic chamber (atmospheric composition: 97-98% N_2, 2-3% H_2 and < 1 ppmv of O_2) using 0.5 N HCl to avoid subsequent oxidation and precipitation. All solutions used were prepared with analytical grade reagents and 18.2 MΩ cm^{-1} (Millipore) unless otherwise stated.

4.3.2 Batch experiment

To simulate the interaction of anoxic porewater mixing with oxic water at the sediment-water interface, co-precipitation experiments modified from Voegelin et al. (2010) were conducted in 2 L Teflon batch reactors. 20 mM HEPES or MOPS in Milli-Q water was used as pH buffer, and pH was adjusted to the target value (6.5, 7.0, 7.5) with NaOH and HCl. After adding 10 mM NaCl as a background electrolyte, Na_2SiO_3 and NaH_2PO_4 stock solution were added into the solution to obtain an initial Si concentration of 300 μM, and initial P concentrations of 0, 75, 150, and 300 μM. Humidified ultra-pure air (where CO_2 is less than 0.5ppm) was continuously sparging for three hours before Fe(II) was added to avoid reactions involving bicarbonate. 4.5 mL of 100 mM Fe(II) stock was added to 1.5 L background solution to achieve an initial concentration of 300 μM. Duplicate experiments were conducted, and the reactors were wrapped with aluminum foil to keep out light. During the experiment, humidified ultra-pure air was continuously sparging with vigorous stirring, and DO and pH values were monitored with an Orion Versa Star electrochemistry meter (Thermo Scientific). This meter was equipped with pH and oxygen probes that were calibrated prior to each use. Before starting the experiments, metal-free 15 mL polypropylene centrifuge tubes containing 102 μL of 6N trace-metal hydrochloric acid were labeled and weighed. 10 mL of suspension samples were collected at designated intervals via syringe through a sampling port. These samples were collected periodically by filtering the samples through 0.2 μm pore-size polypropylene syringe filters into tubes with corresponding labels containing 102 μL HCl. After sampling, tubes were weighed and the volumes of sample were recorded. The total volume removed during the experiment was less than 10% of total volume. All experiments were conducted in an environmental chamber with the temperature set at 25±1 °C.

Table 4.1. Initial chemical compositions of working solutions for oxidation experiments and chemical compositions of the co-precipitates. All solutions were prepared by carefully weighing every reagent and solvent. Bulk suspensions were collected and acidified without filtration for the determination of initial concentration of Fe, Si, and P.

No.	Initial solution characteristics					Chemical composition of the co-precipitates	
	Buffer	pH	Fe	Si	P	Si:Fe	P:Fe
			μM				
1	MOPS	6.5	150	150	0	0.09	0
2			295±5	270±10	76±3	0.08	0.27
3					150±5	<0.01	0.49
4					300±5	<0.01	0.52
5	HEPES	7.0			0	0.15	0
6					76±3	0.08	0.26
7					150±5	0.02	0.49
8					300±5	0.01	0.58
9		7.5			0	0.33	0
10					76±3	0.17	0.26
11					150±5	0.08	0.42
12					290±5	0.05	0.54

4.3.3 Column experiment

For simplification, agarose columns with a porosity close to 100% (the porosity of 2% agarose gel is 98%) (Pluen et al., 1999) were used as a column medium to facilitate the diffusion of oxygen into the initially anoxic columns from the air, and to provide a medium for co-precipitation (Figure 4.2). Like the solution in batch experiment, the background solution contained 20 mM HEPES and 10 mM NaCl was used as a background electrolyte. The background solution with a pH adjusted to 7.0 was sparged with N_2 for at least 3 hours while boiling, and then was brought into an anaerobic chamber (with an atmospheric composition of 97-98% N_2 and 2-3% H_2). After a day of cooling down in the chamber, 1.0 g of ultra-pure agarose (Invitrogen, Fisher Scientific) was added to a 140 mL serum bottle containing 100 mL of background solution, *i.e.*, 1 wt. % agarose in the background solution. The serum bottles were sealed with rubber stoppers and aluminum caps to avoid contamination by O_2, and then taken out of the anaerobic chamber. The agarose particles were then dissolved in the sealed serum bottle by placing them in a preheated 100 °C water bath for 30 minutes. The bottles were then brought back into the anaerobic chamber and the $FeCl_2$, Na_2SiO_3, and NaH_2PO_4 stock solutions were added into the 1% agarose background solution. 10 mL of this agarose-containing working solution, which had initial concentrations of Fe(II), DSi, and DP as indicated in Table 4.1, was added to metal male luer-lock glass syringes (Cadence Science, Fisher Scientific). The bottom outlets of all the syringes were equipped with one-way stopcocks (Cole-Parmer) whose seals had been checked with soapy water. The integrity of this seal was ensured by wrapping the outlet of the stopcock with sealing film (Parafilm, Sigma Aldrich).

After the agarose had solidified, all of the syringes were taken out of the anaerobic chamber and placed in a constant temperature environmental chamber at 25±1 °C. From that point on, two syringe reactors were sacrificially sampled at the elapsed times of 6, 21, 45, 79, 93, and 152 hours. To sample the agarose columns, the syringes containing the agarose were brought into the anaerobic chamber where the agarose was pushed out of the end of the syringes with the large opening by supplying the opposite narrow opening with gentle gas pressure from another syring containing gas from the anaerobic chamber atmosphere. As the agarose was pushed out, it was carefully sliced into around 2 mm thick slices with a razor blade which was wiped with ethanol between each use. The agarose slices were weighed and placed in tubes containing 2 mL of

Figure 4.2. Photo of agarose column experiment. 1% agarose (wt. %) was melted under anoxic conditions, Fe(II) was added to the solution for the three columns pictured on the right, and the solution was allocated to 10 mL metal male luer-lock glass syringes to solidify in the anaerobic chamber. After the solidification of the agarose, columns were taken out of the chamber and exposed to air at one end. This photo was taken after 6 hours of exposing the columns to air at 25±1 °C. The three columns shown on the left contain background solution with sodium resazurin to show the diffusion of oxygen (Uzarski et al., 2017). The diffusion of oxygen in these columns is evident by the blue-purple colour that can be seen in the near-surface agarose. The three columns shown on the right contain about 300 µM initial Fe(II) concentration in their background solution.

Table 4.2: Initial Fe, Si, and P concentration in working solution for column experiment.

Exp. No	Initial Fe	Initial Si	Initial P
		µM	
1	300	150	0
2	300	150	50

background solution to equilibrate solution-extractable dissolved Fe, DSi and DP. After equilibrating agarose slices with the solution for 6 hours, 1.8 mL of sample was collected from each tube, and the supernatant was diluted, acidified, and taken out of the anaerobic chamber for further analysis. For the solid phase analyses, 1.8 mL of 6N HCl was added into each tube containing an agarose slice to dissolve any Fe(III) precipitates, and 6 mL of background solution was added 12 hours later. Before analysis of the extracted solid phase, the agarose slices were removed by centrifuging at 5000 rpm for 20 minutes.

4.3.4 Analytical methods

Both the solution-extractable and solid phase extraction samples were filtered with 0.2 μm pore-size polypropylene syringe filters, acidified with trace-metal hydrochloric acid to pH < 2, and analyzed by Inductively Coupled Plasma-Optical Emission Spectrophotometry (ICP-OES, Thermo Scientific iCAP 6300) to determine the concentration of total dissolved Na, Si, and Fe using the US EPA Method 200.7 (U.S. EPA., 1994). Matrix-matched standards were prepared from Fisher Scientific stock standards (Thermo Fisher Scientific) to eliminate the matrix interference. Reference solutions were prepared with multi element standards (Delta Scientific Laboratory Products Ltd.) and were analyzed along with all samples for quality control. Fe(II) was determined by the ferrozine method (Viollier et al., 2000) after filtration and acidification of samples (MDL 3.8 μM). All aqueous analyses were conducted in triplicate. The accuracy of the reference solution measurements across all sample run was better than 10% and the relative standard deviation of 5 replicates was well within 5%.

4.3.5 Kinetic modeling of co-precipitation

To evaluate the contributions of different, sometimes competing reactions to the overall Fe(II), DSi and DP removal rates observed in the batch experiments, I developed a kinetic model that accounted for the potential reactions occurring in solution. To account for the diffusive transport of chemicals in the agarose columns, I incorporated diffusion into the kinetic reaction model, herein referred to as the diffusion-reaction model. The reactions included in the model are listed in Table 4.3. The model included the least number of reactions possible while still describing the co-precipitation process adequately. Briefly, the model includes the homogenous oxidation of Fe(II) (Reaction 1), the polymerization and condensation of Fe(III) (Reaction 2), the adsorption

and desorption of Fe(II) to the surface sites of Fe(III) oxyhydroxide (Reaction 3), the heterogeneous oxidation of Fe(II) and surface precipitation of Fe(III) (Reaction 4), the complexation and dissociation of Fe(II) and DSi (Reaction 5), the oxidation of Fe(II) and DSi complexes (Reaction 6), the adsorption and desorption of DSi to the surface sites of Fe(III) oxyhydroxides (Reaction 7), the complexation and dissociation of Fe(II) and DP (Reaction 8), the oxidation of Fe(II) and DP complexes (Reaction 9), and the adsorption and desorption of DP to the surface sites of Fe(III) oxyhydroxides (Reaction 10). The value of *n* in Reactions 3 and 4 was set to 2.0, representing the growth of surface sites of Fe(III) oxyhydroxides during precipitation (see more details in Appendix C.).

The Python toolbox PorousMediaLab (Markelov, 2019) was used to model the experimental data collected, fit the kinetic parameters using an optimization procedure, and perform a sensitivity analysis. Full details of the chemical reaction stoichiometries for all the reactions represented and how the kinetics parameters were optimized can be found in Appendix C.

4.4 Results

4.4.1 DSi removal during Fe(II) oxidation in the absence of DP in batch system

4.4.1.1 Effect of pH on Fe(II) oxidation kinetics

Fe(II) oxidation in the presence of DSi was studied over the pH range of 6.5-7.5 at 25±1 ºC and at an ionic strength of 10 mM NaCl. At all pH values, the concentration of dissolved Fe(II) decreased with time from its initial value of 300 µM. However, the rates of decrease varied significantly with pH: it took less than 10 minutes for the reaction to reach equilibrium at pH 7.5, while at pH 6.5, it took more than 20 hours (Figure 4.3). At low initial pH values of 6.5 and 7.0, both pH and DO did not significantly change over the course of the experiments, as they both varied within 0.1 unit. In contrast, at pH 7.5, where around 95% of the initial Fe(II) amounts were oxidized within the first two minutes, the fast oxidation of Fe(II) led to a significant decrease of pH and DO (about 1 unit of both pH and DO in mg L^{-1}) in a short time period.

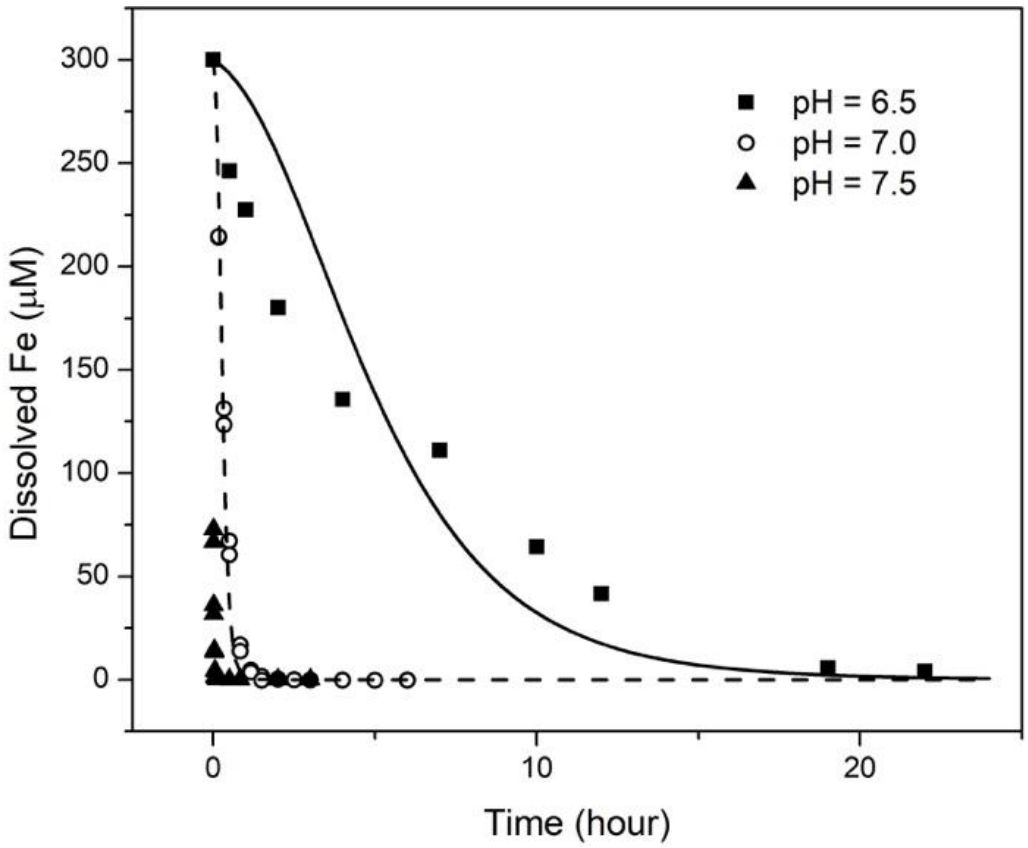

Figure 4.3. The oxidation kinetics of 300 μM Fe(II) in 10 mM NaCl solution at pH 6.5, 7.0 and 7.5 in the presence of 270±10 μM dissolved silicon (DSi). The data points are experimental data points. The solid line is the output of model prediction at pH 6.5, and the dashed line is the output of model prediction at pH 7.0. The oxidation kinetics of Fe(II) at pH 7.5 was so fast that both pH and DO changed during experiment. Therefore, kinetic information was not used for modeling at pH 7.5.

4.4.1.2 Effect of pH on DSi removal during Fe(II) oxidation

In the absence of DP, the relationship between the amounts of DSi and Fe removed can be categorized into two stages (Figure 4.4). At first, the amount of DSi removed increased linearly with an increasing amount of dissolved Fe removed (Stage 1 in Figure 4.4). The slopes of these linear relationships were highly pH dependent, increasing from 0.05 at pH 6.5 to 0.27 at pH 7.5. Following the initial stage, DSi continued to be removed from solution while dissolved Fe concentrations were either under the detection limit or were no longer changing over time (Stage 2 in Figure 4.4). The DSi concentrations remaining at the end of experiments were highly pH-dependent; around 190 µM of DSi remained at pH 7.5 after 2 hours of oxidation, while about 255 µM of DSi remained at pH 6.5 after 22 hours of oxidation. Overall, the Si:Fe molar ratio (with initial concentrations of DSi of 270±10 and of Fe(II) of 295±5 µM, and in the absence of DP) in their co-precipitates increased from 0.09 to 0.33 (µmol Si per µmol Fe), as the pH increases from 6.5 to 7.5 (Table 4.1).

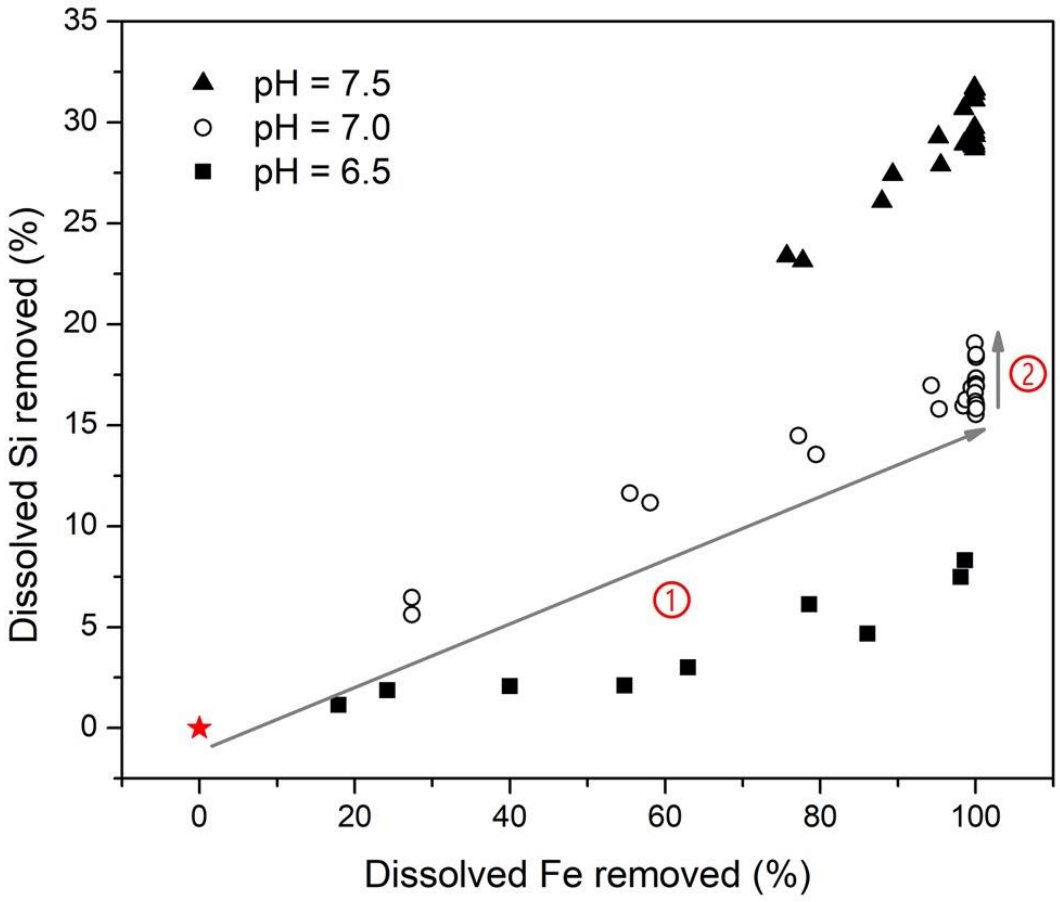

Figure 4.4. DSi removal during Fe(II) oxidation in the absence of DP. The relationship between precipitated Fe and Si at different pH values (Initial Fe and DSi were 295±5 and 270±10 µM, respectively, in the absence of DP). Number 1 and 2 represent different stages corresponding to the removal of DSi during the oxidation of Fe(II). The red star represents the initial status.

4.4.2 DSi removal during Fe(II) oxidation in the presence of DP in batch system

4.4.2.1 Effect of DP on Fe(II) removal kinetics

The effects of DP on Fe removal kinetics were highly pH dependent. Fe(II) removal is used here to describe Fe(II) removal from the aqueous phase instead of oxidation, as Fe(II) was detected in the solid phase for the incubation at pH 7.5. For example, more than 30% of the total Fe was incorporated into the solid phase as Fe(II) at the beginning of the oxidation/precipitation process at pH 7.5 at the highest initial DP concentration (higher than 150 µM). Fe(II) oxidation can be used to describe the removal of Fe(II) in the presence of DP at pH values 6.5 and 7.0, because almost no Fe(II) was detected in the solid phase (it was always detected as less than 1% of the total Fe). At pH 7.5 (the highest pH in this study), DP inhibited Fe(II) precipitation, and this inhibition effect decreased with increasing DP concentration. At pH 6.5 (the lowest pH in this study), the presence of DP enhanced Fe(II) precipitation and this enhancement effect increased with increasing DP concentration. At pH 7.0, DP in low concentrations inhibited Fe(II) oxidation, while at high DP concentrations, DP enhanced Fe(II) oxidation.

The amount of DP removed, as long as some remained in solution, increased linearly with the amount of dissolved Fe removed (Figure 4.5) for initial Fe and DP concentrations of 295±5 and 150±5 µM, respectively. The ratios of P:Fe precipitated, were slightly pH dependent: a ratio of 0.42 (µmol P per µmol Fe) at pH 7.5 increased to 0.51 at pH 6.5 (Figure 4.5). For the same initial solution Fe:P ratio, the dissolved Fe and DP concentrations remaining in solution at equilibrium (*i.e.*, at the point when dissolved Fe was no longer changing over time) differed with pH. Around 20 µM of dissolved Fe and 40 µM of DP remained at pH 7.5 after 2 hours of aeration (*i.e.*, oxygenation), while around 3 µM of Fe and 5 µM of P remained at pH 6.5 after 22 hours of aeration.

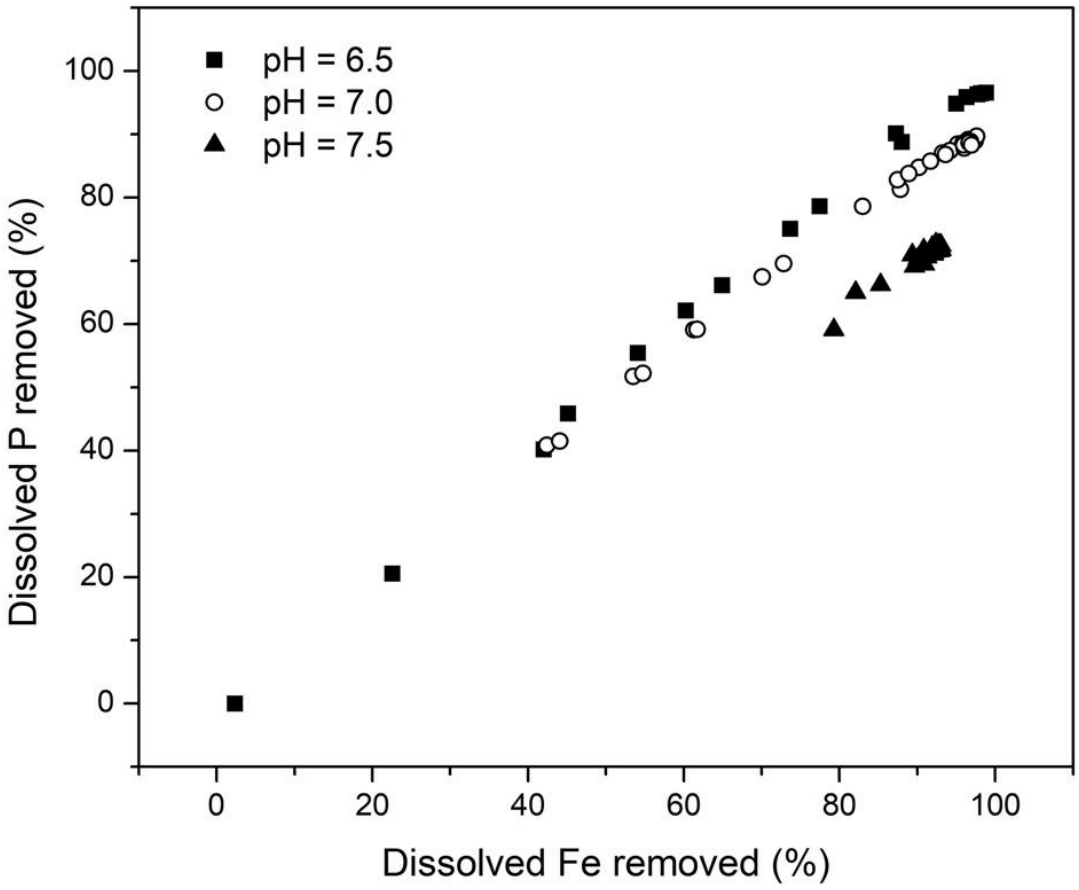

Figure 4.5. The removal of dissolved phosphate (DP) during oxidation of Fe(II) in the presence of dissolved Si (Initial dissolved Fe and DP were 295±5 and 150±5 µM, respectively, initial DSi concentration was 270±10 µM).

4.4.2.2 Effect of DP on DSi removal during Fe(II) oxidation

The effect of DP on DSi removal was studied by varying the initial P concentration at pH 7.0 and with 295±5 µM of initial dissolved Fe(II) provided in solution. Figure 4.6a shows how the amount of Si removed is dependent on the initial DP concentration. Specifically, when the initial DP concentration was high (higher than 150 µM, or initial DP:Fe > 0.5), the DP concentrations remaining in solution decreased throughout the course of Fe(II) oxidation, while DSi concentrations hardly decreased until DP concentrations were lower than 25 µM. At equilibrium, about 17.9% of the initial DSi was removed in absence of DP, while the amount in the presence of high initial DP concentration (150 and 300 µM) was much less, amounting to around 1.2% of the initial DSi.

The effect of DP on the removal of DSi during the oxidative precipitation of Fe(II) was also studied at different pH values (Figure 4.6b). DSi concentration decreased slightly with that of DP at high pH during the oxidation of Fe(II) (pH = 7.5 in Figure 4.6b), but barely changed at low pH (pH = 6.5 in Figure 4.6b). At equilibrium, about 31.5% of initial DSi was removed in absence of DP, while the amount at pH 6.5 was about 5.4%.

Overall, the trends in the relative concentrations of DSi and DP in solution during their competition for co-precipitation with Fe was described as three regions (which corresponded to stages that progress with time and extent of oxidation/precipitation): the initial stage where only DP, and not DSi, was removed from solution, the intermediate stage where DP continued to be removed and a comparatively smaller amount of DSi was removed, and the final stage where the solution DP had been depleted and the highest amount of DSi was removed (compared to the other regions) (Figure 4.6). At higher initial DP concentrations where the initial DSi concentration was fixed, the initial stage was more predominant, and the intermediate and final stages (when DSi removal and presumably co-precipitation occur) were more delayed (Figure 4.6a).

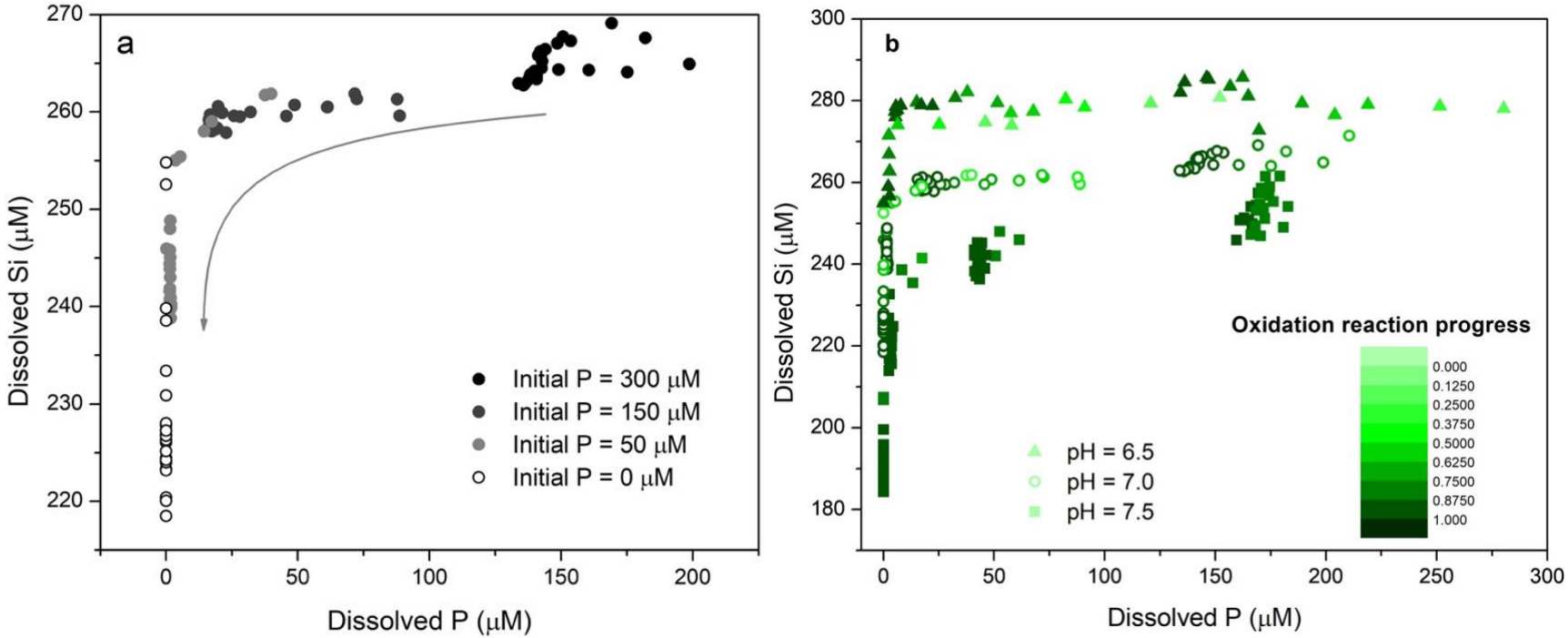

Figure 4.6. The relationship between DSi and DP concentration remaining in solution during Fe(II) oxidation (the initial Fe concentration was 295±5 μM, the initial DSi concentration was 270±10 μM, and there were different initial P concentrations). (a) The effect of variable initial DP concentrations on the removal of DSi during Fe(II) oxidation at pH 7.0. (b) The effects of different pH values on the removal of DP and DSi during Fe(II) oxidation. It should be noted that DP remaining decreases with the progress of oxidation. The rightmost data points of each groups with different initial P concentrations represent samples collected at the beginning of experiments, and the leftmost represents the last data points collected in each experiment. The arrows represent the direction of the progress of the co-precipitation reaction. Different colours represent the progress of oxidation reactions: 0 indicates almost no oxidation of Fe(II), 1 indicates the complete oxidation of all Fe(II).

4.4.3 Agarose column results

4.4.3.1 Vertical distribution of dissolved Fe, DP and DSi in agarose columns

The effects of diffusion on the co-precipitation of Fe, Si, and P during Fe(II) oxidation were studied by measuring their concentrations remaining in solution in agarose columns whose top ends were open to air. Before starting the extensive sacrificial column experiment, a preliminary experiment was conducted to test the diffusion of DO in an agarose column after exposure to air for 6 hours, at which point the column was sacrificed to measure the concentration-depth distributions of dissolved Fe and DSi. After 6 hours of air exposure, Fe(II) from greater depths in the column diffused towards the air-exposed surface, and precipitated at the oxidation front (Figure 4.7). In the absence of DP, DSi concentrations in the agarose columns showed a slightly decrease at the oxidation front compared to concentrations at depths below the oxidation front (Figure 4.7). There were abnormally high DSi concentrations near the surface of the columns that were greater than the concentrations observed at depths above the oxidation front (Figure 4.7). Although the concentrations of DO with depth in the agarose columns were not monitored directly, they can be inferred based on the concentration-depth profile of dissolved Fe that DO penetrates to a depth of around 1.2 cm below the column surface after 6 hours. Dissolved Fe was measured as total dissolved Fe in the anoxic porewater of the agarose columns on the ICP-OES, which is presumably mostly Fe(II). A comprehensive understanding of the concentration-depth distribution of solid phase Fe and Si in the preliminary experiment was not possible, because their profiles were not complete, as agarose slices from deeper depths of the columns were not analyzed.

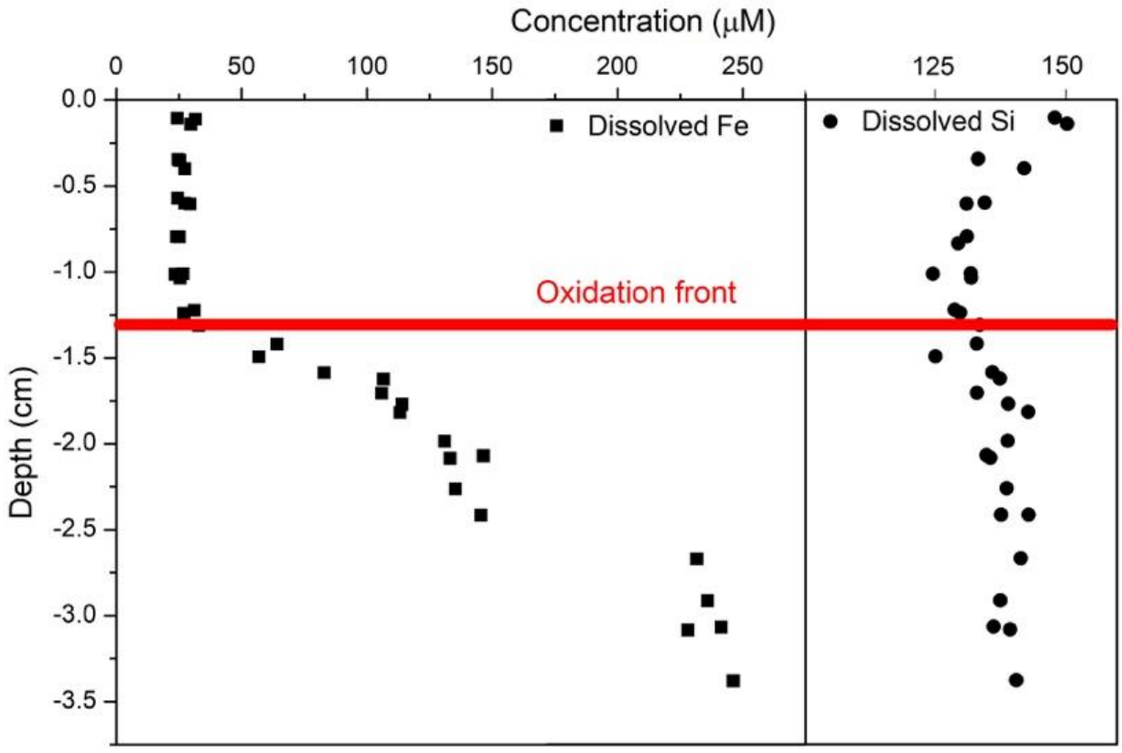

Figure 4.7. Dissolved Fe and DSi concentration-depth profiles after exposure to air for 6 hours. Oxidation front (red line) is the boundary of oxic and anoxic zone in the agarose column: oxic zone is above the oxidation front, anoxic is below the oxidation front.

In the main column experiment, where DSi, DP and dissolved Fe(II) were all present in the agarose medium initially and the columns were sacrificially sampled over time, the complete concentration-depth profiles of dissolved Fe, DSi, and DP were measured, as well as their evolution over time (

Figure 4.8, 4.9 and C.1). Dissolved Fe concentrations measured at depths close to the bottoms of the columns were equal to the initial concentration of dissolved Fe, which was around 270 µM. The initial dissolved Fe concentration should have been 300 µM based on the careful preparation of the solution, which involved weighing every solution and reagent. The discrepancy between these measured dissolved Fe concentrations and the initial solution concentration is likely attributable to the incomplete recovery rate during the extraction of the aqueous phase by the background solution.

After 6 hours of air exposure, the oxidation front where Fe precipitated was around 1.2 cm below the surface (

Figure 4.8). The concentration of dissolved Fe above the oxidation front was around 37 µM. Below the oxidation front, dissolved Fe concentration increased with depth within the first centimeter and remained constant (and equal to the initial dissolved Fe concentration) with depth in the columns (deeper than 2.5 cm below the surface). With increased elapsed time since air exposure and the progression of diffusion, the oxidation front moved deeper into the column with time of air exposure and reached a depth of around 5.5 cm below the surface after 152 hours. During this time period, dissolved Fe concentrations in the oxidized zone remained constant (at about 37 µM), while concentration deeper in the column decreased from 270 µM at the beginning of the experiment to 37 µM by the end of experiment as the oxidation front moved down and oxidized Fe(II). DP remaining in the agarose columns is correlated with dissolved Fe remaining, which is itself dependent on the concentration of DO (

Figure 4.8 and C.1). The initial concentration of DP was 54 µM. With the diffusion of oxygen into the agarose columns, DP co-precipitated with Fe at the oxidation front. Consequently, DP from the deeper the columns diffused towards the oxidation front until there was no concentration gradient, which occurred when DP was around 5 µM.

The vertical distribution of DSi in the agarose columns, which differed from the distribution observed in the absence of DP (Figure 4.7), did not show an obvious correlation with dissolved Fe (

Figure 4.8 and Figure 4.9). Despite the scattered data points, DSi concentrations in the agarose columns followed a general trend: above the oxidation front, near the surface of the columns, DSi decreased with increasing depths then increased slightly with depth at depths below the oxidation front depth. At the oxidation front, a decrease of DSi at oxidation front was also observed. At the oxidation front, DSi decreased to 141±8 µM after 152 hours of air exposure from its initial concentration of 150 µM.

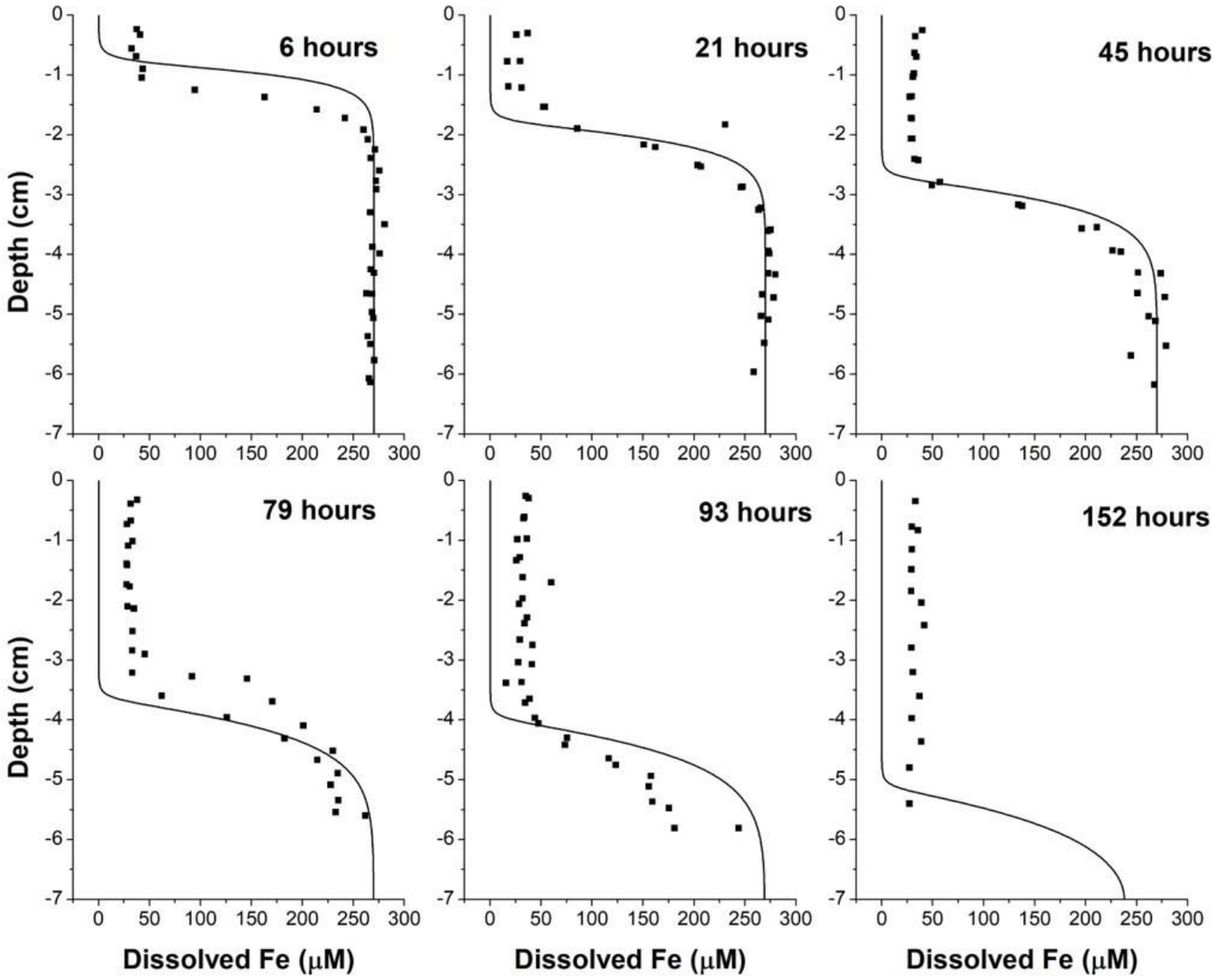

Figure 4.8. The evolution of dissolved Fe profiles in agarose columns with time. Each subplot representing a different elapsed time and sacrificial sampling of the columns. Before exposure to air, the initial chemical composition is homogeneous throughout the agarose columns with Fe(II), P, and Si concentrations being 270, 54, and 150 μM respectively. Points represent experimental data of dissolved Fe extracted, and solid lines represent model predicted dissolved Fe(II) concentrations (See details in Discussion).

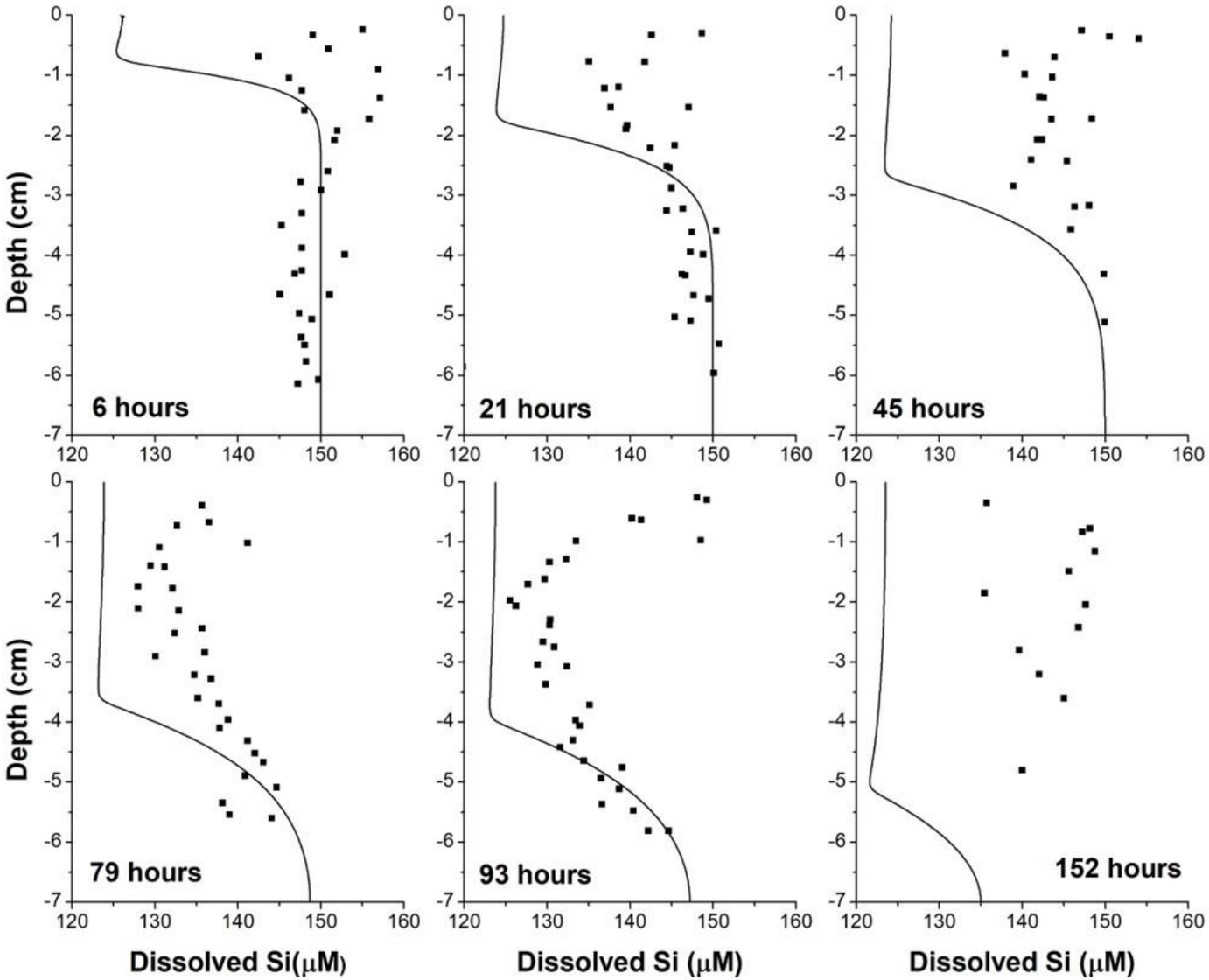

Figure 4.9. The evolution of dissolved Si (DSi) concentration-depth profiles in agarose columns with time. Each subplot representing a different elapsed time and sacrificial sampling of the columns. Before exposure to air, the initial chemical composition is homogeneous throughout the agarose columns with Fe(II), P, and Si concentrations being 270, 54, and 150 μM respectively. Points represent experimental data of DSi extracted, and solid lines represent model predicted DSi concentrations (See details in Discussion).

4.4.3.2 Elemental composition of co-precipitates in agarose columns

The diffusion of dissolved Fe(II) from the anoxic zone toward the oxic zone and its subsequent oxidation by DO and precipitation as Fe(III) oxyhydroxides led to the slight accumulation of solid Fe in the agarose close to the oxidized surface of the columns (Figure 4.10). P precipitated at the same depth as Fe (

Figure 4.8 and Figure C.1). The elemental ratio of Fe and P in the solid phase was equal to their initial ratio in the dissolved phase (P:Fe = 0.2) and did not change over the course of the oxidation process (Figure 4.11). DSi removal was not correlated with the amount of Fe(II) removed by precipitation in the agarose columns (Figure 4.11), whereas they were correlated in the batch experiment (Figure 4.4). The elemental ratio of Si and Fe removed was less than 0.03 (Figure 4.11).

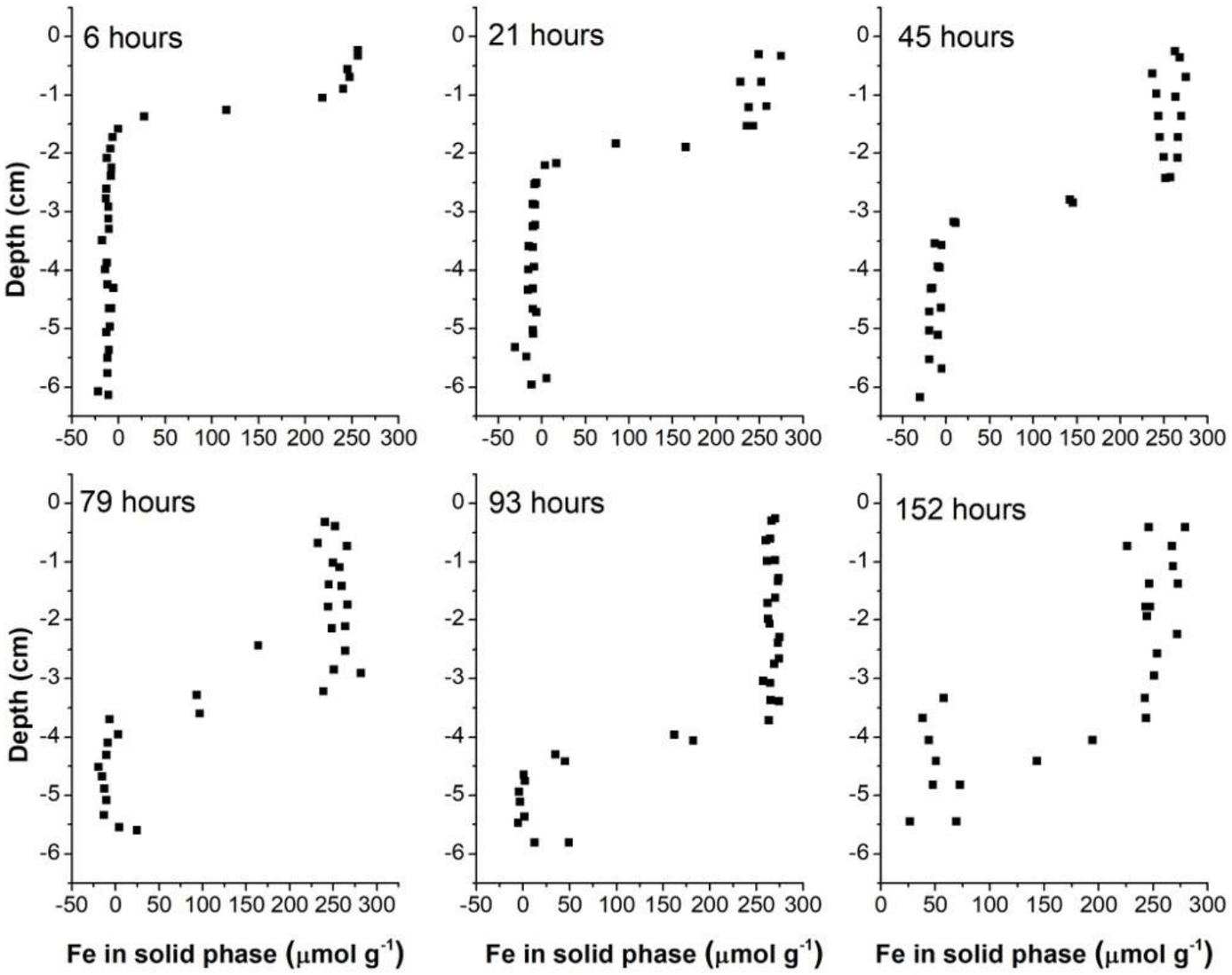

Figure 4.10. The evolution of Fe (III) oxyhydroxides concentration-depth profiles in agarose columns with time. Each subplot representing a different elapsed time and sacrificial sampling of the columns. Initial Fe(II), P and Si concentrations are 270, 54 and 150 μM respectively. The initial pH is 7.0 with 20 mM HEPES as the pH buffer and temperature of oxidation is controlled at 25±1 °C.

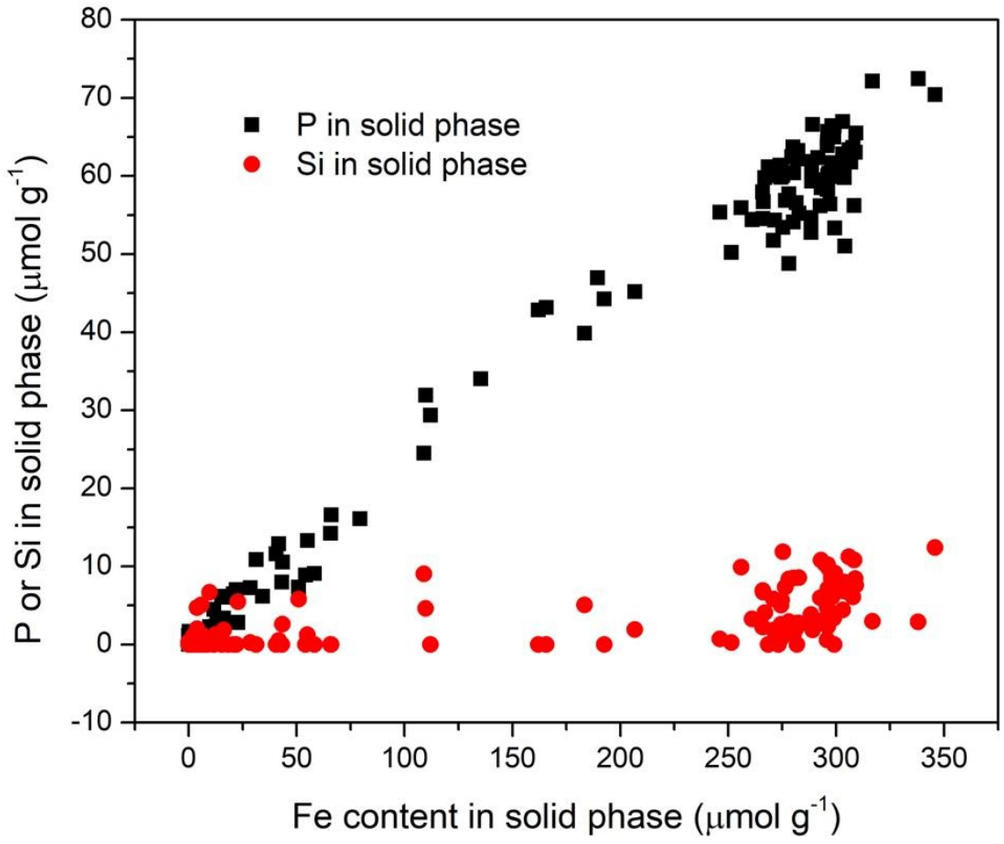

Figure 4.11. Solid phase Si or P versus solid phase Fe precipitated in agarose columns.

4.4.4 Kinetic reaction modeling

The rate constant parameters for the Reactions 3-10 represented in the model were fitted to the batch experiment data using the optimization procedure included within PorousMediaLab. The optimized rate constant parameters are summarized in Table 4.3. The reaction rate constants of dissolved Fe(II) and DSi complexation (Reaction 5) are much smaller than the rate constant for the surface adsorption of dissolved Fe(II) (Reaction 3) and the complexation of dissolved Fe(II) and DP (Reaction 8). The rate constants for the homogeneous oxidation of Fe(II)-DSi and Fe(II)-DP complexes (Reaction 6 and Reaction 9) are much larger than that of the homogeneous oxidation of Fe(II) alone (Reaction 1). The kinetic reaction model was implemented using the rate constants derived from the PorousMediaLab optimization to predict the reaction rates for each reaction in Table 4.3 at pH 6.5 and 7.0. The evolution of the model-predicted homogeneous and heterogeneous oxidation rates with time indicates that the heterogeneous oxidation of Fe(II) is inhibited in the presence of both DSi and DP (Figure 4.12). As per the optimized rate constants, the presence of DSi, and thus the presence of Fe(II)-DSi complexes, accelerates the homogeneous oxidation of Fe(II) relative to the rate for Fe(II) alone, and the enhancement effect of DP on the homogeneous oxidation of Fe(II) is even greater than that of DSi (Table 4.3).

Table 4.3. Reactions and rate constants accounting for the co-precipitation of Fe, Si, and P.

No.	Reaction	Rate constant ($M^{-1} s^{-1}$)	
		pH 6.5	pH 7.0
1	$Fe^{II} + (1/4)O_2 \rightarrow Fe^{III}$	3.5×10^{-3}	2.7×10^{-1}
2	$Fe^{III} + Fe^{III} \rightarrow 2$ >FeOH	5.0×10^{5}	1.0×10^{6}
3	>FeOH + $nFe^{II} \leftrightarrow$ >$FeO(Fe^{II})_n$	2.7×10^{-1}	5.0×10^{-1}
4	>$FeO(Fe^{II})_n + (n/4)O_2 \rightarrow Fe(OH)_3$(s) + n>FeOH	2.1×10^{0}	6.9×10^{0}
5	$Fe^{II} + Si \leftrightarrow Fe^{II}Si$	1.6×10^{-2}	3.2×10^{-2}
6	$Fe^{II}Si + (1/4)O_2 \rightarrow$ FeOHSi(s)	1.2×10^{-1}	1.2×10^{0}
7	>FeOH + Si $\leftrightarrow$ >FeOSi	2.4×10^{-3}	4.8×10^{-3}
8	$2Fe^{II} + P \leftrightarrow (Fe^{II})_2P$	2.5×10^{1}	4.9×10^{1}
9	$(Fe^{II})_2P + (1/2)O_2 \rightarrow (Fe^{III})_2P$(s)	5.8×10^{-1}	2.9×10^{0}
10	>FeOH + P $\leftrightarrow$ >FeOP	4.8×10^{1}	9.6×10^{1}

Rate constants of Reactions 1 and 2 are from (Kinsela et al., 2016). Rate constants for Reactions 3 and 4 are interpreted from data supplied in Pham et al. (Pham and Waite, 2008) and Kinsela et al. (Kinsela et al., 2016). All other values are derived from model fit to experimental data in this study. Values of Reactions 3, 5, 7, 8, and 10 represent equilibrium constants ($k_{complexation}/k_{dissociation}$). >FeOH represents surface sites, $Fe(OH)_3$(s) is iron precipitated in bulk solid that is inaccessible, and *n* is used to express the growth of surface sites of Fe(III) oxyhydroxides during precipitation.

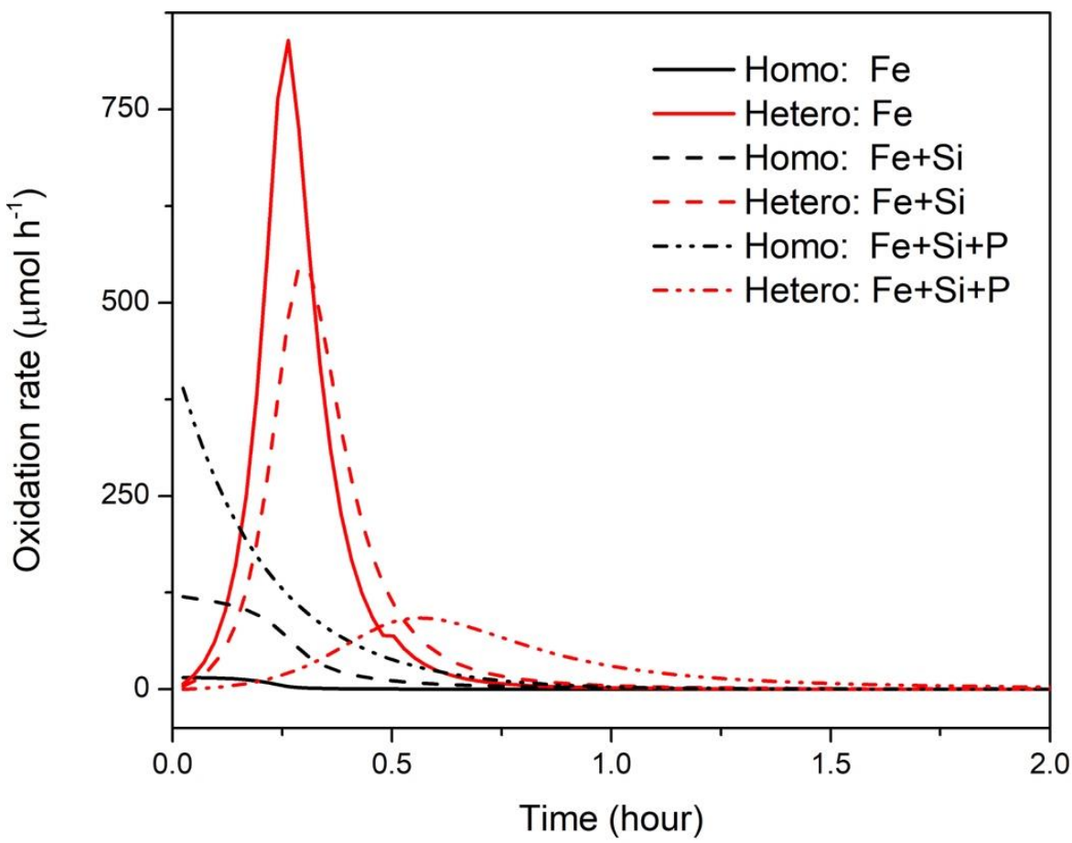

Figure 4.12. Model prediction of the homogeneous (black lines) and heterogeneous oxidation (red lines) rates of Fe(II) at pH 7.0. Solid lines correspond to the oxidation of 300 µM Fe(II) in the absence of complexation agents; dashed lines correspond to the oxidation of 300 µM Fe(II) in the presence of 270 µM DSi; dash-dotted lines correspond to the oxidation of Fe(II) in the presence of 270 µM DSi and 80 µM DP. Homo is short for homogeneous oxidation of Fe(II), including free Fe(II), Fe(II)-DSi complexes, as well as Fe(II)-DP complexes. Hetero is short for heterogeneous oxidation of Fe(II).

4.5 Discussion

4.5.1 Effect of pH on DSi removal during Fe(II) oxidation in the absence of DP

The kinetic data obtained in the batch experiment were used to decipher the mechanisms of co-precipitation of Fe and DSi. While a constant initial DSi concentration was used in this study and I am thus unable to directly assess the effect of DSi on the overall oxidation kinetics of Fe(II), a previous study showed that the presence of DSi inhibits the Fe(II) oxidation within the pH range of 6.0 to 7.0 (Kinsela et al., 2016). Kinsela et al (2016) propose that silica-ferrihydrites, the co-precipitates of Si and Fe(III), prevent Fe(II) from forming inner-sphere complexes, inhibiting the heterogeneous Fe(II) oxidation pathway. DSi has also been proposed to inhibit heterogeneous Fe(II) oxidation by competing with Fe(II) for surface sites by forming inner-sphere complexes on the surface of Fe(III) oxyhydroxides (Hansen et al., 1994; Sabur, 2019; Stumm, 1992; Wolthoorn et al., 2004). These mechanisms, however, do not explain the fast decrease of DSi concentration at the beginning of oxidation (Stage 1 in Figure 4.4, Figure C.2). Because surface sites for DSi and Fe(II) adsorption at the beginning of oxidation are limited by the small Fe(II) homogeneous oxidation rate constant (Kinsela et al., 2016).

The formation and oxidation of Fe(II)-DSi complexes explain the fast removal of DSi at the beginning of the Fe(II) oxidation process in the batch experiment. Fe(II)-DSi complexes enhance the homogeneous oxidation rate of Fe(II) compared to the homogeneous oxidation of free Fe^{2+}, although the exact speciation and reactivity of these complexes have never been identified (Wolthoorn et al., 2004). Instead of complexing with aqueous Fe(III) or surface sites of Fe(III) oxyhydroxides, DSi is more likely to form complexes with Fe(II) at the beginning of oxidation (Schenk and Walter, 1968).

Predictions made by the kinetic reaction model incorporating Reactions 1-7 in Table 4.3 (*i.e.*, not including reactions involving DP) support this interpretation of the relative contribution of two DSi removal mechanisms during Fe(II) oxidation/precipitation at pH 7.0. The amount of DSi removed by homogeneous oxidation of Fe(II)-DSi complexes starts to increase at the beginning of oxidation and reaches its maximum value after 0.5 hours, while DSi removal by surface adsorption begins after around 0.25 hours of oxidation (Figure 4.13). At equilibrium, the amount of DSi removed by homogeneous oxidation is about three times the amount removed by surface adsorption with initial DSi:Fe(II) close to 1 at pH 7.0.

The elemental ratio of Si:Fe removed from solution is highly pH dependent, increasing from 0.09 at pH 6.5 to 0.33 at pH 7.5 when the initial solution's DSi:Fe ratio was close to 1. The effect of pH on DSi removal during Fe(II) oxidation can be induced in the model by (i) changing the partitioning of Fe(II) and DSi species, and (ii) altering the surface charge of Fe(III) oxyhydroxides. In the absence of DSi, the oxidation rate constants of the three dominant Fe(II) species (Fe^{2+}, $Fe(OH)^{+}$, $Fe(OH)_2$, panel a in Figure 4.14) differ from each other by five orders of magnitude (Morgan and Lahav, 2007). In the presence of DSi, the oxidation rate constant of Fe(II)-DSi complexes (Reaction 6) increases by about one order of magnitude as pH increases from 6.5 to 7.0.

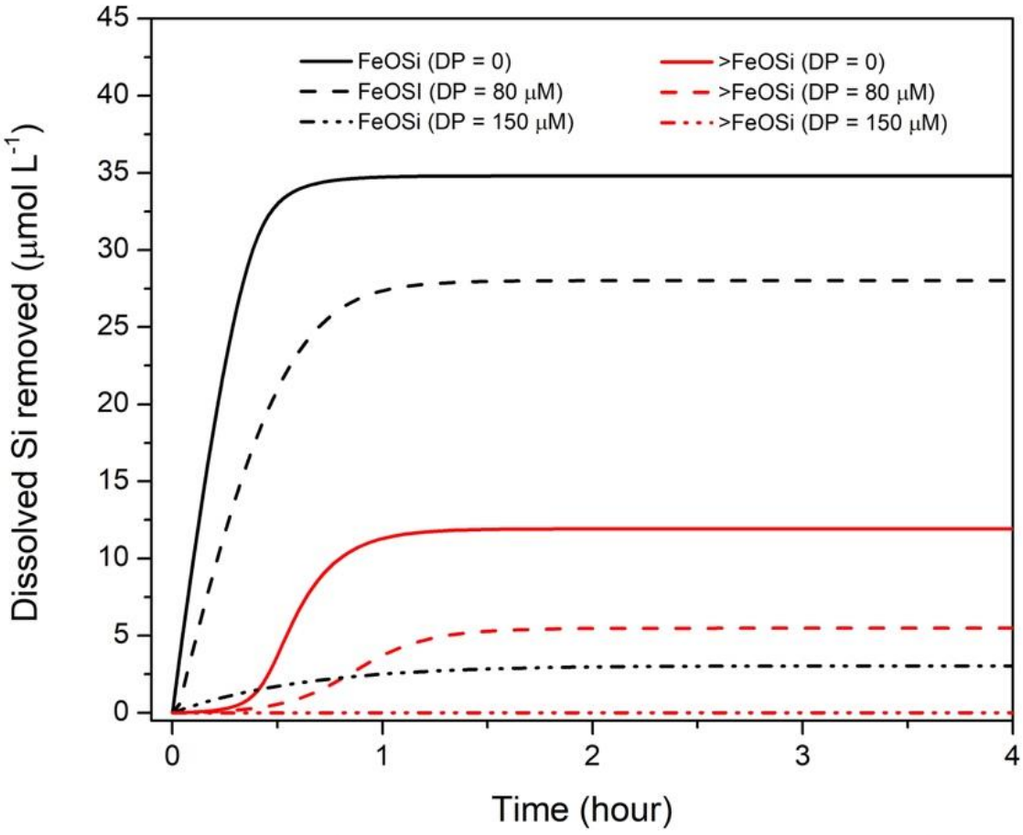

Figure 4.13. Model prediction of the DSi removed by homogeneous oxidation of Fe and DSi complexes (black lines) and by surface adsorption (red lines) at pH 7.0. Solid lines correspond to the oxidation of 300 μM Fe(II) in the presence of 270 μM DSi and in the absence of DP; dash lines correspond to the oxidation of 300 μM Fe(II) in the presence of 270 μM DSi and 80 μM DP; dash-dotted lines correspond to the oxidation of Fe(II) in the presence of 270 μM DSi and 150 μM DP. FeOSi represents products of homogeneous oxidation of Fe(II) and DSi complexes. >FeOSi represents products of DSi adsorbed by surface sites of Fe(III) oxyhydroxides.

This may be because DSi forms different complexes with Fe(II) at different pH values, for example $FeH_3SiO_4^+$ and FeH_2SiO_4, whose oxidation rate constants could be orders of magnitude different. However, the species and stability constants of Fe(II)-DSi complexes have never been identified and defined. Without information about the rate constants of the different Fe(II)-DSi complexes species, the effects of pH on the homogeneous oxidation rate of Fe (II)-DSi complexes cannot be assessed at pH values other than 6.5 and 7.0.

The effects of pH on the surface adsorption of DSi on Fe(III) oxyhydroxides have been widely studied (Davis, 2000; Davis et al., 2002; Hansen et al., 1994; Sabur, 2019; Stumm, 1992; Swedlund et al., 2010). It is widely accepted that both the concentration and charge of surface groups affect the amount of DSi adsorbed by Fe(III) oxyhydroxides. pH affects the aggregation rate of Fe(III) colloids, which can affect the particle size and surface site density of Fe(III) oxyhydroxides (Hiemstra, 2013; Villalobos et al., 2003; Wang et al., 2013a). This is not considered in this study given the small pH range (6.5-7.0) imposed in the experiments. However, if the model is extrapolated to a larger pH range, the effect of pH on the concentration of surface groups would need to be considered. Ferrihydrites, the products of Fe(II) oxidation in the presence of DSi, have been reported to have a point of zero charge (PZC) of 8.6±0.2 (Langmuir, 1997). Below this pH value, DSi, exists mostly as monomeric silicic acid (H_4SiO_4), which can be adsorbed relatively well by the positively charged surface of Fe(III) oxyhydroxides. As pH increases, the relative abundance of $H_3SiO_4^-$, which has a higher affinity for adsorption sites, increases, increasing the amount of DSi adsorbed. However, negatively charged surface groups would become more predominant on the ferrihydrite surface as pH increases to 9.8 (pKa of H_4SiO_4), and above this pH, surface adsorption of DSi will be inhibited by the electrostatic repulsion.

4.5.2 Effect of DP on DSi removal during Fe(II) oxidation

The pH-dependent inhibition or enhancement effect of DP on Fe(II) oxidation rates is attributed to DP enhancing the homogeneous oxidation of Fe(II) while inhibiting its heterogeneous oxidation (Mao et al., 2011; Millero, 1985; Morgan and Lahav, 2007; Stumm and Morgan, 1996; Wolthoorn et al., 2004). The optimized rate constants from the chemical reaction model support this explanation. There is a pH-dependent change in the overall inhibition/enhancement effect of DP because of the pH-dependent speciation of dissolved Fe(II) species, including aqueous Fe(II) complexes with DP (Mao et al., 2011; Millero, 1985; Morgan and Lahav, 2007; Stumm and Morgan, 1996; Wolthoorn et al., 2004). According to the reaction model, at pH 6.5, more than 99.88% of dissolved Fe(II) exists as free Fe^{2+}. Free Fe^{2+} has the smallest oxidation rate constant among all Fe(II) species in the absence of complexation agents. In the presence of DP, additional Fe(II) species (i.e., Fe(II)-DP complexes) are presented in solution (Figure 4.14). The oxidation rate constants of these Fe(II) species decrease in the order of $Fe(OH)_2 > Fe(OH)^+ > FePO_4^- > FeHPO_4 > FeH_2PO_4^+ > Fe^{2+}$ (Mao et al., 2011; Mitra and Matthews, 1985b). Given that they have larger oxidation rate constants than free Fe^{2+}, Fe(II)-DP complexes, whose speciation was not identified in this study, enhance the overall oxidation rate by enhancing the homogeneous oxidation of Fe(II) at pH 6.5. At pH 7.5, the products of the homogeneous oxidation of $Fe(OH)^+$ catalyze further oxidation of Fe(II) via heterogeneous oxidation (Tamura et

al., 1976; Wolthoorn et al., 2004). Fe(II)-DP complexes can inhibit this heterogeneous oxidation process by preventing the surface adsorption of Fe(II). DP can also compete with Fe(II) for sorption sites, inhibiting heterogeneous oxidation (Wolthoorn et al., 2004).

The contradictory effects of DP on the oxidation rate of Fe(II) also control the elemental ratio of P:Fe in their co-precipitates: At variable initial solution DP:Fe ratios (from 0 to 1) and at different pH values, I observed different P:Fe molar ratio in the resulting co-precipitates, ranging from 0.51 at pH 6.5 to 0.42 at pH 7.5 when initial DP:Fe was 1. The maximum P:Fe ratio observed of 0.5 closely matches the value observed in previous studies (Lienemann et al., 1999; Mayer et al., 1982; Mayer and Jarrell, 1995; Thibault et al., 2009). At low DP concentrations, both homogeneous and heterogeneous oxidation of free Fe(II), as well as the oxidation of Fe(II)-DP complexes, proceed simultaneously. Therefore the relative rate of each pathway determines the P:Fe molar ratio in their final co-precipitates. At high DP concentrations, the oxidation of Fe(II)-DP complexes is the dominant oxidation pathway at pH 6.5 and 7.0. Regardless of the unknown mineralogy of the co-precipitates, these Fe(III) phosphates are proposed to have an elemental ratio of P:Fe = 0.5.

The presence of DP affects not only the Fe(II) oxidation rate but also the amount of DSi removed (Figure 4.6). Unlike Fe(II)-DP complexes, the oxidation rate constant of Fe(II)-DSi complexes have not been calculated and reported in the literature before. The kinetic modeling results show that the oxidation rate constant of Fe(II)-DP complexes, although larger, has the same order of magnitude as that of Fe(II)-DSi complexes (Table 4.3). In contrast, DP has a much higher affinity for complexing with Fe(II) than with DSi (Table 4.3). This is likely due to that less protonated forms of DSi is less electrostatic favorable for binding with Fe compared to DP because of the lower deprotonation constants of DP (Sabur, 2019). Thus, the amount of DSi removed by homogeneous oxidation decreases with increasing DP concentrations within the pH range studied (Figure 4.13). DP can also compete with ions for adsorption to the surface sites of Fe(III) oxyhydroxides (Roberts et al., 2004; Zhang and Huang, 2007; Zhao and Stanforth, 2001), and there is evidence that DP outcompetes DSi for surface sites of goethite at pHs lower than 7.5 (Sabur, 2019). Consequently, the presence of DP limits the removal of DSi during Fe(II) oxidation by outcompeting DSi in both potential pathways of DSi removal.

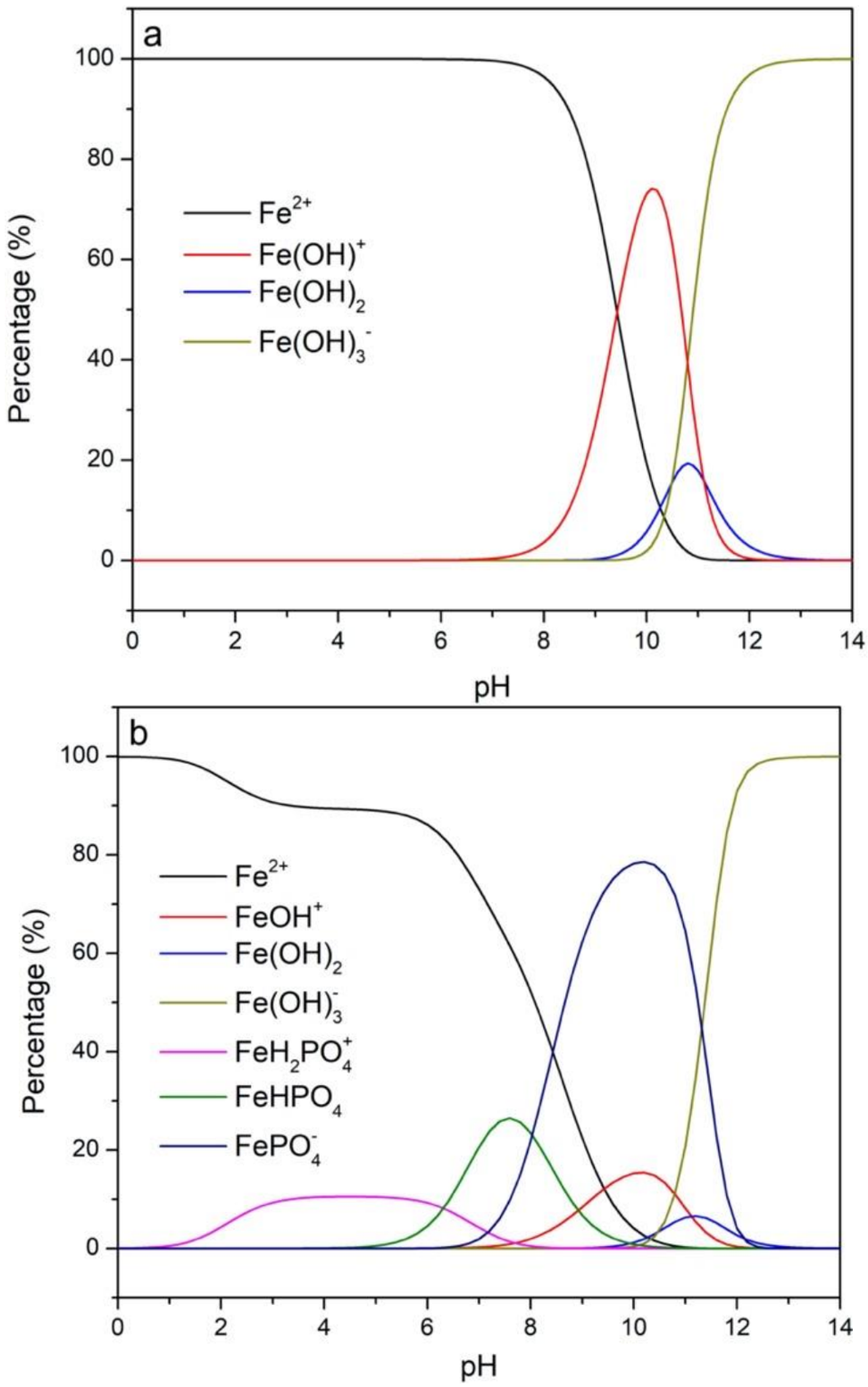

Figure 4.14. The species composition of aqueous Fe(II) in the absebce (a) and presence (b) of DP. $Fe(OH)_2$ does not precipitate at pHs below 8.5. Initial P:Fe(II) in panel b is 300:300 µM. Stability constants for different Fe(II) species in this figure were sorted from a previous study (Mao et al., 2011). Vivianite starts to precipitate at pH above 5.3, and $Fe(OH)_2$ does not precipitate at pH below 8.5. Overall, more than 95% of Fe(II) is in aqueous phase at pH below 8.5.

4.5.3 Comparing observed and diffusion-reaction model prediction DSi concentrations

Although the diffusion-reaction model (DRM) effectively predicted the decrease in DSi concentrations at the oxidation front, the DSi concentrations predicted were lower than those observed (Figure 4.9). The decrease of DSi at the oxidation front, similar to that of DP, can be attributed to the homogeneous oxidation of Fe(II) and DSi complexes. One plausible explanation for the slightly higher observed DSi concentrations, compared to those predicted by the model, is the limited accessibility of Fe(III) oxyhydroxide surface sites to Fe(II) and DSi for sorption, caused by the porous agarose medium. The DRM also failed to predict the observed high DSi concentrations at depths near the surface of the column. One reason for this discrepancy could be the desorption of surface-adsorbed DSi during the equilibration step with the background solution to extract the aqueous phase, given that the fast oxidation of Fe(II) at the surface of the columns would generate a large number of surface sites to adsorb DSi. Another reason for this discrepancy could be that slicing the columns can lead to the losses from the agarose pores. This is quite feasible as particles of Fe(III) oxyhydroxides can be as small as 2.5 nm (Hiemstra, 2013) and some pores in agarose media have been shown to have diameters as large as 150 nm (Pluen et al., 1999). This fraction of Fe(III) oxyhydroxides lost during the extraction step could be the reason for the abnormal non-zero value of dissolved Fe measured in the oxic zone of the columns

4.5.4 Comparing batch and column experiments: Diffusive transport limitation effects

After 6 hours of oxidation in the fully oxic, O_2-saturated batch experiment, almost all of the initial dissolved Fe(II) had precipitated, whereas after 6 hours of exposure to air at the top of the agarose columns, around 20% of the initial dissolved Fe(II) had precipitated (Figure C.2 and

Figure 4.8). This is because diffusion of the aqueous species O_2 and Fe(II) is slow relative to Fe(II) oxidation rates, and Fe(II) oxidation is therefore limited by the diffusion of the participating chemicals (Bircumshaw and Riddiford, 1952; Guy and Schott, 1989). Transport-limitation of reaction rates has also been observed in natural environments such as peat (Beer and Blodau, 2007), estuarine sediments in flow-through reactors (Pallud and Van Cappellen, 2006), and marsh sediments in flow-through reactors (Sabur, 2019). The DRM-predicted oxidation rates for the batch and column systems and O_2 concentrations in the columns illustrate this diffusion limitation effect (Figures 4.12 and 4.17). At each elapsed time point, the top surface of any of the columns is saturated with O_2, while the O_2 concentration decreases with depth (Figure 4.15). The oxygen penetration depth (i.e., the first depth at which O_2 is not zero) increases with time due to continuous O_2 diffusion from the top open end of the columns, and the overall O_2 concentration profiles evolve with time (Figure 4.15). The DRM predicts that Fe(II) oxidation at a depth of 1.25 cm starts after 2 hours of air exposure, while at a depth of 3.0 cm, it starts at an elapsed time of 20 hours, and that the maximum instantaneous homogeneous oxidation rate of Fe(II) at a depth of 3.0 cm is one sixth of that at 1.2 cm (Figure 4.16).

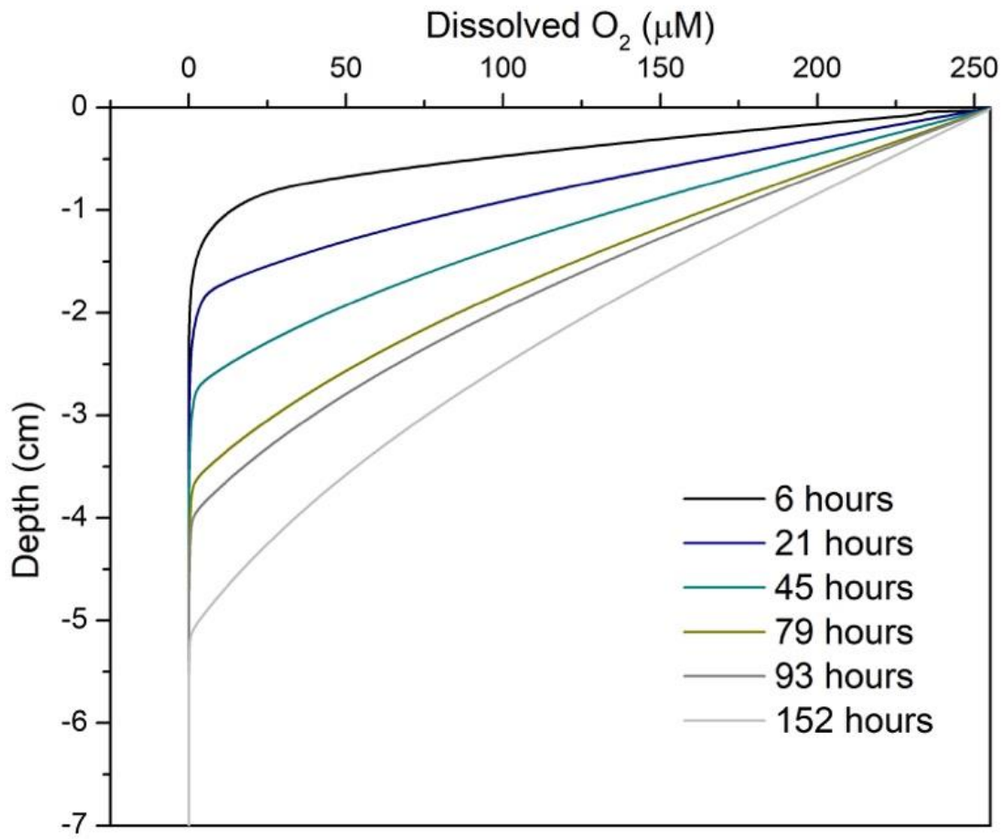

Figure 4.15. Model-predicted dissolved oxygen profiles in an agarose column and its evolution with time.

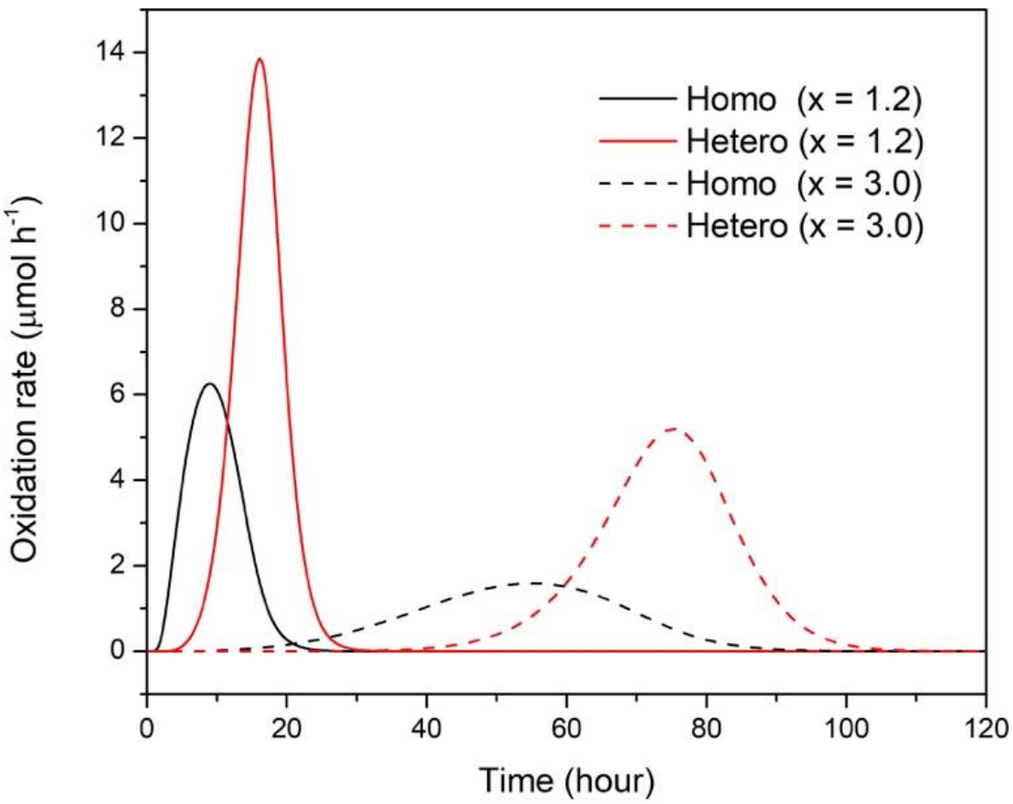

Figure 4.16. Model-predicted homogeneous (black lines) and heterogeneous oxidation (red lines) rates of Fe(II) at different depths of in a simulated agarose column (The oxidation of 270 μM Fe in the presence of 150 μM DSi and 54 μM DP at pH 7.0). Solid lines correspond to the oxidation rates of Fe(II) at a depth of 1.2 cm; dashed lines correspond to the oxidation rates of Fe(II) at a depth of 3.0 cm. Homo is short for homogeneous oxidation of Fe(II), including free Fe(II), Fe(II)-DSi complexes, as well as Fe(II) and DP complexes. Hetero is short for heterogeneous oxidation of Fe(II).

Both the homogeneous and heterogeneous oxidation rates of Fe(II) simulated by the DRM to be occurring in the columns are much slower than those predicted in the batch system (compare the oxidation rates in Figure 4.16 to those in Figure 4.12). Because DSi is mainly removed via the homogenous oxidation of Fe(II)-DSi complexes, the diffusive transport of dissolved Fe(II) and O_2 necessary for Fe(II) oxidation to occur limits the removal rate of DSi during Fe(II) oxidation in the heterogeneous column system. This has important implications for natural systems where diffusion is the dominant control on the supply of reactants such as O_2 and Fe(II), and DSi removal rates in these systems are therefore likely much smaller than observations made in batch experimental systems indicate. Collectively, these results show that Fe-bound Si is likely a much smaller Si pool in near-natural systems where diffusion limits the fast Fe(II) oxidation rates that are necessary for DSi co-precipitation with Fe than what would be predicted based on batch experiments alone.

The interplay between the diffusive transport rates of the participating chemicals (*i.e.*, O_2 and dissolved Fe(II) and its aqueous complexes) and the Fe(II) oxidation rate determines where Fe precipitates in the agarose column, which in turn affects the concentration profiles of DP (Figure C.1). Although dissolved Fe(II) and DP have distinct diffusion coefficients (Couture et al., 2010), they precipitate at the same depth and the P:Fe molar ratio in their co-precipitates is 0.2. This is in accordance with the mechanism proposed above: DP is mainly removed through the homogeneous oxidation of Fe(II)-DP complexes instead of by surface adsorption.

4.5.5 Implications for internal DSi loading

Unraveling the mechanisms and kinetics of DP competing with DSi during coprecipitation with Fe(II) has important implications for predicting the magnitude and timing of DSi retention. In oligotrophic freshwater systems, the incorporation of DSi during Fe(II) oxidative precipitation, which corresponds mostly to the final stage of the competition progress of DSi and DP in Figure 4.6 (*i.e.*, low DP and high Fe(II)), can retain considerable amount of DSi in oxic surface sediment. This will lead to the redox dependent of DSi flux out of sediment. Since the industrial revolution, large amounts of P have been loaded to water bodies by the use of P-containing fertilizers and detergents, which has changed some freshwater systems from mesotrophic to eutrophic (Filippelli, 2008). I predict, based on these results, that in sediment porewaters of eutrophic freshwater systems with a high DP concentration (corresponding to the intermediate to initial stage the competition progress of DSi and DP in Figure 4.6 with high DP and Fe(II)), there will be a lack of redox-dependence of DSi fluxes out of the sediment to the overlying water because of the limited amount of Fe-bound Si that is formed in the sediment during fully oxygenated conditions.

I expect that other sediment geochemical factors that influence Fe oxidation rates and the extent of potential Fe oxidation and co-precipitation with DSi and DP, such as pH, the dissolved Fe concentration and the steady state oxygen penetration depth, would influence the amount of DSi retained during Fe(II) oxidative precipitation. For example, I hypothesize that for a fixed initial DP:DSi ratio, DSi retention would increase with increases in the sediment dissolved Fe concentration and in the steady state oxygen penetration depth, because the amount of Fe(III)

oxides formed by oxidation and subsequent precipitation would increase under both scenarios. Simulating these different scenarios using the DRM could provide valuable insight and realistic predictions and would therefore be a valuable future application of the DRM.

4.6 Conclusions

This study investigated the effect of oxidative precipitation of Fe(II) on the immobilization of dissolved silicon (DSi). The experimental data showed that the co-precipitation of Fe(II) and DSi can be categorized into two stages: (i) the initial removal of DSi during oxidation of Fe(II), and (ii) the removal of DSi after complete oxidation of Fe(II). The amount of DSi removed during Fe(II) oxidation increases with increasing pH and decreases with increasing dissolved phosphate (DP) concentration. Reaction rates simulated by a kinetic model indicates that the oxidation of Fe(II)-DSi complexes enhances the homogeneous oxidation of Fe(II) and induces the fast removal of DSi at the beginning of oxidation. The adsorption of DSi to surface sites of Fe(III) oxyhydroxides is responsible for the removal of DSi after complete oxidation of Fe(II), whose contribution to the removal of DSi is smaller. The presence of DP competes with DSi effectively for not only aqueous Fe(II) but also surface sites of Fe(III) oxyhydroxides, enhancing the homogeneous oxidation, inhibiting the heterogeneous oxidation of Fe(II), and limiting the removal of DSi during Fe(II) oxidation by both the homogeneous oxidation of Fe(II)-DSi complexes and the adsorption of DSi to Fe(III) oxyhydroxides.

The results from an experiment using agarose columns indicate that the removal of DSi during Fe(II) oxidation may be transport-limited in natural and near-natural systems where diffusive transport controls the oxidation rate of Fe(II). Reaction rates simulated by a diffusion-reaction model indicates that the transport of participating chemicals (*i.e.*, dissolved Fe(II) (free Fe^{2+} and its aqueous complexes), and DO) limits Fe(II) oxidation kinetics and DSi removal kinetics compared. The distinct Si:Fe molar ratios in co-precipitates formed in the columns compared with those formed in the batch experiment demonstrate Fe-bound Si is a much smaller Si pool in near-natural systems where diffusion limits the fast Fe oxidation rates that are necessary for DSi co-precipitation with Fe.

Chapter 5
Controls on the release of dissolved silicon from natural freshwater sediments: Roles of oxygen and iron

5.1 Summary

The availability of nutrient dissolved silicon (DSi), relative to dissolved phosphate (DP), exerts an important control on the relative importance of siliceous phytoplankton in algal communities in natural waters. The mechanisms controlling internal DSi loading from aquatic sediments are not yet well understood, however. Experiments exploring these mechanisms often use pure materials under well-controlled laboratory conditions and, therefore, may not provide realistic analogs for complex natural sediments. Here, surficial sediments collected from the open water area of a freshwater marsh were used in a series of flow-through column experiments to elucidate the roles of different reaction pathways in the immobilization and release of DSi. In a series of 10 parallel flow-through columns, anoxic solutions containing variable concentrations of dissolved Fe(II), DSi and DP were pumped upwards through 10 cm of the sediment and collected from a 1 cm layer of overlying water that was initially kept aerated. In six of the columns, the oxic phase was followed by a period of several weeks during which the overlying water remained anoxic. As expected, Fe(II) supplied via the inflow was efficiently retained in the sediment when the overlying water was aerated. When the overlying water became anoxic, efflux of Fe(II) from the columns was observed. The DP retention and efflux dynamics were similar to those of Fe(II), although even under oxic conditions measurable DP efflux was detected. The latter implies that the active precipitation of Fe(III) oxyhydroxides in the uppermost sediment under the oxic water layer was unable to retain all the DP supplied to, as well as produced within, the sediment columns. In contrast to Fe(II) and DP, there was little evidence of DSi retention in sediments during oxic periods. In addition, no systematic changes were observed in the DSi efflux upon switching to anoxic overlying water. The data also indicated net production of DSi in the sediment, likely from the dissolution of amorphous silica (ASi). The conclusions drawn from the aqueous concentration time series measured in the outflow were supported by buffered ascorbate-citrate extractions that showed net enrichments of Fe and P but not Si in the upper 1 cm of sediment at the end of the experiments. Overall, the results with the natural sediment confirm that, at near-neutral pH, the presence of high DP concentrations inhibit the co-precipitation and adsorption of DSi, hence preventing DSi retention in sediments under oxic overlying water. We conclude that the relative production rates of pore water DP and DSi likely represents the major control on the redox dependence of internal Si loading in freshwater systems. The speciation and stability of legacy P pools in freshwater sediments, as well as recent depositional P inputs, therefore, likely play a major role in determining whether soluble Si is retained in the sediments or released back to the overlying water column.

5.2 Background and Rationale

Harmful algal blooms and the degradation of water quality due to eutrophication afflict many freshwater systems around the world (Dittrich et al., 2013; Sondergaard et al., 2007). Increased dissolved phosphate (DP) loads and concentrations are regarded as one of the most important factors controlling excessive algal growth (Correll, 1998; Daniel et al., 1998; Lee, 1973; Van der Molen and Boers, 1994). However, nutrient enrichment in aquatic ecosystems is not the only factor that controls the community composition and abundance of phytoplankton, as nutrient stoichiometry is also an important controlling factor (Collins, 1988; Marchetti et al., 2010). Specifically, the major nutrients phosphorus (P) and silicon (Si) are required for photosynthesis by siliceous diatom algae in an atomic ratio of approximately Si:P = 16:1 (Officer and Ryther, 1980; Redfield et al., 1963). A supply of dissolved silicon (DSi) that result in an DSi:DP ratio above this threshold ratio may decrease the likelihood of harmful algal blooms in eutrophic waters (Egge and Aksnes, 1992; Makulla and Sommer, 1993; Officer and Ryther, 1980; Redfield et al., 1963; Sommer, 1989).

Although efforts have been made to reduce external nutrient phosphorus loading, eutrophication remains a major problem in lakes and other lentic water bodies, in part because of the remobilization of accumulated legacy P from their sediments, which is known as internal loading (Muller et al., 2005; Parsons, 2017; Sondergaard et al., 2007; Van der Molen and Boers, 1994). The mechanisms that control the internal loading of nutrients P have been widely studied (Gächter and Mülle, 2003; Gachter and Muller, 2003; Katsev et al., 2006; O'Connell et al., 2020; Orihel et al., 2017; Sabur, 2019; Smolders et al., 2017; Sondergaard et al., 2003; Van der Molen and Boers, 1994). The bottom water oxygen concentration is known to be one of the main factors controlling DP loading, due to the high affinity of DP to adsorb to, or co-precipitate with, redox-sensitive iron oxyhydroxides, whose reduced forms are soluble and their oxidized forms are not. These mineral phase are therefore solubilized during anoxic conditions, releasing bound P to solution (Gächter and Mülle, 2003; Gachter and Muller, 2003; Jensen et al., 1992; Markelov et al., 2019; Mortimer, 1941; Parsons et al., 2017; Ridenour, 2017; Sabur, 2019; Zhang and Huang, 2007).

Bottom water oxygen conditions have also been shown to affect the release of DSi from sediments in some lacustrine environments, although for other lakes the contrary has been reported (Danielsson, 2014; Ekeroth, 2015; Lehtimaki et al., 2016; Nteziryayo and Danielsson, 2018a; Ridenour, 2017). The widely accepted mechanism for a dependence of DSi release on bottom water oxygenation is the same as that of DP, DSi can be adsorbed by Fe(III) oxyhydroxides through ligand exchange and subsequently released when the Fe(III) oxyhydroxides are reductively dissolved during anoxic periods (Kaegi et al., 2010; Sung and Morgan, 1980; van der Grift et al., 2014; Voegelin et al., 2010). In Chapter 4 of this thesis, the removal of DSi by the oxidative precipitation of Fe(II) was simulated at different pH values and in the presence of different DP concentrations, and along an oxidative front propagating in agarose columns. The results showed that DSi incorporation into the actively forming Fe(III) oxyhydroxides is highly dependent on the pH and the concentration of DP, with higher pHs and lower DP concentrations and resulting in more incorporation of DSi, and is limited by the slow diffusive transport rate of

participating chemicals. Oxygen conditions have also been proposed to affect the dissolution rate of biogenic amorphous silica (ASi), with oxic conditions decreasing the bacterial protease-catalyzed degradation rate of the organic matter surrounding ASi (Bauerfeind and von Bodungen, 2006; Holstein and Hensen, 2010; Lehtimaki et al., 2016) and/or influencing the availability of reactive surface sites on ASi (Chapter 3 of this thesis).

Up to this point in the thesis, laboratory experiments have been used to study the interactions between Si, Fe and P in sediments under changing dissolved oxygen availability. The experiments were conducted using synthetic materials under well-controlled conditions and were focused on unraveling specific chemical interactions between DSi, DP and/or dissolved Fe(II), and with one of the reactive particulate Si endmembers (ASi or Fe-bound Si). Thus, these experiments do not necessarily represent the full complexity of processes occurring in natural sediments, where more than one reactive particulate Si endmember may be contributing to DSi (im)mobilization, multiple geochemical interactions are occurring simultaneously, geochemical conditions are variable in space and time, and transport processes are coupled biogeochemical reactions.

In the present chapter, I investigate the interactions between dissolved Fe(II), DSi and DP, and the redox dependence of internal DSi loading in natural sediments by incubating sediments from a freshwater marsh in a series of small flow-through column systems. The sediment columns were supplied with anoxic inflow solutions containing different combinations of dissolved Fe(II), DSi and DP and their outflow concentrations were monitored in a layer of overlying water that was variably kept oxygenated or not. I hypothesized that the supply of high level of dissolved Fe(II) would lead to significant retention of DSi in sediment columns under oxic conditions, DSi outflow would depend on the presence of oxygen in the overlying water, and the supply of DP would suppress the redox dependence of DSi outflow.

5.3 Materials and Methods

5.3.1 Materials

The top 10 cm of sediments were collected from the West Pond (43°16’12.0” N 79°55’43.9” W) in Cootes Paradise marsh in October 2017 using a stainless steel spade. The sediment was stored in a polyethylene sampling bag, in the dark, in a fridge (4.3 °C) prior to use. Cootes Paradise is a hypereutrophic marsh within the City of Hamilton with a long history of severe ecological degradation. Because of this, various studies have been conducted to better understand the influences of nutrient cycling on water quality in the marsh (Chow-Fraser et al., 1998; Thomasen and Chow-Fraser, 2012). The West Pond is one of the most eutrophied areas of the marsh and has accumulated extensive legacy phosphorus within surficial sediments due to high external phosphorus loads from a nearby wastewater treatment plant (Parsons et al 2017). The geochemistry, mineralogy and phosphorus speciation of sediment from the West Pond have been characterised previously (Parsons, 2017; Ridenour, 2017) allowing for a greater focus on the release mechanisms of DSi from the sediments within this study.

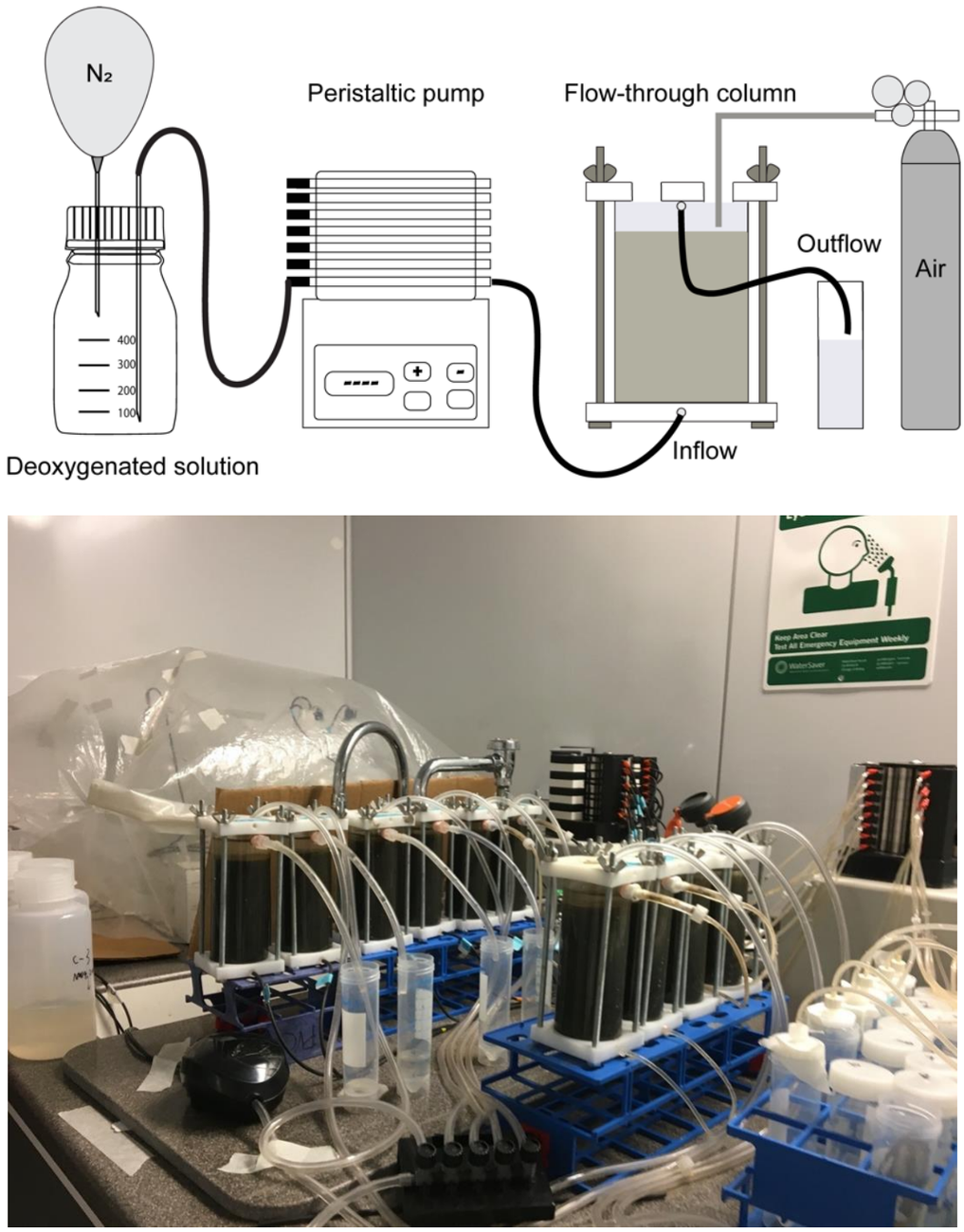

Figure 5.1. Diagram of the flow-through column system (top) and a photo of the experimental set-up (bottom). Illustrated in the top diagram, from left to right of: deoxygenated influent reservoir with a Tedlar bag (5 L, Millipore Sigma) filled with pure N_2, a peristaltic pump for maintaining the flow rate of 5 mL h^{-1}, the sediment column with overlying water and a top plate with openings that remain open during oxic periods and are closed under anoxic conditions, a falcon tube for sampling the outflow of overlying water, and compressed air to keep overlying water well oxygenated (during oxic periods).

5.3.2 Flow-through column experiments

Ten 12 cm long flow-through reactors, modified after Pallud and Van Cappellen (2006), Ridenour (2017) and Sabur (2019), were used. The reactors with a 12 cm length were enclosed on both ends by caps lined with an O-ring to prevent leakage of water and gas. A 47 mm diameter 0.2 µm pore-size polypropylene membrane filter was used to evenly distribute flow across the bottom of the columns and to prevent blockage of the inflow port. Two holes, each with 2 cm in diameter, were cut into the top cap to allow the exchange of gas. Threaded rods and nuts kept the top and bottom caps in place with a tight seal. Before filling the columns, the sediments were passed through a <500 µm sieve to remove larger debris and macro-invertebrates. The sediments were then thoroughly mixed before use to decrease physical variability between replicate columns. The homogenized sediments were introduced into the reactors and kept overnight in a dark environmental chamber whose temperature was set at 25±1 °C. Each reactor contained 10 cm of sediment and 1 cm of overlying water. The entire experimental set-up is illustrated in Figure 5.1.

The influent solutions to each reactor consisted of deoxygenated artificial porewater (APW) solution, whose composition was based on porewater concentrations at 5 cm depth previously measured at the sampling site using peeper's (Ridenour, 2017; Chris Parsons, unpublished data), with different dissolved Fe(II), DP and DSi concentrations (Table 5.1): "APW" without dissolved Fe(II), DP and DSi was used as a control, "DSi" was APW with the addition of DSi, "Fe, DSi" was APW with the addition of DSi and dissolved Fe(II), "Fe" was APW with the addition of dissolved Fe(II), "Fe, P" was APW with the addition of DP and Fe(II), and "P" was APW with the addition of DP (Table 5.1). The pH of all of the influent solutions was adjusted to 7.00±0.02 with HEPES (4-(2-hydroxyethyl)-1-piperazineethanesulfonic acid) to prevent the precipitation of ferrous phosphate minerals and inhibit the oxidation of Fe(II). HEPES was chosen rather than a carbonated buffer to avoid the precipitation of Fe(II) carbonate phases.

In what follows, oxic and anoxic conditions refer to the 1 cm overlying water layer that was either sparged with purified air or not, respectively. The top cap of the reactors had two holes having diameters of 2 cm. During oxic periods, air was bubbled continuously into the overlying water by an air pump through one of the holes to enhance air exchange. Influent solutions were delivered through the side port of the bottom caps at a rate of approximately 5 mL h^{-1} using peristaltic pumps. Effluent solutions were collected through a side port at 1 cm from the top of the reactor using a peristaltic pump operating at the same rate as that of the influent solution. During anoxic periods, the two holes in the end caps were plugged by rubber stoppers and silicone sealant was applied to minimize gas exchange. Effluent solutions were then collected with syringes instead of using the peristaltic pump to avoid contamination by air.

Table 5.1. Chemical compositions of the various influent solutions used in the flow-through column experiments. Bromide, Br^- added as KBr was used as non-reactive tracer, Ca^{2+} ($CaCl_2.2H_2O$) and Mg^{2+} ($MgCl_2$) concentrations were chosen to match the chemical composition of porewater. HEPES (4-(2-hydroxyethyl)-1-piperazineethanesulfonic acid) was used as pH buffer instead of $NaHCO_3$ to avoid the precipitation of Fe(II) carbonate, acetate was used to avoid the depletion of organic carbon substance during the incubations, Si ($Na_2O_3Si.9H_2O$) concentration was chosen to enable co-precipitation with Fe(II) and to minimize the effects of amorphous silica dissolution in sediment on the DSi release, Fe(II) ($FeCl_2.4H_2O$) concentration was designed to enable the retention of DSi, and P (NaH_2PO_4) was added in some columns to assess its effects on the release of DSi. APW = artificial porewater.

Influent composition	Concentration (µmol L^{-1})					
	APW	DSi	Fe, DSi	Fe	Fe, P	P
Br^-	125	125	125	125	125	125
Ca^{2+}	500	500	500	500	500	500
Mg^{2+}	250	250	250	250	250	250
pH Buffer	1000	1000	1000	1000	1000	1000
Acetate	100	100	100	100	100	100
Si	0	**430**	**400**	0	0	0
Fe(II)	0	0	**783**	**776**	**793**	0
P	0	0	0	0	**208**	**208**

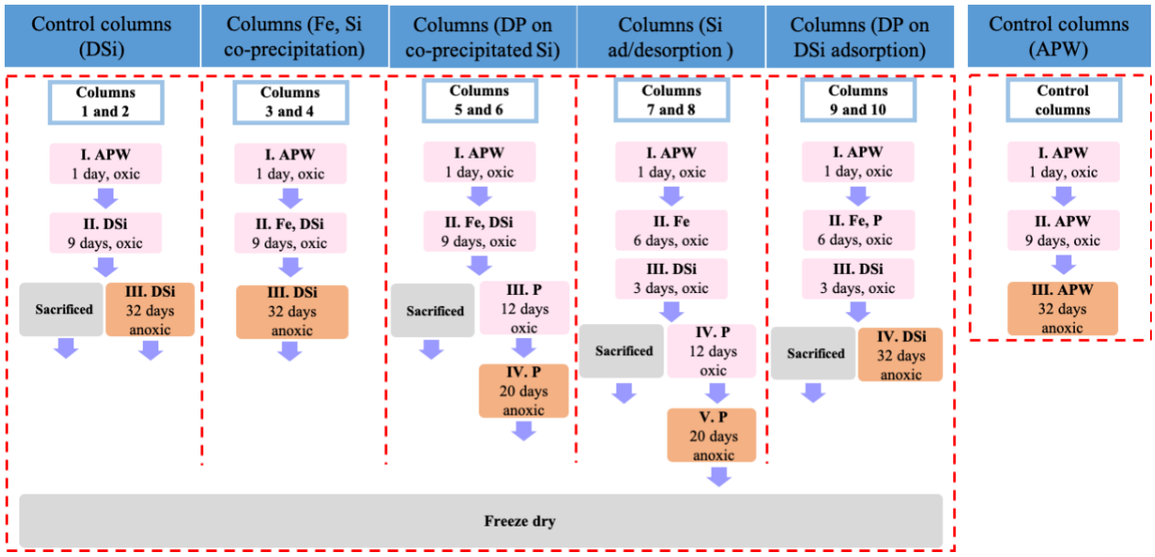

Figure 5.2. Experiment plan with 10 sediment column reactors. "APW" corresponds to artificial porewater, "DSi" is APW with the addition of dissolved silicon (DSi), "Fe" is APW with the addition of dissolved ferrous iron (Fe(II)), "Fe, DSi" is APW with the addition of dissolved Fe(II) and Si, "Fe, P" is APW with the addition of dissolved phosphate (P) and Fe(II), and "P" is APW with the addition of DP. Oxic and anoxic represent overlying water with and without dissolved O_2, respectively. The sediment columns in this figure represent different scenarios: (i) columns 1 and 2 (DSi) were designed as comparison with the supply of DSi under oxic and anoxic conditions, (ii) columns 3 and 4 (Fe, Si co-precipitation) were designed to promote the co-precipitation of Fe(II) and DSi, (iii) columns 5 and 6 (DP on co-precipitated Si) were designed to promote the co-precipitation of Fe(II) and DSi under oxic conditions and to study the effect of DP on the release of co-precipitated DSi under oxic and anoxic conditions, (iv) columns 7 and 8 (Si ad/desorption) were designed to promote the adsorption of DSi on the surface of newly precipitated Fe(III) oxyhydroxides and to study the effect of DP on the desorption of adsorbed DSi, and (iv) column 9 and 10 (DP on DSi adsorption) were designed to promote the adsorption of DSi on the co-precipitates of Fe and P. Note that another two columns were flushed with only "APW" throughout the incubations as another control.

APW was pumped through the column reactors for 1 day to ensure complete porewater saturation and uniformity of the initial porewater composition between replicate columns. Starting the next day, different influent solutions were supplied: the influent compositions, their duration and the overlying water oxygenation are shown in Table 5.1and Figure 5.2. The sampling resolution was higher at the beginning of each new stage (3 times per day) and less near the end of the stage (1-2 times per day).

Upon completion of the flow-through column experiment, the sediments in the column reactors were retrieved, frozen at -20 °C, and sliced into 6 sections (0-0.5, 0.5-1, 1-2, 2-4, 4-6, and 6-10 cm) using a bandsaw. After freeze-drying, the sediment sections of all columns 1-9 were extracted with a buffered ascorbate-citrate solution (BAC) at pH 7.5, and sediment sections of columns 1, 2, 4 and 5 were extracted with a 1 M NaOH solution. The BAC solution contained 10 g L^{-1} of ascorbic acid ($C_6H_8O_6$, Sigma, purity ≥98%), 50 g L^{-1} sodium citrate ($Na_3C_6H_5O_7$, Sigma, purity ≥99%), and 50 g L^{-1} sodium bicarbonate ($NaHCO_3$, Sigma, 99.5-100.5%). This extractant solution has been shown to extract the highly reactive solid Fe(III) sediment pool (Hyacinthe and Van Cappellen, 2004; Kostka and Luther, 1994). Here, 50 mL BAC solution with a pH of about 7.5 was added into 60 mL serum bottles containing 25 mg sediment in an anaerobic chamber. The serum bottles were sealed with rubber stoppers and transferred to an environmental chamber and agitated on a rotating shaker at 30 rpm at 25±1 °C. After 24 hours, the suspensions were filtered through 0.2 µm pore-size syringe filters. The supernatant was acidified with HCl to pH < 2 and stored in the fridge until analysis. Reactive particulate silica in the sediments was extracted following a modified single-point ASi extraction method (Koning et al., 2002; Ohlendorf and Sturm, 2008): 10 mL of 1 M NaOH was added to a Teflon liner containing 10 mg of dry sediment. These Teflon liners were placed in metal pressure vessels. After placing these vessels in a pre-heated oven at 100 °C for 3 hours, supernatants were collected and filtered using 0.2 µm pore-size syringe filters, acidified with HNO_3 and then analyzed for major elements and DSi by ICP-OES. The total NaOH extractable Si was corrected for the contribution of silicate mineral dissolution by assuming a Si:Al ratio of 2:1 to get the NaOH extractable amorphous silica (ASi) (Ohlendorf and Sturm, 2008).

5.3.3 Analytical methods

The aqueous samples and solid phase extraction samples collected were filtered through 0.2 µm pore-size polypropylene syringe filters, acidified with trace-metal hydrochloric acid to pH < 2 and stored at 4 °C until the analysis of major elements and DSi with Inductively Coupled Plasma-Optical Emission Spectrophotometry (ICP-OES, Thermo Scientific iCAP 6300). Standards were prepared from Fisher Scientific stock standards (Thermo Fisher Scientific). Reference solutions were prepared with multi element standards (Delta Scientific Laboratory Products Ltd.) and were analyzed along with all samples for quality control. The precision of reference samples measurement across sample run was better than 10% and the relative standard deviation was well within 5%. 2 mL aqueous samples were also filtered through 0.2 µm polythersulfone (PES) syringe filters for analysis of major anions (Br^-, NO_2^-, NO_3^-, and SO_4^{2-}) with Ion Chromatography (Dionex ICS-5000). Detection limits in µM for each anion analysed are given in brackets; Br^- (1.2), NO_2^-

(2.1), NO_3^- (1.5), and SO_4^{2-} (0.8). Typical precision was <5% RSD and quantified values for certified standards were always within 10%.

5.3.4 Mass balances

To compare the elemental masses supplied to the sediment columns to those released to the overlying water, the following cumulative masses were calculated:

$$Mass_D^{Outflow}(t) = \sum_{i=1}^{n} Mass_D(t_i) \quad (5.1)$$

$$Mass_D^{Inflow}(t) = C_D \cdot Q \cdot t \quad (5.2)$$

where $Mass_D^{Outflow}(t)$ is the cumulative mass of dissolved Fe, DSi or DP (µmol) released to the overlying water at time t, $Mass_D(t_i)$ is the mass of dissolved Fe, DSi or DP (µmol) accumulated in the overlying water sample collected at time t_i ($\leq t$), and n is the number of samples collected over the time interval t, $Mass_D^{Inflow}(t)$ is the cumulative mass of dissolved Fe, DSi or DP supplied to the sediment columns up to time t, C_D is the concentration of dissolved Fe, DSi or DP in the influent solutions (µmol L^{-1}), Q is the flow rate at which the influent solution is supplied (5 mL h^{-1}).

Equations (5.1) and (5.2) were integrated over the oxic and anoxic time intervals. However, because these intervals had different durations, the cumulative inflow and outflow masses were normalized to the corresponding durations. The net release or retention rate (R_D^{Net}) during a given interval was then computed by subtracting the normalized cumulative inflow masses from the corresponding outflow masses:

$$R_D^{Net} = (Mass_D^{Outflow}(\Delta t) - Mass_D^{Inflow}(\Delta t))/\Delta t \quad (5.3)$$

where Δt is the duration of oxic or anoxic period, with $t = 0$ corresponding to the start of the period. Negative values of R_D^{Net} indicate net retention of the dissolved element supplied to the sediment column, positive values imply net release. The latter implies production of dissolved Fe, DSi or DP within the sediment.

When an experiment with a given column was terminated, the concentrations of BAC extractable Fe, Si, P, and NaOH-extractable reactive Si were determined at different depths along the column. The final depth distributions were then compared to the initial (homogeneous) concentration distributions in order to identify depth intervals of accumulation or depletion of the extractable element pools. Furthermore, by integrating the concentrations over the entire length of the column, the total masses of the extractable elements were calculated to quantify whole-column accumulation or loss of solid-bound Fe, P and Si:

$$Mass_S = \sum_{j=0} C_S(j) \cdot m_j \quad (5.4)$$

where $Mass_S$ is the total amounts of BAC extractable Fe, Si, P or NaOH-extractable ASi in the sediment columns, $C_S(j)$ is the concentration of BAC extractable Fe, Si, P or NaOH-extractable

ASi (μmol g^{-1}) at depth *j (≤ 10cm)*, m_j is the mass of sediment (g) at depth *j*. The change rates of solid phases, *i.e.*, BAC extractable Fe, Si, P and NaOH-extractable ASi were also calculated:

$$\frac{dMass_S^I}{dt} = (Mass_S^{tI} - Mass_S^0)/(t_I) \quad (5.5)$$

$$\frac{dMass_S^{II}}{dt} = (Mass_{S,i}^{tII} - Mass_S^{tI})/(t_{II} - t_I) \quad (5.6)$$

where $Mass_S^0$, $Mass_S^{tI}$, and $Mass_S^{tII}$ are the total amount of BAC extractable Fe, Si, P or NaOH-extractable ASi of initial sediment columns (at time zero), sediment columns after oxic incubation periods, and sediment columns after the whole incubation experiments (include both oxic and anoxic periods), t_I is the duration of oxic incubation, t_{II} is the duration of the whole incubation.

5.4 Results

5.4.1 Sediment columns: operating conditions

The transport properties of the sediment columns, pH and dissolved oxygen (DO) conditions in the overlying water layers were presented in detail in a previous study (Sabur, 2019) and briefly summarized here. The porosity of the sediment was about 0.81. With an inflow rate of 5 mL h^{-1}, the non-reactive tracer (Br^-) reached 65% of its inflow concentration within about 1 day. The Br^- breakthrough curves of the different columns were similar (Figure 5.3), indicating column reactors were comparable in terms of physical transport.

The pH of the overlying water layer of all sediment columns had an initial value of 8.50 in all columns. This value decreased to 7.60±0.10 within 12 hours of supplying pH 7.0 APW to the columns. The pH value remained stable during the oxic periods. However, when the top cap was sealed during the anoxic periods, the pH of overlying water decreased to 7.25±0.05.

Without the continuous air bubbling in the first day of incubation (Step I in Figure 5.2), when open to the atmosphere the DO concentration in the overlying water was less than 50% saturation at 25 °C (Sabur, 2019). With the continuous air sparging (other steps during oxic incubations in Figure 5.2), the overlying water was fairly well oxygenated (more than 70% of saturated DO concentration at 25 °C). Although the porewater DO profile in the sediment was not monitored, the yellowish color of the topmost sediment during the oxic periods indicated that the oxidation front might extend to about 1 cm below the sediment surface.

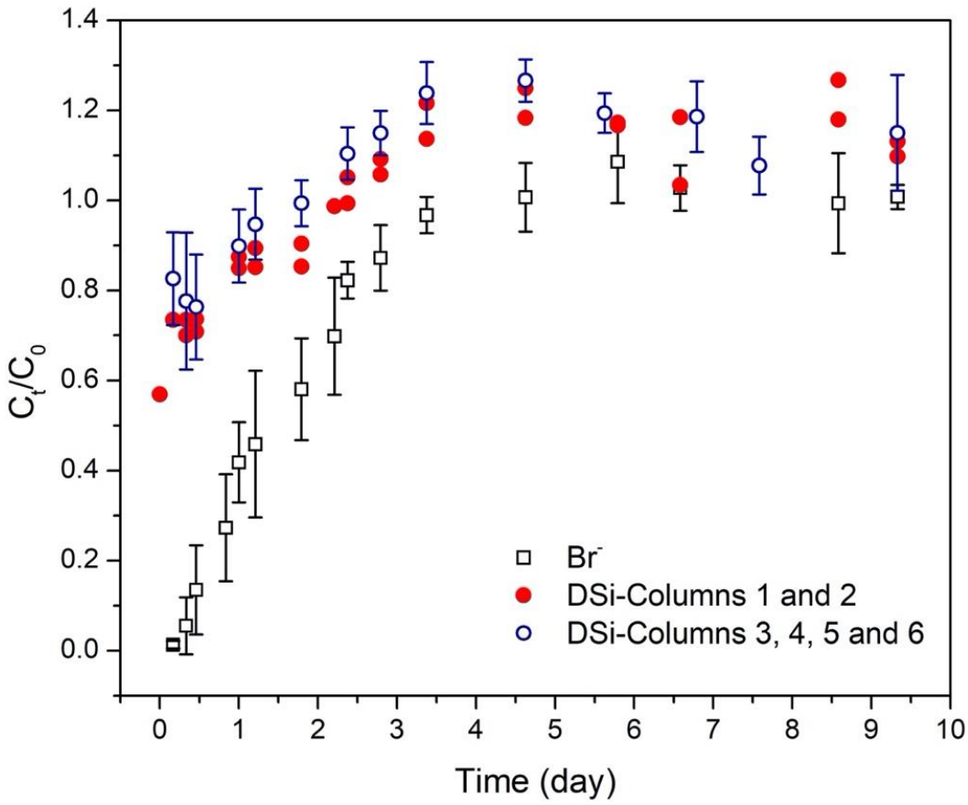

Figure 5.3. The normalized concentration (C_t/C_0) of Br^- and DSi measured in the effluents from the columns over time (n = 10). C_t is the concentration of Br^- or DSi in the effluents at time t, C_0 is the (constant) concentration of Br^- or DSi in the influent. C_t of Br^- is the average of columns 1, 2, 3, 4, 5, and 6. Columns 1 and 2 were control columns supplied with "DSi", columns 3, 4, 5 and 6 were supplied with "Fe, DSi". Note that the greater than one C_t/C_0 values for DSi imply production of DSi in the sediment columns, likely through the dissolution of amorphous silica.

5.4.2 Dissolved Fe, P, and Si concentrations: oxic periods

During the oxic periods, dissolved Fe concentrations in the effluent from all columns remained low, often below 1.0 µmol L^{-1}, even though a relatively high concentration of dissolved Fe(II) was supplied in the influents for columns 3-10 (top panels in Figure 5.4 and Figure 5.5). In contrast to dissolved Fe, DP concentrations in effluent showed different temporal trajectories between different columns. The highest DP concentrations were observed for columns 1 and 2, which were supplied with only DSi. In these columns, the DP concentration increased during the first 3 days and decreased afterwards, with maximum concentrations close to 190 µmol L^{-1}. Columns 3-10, which were supplied with dissolved Fe(II) had lower DP concentrations, in the range of 5-100 µmol L^{-1}. Overall, DP concentrations in the effluent of most columns progressively decreased with time within the first 9 days of (oxic) incubation. In columns 6 and 8, DP concentrations in effluent increased with time after 9 days of aeration, because DP was supplied in the influent, while oxic conditions were continued for another 12 days (middle panel in Figure 5.5).

Columns 7, 8, 9, and 10, which did not receive DSi-containing influents during the first half of the oxic period, exhibited relatively low DSi concentrations of around 250 µmol L^{-1} at equilibrium. Columns 1, 2, 3, 4, 5 and 6 that were supplied with DSi throughout their oxic periods had similar high DSi concentrations of around 500 µmol L^{-1}, that was higher than the influent DSi concentration, implying a production of DSi inside the sediment column. This can be seen in Figure 5.3 where the normalized DSi concentration (C_t/C_0, where C_t is the effluent concentration of DSi at time t, and C_0 is the concentration of DSi in the influent) are shown as a function of time. The normalized DSi concentrations peaked around the same time as those of Br^-, but their maximum value was around 1.2 as opposed to that of 1.0 for the non-reactive Br^- tracer. Figure 5.3 also shows that the simultaneous supply of dissolved Fe(II) (columns 3, 4, 5 and 6) or not (columns 1 and 2) did not affect the DSi breakthrough curves.

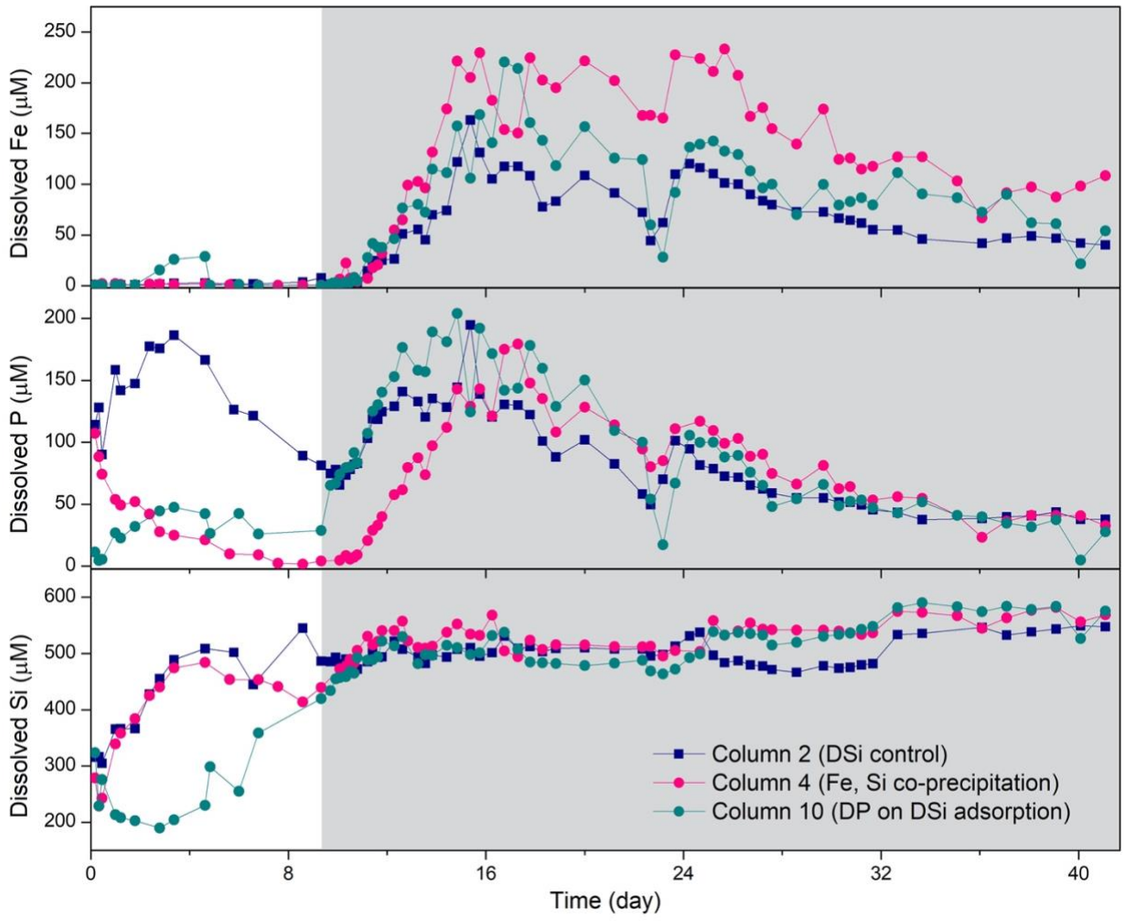

Figure 5.4. Concentration of dissolved Fe, P, and Si in the overlying water of columns 2, 4 and 10 as a function of time. White portions in the panels correspond to time period of oxic conditions, grey portions correspond to time period of anoxic conditions. Column 2 was supplied with "DSi" for 9 days under oxic conditions; column 4 (refers to the average value of columns 3 and 4) were supplied with "Fe, DSi" for 9 days under oxic conditions; column 10 was firstly supplied with "Fe, P" for 6 days, and then with "DSi" for 3 days under oxic conditions. When switching to anoxic conditions, all columns were switched to "DSi" containing influent solutions.

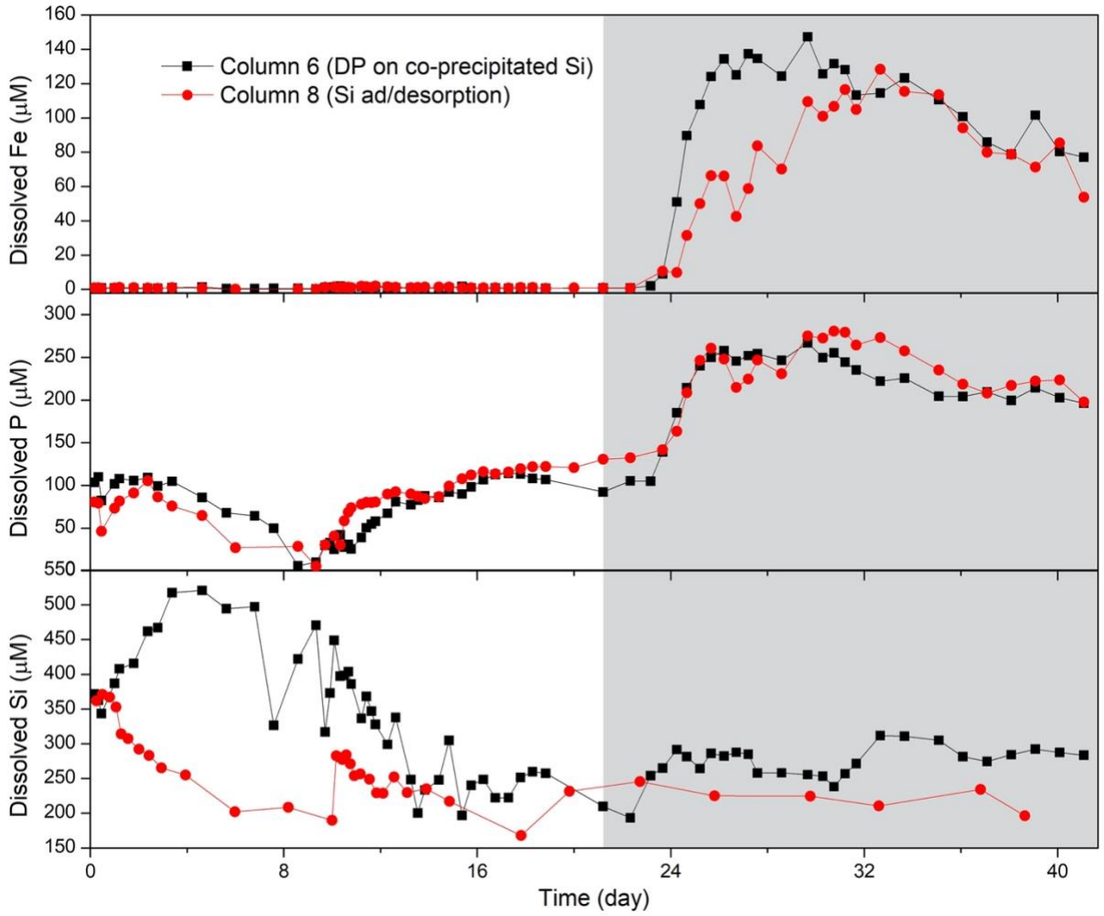

Figure 5.5. Concentration of dissolved Fe, Si and P in the overlying waters of columns 6 and 8 as a function of time. White portions in the panels correspond to the time period of oxic conditions, grey portions correspond to time period of anoxic conditions. Column 6 was firstly supplied with "Fe, DSi" for 9 days, and then with "P" for 12 days under oxic conditions; column 8 was firstly supplied with "Fe" for 6 days, then with "DSi" for 3 days, and finally with "P" for 12 days under oxic conditions. The influent to all columns was switched to "P" during anoxic incubations.

5.4.3 Dissolved Fe, P, and Si concentrations: anoxic periods

After 9 days of aeration, the holes in the caps of columns 2, 4 and 10 were closed to allow for the establishment of anoxic conditions in the overlying water layer. At the same time, the influents to these columns were switched to "DSi", that is, de-oxygenated APW with DSi added (Figure 5.2 and Table 5.1). Effluent dissolved Fe and DP concentrations started to increase about 1.5 days after closing the sediment columns. The maximum concentrations of dissolved Fe and DP were reached after about 4 days of anoxic conditions and progressively decreased afterwards. The highest dissolved Fe concentrations were observed for those columns that had previously (i.e., during the oxic period) been supplied by Fe-containing influent (columns 4 and 10, with an average of 193±26 and 149±30 µM, respectively), and the highest effluent DP concentrations for the column that had received P-containing influent (column 10, with an average of 161±29 µM).

Unlike DP and dissolved Fe, the effluent DSi concentration did not show a marked increase after the oxic to anoxic transition. Additionally, no significant differences in the effluent DSi were observed between columns 2, 4 and 10 (bottom panel in Figure 5.4). Over the entire duration of the anoxic period, the effluent DSi concentrations remained fairly constant, but in excess to the influent concentrations supplied to the three columns.

The oxic periods of columns 6 and 8 lasted 21 days, upon which the influent solutions were switched to "P", that is, de-oxygenated APW with the addition of DP (Figure 5.2). In both columns, effluent dissolved Fe and DP increased approximately 4 days after aeration was terminated. The DSi concentrations released by columns 6 and 8, however, did not show a systematic change when the overlying water transitioned from oxic to anoxic (grey panels in Figure 5.5).

5.4.4 Net release/retention rates of dissolved Fe, P and Si

Column 2 and the control column received no dissolved Fe(II) and showed little Fe release during their oxic incubation periods. However, during the anoxic period, the net release rate of Fe from these two columns was more than 7 µmol day^{-1} to the overlying water (Figure 5.6). In columns 4, 6, 8 and 10, which were supplied with dissolved Fe(II) during their oxic periods, net Fe retention rates varied from 28 to 83 µmol day^{-1}. During the anoxic periods, the net release rate of dissolved Fe from these columns amounted to 5-15 µmol day^{-1}. This implied net retention of Fe in the columns over the entire duration of the experiment.

Columns 2 and 4 and the control column were not supplied with influent DP, yet they released DP during both the oxic and anoxic periods. For columns 6 and 8, which were supplied with DP, net retention of P occurred during both oxic and anoxic periods. For column 10, which also received DP during the oxic period, net retention was observed during the oxic period, while net release was observed during the anoxic period.

Net DSi release was observed for all the columns under both oxic and anoxic conditions. The net release rate from control column was more than 5 times of that from columns 2, 4 and 10. Columns 2, 4 and 10 experienced the same durations of oxic and anoxic incubation as the control column, but in addition were also supplied by influent DSi. Columns 6 and 8 were incubated under anoxic

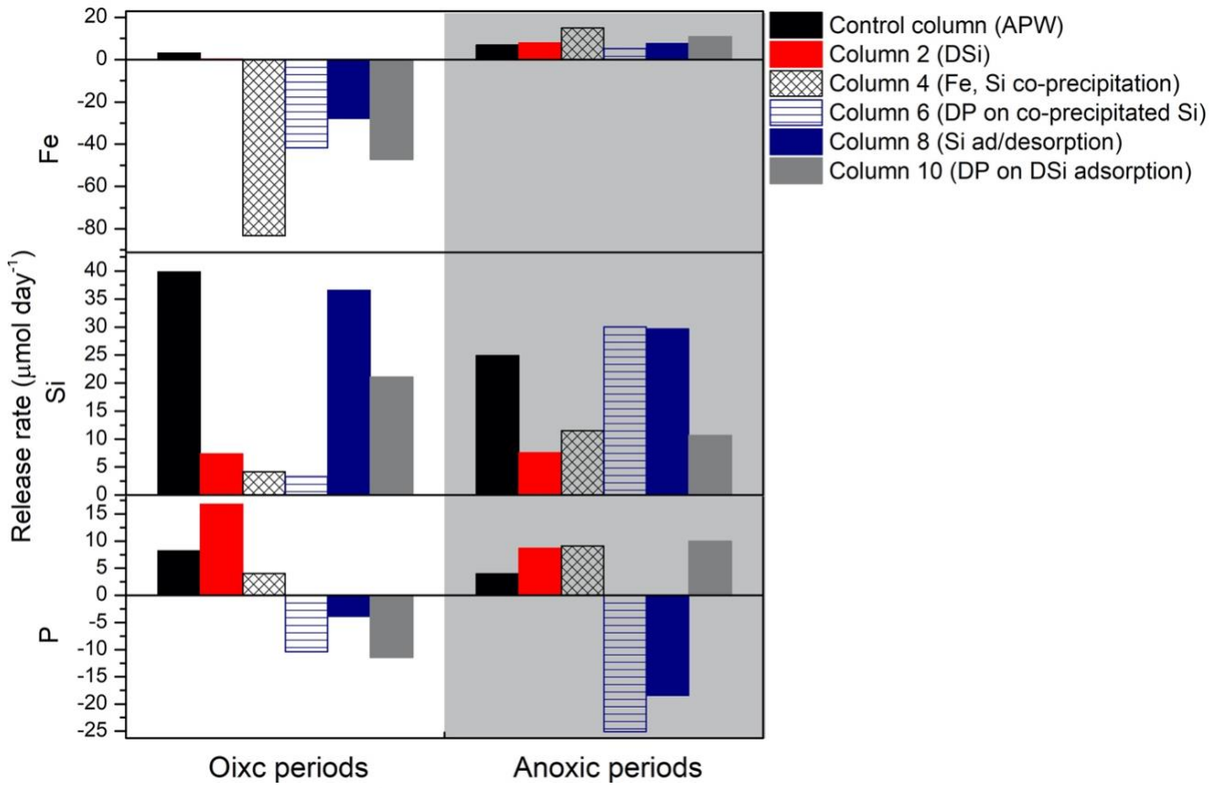

Figure 5.6. Net release rates of Fe, DSi, and DP to the overlying water under oxic and anoxic conditions. Positive values (+) indicate the net release of the dissolved elements to the overlying water, negative values (-) indicate the net retention of dissolved elements supplied by the influent solutions. Column 2 was supplied with "DSi" for around 9 days under oxic conditions; column 4 was supplied with "Fe, DSi" for around 9 days under oxic conditions (the value in the figure is the average of column 7 and 8); column 10 was firstly supplied with "Fe, P" for around 6 days, and then with "DSi" for 3 days under oxic conditions. The influent to columns 2, 7, 8 and 9 was switched to "DSi" under anoxic conditions. Column 6 was firstly supplied with "Fe, DSi" for around 9 days, and then with "P" for around 9 days under oxic conditions; column 8 was firstly supplied with "Fe" for around 6 days, then with "DSi" for around 3 days, and finally with "P" for around 9 days under oxic conditions. The influent to columns 6 and 8 was switched to "P" under anoxic conditions. Control column was flushed with "APW" only throughout the experiment (data from Sabur, 2019). Columns 2, 4, 10 and control columns were incubated under anoxic conditions for 32 days. Columns 6 and 8 were incubated under anoxic conditions for 23 days.

conditions for 20 days but without the addition of DSi in the influent solution. The net release rate of DSi from columns 6 and 8 under anoxic conditions was around 30 μmol day^{-1}, close to that from the control column during the same incubation period.

5.4.5 Solid phase characterization

The buffered ascorbate-citrate solution (BAC) extractable Fe concentration of the initial homogenized sediment was 143 μmol g^{-1}. The BAC extractable Fe concentrations decreased in all the columns over the course of the experiment, although dissolved Fe(II) was supplied to some columns (Table 5.2, Figure 5.7 and Figure 5.8). Sediments supplied with influent solutions containing dissolved Fe(II) during the oxic periods (columns 3-9) had more BAC extractable Fe than sediments in columns without Fe addition (columns 1 and 2). Nonetheless, even columns 3-9 had lower BAC extractable Fe concentrations than the initial sediment by the end of the incubation. The vertical distributions of BAC extractable Fe showed that the topmost sediment layers (defined here as the top 1 cm) became enriched in BAC extractable Fe compared to the deeper sediments in all the columns during oxic periods (top panels in Figure 5.7 and Figure 5.8).

BAC extractable P concentrations were between 25 and 37 μmol g^{-1}, and correlated positively with BAC extractable Fe (r^2 = 0.47, p < 0.05, Table 5.2). The vertical distribution pattern of BAC extractable P was similar to that of BAC extractable Fe (Figure 5.7 and Figure 5.8), showing net enrichments in the upper 1 cm of sediment during oxic periods. BAC extractable Si in sediment of different columns was 34.3±3.0 μmol g^{-1} and did not show any correlations with BAC extractable Fe (r^2 = 0.14, p > 0.05, Table 5.2, Figure 5.7 and Figure 5.8).

The initial sediment contained 310 μmol g^{-1} of NaOH extractable Si. After 9 days of oxic incubation, NaOH extractable Si from the sediment in column 1 decreased to 280±19 μmol g^{-1}. Column 3, which was supplied with dissolved Fe(II) and DSi during the oxic incubation period, contained 329±19 μmol g^{-1} NaOH extractable Si in the sediment after the end of the whole experiment, which was around 10 times greater than the BAC extractable Si. Additionally, gathering all the data of NaOH extractable Si from columns 1, 2, 4 and 5 indicated that the Si concentrations correlated positively with the NaOH extractable Al and Fe concentrations (Figure D.2). After correcting for the contribution of silicate minerals, NaOH extractable ASi was 20% of the total NaOH extractable Si (rightmost panels in Figure 5.7 and Figure 5.8). NaOH extractable ASi seemed to be evenly distributed in the columns. Columns 4 and 5, which were supplied with dissolved Fe(II) and DSi had a higher NaOH extractable ASi concentrations than the initial sediment by the end of the experiment.

Table 5.2. Concentrations of buffered ascorbate-citrate (BAC) extractable Fe, Si and P, and 1 M NaOH extractable Si. Sediment columns were flushed with different influents and sacrificed after oxic cycle or anoxic cycle. Note that the masses of dry sediment in the different columns were nearly identical, 56.3±3.0 g.

	Oxygen conditions	**Influent**		**Buffered ascorbate-citrated extractable (μmol g^{-1})**			**1 M NaOH extractable (μmol g^{-1})**	
		Oxic	Anoxic	Fe	Si	P	Al	Si
Initial sediment	--	--	--	141.3	39.4	37.4	127.2	310.4
Column1	Oxic	DSi, 9d	--	98.2	30.3	31.8	112.7	282.1
Column2	Anoxic	DSi, 9d	DSi	88.3	32.4	25.1	105.5	259.6
Column3	Anoxic	Fe, DSi, 9d	DSi	104.3	35.6	30.0	--	--
Column4	Anoxic	Fe, DSi, 9d	DSi	106.9	36.0	27.8	143.5	359.1
Column5	Oxic	Fe, DSi, 9d	--	110.4	32.4	35.0	132.0	332.4
Column6	Anoxic	Fe, DSi→ P, 21d	DP	114.4	32.4	35.4	--	--
Column7	Oxic	Fe→DSi, 9d	--	115.5	31.2	33.6	--	--
Column8	Anoxic	Fe→DSi→P, 21d	DP	112.0	37.7	37.4	--	--
Column 9	Oxic	Fe, P→DSi, 9d	--	111.1	33.3	34.6	--	--
Column10	Anoxic	Fe, P→DSi, 9d	DSi	--	--	--	--	--

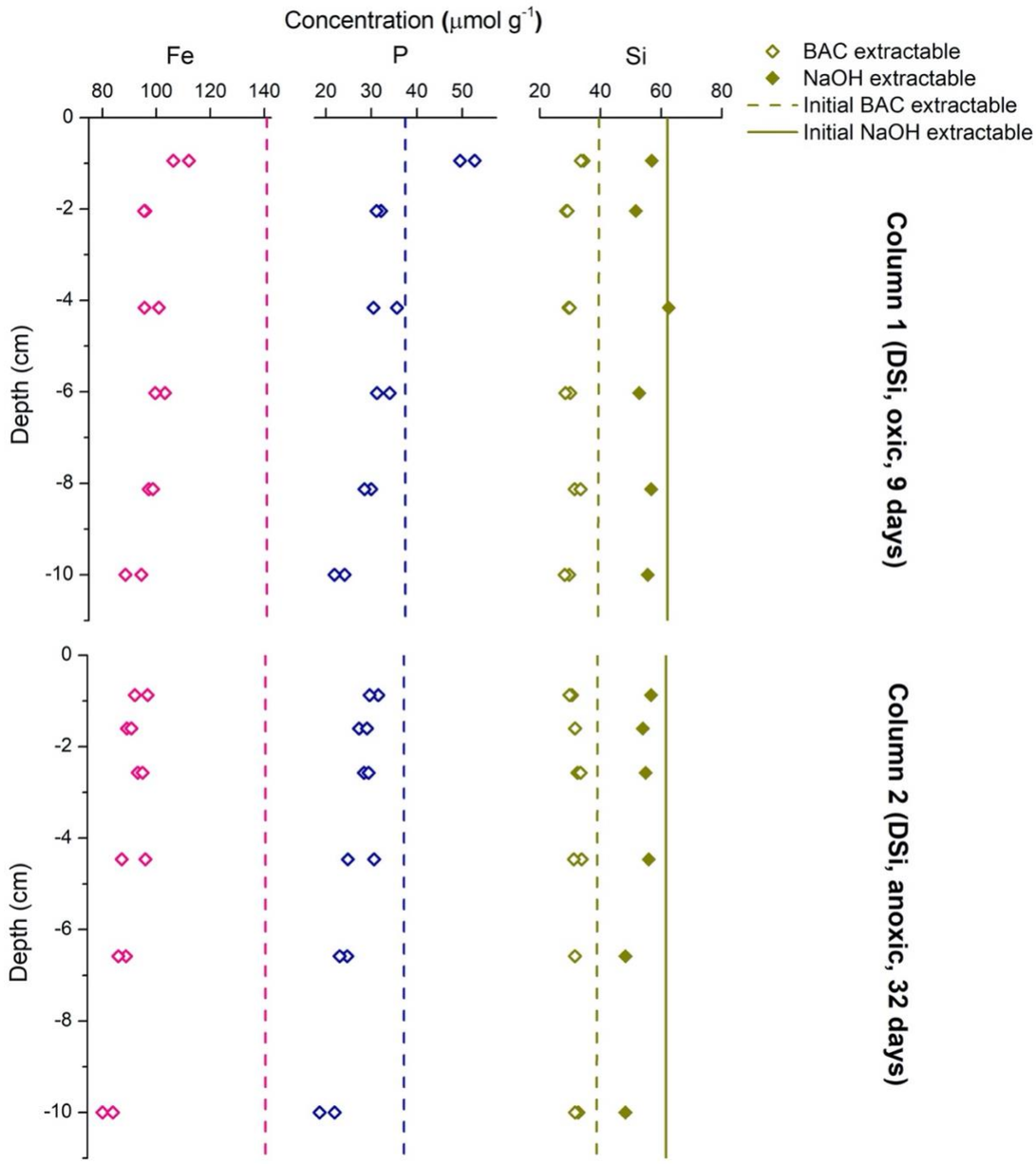

Figure 5.7. Vertical distributions of buffered ascorbate-citrate (BAC) extractable Fe, Si and P, and NaOH extractable ASi. The top panels show results of column 1 (supplied with "DSi", and was sacrificed after the oxic period, *i.e.*, 9 days), the bottom panels show results of column 2 (supplied with "DSi", and sacrificed after anoxic period, *i.e.*, 32 days after anoxic cycle). Solid lines represent the concentrations of 1 M NaOH extractable ASi in initial sediment prior to the supply of influent solutions. Dashed lines represent the concentrations of BAC extractable Fe, Si and P in initial sediment prior to supplying influent solutions. Note that NaOH extractable ASi was 20% of total NaOH extractable Si in Table 5.2, *i.e.*, the contribution of silicate minerals was corrected.

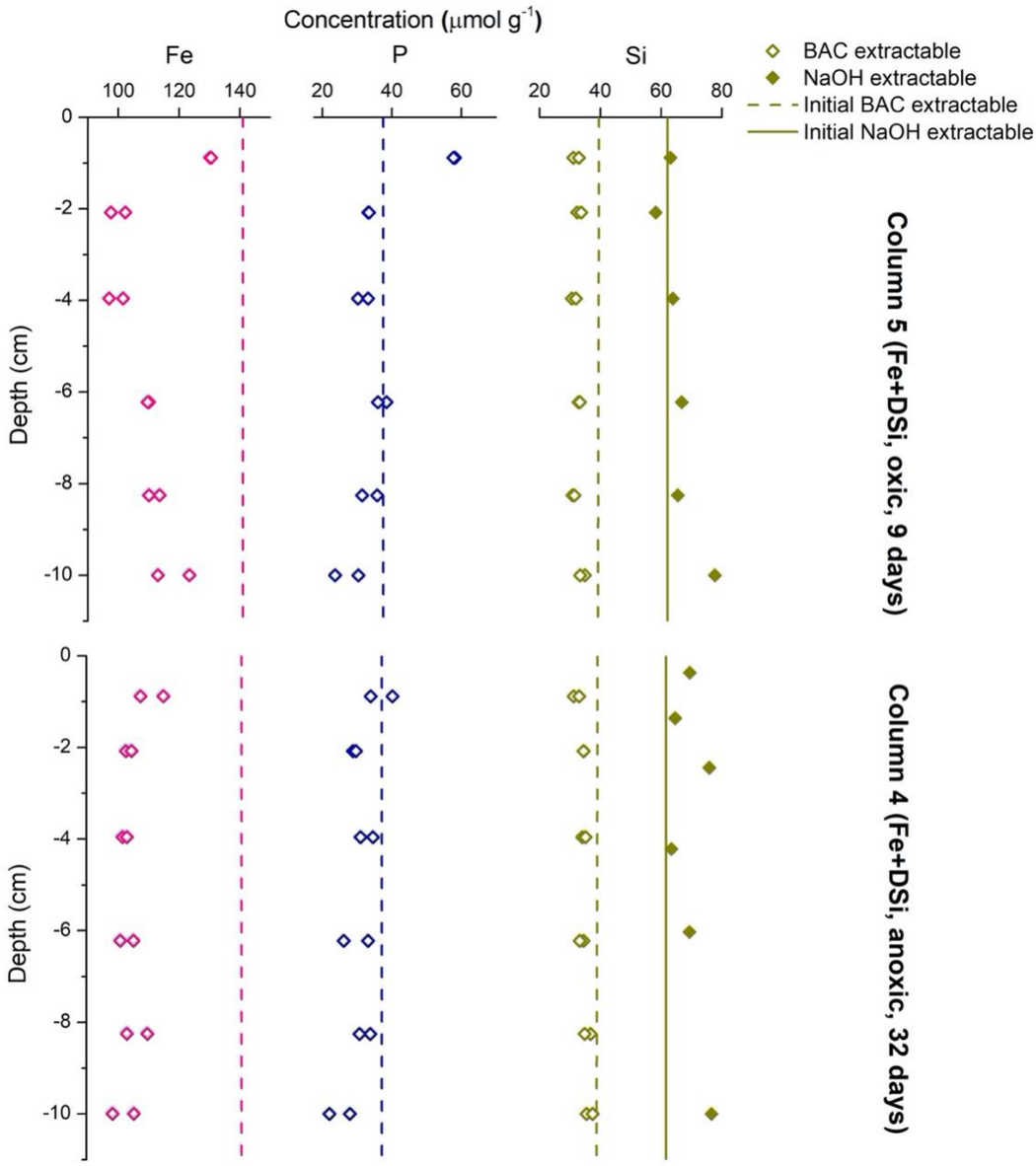

Figure 5.8. Vertical distributions of buffered ascorbate-citrate (BAC) extractable Fe, Si and P, and NaOH extractable Si. The top panels show results of column 5 (supplied with "Fe, DSi", and was sacrificed after oxic period, *i.e.*, 9 days), the bottom panels show results of column 4 (supplied with "Fe, DSi" under oxic conditions for 9 days and "DSi" under anoxic conditions for 32 days, and was sacrificed after anoxic period). Solid lines represent the concentrations of NaOH extractable ASi in the initial sediment prior to use. Dashed lines represent the concentrations of BAC extractable Fe, Si, and P in the initial sediment prior to use. Note that NaOH extractable ASi was 20% of total NaOH extractable Si in Table 5.2, *i.e.*, the contribution of silicate minerals was corrected.

5.4.6 Mass balance between aqueous and solid phases

The change rates of dissolved and extractable Fe, Si and P of columns 2 (control column supplied with DSi) and 4 (column that studied the effect of Fe and Si co-precipitation on DSi (im)mobilization) were calculated for oxic and anoxic periods using Equations (5.3, 5.5 and 5.6) (Figure 5.9 and Figure 5.10). During oxic periods, BAC extractable Fe in column 2 decreased with a rate of 280 μmol day^{-1}, while there was no dissolved Fe released. BAC extractable Fe in column 4 decreased with a rate of 202 μmol day^{-1}, which was 78 μmol day^{-1} smaller than that of column 2, as column 4 retained Fe(II) supplied in influent with an rate of 83 μmol day^{-1}. During anoxic periods, the loss rates of BAC extractable Fe from columns 2 and 4 were 6 and 2 times, respectively, faster than the release rate of dissolved Fe from columns 2 and 4. The loss rate of BAC extractable P was around 2 times faster than the release rate of DP from columns 2 and 4 during both oxic and anoxic periods.

BAC extractable Si showed much faster loss rates during oxic periods than that during anoxic periods from columns 2 and 4, while the release rates of DSi from both columns were not altered by oxygen conditions. In contrast, the loss rate of NaOH extractable ASi during oxic period was slightly faster than that during anoxic periods from column 2. In column 2, the NaOH extractable ASi loss rates were more than 2.5 times faster than the DSi release rate from column 2. Unlike column 2, in column 4, NaOH extractable ASi increased at a rate of 29 μmol day^{-1} during its oxic incubation period, while the NaOH extractable ASi loss rate during anoxic periods was close to the DSi release rate (Figure 5.9 and Figure 5.10).

The DSi release rates calculated for the control columns were used to represent the internal DSi production rates in all of the columns, although the NaOH extractable ASi in the control columns was not measured. DSi concentrations in the overlying water of the control columns, which were supplied with only APW, decreased from their initial concentration of around 375 μM to around 250 μM within 4 days of incubation and remained stable until the end of the incubation experiment (Figure D.1). If the DSi at steady-state was all produced from ASi dissolution, the dissolution rate of biogenic ASi in sediment columns, R (μmol day^{-1}), can be expressed by:

$$\mathrm{R} = ([DSi]_{out} - [DSi]_{in}) \cdot Q \qquad (5.7)$$

where $[DSi]_{out}$ and $[DSi]_{in}$ are the concentrations of DSi in effluent and influent (μM), respectively, Q is the volumetric flow rate through the column (*i.e.*, 5 mL h^{-1}). Therefore, the loss rate of ASi from the control columns was around 30 μmol day^{-1}, which is smaller than the DSi release rate in control columns of 40 μmol day^{-1} calculated with Equation (5.3).

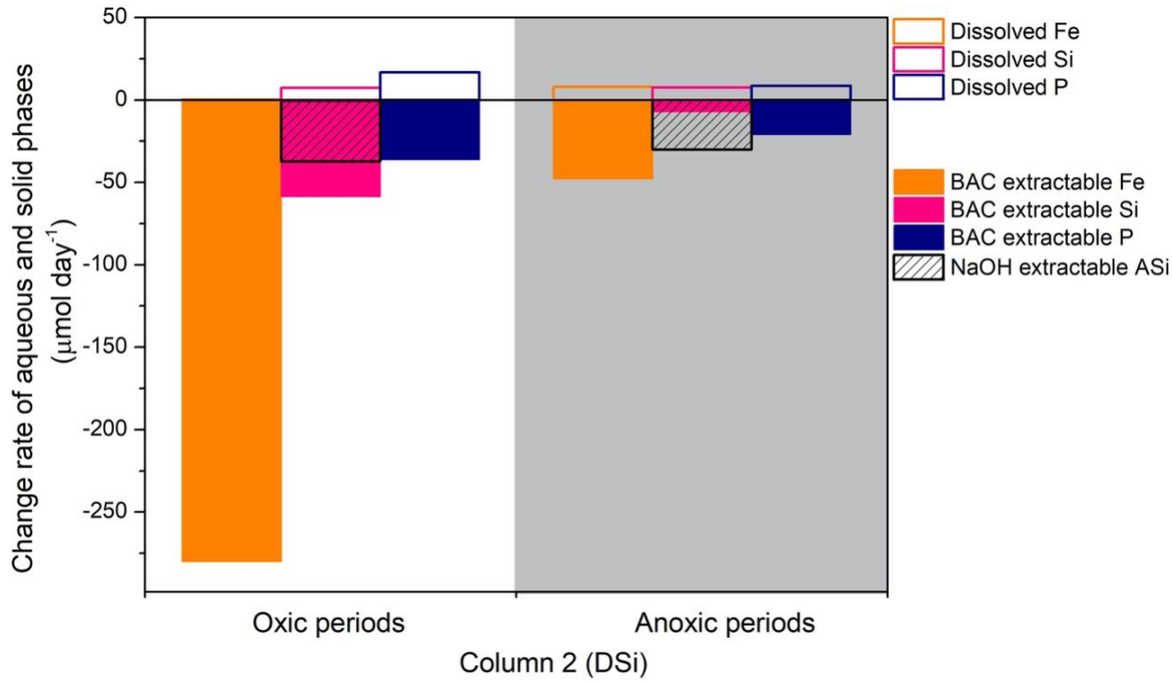

Figure 5.9. Release rate of dissolved Fe, Si and P from column 2 (open columns), and change rate of buffered ascorbate-citrate (BAC) extractable Fe, Si and P, and 1 M NaOH extractable ASi (solid columns) in columns 2 after oxic and anoxic incubation periods. Columns 2 was firstly supplied with "DSi" for around 9 days under oxic conditions, and then supplied with "DSi" for around 32 days under anoxic conditions. Note that the change rate of solid phase during oxic periods was calculated from column 1 that had the same treatment as column 2 but was sacrificed at the end of oxic incubation.

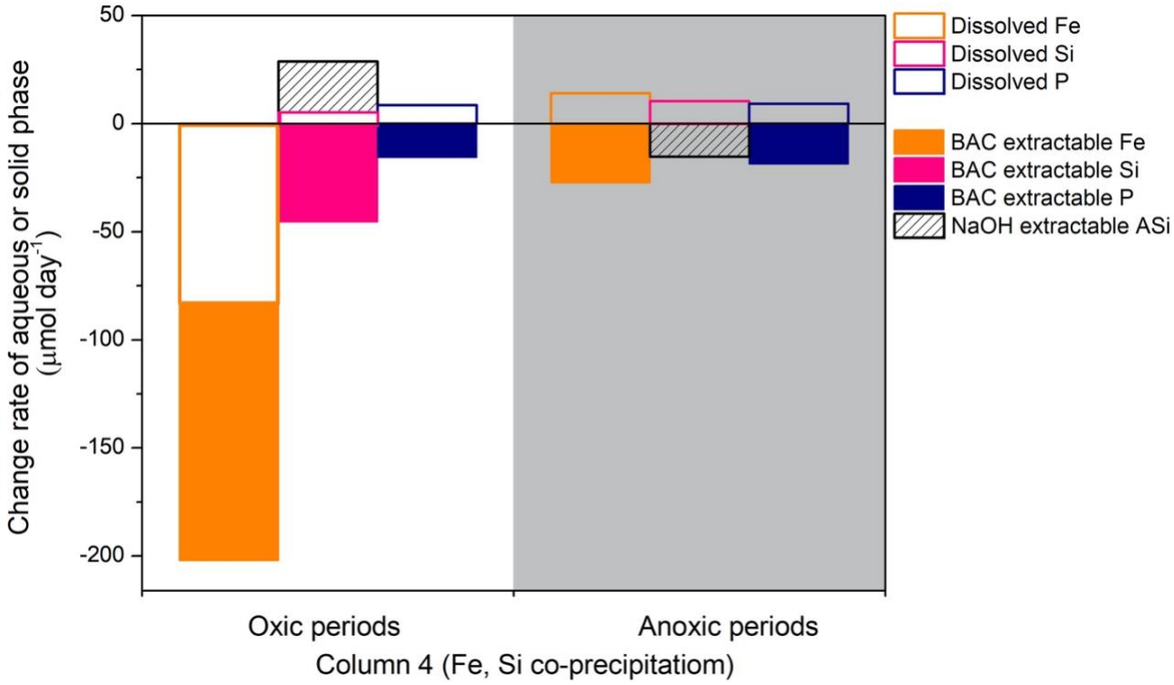

Figure 5.10. Release rate of dissolved Fe, Si and P from column 4 (open columns), and change rate of buffered ascorbate-citrate (BAC) extractable Fe, Si and P, and 1 M NaOH extractable ASi (solid columns) in column 4 after oxic and anoxic incubation periods. Column 4 was firstly supplied with "Fe, DSi" for around 9 days under oxic conditions, and then supplied with "DSi" for around 32 days under anoxic conditions. Note that the change rate of solid phase during oxic periods was calculated from column 5 that had the same treatment as column 4 but was sacrificed at the end of oxic incubation.

5.5 Discussion

Chapter 4 of this thesis demonstrated that molecular diffusion limits the co-precipitation kinetics of Si and Fe in heterogeneous agarose columns, leading to the minor immobilization of DSi during the oxidative precipitation of Fe under oxic conditions. Natural sediments were used in this chapter to represent the complexity of processes occurring in nature. Transport processes were accelerated by pumping influent solution containing different combinations of dissolved Fe(II), DSi and DP, aiming to extenuate the effects of differing oxygen conditions on the (im)mobilization of DSi. The results show that Fe(II) and DP supplied in the influent solutions were effectively retained in the sediments when an oxic sediment-water interface was present. The oxygen dependence of dissolved Fe and DP released from sediments is consistent with that observed in previous studies (Gächter and Mülle, 2003; Gachter and Muller, 2003; Jensen et al., 1992; Mortimer, 1941; Parsons et al., 2017; Ridenour, 2017; Sabur, 2019; Zhang and Huang, 2007). In contrast to dissolved Fe(II) and DP, there was little evidence of DSi retention during oxic periods, despite the fact that dissolved Fe(II) was supplied in the influent solutions, which is different from our hypothesis. In addition, no changes were observed in the DSi efflux upon switching to anoxic overlying water. In this section, I discuss the dominant mechanisms that may control the response of the release dynamics of dissolved Fe, DP and DSi to oxygen conditions.

5.5.1 Oxygen dependence of dissolved Fe release from flow-through columns

The sediment column acted as a sink of dissolved Fe when oxic conditions prevailed at the sediment-water interface, retaining all the dissolved Fe(II) supplied to, as well as any produced within, the sediment columns (Figure 5.4, Figure 5.5 and Figure 5.6). The enrichment of Fe(III) oxyhydroxides in the uppermost sediment indicates that the oxidative precipitation of Fe(II) contributes to the retention of Fe in sediment under the oxic water layer. Under anoxic conditions, substantial release of dissolved Fe to the anoxic overlying waters was observed for all columns. This is partly due to that the reductive dissolution of Fe(III) oxyhydroxides which accumulated in the uppermost sediment under oxic conditions (Lovley, 1997; Parsons et al., 2017; Sabur, 2019). Fe(II) produced by the reductive dissolution of ferric minerals and the dissolution of ferrous mineral in the anoxic zone of sediment columns, if not precipitated as secondary iron mineral phases, can be released to the anoxic overlying water (Gächter and Mülle, 2003).

The dramatic loss of BAC extractable Fe during oxic periods could be due to the reductive dissolution of Fe(III) oxyhydroxides formed during homogenization of the sediment prior to the experimental period. Homogenization of the sediment was conducted under oxic conditions and would have resulted in uniformly oxidized sediments. Conditions below the zone of oxygen penetration within the columns would have rapidly become anoxic during the experimental period. Fe(II) released via reductive dissolution of these Fe(III) oxyhydroxides within the columns could react with S^{2-}, HPO_4^{2-}/ $H_2PO_4^-$ or HCO_3^- to form secondary, authigenic ferrous iron mineral phases which may not be extracted by the BAC extractant (Cornell et al., 1987; Gehin et al., 2007; Hyacinthe and Van Cappellen, 2004; Jensen et al., 2002; Jones et al., 2009; Kostka and Luther, 1994; Voegelin et al., 2010). The transformation of reactive Fe(III) oxyhydroxides to more

crystalline phases with time could be another reason leading to the rapid decrease of BAC extractable Fe during the initial days of the experiment, which coincided with the oxic conditions at the sediment-water interface (Rzepa et al., 2016; Scharer et al., 2009; Swedlund et al., 2010; Thompson et al., 2006; Yee et al., 2006). It should be clarified that the sediment columns were flushed with anoxic APW for one day before starting the experiment (Step 1 in Figure 5.2). During the first day of incubations, the overlying waters in all columns were not sparged with air. Therefore, dissolved Fe released via the reductive dissolution of Fe(III) oxyhydroxides in the anoxic zone of the sediment columns may have been exported from the columns during this time, which would account for the significant decrease in BAC extractable Fe. However, the amounts of dissolved Fe released during the first day of incubation were not monitored.

5.5.2 Oxygen dependence of DP release from flow-through columns

Measurable DP effluxes were detected under oxic conditions in all columns, although varying amounts of Fe(II) were pumped through the sediment column. Firstly, organic bound P is usually the most abundant soluble P endmember in organic matter-enriched surficial sediments (Parsons et at., 2017; Sabur, 2019). The microbial degradation of organic matter, in combination with the reductive dissolution of Fe(III) with co-precipitated P in the anoxic zone of the sediment column, could lead to considerable internal DP production (Parsons et al., 2017; Ridenour, 2017). In the case of this study, if not retained in the thin oxic zone at the sediment-water interface, sediment columns released dissolved Fe and DP at a constant rate of 5.0±1.0 and 4.4±0.8 μmol day^{-1}, respectively. The DP:Fe(II) ratio from internal production therefore exceeds the maximum molar stoichiometric P:Fe ratio in ferric phosphate, *i.e.*, 0.5 (Gächter and Mülle, 2003; Thibault et al., 2009) which is typically the dominant mechanism for DP immobilization, and DP escapes from the oxic sediment surface. Secondly, Fe(II) supplied to sediment columns should have been sufficient to retain all DP produced in the column. However, the retention of Fe(II) in the anoxic zone through precipitation of ferrous mineral phases and adsorption to the surfaces may have decreased the amount of Fe(II) to actually reach the oxic zone at the surface of the sediment columns. Consequently, the active precipitation of Fe(III) oxyhydroxides in the uppermost sediment under the oxic water layer was unable to retain all the DP supplied to, as well as produced within, the sediment columns. Under anoxic conditions, the DP released was enhanced significantly and DP efflux dynamics were similar to those of Fe(II). This is likely due the reductive dissolution of Fe(III) oxyhydroxides leading to the release of Fe(III)-bound P under anoxic conditions (Gächter and Mülle, 2003; Gachter and Muller, 2003; Katsev et al., 2006; Orihel et al., 2017; Parsons et al., 2017; Sabur, 2019; Smolders et al., 2017; Sondergaard et al., 2003; Van der Molen and Boers, 1994).

The discrepancy between loss rates of BAC extractable P and release rates of DP indicates the redistribution of DP released from reductive dissolution of Fe(III) oxyhydroxides into other sedimentary pools, *e.g.*, re-adsorption to the Al oxides and carbonate minerals, precipitation as vivianite (Connell et al., 2015; Gächter and Müller, 2003; Orihel et al., 2017; Rothe et al., 2014; Parsons et al., 2017) and/or precipitation as carbonate fluorapatite (Orihel et al., 2017).

5.5.3 Oxygen dependence of DSi release from flow-through reactors

DSi released from the sediments did not shown a clear dependence on overlying water oxygen concentrations in any of the columns, regardless of the concentration of DSi, DP, and dissolved Fe in the artificial porewater solutions that they were supplied, which was different from our hypothesis. Below, I discuss the mechanisms that may have been responsible for this lack of oxygen dependence by considering the roles of two reactive particulate Si endmembers, ASi and Fe-bound Si, to the DSi efflux under oxic and anoxic conditions. I then go on to compare these results to the findings of other studies that have or have not shown a clear dependence of DSi effluxes on oxygen conditions and discuss the implications for understanding DSi loading.

5.5.3.1 Contribution to DSi release dynamics by amorphous silica (ASi)

Amorphous silica (ASi) is one of the dominant reactive particulate Si endmembers in natural sediments (Aston, 1983; Hurd, 1973; Koning et al., 2002; Laruelle et al., 2009; Maavara et al., 2014). If all DSi released from the sediment columns in this study were attributed to ASi dissolution, the corresponding ASi dissolution rates would be 7 (with DSi in influent) to 40 (without DSi in influent) μmol day^{-1}. This is within the range of dissolution rates of 0.5 to 80 μmol day^{-1} observed for different ASi materials in a previous study (Loucaides et al., 2008). Therefore, the dissolution of ASi materials in the columns is able to explain most of the DSi released. This mechanism has been proposed in previous studies (Lehtimaki et al., 2016; Tallberg et al., 2013). However, the contribution of other reactive particulate Si endmembers to DSi release can not be excluded. For example, the relatively fast release rate of DSi from the control columns (APW) during the first 4 days of incubation could be attributed to the desorption of loosely adsorbed and Fe-bound (Sauer et al., 2006; Tallberg et al., 2009).

The dissolution kinetics of ASi have been reported to depend on oxygen conditions in previous studies. The proposed mechanism is that the microbially mediated dissolution of diatom detritus in sediments can be enhanced under hypoxic conditions by changing the composition of bacterial community (Lehtimaki et al., 2016; Villnas et al., 2012). Oxygen conditions at the sediment-water interface did not drastically affect the measured rate of NaOH extractable ASi loss from sediment during the incubation experiment, *i.e.*, the dissolution kinetics of ASi, in column 2 (control column supplied with DSi) (Figure 5.9), which was consistent with the independent release of DSi on oxygen conditions. This is likely because oxygen conditions in the experimental columns only varied within approximately the uppermost 1 cm of sediment and therefore only the sediments in this zone would be subject to oxygen dependent differences in the dissolution kinetics of ASi, *i.e.*, ASi in sediments below the oxidation front (which is located around 1 cm below the sediment surface) were subjected to anoxic conditions throughout the incubation regardless of the conditions at the sediment-water interface. Therefore, the effect of oxygen conditions on the release of DSi from ASi dissolution in the experiments may be minor, especially as there was no deposition of fresh ASi during experiment.

The supply of Fe(II) via inflow solution increased the concentration of NaOH extractable Si in column 4 (left panel in Figure 5.10). It has been proposed that DSi can form amorphous aggregates with Fe, P and Al in subsurface sediments even at low concentrations which below the concentration required to cause supersaturation with respect to ferrous silicate (Tosca et al., 2016; Wang et al., 2013b). The physiochemical properties of such aggregates and their roles on the release of DSi from sediment require further study. Additionally, the supply of Fe(II) under oxic conditions seemed to decrease the loss rates of ASi in sediment column. This could be due to Fe(II) adsorption to the surface of ASi via the formation of bidentate surface complexes. The adsorption of trace amounts of Fe(II) that preferentially occupy more reactive doubly coordinated surface sites has been shown to inhibit ASi dissolution effectively (see details in Chapter 3).

5.5.3.2 Contribution to DSi release dynamics by Fe(III) oxyhydroxides

The porewater compositions supplied to multiple columns were designed to study the different effects of co-precipitation during Fe(II) oxidation (columns 3, 4, 5 and 6) versus surface adsorption of DSi by Fe(III) oxyhydroxides (columns 7, 8, 9 and 10) on DSi (im)mobilization. DSi retention in the sediment columns was not altered significantly in either scenario compared to the columns which were supplied with only DSi (columns 1 and 2). One possible explanation for the lack of an observable effect of Fe(II) additions on DSi retention is that Fe(II) supplied to the columns was retained in the columns' anoxic zone. Fe(II) retention in the columns' anoxic zone would limit the Fe reaching the oxic zone that would be available for DSi co-precipitation reaching oxic zone (see details in 5.5.1). Other than Fe(II) removal processes in the anoxic zone discussed above, one previous study has also shown that Fe may form amorphous aggregates with Si, P and Al in subsurface sediments even at low concentrations (Wang et al., 2013b). This is supported by the linear relationships between NaOH extractable Si and Fe, and Si and Al (Figure D.2).

More likely, the reason for this lack of clear observable differences between columns due to the formation of Fe-bound Si is that the internal production of DP from the sediments (see details in 5.5.2) may compete with DSi for complexing with Fe(II) and/or adsorbing to Fe(III) oxyhydroxides during the oxidative precipitation of Fe(II). As is shown in Chapter 4, DSi immobilization during Fe(II) oxidation occurs by two pathways: DSi is either removed by direct co-precipitation with Fe(II) during the oxidation of Fe(II)-DSi complexes, or by adsorption to Fe(III) oxyhydroxides formed by Fe(II) oxidation. At near-neutral pH values, DP limits the removal of DSi via both of these pathways by successfully outcompeting DSi for complexation with aqueous Fe(II) and for sorption to surface sites of Fe(III) oxyhydroxides. In Chapter 4, I demonstrated that DSi will be barely immobilized via co-precipitation with Fe unless a low DP concentration threshold is reached at near-neutral pH (below ~ 10 µM). By comparing DSi and DP concentrations in the oxic effluents to results in Chapter 4, it can be seen that DP in the effluents of all the flow-through columns had such a high DP concentration that DSi incorporation into Fe(III) oxyhydroxides would have been very limited (Figure 5.11).

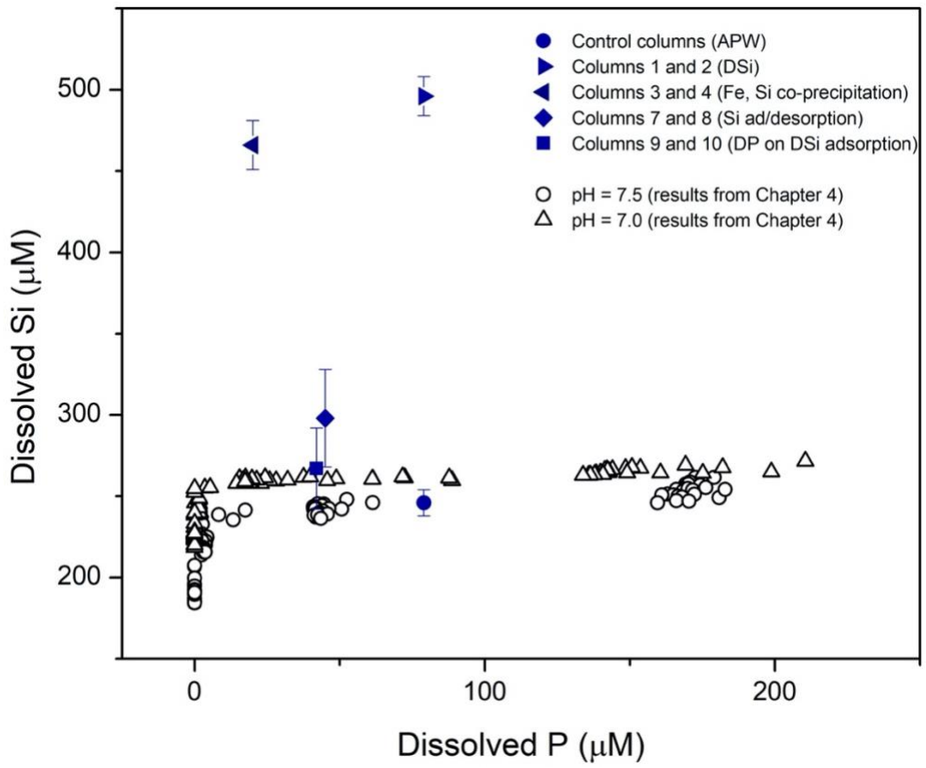

Figure 5.11. Concentrations of dissolved phosphate (P) and silicon (Si) in column effluents under oxic conditions (n = 6, data points between 4 and 6.3 days). Open triangles and circles are data points sorted from the co-precipitation of Fe(II), Si, and P with an initial Fe(II) concentration of 300 µM (refer to Chapter 4). Dissolved P and Si concentrations in effluents from different sediment columns with different chemical compositions of influents: Control columns were flushed with "APW", column 1 and 2 were flushed with "DSi", column 5 and 6 were flushed with "Fe", columns 7 and 8 were flushed with "Fe, DSi", column 9 and 10 were flushed with "Fe, P". Control column was flushed with "APW" only throughout the experiment (data from Sabur, 2019).

5.5.4 Implications for internal DSi loading

Our results show that the release of DSi from sediment does not necessary show dependency on oxygen conditions, which is consistent with observations from previous studies (Table 1.1). The dominant mechanisms accounting for DSi release included in this chapter are (i) ASi dissolution and (ii) oxidative precipitation and/or reductive dissolution of Fe(III)-bound Si. The relative contributions of these two endmembers can lead to different responses of internal DSi loading to variations in oxygen conditions at the sediment-water interface.

The first step to assess the likely effect of oxygen conditions at the sediment-water interface on internal DSi loading would be to determine the speciation of reactive particulate Si (RPSi) in surface sediments. If ASi is the predominant RPSi endmember in sediments, dissolution of ASi will likely control the release rate of DSi from sediment so that the effects of iron minerals will likely be negligible. Although not investigated in this study, anoxic/hypoxic conditions have been shown to enhance the dissolution kinetics of diatom detritus by changing the benthic microbial community and activities (Lehtimaki et al., 2016; Villnas et al., 2012). Physicochemical properties of ASi materials in natural sediments, including their sources and age need to be well characterized to assess the response of ASi dissolution kinetics to oxygen conditions.

If not retained by subsequent biogeochemical processes in surface sediments, DSi released from ASi dissolution will be diluted quickly into overlying waters. Otherwise, DSi released from ASi dissolution can adsorb to iron minerals and/or co-precipitate with Fe(III) during the oxidative precipitation of Fe(II) (Gehlen and Van Raaphorst, 2002; Hansen et al., 1994; Kandori et al., 1992; Kinsela et al., 2016; Sabur, 2019; Swedlund et al., 2010), leading to the immobilization of DSi in oxic surface sediments. Substantial retention of DSi occurs only if Fe concentration, including solid iron minerals and aqueous Fe(II), are high and the concentrations of competing anions, notably DP, are low (left scenario, Figure 5.12). The ability of iron minerals to immobilize DSi decreases with increasing DP concentration (see details in Chapter 4), as DP outcompetes DSi for sorption sites of iron minerals in the oxic surface sediment. After being buried, reductive dissolution of iron minerals leads to the accumulation of DP and dissolved Fe(II) in porewater. When the solubility product is exceeded, ferrous phosphate (*e.g.*, vivianite) precipitates, which consequently decreases (i) the amount of Fe(II) available to diffuse upward to the oxic zone and (ii) the availability of Fe for DSi immobilization (right scenario, Figure 5.12).

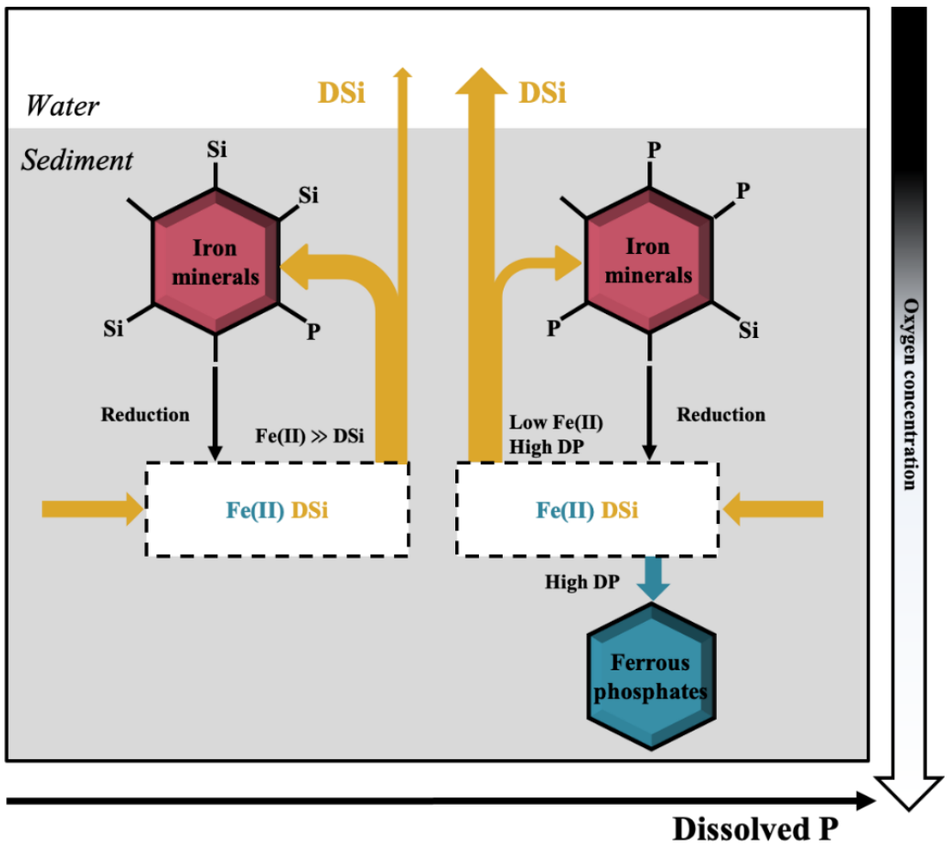

Figure 5.12. Proposed interactions between Si, P and Fe in iron minerals which control the DSi effluxes from freshwater sediments overlain by oxygenated bottom waters. Left-hand side: High availability of reactive Fe and low porewater DP concentrations result in lower DSi efflux to overlting water compared to concentrations in anoxic sediment porewater; Right-hand side: Reduced ability of Fe(III) oxyhydroxides to retain DSi when high DP concentrations outcompete DSi for sorption sites on Fe(III) oxyhydroxides, and higher DSi efflux to overlying water compared to conditions with lower DP concentrations illustrated on the left-hand side.

The dominant biogeochemical processes that may be sensitive to oxygen conditions in surface sediments are described in this section. A general conclusion on the dependence of internal DSi loading on oxygen conditions at the sediment-water interface cannot be given, because natural freshwater systems are far more complex than is discussed above. For example, the decrease in pH that usually accompanies with transition from oxic to anoxic conditions can decrease ASi dissolution rates but limit DSi immobilization by co-precipitation. The relative magnitudes of these two processes determines the direction of the redox dependence of DSi release. In combination with interactions with environmental factors and different feedback loops, the biogeochemical processes described above provide a general framework for assessing the effect of oxygen conditions on internal DSi loading from sediment.

5.6 Conclusions

To investigate the interactions between Fe(II), DSi and DP, and their contribution to the redox dependence of internal DSi loading in natural sediments, I incubated surficial sediments from the open water area of a freshwater marsh in flow-through column systems. These experiments were considerably more complex than those conducted in previous chapters due, in part, to the presence of both Fe bound Si and other reactive Si endmembers. Anoxic solutions containing variable concentrations of Fe(II), DSi and DP were pumped upward through 10 parallel flow-through columns. During oxic incubation, when the overlying water was aerated, the sediment column acted as a sink of Fe under oxic conditions, retaining all the dissolved Fe(II) supplied to, as well as produced within, the sediment columns. When the overlying water became anoxic, efflux of Fe(II) from the columns was observed. However, a smaller amount of Fe was released than was retained under oxic conditions. This indicates that Fe(II) was also likely retained via the formation of ferrous minerals and/or adsorption to mineral surfaces when passing through the anoxic zone of the columns. The DP retention and efflux dynamics were similar to those of Fe(II), although even under oxic conditions measurable DP efflux was detected. This implies that a strong coupling of Fe and P cycling and that the active precipitation of Fe(III) oxyhydroxides was effective at retaining DP. However, DP can escape from the oxic sediment surface when DP concentrations in porewaters exceed the capacity of Fe(III) oxyhydroxides. In contrast to Fe(II) and DP, there was little evidence of DSi retention during oxic periods. In addition, no changes were observed in the DSi efflux upon switching to anoxic overlying water, indicating a decoupling of the Fe and Si cycles. This net and constant release of DSi is likely due to ASi dissolution under both oxic and anoxic conditions. Overall, the results with the natural sediment confirm that the presence of high DP levels inhibit the co-precipitation and adsorption of DSi, hence preventing DSi retention in sediments under oxic overlying water. I conclude that the relative production rates of porewater DP and DSi likely represents the major control on the redox dependence of internal Si loading in freshwater systems, assuming that reactive Fe is present in sediments. Increased DP loads and concentrations in natural freshwater may actually enhance the mobilization of DSi released from ASi dissolution in sediments, leading to increased internal DSi loading.

Chapter 6
Conclusions and Perspectives

6.1 Conclusions

In this thesis, I used controlled laboratory experiments to unravel the roles of different reaction pathways in controlling the immobilization and release of dissolved silicon (DSi) in freshwater environments. To do this, I built experimental systems of increasing complexity: I started with simple synthetic reaction systems consisting of amorphous silica (ASi) suspended in electrolyte solution, and progressively included additional components, specifically iron (Fe) and phosphorus (P), in order to mimic more realistic biogeochemical reaction networks. Ultimately, I performed experiments with real freshwater sediments. In each synthetic reaction system experiment, I focused on the reactivity of one of two major reactive particulate Si endmembers: ASi and Fe-bound Si. In the experiment with real sediments I used the previously acquired knowledge to interpret the observations. Below, I highlight the major findings of this thesis and how these findings have collectively advanced our understanding of the mechanisms controlling the recycling of nutrient silicon in freshwater environments, in particular bottom sediments and stratified water columns.

6.1.1 Dissolution kinetics of ASi

6.1.1.1 Surface-reaction controlled dissolution kinetics of ASi

The dissolution of ASi is the first step in the recycling of bioavailable DSi to the water column. By conducting batch experiments under well-controlled conditions, the dissolution kinetics and rate constants of different ASi materials were compared in Chapter 2. In the absence of surface complex forming agents, variations in the ASi dissolution rate constant can be explained with a surface reaction model, which shows that the concentrations, charge distribution, and accessibility of surface sites control the dissolution kinetics. The results confirm the non-linear relationship between the ASi dissolution rate constant and the degree of undersaturation, implying that at least two dissolution rate constants are needed to describe the dissolution kinetics from high (on average >0.4) to low (on average <0.4) degree of undersaturation of the solution with respect to ASi. The quantitative relationships between the ASi dissolution rate constant and environmental variables, including pH, degree of undersaturation and salinity, observed in Chapter 2 contribute to the general framework to quantitatively predict dissolution rates of ASi in different freshwater systems.

6.1.1.2 Dissolution kinetics of ASi: effect of dissolved Fe(II)

In Chapter 3, the dissolution rate of a model ASi (Aerosil OX 50 in this chapter) was measured in the presence of variable amounts of Fe(II) under anoxic conditions. The results indicate that the adsorption of Fe(II) generally inhibits dissolution. However, the surface reaction model presented in Chapter 2 cannot fully account for the effects of Fe(II). Instead, a Langmuir adsorption model that incorporates two types of surface groups (surface silicate groups bonded to the silica lattice

via two bridging oxygens, Q_2, and surface silicate groups bonded to the silica lattice via three bridging oxygens, Q_3) was used to describe the effect of Fe(II) on the dissolution kinetics of ASi. The adsorption model suggests that Fe(II) preferentially binds to Q_2 groups, which causes the dissolution to slow down. The adsorption of Fe(II) to Q_3 groups is less favorable and therefore only happens when most Q_2 groups are occupied. However, binding of Fe(II) to Q_3 increases the reactivity of the surface groups, hence, accelerating ASi dissolution. Thus, the coordinative arrangements of exposed surface groups affect the dissolution of ASi in the presence of Fe(II).

6.1.2 Co-precipitation of Si during oxidative precipitation of Fe(III) oxyhydroxides

In Chapter 4, I studied the effects of dissolved phosphate (DP), pH and molecular diffusion on DSi immobilization during the oxidative precipitation of Fe(III) oxyhydroxides by exposing anoxic solutions containing mixtures of dissolved Fe(II), DSi and varying concentrations of DP to oxygen in both batch and agarose column systems. The experimental results from the homogeneous batch experiments show that the oxidative precipitation of Fe(II) can immobilize considerable amounts of DSi at high pH values, unless high concentration of DP are present. DP effectively outcompetes DSi for complexation with aqueous Fe(II) and for adsorption to newly formed Fe(III) oxyhydroxides. In contrast to the DSi uptake observed in the batch Fe(II) oxidation experiments, the results of the column experiment indicate that diffusive transport decreases not only the oxidation rate of Fe(II), but also the extent of Si co-precipitation. Collectively, the results in this chapter show that DSi retention by oxidative precipitation of Fe(II) is controlled by the relative abundance of DP and the rate of Fe(II) oxidation, which along redox gradients is in turn controlled by the diffusion rates of aqueous Fe(II) and O_2.

6.1.3 DSi and DP effluxes from natural freshwater sediment

In Chapter 5, I investigated the interactions between Fe(II), DSi and DP, and their roles in the internal DSi loading from natural sediments, using a series of parallel flow-through columns filled with homogenized sediment collected in a freshwater marsh. Anoxic solutions containing variable concentrations of Fe(II), DSi and DP were pumped upward through the columns. The overlying water was either kept oxic by remaining open to the atmosphere and purging with O_2 or allowed to go anoxic by sealing the top caps of the columns. During the oxic periods, the sediment column acted as a sink of Fe and DP, retaining all the dissolved Fe(II) and most of the DP supplied via the inflow. When the overlying water turned anoxic, efflux of Fe(II) and DP from the columns was observed. This implies a strong coupling of Fe and P cycling where the precipitation of Fe(III) oxyhydroxides in the topmost sediment effectively retained DP. In contrast to Fe(II) and DP, there was little evidence of DSi retention during oxic periods. In addition, no systematic changes were observed in the DSi efflux upon switching to anoxic overlying water, indicating a decoupling of the Fe and Si cycles. A net efflux of DSi was also observed for DSi-free inflow solution, implying dissolution of reactive (bio)siliceous debris originally present in the natural sediment. Overall, the results with the natural sediment confirm that the presence of high DP levels inhibit the co-precipitation and adsorption of DSi, hence preventing DSi retention in sediments under oxic overlying water. I conclude that the relative production rates of porewater DP and DSi likely

represents a major control on the redox dependence of internal Si loading in freshwater systems. These results show that DSi release from sediments does not necessary exhibit a simple dependency on bottom water oxygen conditions.

6.2 Research perspectives and future directions

6.2.1 Significance of the research

Dissolved silicon (DSi) is an important auxiliary nutrient in freshwater aquatic environments with implications for the species composition of phytoplankton communities. Exchanges of nutrients between water column and sediment in freshwater aquatic environments, such as wetlands, lakes and reservoirs, are an important control on nutrient cycling. This is especially true for nutrient Si because of the biological production of amorphous silica (ASi), whose subsequent dissolution regenerates DSi. Furthermore, interactions between Si and Fe may lead to the immobilization of Si by co-precipitation with and adsorption to ferric iron phases. In these latter processes, however, DSi competes with DP. In this thesis, I have shown that controlled experiments of increasing complexity provide one way to unravel the roles of different reaction pathways in controlling the release and/or immobilization of DSi via interactions involving ASi and Fe mineral phases. The outcomes of the experiments represent important contributions to our understanding of Si cycling in freshwater ecosystems. These contributions include the following.

Firstly, my work confirmed the quantitative framework for relating the ASi dissolution rate constant to key environmental variables, including pH, salinity and degree of undersaturation. More importantly, the ASi dissolution rate can be represented using two rate constants that are based on the degree of undersaturation. Then, by studying the role of particle-active Fe(II) and conducting dissolution experiment under anoxic conditions, I show, for the first time, that the coordinative arrangements of surface groups affect the dissolution rate of ASi and accounts for the effect of a major constituent of many anoxic environments. Unraveling the mechanisms of ASi dissolution helps not only to predict the recycling rate of ASi in different freshwater systems, but also to interpret ASi distributions in lake sediments for reconstructing paleolimnological conditions, hence providing insights into change in trophic state of lakes over time.

Secondly, I have demonstrated that the DSi produced by ASi dissolution can be immobilized during the oxidative precipitation of Fe(II), in particular under alkaline pH values and in the presence of low concentrations of DP. However, the contribution of co-precipitation to DSi immobilization under oxic conditions may have been overestimated in previous studies, because DSi incorporation into ferric iron co-precipitates can be limited by relatively high DP concentrations and slow transport-controlled rates of Fe(II) oxidation in redox-stratified environments. The results imply that the speciation and stability of legacy P pools in sediments, as well as recent depositional P inputs exert an important control on the internal loading of DSi in freshwater lakes and wetlands.

Lastly, with the mechanisms unravelled and the kinetic information obtained in this study, geochemical reactions that control DSi release can be incorporated into the reactive transport

model developed for P, thus predicting internal loading of DSi, DP and dissolved Fe at the same time.

6.2.2 Future directions

To better understand the mechanisms of internal DSi loading from natural freshwater sediments, the effects of biotic processes and the relative importance of other forms of reactive particulate silica need to be further studied. Below, I highlight some of the topics that could be the focus of future research that builds on this thesis' work.

6.2.2.1 ASi dissolution mediated by microbial processes under different oxygen conditions

The diatom frustules used in this study (Chapter 2) to study ASi dissolution kinetics were pretreated with concentrated nitric acid to remove any organic matter. However, biogenic ASi in nature is usually intimately associated with, and protected by, an organic matrix (Bidle and Azam, 1999; Lehtimaki et al., 2016; Lewin, 1961). After the death of a diatom, either after the end of its lifecycle or after processing through the digestive system, colonization by bacterial assemblages and the activity of extracellular hydrolytic enzymes lead to the removal of the organic matrix, progressively exposing the silica surface to the aqueous medium. In addition to the removal of organic matrix, microbe-associated biofilms can also locally shift the pH to higher than 9, enhancing ASi dissolution (Lehtimaki et al., 2016). Oxygen conditions have been shown to affect the composition of the microbial community that mediates the decomposition of the organic matrix surrounding ASi by modifying dissolution of ASi as shown by Lehtimaki et al. (2016) and Villnas et al. (2012). However, the latter two studies provide preliminary insights and further research with real benthic communities remain to be carried out. Overall, the net effects of microbial processes under different oxygen conditions on the dissolution of ASi remains a subject of debate (Figure 6.1).

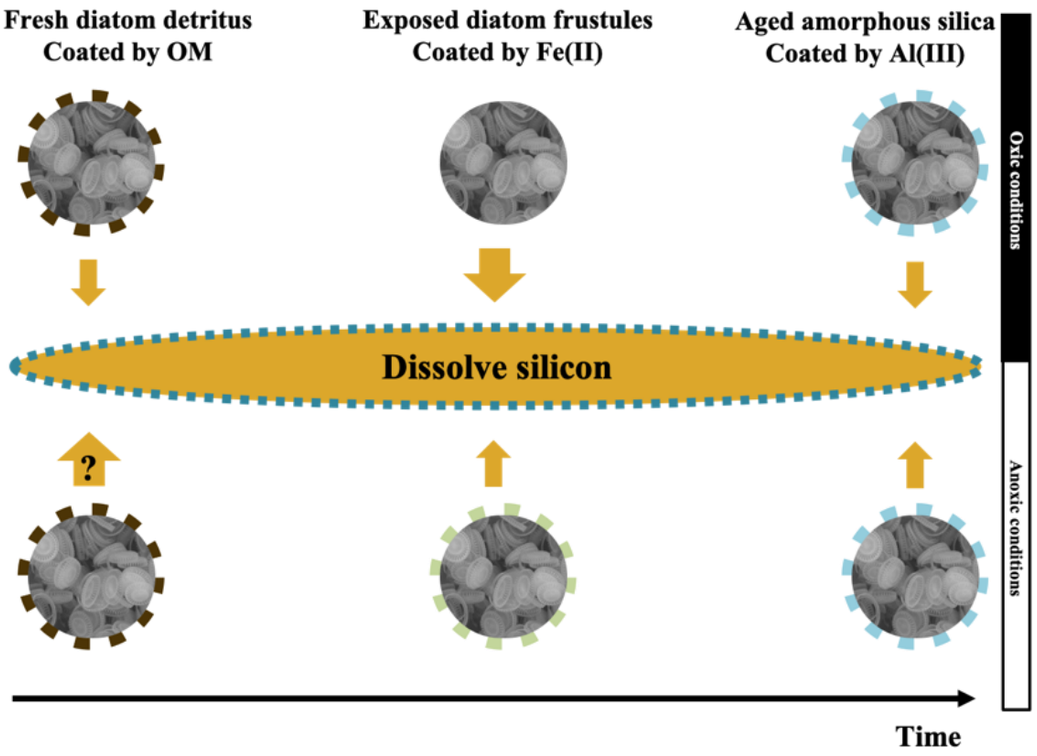

Figure 6.1. Three species of amorphous silica (ASi) in surface sediments and their relative dissolution kinetics under different oxygen conditions. These three ASi materials represent ASi species under end-member conditions. Fresh diatom detritus comprises dead diatoms settling through the water column: they are characterized by having an organic matter matrix coating and are typically found in shallow fresh waters with recent diatom blooms. Exposed diatom frustules are diatom detritus after the disappearance of the organic matrix coatings and exposed to adsorbates, such as Fe(II) under anoxic conditions. Aged ASi represents ASi imported from external sources and can be terrestrial phytoliths and diatom frustules transported by surface runoff to streams and lakes.

6.2.2.2 Microbial Fe(II) oxidation and its role in DSi immobilization

The oxidative precipitation of Fe(II) appears to play a smaller role in the real-world immobilization of DSi than may be deduced from simple batch reaction systems (Chapter 4). However, care needs to be taken when extrapolating this conclusion to complex natural sediments. On one hand, ternary complexes with humics and Fe(III) oxyhydroxides may form in natural sediments (Gerke, 1993; Hermann and Gerke, 1992), which can also contribute to the redox-dependent behavior of internal DSi loading. The formation of ternary complexes has been recognized to enhance the adsorption of P to humic substances. Mortimer (1941) proposed that the dissolution of the adsorbent complex, ferric-silico-humate, may lead to a rise in DSi concentration under anoxic conditions. However, the role of ternary complexes on the immobilization of DSi has not been identified directly. Furthermore, microorganisms affect not only the degradation of organic matter coating of ASi, but also the oxidation and reduction mechanisms of Fe (Davison, 1993). For example, Fe(III) oxyhydroxides produced by the oxidation of Fe(II) mediated by Fe-oxidizing bacteria exhibit smaller particle sizes than those obtained via abiotic oxidation (Chatellier et al., 2004), which affects the surface sites density for the adsorption of DSi. Additionally, the presence of DSi has also been shown to increase the oxidation rate of Fe(II) mediated by Fe-oxidizing bacteria (Gauger et al., 2016; Konhauser et al., 2007). Therefore, further studies are required to assess the roles of microbial Fe(II) oxidation on the immobilization of DSi in natural sediments.

6.2.2.3 Importance of other reactive particulate Si phases

The adsorption of Fe(II) blocks reactive surface sites and inhibits ASi dissolution (Chapter 3). However, the inhibition reaches a maximum with increasing adsorbed Fe(II), leading to the conclusion that different surface groups react differently to the binding of multi-valent cations. Overall, trace amounts of Fe(II) adsorption can lead to a significant decrease of the dissolution rate constant of ASi. Although the solubility of dissolved Al is very low (Lydersen, 1990), the adsorption of traces amounts of Al may similarly inhibit the dissolution of ASi drastically. Previous studies have shown that the dissolution rate constant of ASi decreases with increasing Al incorporated in silica (Van Cappellen et al., 2002), while the solubility of ASi also decreases with increasing Al concentration (Dove, 1995; Lewin, 1961). The decreased solubility could be due to the inhibition effects of Al adsorption or surface precipitation during ASi dissolution resulting in the precipitation of an aluminosilicate phase (Houston et al., 2008); either way, Si is immobilized. The interaction between Al and Si does not in itself induce a redox-dependent behavior of DSi. However, Fe(II) and Al exist in porewater simultaneously. Therefore, the presence of Al may compete with Fe(II) for surface sites of ASi , indirectly causing redox conditions to affect ASi dissolution kinetics.

In addition, DSi immobilized by Fe(III) oxyhydroxides in oxic surficial sediments will ultimately be buried into deeper, anoxic layers. The ensuing reductive dissolution of Fe(III) oxyhydroxides leads to the release of DSi whose transport into the overlying water is limited by relatively slow diffusion. The accumulation of DSi near the oxic-anoxic transition can lead to the precipitation of aluminosilicate minerals, especially when the Al^{3+} concentration is high (Beardmore et al., 2016;

Exley and Birchall, 1993; Gallup, 1997; Gallup, 1998; Iler, 1973), which could be a terminal sink of DSi (as proposed in the scenario on the left in Figure 6.2). There are some indications that Si released from Fe(III) oxyhydroxides under anoxic conditions may be resorbed by Al oxides (Nteziryayo and Danielsson, 2018a; Siipola et al., 2016). The roles of Al in controlling DSi mobility during the redox cycling of Fe therefore still represents a knowledge gap.

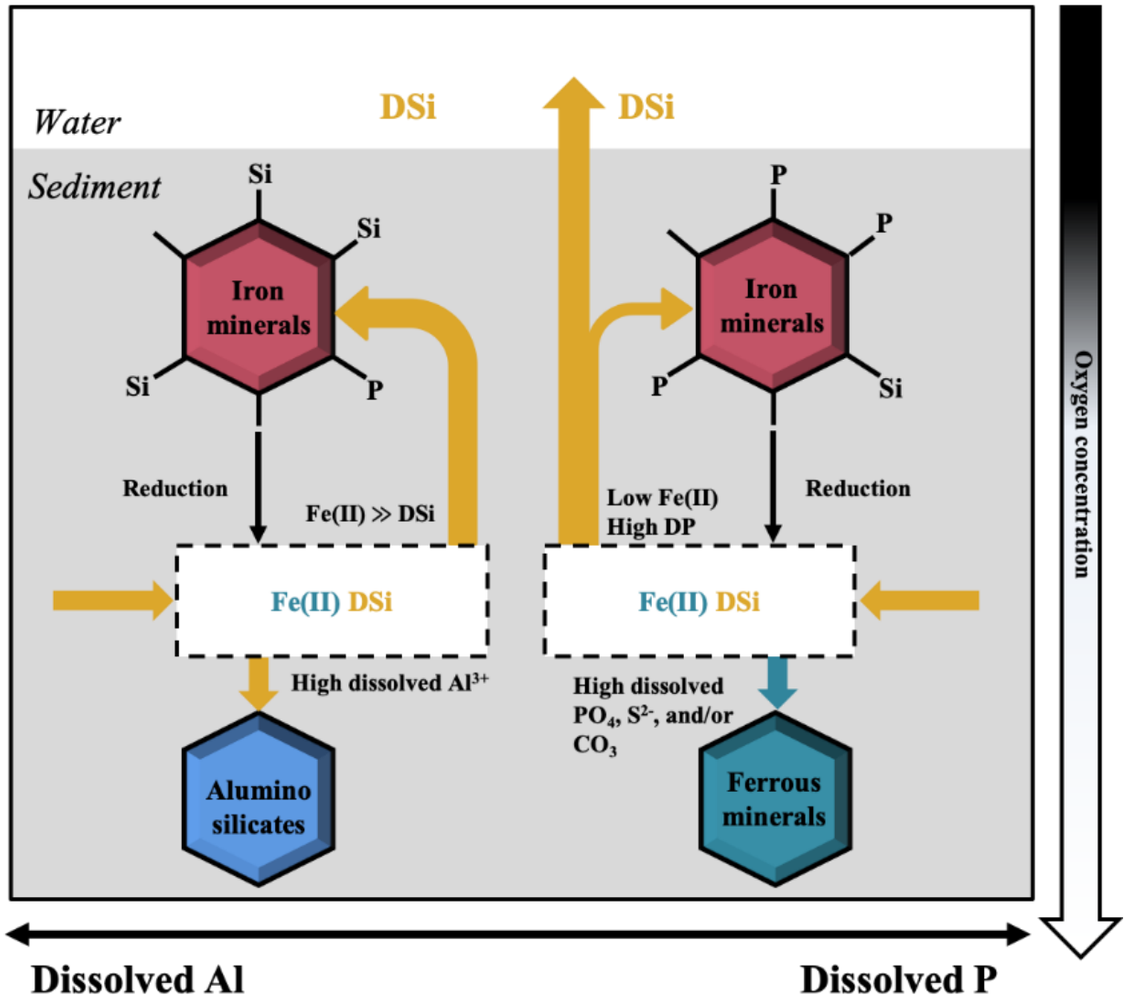

Figure 6.2. Suggested effects of iron minerals on the immobilization of DSi. Substantial retention of DSi occurs only if the Fe concentration, including solid iron minerals and aqueous Fe(II), are high and the concentrations of competing anions, notably DP, are low (left scenario). The ability of iron minerals to immobilize DSi is minor when the concentrations of DP and/or other anions that outcompete DSi for sorption sites and/or precipitate with Fe(II) are high (right scenario).

6.2.2.4 Bioturbation-induced disturbance to transport may be important to consider

The transport of participating solutes affects the reaction kinetics of DSi immobilization in column systems (Chapter 4 and 5). In this study, only diffusion and advection were considered. Benthic biota may also substantially influence internal DSi loading. Specifically, the transport of solute and particulate in sediments will be affected by bioirrigation and bioconveying, which are collectively referred to as bioturbation (Matisoff et al., 1985; Orihel et al., 2017; Parsons et al., 2017). Bottom feeding fish such as carp can disturb surface sediment, leading to the release of DSi to porewater and thus increasing DSi efflux to the overlying water. Tube-dwelling organisms, including invertebrates and vertebrates increase the complexity of oxygen conditions in sediments (Aller, 1994). In addition, oxygen conditions of bottom water affect the activity of benthic biota. The net effects of bioturbation on internal DSi loading remains largely unknown.

References

Aduwusu, K., Wilcox, W.R., 1991. Sorption and desorption isotherms for silicate on gibbsite. Journal of Colloid and Interface Science, 143(1): 139-145.

Afonso, M.D., Stumm, W., 1992. Reductive dissolution of iron(III) (hydr)oxides by hydrogen sulfide. Langmuir, 8(6): 1671-1675.

Alfredsson, H., Clymans, W., Hugelius, G., Kuhry, P., Conley, D.J., 2016. Estimated storage of amorphous silica in soils of the circum-Arctic tundra region. Global Biogeochemical Cycles, 30(3): 479-500.

Aller, R.C., 1994. Bioturbation and remineralization of sedimentary organic matter: effects of redox oscillation. Chemical Geology, 114(3-4): 331-345.

Anderson, D.M., Glibert, P.M., Burkholder, J.M., 2002. Harmful algal blooms and eutrophication: Nutrient sources, composition, and consequences. Estuaries, 25(4B): 704-726.

Armistead, C.G., Tyler, A.J., Hambleton, F.H., Mitchell, S.A., Hockey, J.A., 1969. Surface Hydroxylation of Silica. Journal of Physical Chemistry, 73(11): 3947-+.

Aston, S.R. (Ed.), 1983. Silicon geochemistry and biogeochemistry. Academic Press, New York.

Barker, P., Fontes, J.C., Gasse, F., Druart, J.C., 1994a. Experimental dissolution of diatom silica in concentrated salt -Solutions and implications for paleoenvironmental reconstruction. Limnology and Oceanography, 39(1): 99-110.

Barker, P., Fontes, J.C., Gasse, F., Druart, J.C., 1994b. Experimental dissolution of diatoms silica in concentrated salt-solutions and implication for paleoenvironmental removal reconstruction. Limnology and Oceanography, 39(1): 99-110.

Barron, V., Torrent, J., 2013. Iron, manganese and aluminium oxides and oxyhydroxides. In: Nieto, F., Livi, K.J.T. (Eds.), Minerals at the Nanoscale. European Mineralogical Union Notes in Mineralogy, pp. 297-336.

Bauerfeind, E., von Bodungen, B., 2006. Underestimation of biogenic silicon flux due to dissolution in sediment trap samples. Marine Geology, 226(3-4): 297-306.

Beardmore, J., Lopez, X., Mujika, J.I., Exley, C., 2016. What is the mechanism of formation of hydroxyaluminosilicates? Scientific Reports, 6.

Beer, J., Blodau, C., 2007. Transport and thermodynamics constrain belowground carbon turnover in a northern peatland. Geochimica et Cosmochimica Acta, 71(12): 2989-3002.

Berner, R.A., Lasaga, A.C., Garrels, R.M., 1983. The carbonate-silicate geochemical cycle and its effect on atmospheric carbon-dioxide over the past 100 million years. American Journal of Science, 283(7): 641-683.

Bidle, K.D., Azam, F., 1999. Accelerated dissolution of diatom silica by marine bacterial assemblages. Nature, 397(6719): 508-512.

Bidle, K.D., Azam, F., 2001. Bacterial control of silicon regeneration from diatom detritus: Significance of bacterial ectohydrolases and species identity. Limnology and Oceanography, 46(7): 1606-1623.

Bien, G.S., Contois, D.E., Thomas, W.H., 1958. The removal of soluble silica from fresh water entering the sea. Geochimica Et Cosmochimica Acta, 14(1-2): 35-54.

Boltovskoy, D., 1998. Classification and distribution of South Atlantic Recent polycystine Radiolaria. Palaeontologia Electronica, 1(2): 116.

Bootsma, H.A., Hecky, R.E., Johnson, T.C., Kling, H.J., Mwita, J., 2003. Inputs, outputs, and internal cycling of silica in a large, tropical lake. Journal of Great Lakes Research, 29: 121-138.

Brzezinski, M.A., 1985. The Si:C:N ratio of marine diatoms: Interspecific variability and the effect of some environmental variables Journal of Phycology, 21(3): 347-357.

Buamah, R., Petrusevski, B., Schippers, J.C., 2009. Oxidation of adsorbed ferrous iron: kinetics and influence of process conditions. Water Science and Technology, 60(9): 2353-2363.

Chatellier, X. et al., 2004. Characterization of iron-oxides formed by oxidation of ferrous ions in the presence of various bacterial species and inorganic ligands. Geomicrobiology Journal, 21(2): 99-112.

Chow-Fraser, P. et al., 1998. Long-term response of the biotic community to fluctuating water levels and changes in water quality in Cootes Paradise Marsh, a degraded coastal wetland of Lake Ontario. Wetlands Ecology and Management, 6: 19-42.

Christoffersen, J., Christoffersen, M.R., 1981. Kinetics of dissolution of calcium hydroxyapatite. 4. The effect of some biologically important inhibitors Journal of Crystal Growth, 53(1): 42-54.

Christoffersen, J., Christoffersen, M.R., 1984. Kinetics of dissolution of calcium hydroxyapatite. Faraday Discussions, 77: 235-242.

Cismasu, A.C., Michel, F.M., Tcaciuc, A.P., Brown, G.E., 2014. Properties of impurity-bearing ferrihydrite III. Effects of Si on the structure of 2-line ferrihydrite. Geochimica Et Cosmochimica Acta, 133: 168-185.

Collins, C.D., 1988. Interaction of Nitrogen/Phosphorus and Silica/Phosphorus Ratios in Determining Phytoplankton Species Composition and Abundance in Lake George, New York. Lake and Reservoir Management, 4(2): 261-269.

Conley, D., Schelske, C.L., 2002. Biogenic silica. In: Smol, J.P., Birks, H.J.B., Last, W.M. (Eds.), Tracking Environmental Change Using Lake Sediments. Kluwer Academic Publishers, New York, Boston, Dordrecht, London, Moscow, pp. 281-294.

Conley, D.J., 2002. Terrestrial ecosystems and the global biogeochemical silica cycle. Global Biogeochemical Cycles, 16(4).

Conley, D.J. et al., 2008. Past, present and future state of the biogeochemical Si cycle in the Baltic Sea. Journal of Marine Systems, 73(3-4): 338-346.

Conley, D.J., Schelske, C.L., Stoermer, E.F., 1993. Modification of the biogeochemical cycle of silica with eutrophication. Marine Ecology Progress Series, 101(1-2): 179-192.

Cornell, R.M., Giovanoli, R., Schindler, P.W., 1987. Effect of silicate species on the transformation of ferrihydrite into goethite and hematite in alkaline media. Clays and Clay Minerals, 35(1): 21-28.

Correll, D.L., 1998. The role of phosphorus in the eutrophication of receiving waters: A review. Journal of Environmental Quality, 27(2): 261-266.

Costine, A., Thurgate, S., 2007. Iron adsorption on SiO2/Si(111). Surface and Interface Analysis, 39(8): 711-714.

Couture, R.-M., Shafei, B., Van Cappellen, P., Tessier, A., Gobeil, C., 2010. Non-Steady State Modeling of Arsenic Diagenesis in Lake Sediments. Environmental Science & Technology, 44(1): 197-203.

Couture, R.M., Fischer, R., Van Cappellen, P., Gobeil, C., 2016. Non-steady state diagenesis of organic and inorganic sulfur in lake sediments. Geochimica Et Cosmochimica Acta, 194: 15-33.

Daniel, T.C., Sharpley, A.N., Lemunyon, J.L., 1998. Agricultural phosphorus and eutrophication: A symposium overview. Journal of Environmental Quality, 27(2): 251-257.

Danielsson, A., 2014. Influence of hypoxia on silicate concentrations in the Baltic Proper (Baltic Sea). Boreal Environment Research, 19(4): 267-280.

Daval, D., Hellmann, R., Saldi, G.D., Wirth, R., Knauss, K.G., 2013. Linking nm-scale measurements of the anisotropy of silicate surface reactivity to macroscopic dissolution rate laws: New insights based on diopside. Geochimica et Cosmochimica Acta, 107: 121-134.

Davis, C.C., 2000. Aqueous silica in the environment: Effects on iron hydroxide surface chemistry and implications for natural and engineered systems, Virginia Polytechnic Institute and State University.

Davis, C.C., Chen, H.W., Edwards, M., 2002. Modeling silica sorption to iron hydroxide. Environmental Science & Technology, 36(4): 582-587.

Davison, W., 1993. Iron and manganese in lakes Earth-Science Reviews, 34(2): 119-163.

Dittrich, M. et al., 2013. Phosphorus retention in a mesotrophic lake under transient loading conditions: Insights from a sediment phosphorus binding form study. Water Research, 47(3): 1433-1447.

Dixit, S., Van Cappellen, P., 2002. Surface chemistry and reactivity of biogenic silica. Geochimica Et Cosmochimica Acta, 66(14): 2559-2568.

Dixit, S., Van Cappellen, P., Van Bennekom, A.J., 2001. Processes controlling solubility of biogenic silica and pore water build-up of silicic acid in marine sediments. Marine Chemistry, 73(3-4): 333-352.

Dove, P.M., 1995. Kinetics and Thermodynamic Controls on Silica Reactivity in Weathering Environmnets. In: White, A.F., Brantley, S.L. (Eds.), Chemival Weathering Rates of Silica Minerals. Reviews in Minearalogy. BookCrafters, Inc., Chelsea, Michigan, U.S.A, pp. 235-282.

Dove, P.M., Crerar, D.A., 1990. Kinetics of quartz dissolution in electrolyte-solution using hydrothermal mixed flow reactor. Geochimica Et Cosmochimica Acta, 54(4): 955-969.

Dove, P.M., Elston, S.F., 1992. Dissolution kinetics of quartz in sodium chloride solution: Analysis of existing data and a rate model for 25 °C. Geochimica Et Cosmochimica Acta, 56(12): 4147-4156.

Dove, P.M., Han, N., Wallace, A.F., De Yoreo, J.J., 2008. Kinetics of amorphous silica dissolution and the paradox of the silica polymorphs. Proceedings of the National Academy of Sciences of the United States of America, 105(29): 9903-9908.

Dove, P.M., Han, N.Z., De Yoreo, J.J., 2005. Mechanisms of classical crystal growth theory explain quartz and silicate dissolution behavior. Proceedings of the National Academy of Sciences of the United States of America, 102(43): 15357-15362.

Dove, P.M., Nix, C.J., 1997. The influence of the alkaline earth cations, magnesium, calcium, and barium on the dissolution kinetics of quartz. Geochimica Et Cosmochimica Acta, 61(16): 3329-3340.

Duan, S.W., Kaushal, S.S., 2013. Warming increases carbon and nutrient fluxes from sediments in streams across land use. Biogeosciences, 10(2): 1193-1207.

Duerr, H.H., Meybeck, M., Hartmann, J., Laruelle, G.G., Roubeix, V., 2011. Global spatial distribution of natural riverine silica inputs to the coastal zone. Biogeosciences, 8(3): 597-620.

Dyer, L., Fawell, P.D., Newman, O.M.G., Richmond, W.R., 2010. Synthesis and characterisation of ferrihydrite/silica co-precipitates. Journal of Colloid and Interface Science, 348(1): 65-70.

Egge, J.K., Aksnes, D.L., 1992. Silicate as regulating nutrient in phytoplankton competition. Marine Ecology Progress Series, 83(2-3): 281-289.

Ehrlich, H., Demadis, K.D., Pokrovsky, O.S., Koutsoukos, P.G., 2010. Modern Views on Desilicification: Biosilica and Abiotic Silica Dissolution in Natural and Artificial Environments. Chemical Reviews, 110(8): 4656-4689.

Ekeroth, N., 2015. Benthic fluxes of biogenic elements in the Baltic Sea: Influence of oxygen and macrofauna. Doctoral thesis Thesis, Stockholm University, Stockholm.

Ekeroth, N., Kononets, M., Walve, J., Blomqvist, S., Hall, P.O.J., 2016. Effects of oxygen on recycling of biogenic elements from sediments of a stratified coastal Baltic Sea basin. Journal of Marine Systems, 154: 206-219.

Elvin, D., 1971. Growth rates of siliceous spicules of fresh water sponge Ephydatia-muelleri (Lieberkuhn). Transactions of the American Microscopical Society, 90(2): 219-&.

Evonik Industries AG, 2015. Basic Characteristics and Applications of AEROSIL: AEROSIL-Fumed Silica.

Exley, C., 1998. Silicon in life: A bioinorganic solution to bioorganic essentiality. Journal of Inorganic Biochemistry, 69(3): 139-144.

Exley, C., Birchall, J.D., 1993. A mechanism of hydroxyaluminosilicate formation. Polyhedron, 12(9): 1007-1017.

Falaize, S., Radin, S., Ducheyne, P., 1999. In vitro behavior of silica-based xerogels intended as controlled release carriers. Journal of the American Ceramic Society, 82(4): 969-976.

Farooq, M.A., Dietz, K.J., 2015. Silicon as Versatile Player in Plant and Human Biology: Overlooked and Poorly Understood. Frontiers in Plant Science, 6.

Feitknecht, W., Schindler, P., 1963. Solubility constants of metal oxides, metal hydrox- ides and metal hydroxide salts in aqueous solution:, Pure and Applied Chemistry, pp. 125-206.

Filippelli, G.M., 2008. The global phosphorus cycle: Past, present, and future. Elements, 4(2): 89-95.

Finkel, Z.V. et al., 2010. Phytoplankton in a changing world: cell size and elemental stoichiometry. Journal of Plankton Research, 32(1): 119-137.

Fraysse, F., Pokrovsky, O.S., Schott, J., Meunier, J.D., 2006. Surface properties, solubility and dissolution kinetics of bamboo phytoliths. Geochimica Et Cosmochimica Acta, 70(8): 1939-1951.

Fraysse, F., Pokrovsky, O.S., Schott, J., Meunier, J.D., 2009. Surface chemistry and reactivity of plant phytoliths in aqueous solutions. Chemical Geology, 258(3-4): 197-206.

Frings, P.J. et al., 2014. Lack of steady-state in the global biogeochemical Si cycle: emerging evidence from lake Si sequestration. Biogeochemistry, 117(2-3): 255-277.

Gächter, R., Mülle, B., 2003. Why the phosphorus retention of lakes does not necessarily depend on the oxygen supply to their sediment surface. Limnology and Oceanography, 48(2): 929-933.

Gachter, R., Muller, B., 2003. Why the phosphorus retention of lakes does not necessarily depend on the oxygen supply to their sediment surface. Limnology and Oceanography, 48(2): 929-933.

Gallup, D.L., 1997. Aluminum silicate scale formation and inhibition: Scale characterization and laboratory experiments. Geothermics, 26(4): 483-499.

Gallup, D.L., 1998. Aluminum silicate scale formation and inhibition (2): Scale solubilities and laboratory and field inhibition tests. Geothermics, 27(4): 485-501.

Gao, X., Root, R.A., Farrell, J., Ela, W., Chorover, J., 2013. Effect of silicic acid on arsenate and arsenite retention mechanisms on 6-L ferrihydrite: A spectroscopic and batch adsorption approach. Applied Geochemistry, 38: 110-120.

Garnier, J., Beusen, A., Thieu, V., Billen, G., Bouwman, L., 2010. N:P:Si nutrient export ratios and ecological consequences in coastal seas evaluated by the ICEP approach. Global Biogeochemical Cycles, 24.

Gauger, T. et al., 2016. Influence of organics and silica on Fe(II) oxidation rates and cell-mineral aggregate formation by the green-sulfur Fe(II)-oxidizing bacterium Chlorobium ferrooxidans KoFox - Implications for Fe(II) oxidation in ancient oceans. Earth and Planetary Science Letters, 443: 81-89.

Geelhoed, J.S., Hiemstra, T., Van Riemsdijk, W.H., 1997. Phosphate and sulfate adsorption on goethite: Single anion and competitive adsorption. Geochimica Et Cosmochimica Acta, 61(12): 2389-2396.

Gehin, A. et al., 2007. Reversible surface-sorption-induced electron-transfer oxidation of Fe(II) at reactive sites on a synthetic clay mineral. Geochimica Et Cosmochimica Acta, 71(4): 863-876.

Gehlen, M., Van Raaphorst, W., 2002. The role of adsorption-desorption surface reactions in controlling interstitial Si(OH)(4) concentrations and enhancing Si(OH)(4) turn-over in shallow shelf seas. Continental Shelf Research, 22(10): 1529-1547.

Gomez, J.A.M., de Resende, V.G., Antonissen, J., De Grave, E., 2011. Characterization of the effects of silicon on the formation of goethite. Corrosion Science, 53(5): 1756-1761.

Greenwood, J.E., Truesdale, V.W., Rendell, A.R., 2001. Biogenic silica dissolution in seawater - in vitro chemical kinetics. Progress in Oceanography, 48(1): 1-23.

Grybos, M., Davranche, M., Gruau, G., Petitjean, P., Pedrot, M., 2009. Increasing pH drives organic matter solubilization from wetland soils under reducing conditions. Geoderma, 154(1-2): 13-19.

Gustafsson, J., 2000. Visual MINTEQ Ver. 3.1.

Hansen, H.C.B., Rabenlange, B., Raulundrasmussen, K., Borggaard, O.K., 1994. Monosilicate adsorption by ferrihydrite and goethite at pH 3-6 Soil Science, 158(1): 40-46.

Hanwell, M.D. et al., 2012. Avogadro: an advanced semantic chemical editor, visualization, and analysis platform. Journal of cheminformatics, 4(1): 17.

Harrison, J.A., Frings, P.J., Beusen, A.H.W., Conley, D.J., McCrackin, M.L., 2012. Global importance, patterns, and controls of dissolved silica retention in lakes and reservoirs. Global Biogeochemical Cycles, 26.

Hartikainen, H., Pitkanen, M., Kairesalo, T., Tuominen, L., 1996. Co-occurrence and potential chemical competition of phosphorus and silicon in lake sediment. Water Research, 30(10): 2472-2478.

Hiemstra, T., 2013. Surface and mineral structure of ferrihydrite. Geochimica Et Cosmochimica Acta, 105: 316-325.

Hiemstra, T., Barnett, M.O., Van Riemsdijk, W.H., 2007. Interaction of silicic acid with goethite. Journal of Colloid and Interface Science, 310(1): 8-17.

Hiemstra, T., Mendez, J.C., Li, J., 2019. Evolution of the reactive surface area of ferrihydrite: time, pH, and temperature dependency of growth by Ostwald ripening. Environmental Science: Nano, 6(3): 820-833.

Hiemstra, T., Van Riemsdijk, W.H., 1990. Multiple activated complex dissolution of metal (hydr) oxides - A thermodynamic approach applied to quartz. Journal of Colloid and Interface Science, 136(1): 132-150.

Hingston, F.J., Raupach, M., 1967. The reaction between monosilicic acid and aluminium hydroxide. I. Kinetics of adsorption of silicic acid by aluminium hydroxide. Australian Journal of Soil Research, 5(2): 295-309.

Hoelker, F. et al., 2015. Tube-dwelling invertebrates: tiny ecosystem engineers have large effects in lake ecosystems. Ecological Monographs, 85(3): 333-351.

Holstein, J.M., Hensen, C., 2010. Microbial mediation of benthic biogenic silica dissolution. Geo-Marine Letters, 30(5): 477-492.

Houston, J.R., Herberg, J.L., Maxwell, R.S., Carroll, S.A., 2008. Association of dissolved aluminum with silica: Connecting molecular structure to surface reactivity using NMR. Geochimica Et Cosmochimica Acta, 72(14): 3326-3337.

Hubbard, M.L., Riley, J.P., 1984. Kinetic studies of the rate of dissolution of silica and diatom tests in sea water. Journal of the Oceanographical Society of Japan, 40: 148-154.

Humborg, C. et al., 2000. Silicon retention in river basins: Far-reaching effects on biogeochemistry and aquatic food webs in coastal marine environments. Ambio, 29(1): 45-50.

Hurd, D.C., 1972. Factors affecting solution rate of biogenic opal in seawater. Earth and Planetary Science Letters, 15(4): 411-&.

Hurd, D.C., 1973. Interactions of biogenic opal, sediment and seawater in central equatorial Pacific. Geochimica Et Cosmochimica Acta, 37(10): 2257-&.

Hyacinthe, C., Van Cappellen, P., 2004. An authigenic iron phosphate phase in estuarine sediments: composition, formation and chemical reactivity. Marine Chemistry, 91(1-4): 227-251.

Icenhower, J.P., Dove, P.M., 2000. The dissolution kinetics of amorphous silica into sodium chloride solutions: Effects of temperature and ionic strength. Geochimica Et Cosmochimica Acta, 64(24): 4193-4203.

Iler, R.K., 1973. Effect of adsorbed alumina on solubility of amorphous silica in water Journal of Colloid and Interface Science, 43(2): 399-408.

Iler, R.K., 1979a. Collidal Silica-Concentrated Sols, The chemistry of Silica John Wiley & Sons, USA, pp. P312-439.

Iler, R.K., 1979b. The Occurrence, Dissolution, and Deposition of Silica, The chemistry of Silica John Wiley & Sons, USA, pp. P3-104.

Ingall, E.D. et al., 2013. Role of biogenic silica in the removal of iron from the Antarctic seas. Nature Communications, 4.

Ittekkot, V., Unger, D., Humborg, C., Tac An, N.T. (Eds.), 2006. The Silicon Cycle: Human Perturbations and Impacts on Aquatic Systems. Scientific Committee on Problems of the Environment (SCOPE) Series (Book 66). Island Press, Washington. DC, 296 pp.

Jensen, D.L., Boddum, J.K., Tjell, J.C., Christensen, T.H., 2002. The solubility of rhodochrosite (MnCO3) and siderite (FeCO3) in anaerobic aquatic environments. Applied geochemistry, 17(4): 503-511.

Jensen, H.S., Kristensen, P., Jeppesen, E., Skytthe, A., 1992. Iron:phosphorus ratio in surface sediment as a indicator of phosphate release from aerobic sediment in shallow lakes. Hydrobiologia, 235: 731-743.

Johnson, T.C., Eisenreich, S.J., 1979. Silica in Lake Superior-mass balence consideration and model for dynamic-response to eutrophication. Geochimica Et Cosmochimica Acta, 43(1): 77-91.

Jones, A.M., Collins, R.N., Rose, J., Waite, T.D., 2009. The effect of silica and natural organic matter on the Fe(II)-catalysed transformation and reactivity of Fe(III) minerals. Geochimica Et Cosmochimica Acta, 73(15): 4409-4422.

Joshi, S.R. et al., 2015. Organic Matter Remineralization Predominates Phosphorus Cycling in the Mid-Bay Sediments in the Chesapeake Bay. Environmental Science & Technology, 49(10): 5887-5896.

Jourabchi, P., Regnier, P., Van Cappellen, P., 2005. Quantitative interpretation of pH distributions in aquatic sediments: A reaction-transport modeling approach. Geochimica Et Cosmochimica Acta, 69(10): A173-A173.

Kaegi, R., Voegelin, A., Folini, D., Hug, S.J., 2010. Effect of phosphate, silicate, and Ca on the morphology, structure and elemental composition of Fe(III)-precipitates formed in aerated Fe(II) and As(III) containing water. Geochimica Et Cosmochimica Acta, 74(20): 5798-5816.

Kamatani, A., 1982. Dissolution rates of silica from diatoms decomposing at various temperatures Marine Biology, 68(1): 91-96.

Kamatani, A., Riley, J.P., 1979. Rate of dissolution of diatom silica walls in seawater Marine Biology, 55(1): 29-35.

Kamatani, A., Riley, J.P., Skirrow, G., 1980. The dissolution of opaline silica of diatom tests in sea water. Journal of the Oceanographical Society of Japan, 36: 8.

Kandori, K., Uchida, S., Kataoka, S., Ishikawa, T., 1992. Effect of silicate and phosphate ions on the formation of ferric oxide hydroxide particles. Journal of Materials Science, 27(3): 719-728.

Kanematsu, M., Waychunas, G.A., Boily, J.F., 2018. Silicate Binding and Precipitation on Iron Oxyhydroxides. Environmental Science & Technology, 52(4): 1827-1833.

Katsev, S., Tsandev, I., L'Heureux, I., Rancourt, D.G., 2006. Factors controlling long-term phosphorus efflux from lake sediments: Exploratory reactive-transport modeling. Chemical Geology, 234(1-2): 127-147.

King, D.W., 1998. Role of carbonate speciation on the oxidation rate of Fe(II) in aquatic systems. Environmental Science & Technology, 32(19): 2997-3003.

Kinsela, A.S. et al., 2016. Influence of Dissolved Silicate on Rates of Fe(II) Oxidation. Environmental Science & Technology, 50(21): 11663-11671.

Kolthoff, I.M., 1932. "Theory of coprecipitation" the formation and properties of crystalline precipitates. Journal of Physical Chemistry, 36(3): 860-881.

Konecny, R., 2001. Reactivity of hydroxyl radicals on hydroxylated quartz surface. 1. Cluster model calculations. Journal of Physical Chemistry B, 105(26): 6221-6226.

Konhauser, K.O. et al., 2007. Decoupling photochemical Fe(II) oxidation from shallow-water BIF deposition. Earth and Planetary Science Letters, 258(1-2): 87-100.

Koning, E. et al., 1997. Settling, dissolution and burial of biogenic silica in the sediments off Somalia (northwestern Indian Ocean). Deep-Sea Research Part Ii-Topical Studies in Oceanography, 44(6-7): 1341-1360.

Koning, E., Epping, E., Van Raaphorst, W., 2002. Determining biogenic silica in marine samples by tracking silicate and aluminium concentrations in alkaline leaching solutions. Aquatic Geochemistry, 8(1): 37-67.

Koning, E., Gehlen, M., Flank, A.M., Calas, G., Epping, E., 2007. Rapid post-mortem incorporation of aluminum in diatom frustules: Evidence from chemical and structural analyses. Marine Chemistry, 106(1-2): 208-222.

Kosmulski, M., 2000. Adsorption on silica from aqueous solution. In: Papirer, E. (Ed.), Adsorption on silica surfaces. Marcel Dekker, New York, pp. pp.399-523.

Kostka, J.E., Luther, G.W., 1994. Partitioning and speciation of solid-phase iron in salt-marsh sediments Geochimica Et Cosmochimica Acta, 58(7): 1701-1710.

Koutsopoulos, S., Dalas, E., 2000. Inhibition of hydroxyapatite formation in aqueous solutions by amino acids with hydrophobic side groups. Langmuir, 16(16): 6739-6744.

Kristiansen, S., Hoell, E.E., 2002. The importance of silicon for marine production. Hydrobiologia, 484(1-3): 21-31.

Kwan, W.P., Voelker, B.M., 2002. Decomposition of hydrogen peroxide and organic compounds in the presence of dissolved iron and ferrihydrite. Environmental Science & Technology, 36(7): 1467-1476.

Lagerstrom, G., 1959. Equilibrium studies of polyanions III. Silicate ions in NaClO4 medium. Acta Chemica Scandinavica, 13: 15.

Langmuir, D., 1997. Adsorption-desorption reactions. In: McConnin, R.E. (Ed.), Aqueous Environmental Geochemistry. Prentice-Hall. Inc., New Jersey, pp. pp. 343–402.

LaRowe, D.E., Van Cappellen, P., 2011. Degradation of natural organic matter: a thermodynamic analysis. Geochimica et Cosmochimica Acta, 75(8): 2030-2042.

Laruelle, G.G. et al., 2009. Anthropogenic perturbations of the silicon cycle at the global scale: Key role of the land-ocean transition. Global Biogeochemical Cycles, 23.

Lasaga, A.C., 1995. Fundamental Approaches in Describing Mineral Dissolution and Precipitation Rates. In: White, A.F., Brantley, S.L. (Eds.), Chemival Weathering Rates of Silica Minerals. Reviews in Mineralogy. BookCrafters, Inc., Chelsea, Michigan, U.S.A, pp. 23-81.

Lee, G.F., 1973. Role of phosphorus in eutrophication and diffuse source control Water Research, 7(1-2): 111-128.

Lehtimaki, M., Sinkko, H., Tallberg, P., 2016. The role of oxygen conditions in the microbial dissolution of biogenic silica under brackish conditions. Biogeochemistry, 129(3): 355-371.

Lewin, J.C., 1961. The dissolution of silica from diatom walls. Geochimica Et Cosmochimica Acta, 21(3-4): 182-198.

Li, L. et al., 2012. Modeling As(III) Oxidation and Removal with Iron Electrocoagulation in Groundwater. Environmental Science & Technology, 46(21): 12038-12045.

Li, M., Liu, J., Xu, Y., Qian, G., 2016. Phosphate adsorption on metal oxides and metal hydroxides: A comparative review. Environmental Reviews, 24(3): 319-332.

Lipps, J.H., 1993. Fossil prokaryotes and protists. Blackwell Scientific Publications, Boston.

Liu, C.H.C., Maciel, G.E., 1996. The fumed silica surface: A study by NMR. Journal of the American Chemical Society, 118(21): 5103-5119.

Lomas, M.W., Baer, S.E., Acton, S., Krause, J.W., 2019. Pumped Up by the Cold: Elemental Quotas and Stoichiometry of Cold-Water Diatoms. Frontiers in Marine Science, 6.

Loucaides, S., Behrends, T., Van Cappellen, P., 2010a. Reactivity of biogenic silica: Surface versus bulk charge density. Geochimica Et Cosmochimica Acta, 74(2): 517-530.

Loucaides, S., Koning, E., Van Cappellen, P., 2012a. Effect of pressure on silica solubility of diatom frustules in the oceans: Results from long-term laboratory and field incubations. Marine Chemistry, 136: 1-6.

Loucaides, S. et al., 2010b. Seawater-mediated interactions between diatomaceous silica and terrigenous sediments: Results from long-term incubation experiments. Chemical Geology, 270(1-4): 68-79.

Loucaides, S., Van Cappellen, P., Behrends, T., 2008. Dissolution of biogenic silica from land to ocean: Role of salinity and pH. Limnology and Oceanography, 53(4): 1614-1621.

Loucaides, S., Van Cappellen, P., Roubeix, V., Moriceau, B., Ragueneau, O., 2012b. Controls on the Recycling and Preservation of Biogenic Silica from Biomineralization to Burial. Silicon, 4(1): 7-22.

Lovley, D.R., 1997. Microbial Fe (III) reduction in subsurface environments. FEMS Microbiology Reviews, 20(3-4): 305-313.

Lutz, W., Taeschner, D., Kurzhals, R., Heidemann, D., Huebert, C., 2009. Characterization of Silica Gels by Si-29 MAS NMR and IR Spectroscopic Measurements. Zeitschrift Fur Anorganische Und Allgemeine Chemie, 635(13-14): 2191-2196.

Lydersen, E., 1990. The solubility and hydrolysis of aqueous aluminum hydroxides in dilute fresh waters at different tenpwratures Nordic Hydrology, 21(3): 195-204.

Maavara, T., 2017. Perturbations to nutrient and carbon cycles by river damming, University of Waterloo, UWSpace, 194 pp.

Maavara, T., Durr, H.H., Van Cappellen, P., 2014. Worldwide retention of nutrient silicon by river damming: From sparse data set to global estimate. Global Biogeochemical Cycles, 28(8): 842-855.

Makulla, A., Sommer, U., 1993. Relationships between resource ratios and phytoplankton species composition during spring in five north German lakes. Limnology and Oceanography, 38(4): 846-856.

Maldonado, M. et al., 2005. Siliceous sponges as a silicon sink: An overlooked aspect of benthopelagic coupling in the marine silicon cycle. Limnology and Oceanography, 50(3): 799-809.

Malviya, S. et al., 2016. Insights into global diatom distribution and diversity in the world's ocean. Proceedings of the National Academy of Sciences of the United States of America, 113(11): E1516-E1525.

Mao, Y.P., Pham, A.N., Rose, A.L., Waite, T.D., 2011. Influence of phosphate on the oxidation kinetics of nanomolar Fe(II) in aqueous solution at circumneutral pH. Geochimica Et Cosmochimica Acta, 75(16): 4601-4610.

Marchetti, A. et al., 2010. Iron and silicic acid effects on phytoplankton productivity, diversity, and chemical composition in the central equatorial Pacific Ocean. Limnology and Oceanography, 55(1): 11-29.

Markelov, I., 2019. Modelling Biogeochemical Cycles Across Scales: From Whole-Lake Phosphorus Dynamics to Microbial Reaction Systems. Doctorial thesis Thesis, University of Waterloo, UWSpace.

Markelov, I., Couture, R.M., Fischer, R., Haande, S., Van Cappellen, P., 2019. Coupling Water Column and Sediment Biogeochemical Dynamics: Modeling Internal Phosphorus Loading, Climate Change Responses, and Mitigation Measures in Lake Vansjø, Norway. Journal of Geophysical Research: Biogeosciences, 124(12): 3847-3866.

Marshall, H.G., 2009. Phytoplankton of the York River. Journal of Coastal Research(Special Issue 57): pp. 59 – 65.

Matisoff, G., Fisher, J.B., Matis, S., 1985. Effects of benthic macroinvertebrates on the exchange of solutes between sediments and fresh-water. Hydrobiologia, 122(1): 19-33.

Matisoff, G., Wang, X., 1998. Solute transport in sediments by freshwater infaunal bioirrigators. Limnology and Oceanography, 43(7): 1487-1499.

Matsuoka, A., 2017. Catalogue of living polycystine radiolarians in surface waters in the East China Sea around Sesoko Island, Okinawa Prefecture, Japan. Science reports of Niigata University. (Geology), 32: 57-90.

Mayer, L.M., Jorgensen, J., Schnitker, D., 1991. Enhancement of diatom frustule dissolution by iron oxides. Marine Geology, 99(1-2): 263-266.

Mayer, T.D., Jarrell, W.M., 2000. Phosphorus sorption during iron(II) oxidation in the presence of dissolved silica. Water Research, 34(16): 3949-3956.

McCartney, K. et al., 2014. Fine structure of silicoflagellate double skeletons. Marine Micropaleontology, 113: 10-19.

Millero, F.J., 1985. The effect of ionic interactions on the oxidation of metals in natural waters. Geochimica Et Cosmochimica Acta, 49(2): 547-553.

Milonjic, S.K., Cupic, S.D., Cerovic, L.S., 2006. Sorption of ferric and ferrous ions on silica. In: Uskokovic, D.P., Milonjic, S.K., Rakovic, D.I. (Eds.), Recent Developments in Advanced Materials and Processes. Materials Science Forum, pp. 67-71.

Mitra, A.K., Matthews, M.L., 1985a. Effect of pH and phosphate on the oxidation of iron in aqueous solution. International Journal of Pharmaceutics, 23(2): 185-193.

Mitra, A.K., Matthews, M.L., 1985b. Effects of pH and phosphate on the oxidation of iron in aquesous solution. International Journal of Pharmaceutics, 23(2): 185-193.

Moller, N., Christov, C., Weare, J., 2006. Thermodynamic model for predicting interactions of geothermal brines with hydrothermal aluminum silicate minerals, 32nd Workshop on

Geothermal Reservoir Engineering. Stanford University, Proceedings, , Stanford, California, pp. 8.

Morgan, B., Lahav, O., 2007. The effect of pH on the kinetics of spontaneous Fe(II) oxidation by O-2 in aqueous solution - basic principles and a simple heuristic description. Chemosphere, 68(11): 2080-2084.

Morris, R.C., Fletcher, A.B., 1987. Increased solubility of quartz following ferrous–ferric iron reactions. Nature, 330(6148): 558-561.

Mortimer, C.H., 1941. The exchange of dissolved substances between mud and water in lakes. Journal of Ecology, 29: 280-329.

Mortimer, C.H., 1942. The exchange of dissolved substances between mud and water in lakes. Journal of Ecology, 30: 147-201.

Mortlock, R.A. et al., 1991. Evidence for lower productivity in the Antarctic ocean during the last glaciation. Nature, 351(6323): 220-223.

Moser, K.A., Smol, J.P., MacDonald, G.M., Larsen, C.P.S., 2002. 19th century eutrophication of a remote boreal lake: a consequence of climate warming? Journal of Paleolimnology, 28(2): 269-281.

Muller, B. et al., 2005. Internal carbon and nutrient cycling in Lake Baikal: sedimentation, upwelling, and early diagenesis. Global and Planetary Change, 46(1-4): 101-124.

Nano, G.V., Strathmann, T.J., 2006. Ferrous iron sorption by hydrous metal oxides. Journal of Colloid and Interface Science, 297(2): 443-454.

Nelson, D.M., Tréguer, P., Brzezinski, M.A., Leynaert, A., Queguiner, B., 1995. Production and dissolution of biogenic silica in the ocean: Revised global estimates, comparison with regional data and relationship to biogenic sedimentation. Global Biogeochemical Cycles, 9(3): 359-372.

Nriagu, J.O., 1978. Dissolved silica in the pore waters of Lakes Ontario, Erie, and Superior sediments. Limnology and Oceanography, 23(1): 53-67.

Nriagu, J.O., Dell, C.I., 1974. Diagenetic Formation of lron Phosphates in Recent Lake Sediments. American Mineralogist, 59(9-10): 934-946.

Nteziryayo, L.-R., Danielsson, A., 2018a. Sediment DSi and DIP fluxes under changing oxygen availability in bottom waters. Boreal Environment Research, 23: 159-174.

Nteziryayo, L.R., Danielsson, A., 2018b. Sediment DSi and DIP fluxes under changing oxygen availability in bottom waters. Boreal Environment Research, 23: 159-174.

O'Connell, D. et al., 2020. Changes in sedimentary phosphorus burial following artificial eutrophication of Lake 227, Experimental Lakes Area, Ontario, Canada. Journal of Geophysical Research: Biogeosciences: e2020JG005713.

Oconnor, T.L., Greenberg, S.A., 1958. The kinetics for the solution of silica in aqueous solutions Journal of Physical Chemistry, 62(10): 1195-1203.

Officer, C.B., Ryther, J.H., 1980. The possible importance of silicon in marine eutrophication. Marine Ecology Progress Series, 3(1): 83-91.

Ohlendorf, C., Sturm, M., 2008. A modified method for biogenic silica determination. Journal of Paleolimnology, 39(1): 137-142.

Orihel, D.M. et al., 2017. Internal phosphorus loading in Canadian fresh waters: a critical review and data analysis. Canadian Journal of Fisheries and Aquatic Sciences, 74(12): 2005-2029.

Osthols, E., 1995. Thorium Sorption on Amorphous Silica. Geochimica Et Cosmochimica Acta, 59(7): 1235-1249.

Pallud, C., Van Cappellen, P., 2006. Kinetics of microbial sulfate reduction in estuarine sediments. Geochimica Et Cosmochimica Acta, 70(5): 1148-1162.

Parsons, C.T., Rezanezhad, F., O'Connell, D.W., Van Cappellen, P., 2017. Sediment phosphorus speciation and mobility under dynamic redox conditions. Biogeosciences, 14(14): 3585-3602.

Parsons, C.T., Rezanezhad, F., O' Connell, D. W., and Vappellen, P., 2017. Sediment phosphorus speciation and mobility under dynamic redox conditions. Biogeosciences, 14: 3585-3602.

Pham, A.N., Waite, T.D., 2008. Oxygenation of Fe(II) in natural waters revisited: Kinetic modeling approaches, rate constant estimation and the importance of various reaction pathways. Geochimica Et Cosmochimica Acta, 72(15): 3616-3630.

Pluen, A., Netti, P.A., Jain, R.K., Berk, D.A., 1999. Diffusion of macromolecules in agarose gels: Comparison of linear and globular configurations. Biophysical Journal, 77(1): 542-552.

Pradeep, K. et al., 2016. A study on variation in dissolved silica concentration in groundwater of hard rock aquifers in Southeast coast of India, 10th Curtin University Technology Science and Engineering International Conference. IOP Conference Series-Materials Science and Engineering.

Ragueneau, O., Conley, D., Leynaert, A., Longphuirt, S.N., Slomp, C.P., 2006. Role of Diatoms in Silicon Cycling and Coastal

Marine Food Webs. In: Ittekkot, V., Unger, D., Humborg, C., Tac An, N.T. (Eds.), The Silicon Cycle: Human Perturbations and Impacts on Aquatic Systems. Island Press, Washington. DC, pp. 162-197.

Ragueneau, O. et al., 2000. A review of the Si cycle in the modem ocean: recent progress and missing gaps in the application of biogenic opal as a paleoproductivity proxy. Global and Planetary Change, 26(4): 317-365.

Randsalu-Wendrup, L., Conley, D.J., Carstensen, J., Fritz, S.C., 2016. Paleolimnological records of regime shifts in lakes in response to climate change and anthropogenic activities. Journal of Paleolimnology, 56(1): 1-14.

Redfield, A.C., Ketchum, B.H., Richards, F.A., 1963. The Influence of Organisms on the Composition of the Sea Water. In: Hill, M.N. (Editor), The composition of seawater: Comparative and descriptive oceanography. The sea: ideas and observations on progress in the study of the seas. Interscience Publishers, New York, pp. 26-77.

Reynolds, C.S., 2006. The Ecology of Phytoplankton. Ecology, Biodiversity, and Conservation. Cambridge University Press, Cambridge.

Rickert, D., 2000. Dissolution kinetics of biogenic silica in marine environments, Berichte zur Polarforschung (Reports on Polar Research).

Rickert, D., Schluter, M., Wallmann, K., 2002. Dissolution kinetics of biogenic silica from the water column to the sediments. Geochimica Et Cosmochimica Acta, 66(3): 439-455.

Ridenour, C., 2017. Biogeochemical cycling of nutrient silicon in a human-impacted large lake nearshore environment (Hamilton Harbour Area of Concern, Lake Ontario, Canada), University of Waterloo, 121 pp.

Roberts, L.C. et al., 2004. Arsenic removal with iron(II) and iron(III) waters with high silicate and phosphate concentrations. Environmental Science & Technology, 38(1): 307-315.

Rocha, C., Galvao, H., Barbosa, A., 2002. Role of transient silicon limitation in the development of cyanobacteria blooms in the Guadiana estuary, south-western Iberia. Marine Ecology Progress Series, 228: 35-45.

Rzepa, G., Pieczara, G., Gawel, A., Tomczyk, A., Zalecki, R., 2016. The influence of silicate on transformation pathways of synthetic 2-line ferrihydrite. Journal of Thermal Analysis and Calorimetry, 125(1): 407-421.

S. Plettinck, L.C.a.R.W., 1994. Kinetics and mechanisms of dissolution of silica at room temperature and pressure. Mineralogical Magazine, 58A(2): 728-729.

Sabur, M.A., 2019. Interactions of Phosphate and Silicate with Iron oxides in Freshwater Environments. Doctoral thesis Thesis, University of Waterloo, UWSpace.

Sahai, N., Lee, Y.J., Xu, H.F., Ciardelli, M., Gaillard, J.F., 2007. Role of Fe(II) and phosphate in arsenic uptake by coprecipitation. Geochimica Et Cosmochimica Acta, 71(13): 3193-3210.

Sauer, D., Saccone, L., Conley, D.J., Herrmann, L., Sommer, M., 2006. Review of methodologies for extracting plant-available and amorphous Si from soils and aquatic sediments. Biogeochemistry, 80(1): 89-108.

Scharer, M. et al., 2009. Effect of redox conditions on phosphate exchangeability and iron forms in a soil amended with ferrous iron. European Journal of Soil Science, 60(3): 386-397.

Schelske, C.L., 1985. Biogeochemical silica mass balances in Lake Michigan and Lake Superior. Biogeochemistry, 1(3): 197-218.

Schelske, C.L., Stoermer, E.F., 1971. Eutrophication, silica depletion, and predicted changes in algal quality in lake michigan. Science, 173(3995): 423-&.

Schelske, C.L., Stoermer, E.F., Conley, D.J., Robbins, J.A., Glover, R.M., 1983. Early eutraphication in the lowest Great Lakes- New evidence from biogenic silica in sedements Science, 222(4621): 320-322.

Schenk, E.J., Walter, J.W.J., 1968. Chemical Interactions of Dissolved Silica With Iron (II) and (III). American Water Works Association, 60(2): 199-212.

Schindler, D.W., 1977. Evolution of phosphorus limitation in lakes. Science, 195(4275): 260-262.

Schoen, R., Roberson, C.E., 1970. Structures of aluminum hydroxide and geochemical implications. American Mineralogist, 55(1-2): 43-77.

Sibanda, H.M., Young, S.D., 1986. Competitive adsorption of humus acids and phosphate on goethite, gibbsite and two tropical soils Journal of Soil Science, 37(2): 197-204.

Siipola, V., Lehtimaki, M., Tallberg, P., 2016. The effects of anoxia on Si dynamics in sediments. Journal of Soils and Sediments, 16(1): 266-279.

Simpson, T.L., Volcani, B.E. (Eds.), 1981. Silicon and Silicious Structures in Biological Systems. Springer-Verlag, New York.

Smolders, E. et al., 2017. Internal Loading and Redox Cycling of Sediment Iron Explain Reactive Phosphorus Concentrations in Lowland Rivers. Environmental Science & Technology, 51(5): 2584-2592.

Sommer, U., 1989. Nutrient status and nutrient competition of phytoplankton in a shallow, hypertrophic lake Limnology and Oceanography, 34(7): 1162-1173.

Sondergaard, M., Jensen, J.P., Jeppesen, E., 2003. Role of sediment and internal loading of phosphorus in shallow lakes. Hydrobiologia, 506(1-3): 135-145.

Sondergaard, M. et al., 2007. Lake restoration: successes, failures and long-term effects. Journal of Applied Ecology, 44(6): 1095-1105.

Srithongouthai, S., Sonoyama, Y.I., Tada, K., Montani, S., 2003. The influence of environmental variability on silicate exchange rates between sediment and water in a shallow-water coastal ecosystem, the Seto Inland Sea, Japan. Marine Pollution Bulletin, 47(1-6): 10-17.

Stager, J.C., Johnson, T.C., 2000. A 12,400 C-14 yr offshore diatom record from east central Lake Victoria, East Africa. Journal of Paleolimnology, 23(4): 373-383.

Street-Perrott, F.A., Barker, P.A., 2008. Biogenic silica: a neglected component of the coupled global continental biogeochemical cycles of carbon and silicon. Earth Surface Processes and Landforms, 33(9): 1436-1457.

Struyf, E. et al., 2010. Historical land use change has lowered terrestrial silica mobilization. Nature Communications, 1.

Stumm, W., 1992. The Coordination Chemistry of the Hydrous Oxide-Water Interface, Chemistry of the Solid-Water Interface. John Wiley & Sons, Canada, pp. P 13-41.

Stumm, W., Huper, H., Champlin, R.T., 1967. Formation of polysilicates as determined by coagulation effects. Environmental Science & Technology, 1: 7.

Stumm, W., Morgan, J.J., 1996. Aqueous Chemistry: Chemical Equilibria and Rates in Natural Waters. Wiley-Inter-science, New York.

Sung, W., Morgan, J.J., 1980. Kinetics and product of ferrous iron oxygenation in aqueous systems. Environmental Science & Technology, 14(5): 561-568.

Swedlund, P.J., Hamid, R.D., Miskelly, G.M., 2010. Insights into H4SiO4 surface chemistry on ferrihydrite suspensions from ATR-IR, Diffuse Layer Modeling and the adsorption enhancing effects of carbonate. Journal of Colloid and Interface Science, 352(1): 149-157.

Takasaki, S., Parsiegla, K.I., Katz, J.L., 1994. Calcite growth and the inhibition effect of iron (III). Journal of Crystal Growth, 143(3-4): 261-268.

Tallberg, P., Lukkari, K., Raike, A., Lehtoranta, J., Leivuori, M., 2009. Applicability of a sequential P fractionation procedure to Si in sediment. Journal of Soils and Sediments, 9(6): 594-603.

Tamura, H., Goto, K., Nagayama, M., 1976. Effect of anions on the oxygenation of ferrous ion in neutral solutions. Journal of Inorganic & Nuclear Chemistry, 38(1): 113-117.

Testa, J.M. et al., 2013. Sediment flux modeling: Simulating nitrogen, phosphorus, and silica cycles. Estuarine Coastal and Shelf Science, 131: 245-263.

Thibault, P.J., Rancourt, D.G., Evans, R.J., Dutrizac, J.E., 2009. Mineralogical confirmation of a near-P:Fe=1:2 limiting stoichiometric ratio in colloidal P-bearing ferrihydrite-like hydrous ferric oxide. Geochimica Et Cosmochimica Acta, 73(2): 364-376.

Thomasen, S., Chow-Fraser, P., 2012. Detecting changes in ecosystem quality following long-term restoration efforts in Cootes Paradise Marsh. Ecological Indicators, 13(1): 82-92.

Thompson, A., Chadwick, O.A., Rancourt, D.G., Chorover, J., 2006. Iron-oxide crystallinity increases during soil redox oscillations. Geochimica Et Cosmochimica Acta, 70(7): 1710-1727.

Tonkin, J.W., Balistrieri, L.S., Murray, J.W., 2004. Modeling sorption of divalent metal cations on hydrous manganese oxide using the diffuse double layer model. Applied Geochemistry, 19(1): 29-53.

Tosca, N.J., Guggenheim, S., Pufahl, P.K., 2016. An authigenic origin for Precambrian greenalite: Implications for iron formation and the chemistry of ancient seawater. Geological Society of America Bulletin, 128(3-4): 511-530.

Tréguer, P. et al., 1995. The Silica Balance in the World Ocean: A Reestimate. Science, 268(5209): 375-379.

Tréguer, P.J., De La Rocha, C.L., 2013. The World Ocean Silica Cycle. In: Carlson, C.A., Giovannoni, S.J. (Eds.), Annual Review of Marine Science, Vol 5. Annual Review of Marine Science, pp. 477-501.

Triplett, L.D., 2008. Two Rivers, Two Lakes, Two Legacies: Anthropogenic alterations to silica cycling and heavy metal loading in Lake St. Croix and Lake Pepin, USA, University of Minnesota, Health & Environmental Research Online 111 pp.

Triplett, L.D., Engstrom, D.R., Conley, D.J., 2012. Changes in amorphous silica sequestration with eutrophication of riverine impoundments. Biogeochemistry, 108(1-3): 413-427.

Tuominen, L., Hartikainen, H., Kairesalo, T., Tallberg, P., 1998. Increased bioavailability of sediment phosphorus due to silicate enrichment. Water Research, 32(7): 2001-2008.

Turner, R.E., 2002. Element ratios and aquatic food webs. Estuaries, 25(4B): 694-703.

U.S. EPA., 1978. Method 370.1: Silica, Dissolved, Colorimetric.

U.S. EPA., 1994. Method 200.7: Determination of Metals and Trace Elements in Water and Wastes by Inductively Coupled Plasma-Atomic Emission Spectrometry. Revision 4.4. Cinicinnati, OH.

Uzarski, J.S., DiVito, M.D., Wertheim, J.A., Miller, W.M., 2017. Essential design considerations for the resazurin reduction assay to noninvasively quantify cell expansion within perfused extracellular matrix scaffolds. Biomaterials, 129: 163-175.

Van Bennekom, A.J., Buma, A.G.J., Nolting, R.F., 1991. Dissolved aluminium in the Weddell-Scotia Confluence and effect of Al on the dissolution kinetics of biogenic silica. Marine Chemistry, 35(1-4): 423-434.

Van Cappellen, P., Berner, R.A., 1991. Fluorapatite crystal growth from modified seawater solutions. Geochimica Et Cosmochimica Acta, 55(5): 1219-1234.

Van Cappellen, P., Dixit, S., Gallinari, M., Institut, O., 2004. Biogenic silica dissolution and the marine Si cycle: kinetics, surface chemistry and preservation, Biogeochemical Silicium Cycle: Elemental to Global Scale. Oceanis-Serie de Documents Oceanographiques, pp. 417-454.

Van Cappellen, P., Dixit, S., Van Beusekom, J., 2002. Biogenic silica dissolution in the oceans: Reconciling experimental and field-based dissolution rates. Global Biogeochemical Cycles, 16(4).

Van Cappellen, P., Qiu, L.Q., 1997a. Biogenic silica dissolution in sediments of the Southern Ocean .1. Solubility. Deep-Sea Research Part Ii-Topical Studies in Oceanography, 44(5): 1109-1128.

Van Cappellen, P., Qiu, L.Q., 1997b. Biogenic silica dissolution in sediments of the Southern Ocean .2. Kinetics. Deep-Sea Research Part Ii-Topical Studies in Oceanography, 44(5): 1129-1149.

van der Grift, B., Rozemeijer, J.C., Griffioen, J., Van der Velde, Y., 2014. Iron oxidation kinetics and phosphate immobilization along the flow-path from groundwater into surface water. Hydrology and Earth System Sciences, 18(11): 4687-4702.

Van der Molen, D.T., Boers, P.C.M., 1994. Influence of internal loading on phosphorus concentration in shallow lakes before and after reduction of the external loading. Hydrobiologia, 275: 379-389.

Vicente, J., Silbiger, N.J., Beckley, B.A., Raczkowski, C.W., Hill, R.T., 2016. Impact of high pCO(2) and warmer temperatures on the process of silica biomineralization in the sponge Mycale grandis. Ices Journal of Marine Science, 73(3): 704-714.

Villalobos, M., Trotz, M.A., Leckie, J.O., 2003. Variability in goethite surface site density: evidence from proton and carbonate sorption. Journal of Colloid and Interface Science, 268(2): 273-287.

Villnas, A., Norkko, J., Lukkari, K., Hewitt, J., Norkko, A., 2012. Consequences of Increasing Hypoxic Disturbance on Benthic Communities and Ecosystem Functioning. Plos One, 7(10).

Viollier, E., Inglett, P.W., Hunter, K., Roychoudhury, A.N., Van Cappellen, P., 2000. The ferrozine method revisited: Fe(II)/Fe(III) determination in natural waters. Applied Geochemistry, 15(6): 785-790.

Voegelin, A., Kaegi, R., Frommer, J., Vantelon, D., Hug, S.J., 2010. Effect of phosphate, silicate, and Ca on Fe(III)-precipitates formed in aerated Fe(II)- and As(III)-containing water

studied by X-ray absorption spectroscopy. Geochimica Et Cosmochimica Acta, 74(1): 164-186.

Volcani, B.E., 1981. Cell Wall Formation in Diatoms: Morphogenesis and Biochemistry. In: Simpson, T.L., Volcani, B.E. (Eds.), Silicon and Siliceous Structure in Biological systems. Springer-Verlag, New York, pp. 157-197.

Wang, X.M. et al., 2013a. Effect of Ferrihydrite Crystallite Size on Phosphate Adsorption Reactivity. Environmental Science & Technology, 47(18): 10322-10331.

Wang, Y.H. et al., 2013b. Mobile uranium(IV)-bearing colloids in a mining-impacted wetland. Nature Communications, 4.

Wang, Z., Giammar, D.E., 2013. Mass action expressions for bidentate adsorption in surface complexation modeling: Theory and practice. Environmental science & technology, 47(9): 3982-3996.

White, E.M., Vaughan, P.P., Zepp, R.G., 2003. Role of the photo-Fenton reaction in the production of hydroxyl radicals and photobleaching of colored dissolved organic matter in a coastal river of the southeastern United States. Aquatic Sciences, 65(4): 402-414.

White, P.A., Kalff, J., Rasmussen, J.B., Gasol, J.M., 1991. The effect of temperature and algal biomass on bacterial production and specific growth water and marine habitats. Microbial Ecology, 21(2): 99-118.

Wolthoorn, A., Temminghoff, E.J.M., Weng, L.P., Van Riemsdijk, W.H., 2004. Colloid formation in groundwater: effect of phosphate, manganese, silicate and dissolved organic matter on the dynamic heterogeneous oxidation of ferrous iron. Applied Geochemistry, 19(4): 611-622.

Xiao, Y.T., Lasaga, A.C., 1996. Ab initio quantum mechanical studies of the kinetics and mechanisms of quartz dissolution: OH- catalysis. Geochimica Et Cosmochimica Acta, 60(13): 2283-2295.

Yee, N., Shaw, S., Benning, L.G., Nguyen, T.H., 2006. The rate of ferrihydrite transformation to goethite via the Fe (II) pathway. American Mineralogist, 91(1): 92-96.

Yi, Z.Q., Xu, M.N., Di, X.X., Brynfolfsson, S., Fu, W.Q., 2017. Exploring Valuable Lipids in Diatoms. Frontiers in Marine Science, 4.

Zhang, J., Zhang, G.S., Liu, S.M., 2005. Dissolved silicate in coastal marine rainwaters: Comparison between the Yellow Sea and the East China Sea on the impact and potential link with primary production. Journal of Geophysical Research-Atmospheres, 110(D16).

Zhang, J.Z., Huang, X.L., 2007. Relative importance of solid-phase phosphorus and iron on the sorption behavior of sediments. Environmental Science & Technology, 41(8): 2789-2795.

Zhao, H.S., Stanforth, R., 2001. Competitive adsorption of phosphate and arsenate on goethite. Environmental Science & Technology, 35(24): 4753-4757.

Zhou, X.P., Chen, N.W., Yan, Z.H., Duan, S.W., 2016. Warming increases nutrient mobilization and gaseous nitrogen removal from sediments across cascade reservoirs. Environmental Pollution, 219: 490-500.

Zhuravlev, L.T., 2000. The surface chemistry of amorphous silica. Zhuravlev model. Colloids and Surfaces a-Physicochemical and Engineering Aspects, 173(1-3): 1-38.

Supplementary Information

Appendix A

Supplementary information for Chapter 2

Table A.1. The degree of undersaturation that was shown to be the boundary of fast and slow dissolution of amorphous silica in previous studies.

No.	Sample name	Description of samples	Temperature	Degree of undersaturation	References
1	Quartz	Fused quartz glass	150 ℃	0.48	Dove et al., 2008
	Synthetic silica	Synthetic silica glass		0.46	
2	KTB06-t	Sediment cores were collected from the Subantarctic zone of the Sounthwest Indian Ocean, and sliced for the dissolution of siliceous oozes at different depths	25 ℃	0.53	Van Cappellen and Qiu, 1997
3	KTB05-t			0.6	Van Cappellen and Qiu, 1997b
	KTB05-1			0.8	
	KTB05-3			0.5	
	KTB06-1			0.75	
	KTB06-4			0.54	
	KTB06-6			0.75	
4	Quartz	Dissolution of quartz a batch reactor	300 ℃	0.81	Berger et al., 1994
5	Quartz	Dissolution of quartz in flow-through reactor at 33 Mpa	25-374 ℃	0.48	Zhang et al., 2015
6	M31/2	Sediments from Norwegian Sea enriched with biogenic silica	25 ℃	0.53	Rickert, 2000
	EAST 24-26	Sediments from Arabian Sea enriched with biogenic silica		0.47	
	MC-1-3	Sediments from Norwegian Sea enriched with biogenic silica		0.50	
	PS-2312-1	Sediments from Juan de Fuca Plate		0.53	
	Trap-NB9 1000	Sediment trap from Norwegian Sea		0.74	
	Trap-BO	Sediment trap from Weddel Sea		0.33	
	Pn-T, Antarctica	Phytoplankton bloom, dominated by *Rhizosolenia sp.*		0.75	
	Pn-Nitschia	Cultured *Thalassiosira antarctica*		0.50	
7	H21	Sediments enriched with biogenic silica were collected from Yellow Sea.	20 ℃	0.60	Wu et al., 2017
	B16			0.73	
	H40			0.36	
	H01			0.57	
	HYS			0.28	
8	J3	Sediments enriched with biogenic silica were collected from Yellow Sea.	20 ℃	0.52	Wu et al., 2015
	B1			0.36	
	J2			0.55	
9	FB-V	Sediments that are characterized with seasonal deposition of phytodetritus were collected from northeast Atlantic Ocean in different seasons.	5 ℃	0.54	Gallinari et al., 2008
	FB-IV			0.64	
	BWNGAL			0.67	
10	EqPac	Sediments were collected from equatorial Pacific.	5 ℃	0.48	Gallinari et al., 2005
11	PS63/146-2	Surface sediments were collected from certain regions of Southern Ocean	Not shown	0.50	Gallinari et al., 2008
	PS63/149-2			0.45	
	PS63/139-2			0.62	
	PS63/033-5			0.50	
	PS63/037-4			0.62	
	PS63/130-2			0.48	

All dissolution experiments were conducted with flow-through reactor, unless otherwise stated

Table A.2. First-order rate constants of different ASi materials under the three dissolution regimes observed in the batch experiments. The initial dissolution corresponds to when about 10% of the initial total ASi; fast dissolution corresponds to dissolution at degrees of undersaturation ≥ 0.4; slow dissolution corresponds to dissolution at degrees of undersaturation ≤ 0.4.

ASi type	Initial dissolution k_{ini}	Fast dissolution k	Slow dissolution k_{slow}
	µmol m^{-2} h^{-1}	µmol m^{-2} h^{-1}	µmol m^{-2} h^{-1}
Aerosil OX 50	0.35	0.28	0.20
Cyclotella sp.	0.68	0.40	0.27
Cyclotella meneghiniana	0.49	0.22	0.13
Navicula pelliculosa	0.59	0.32	0.25

**k* corresponding to fast dissolution period is the rate constant used in this study, unless otherwise stated.

Appendix B Supplementary information for Chapter 3

Table B.1. Concentrations of dissolved Si (DSi) after 6000 hours of dissolution in the presence of varying initial Fe(II) concentrations.

	Initial Fe(II) concentration			
	0 µM	2 µM	20 µM	200 µM
DSi concentration after 6000 hours of dissolution (µM)	1712	1712	1700	1575

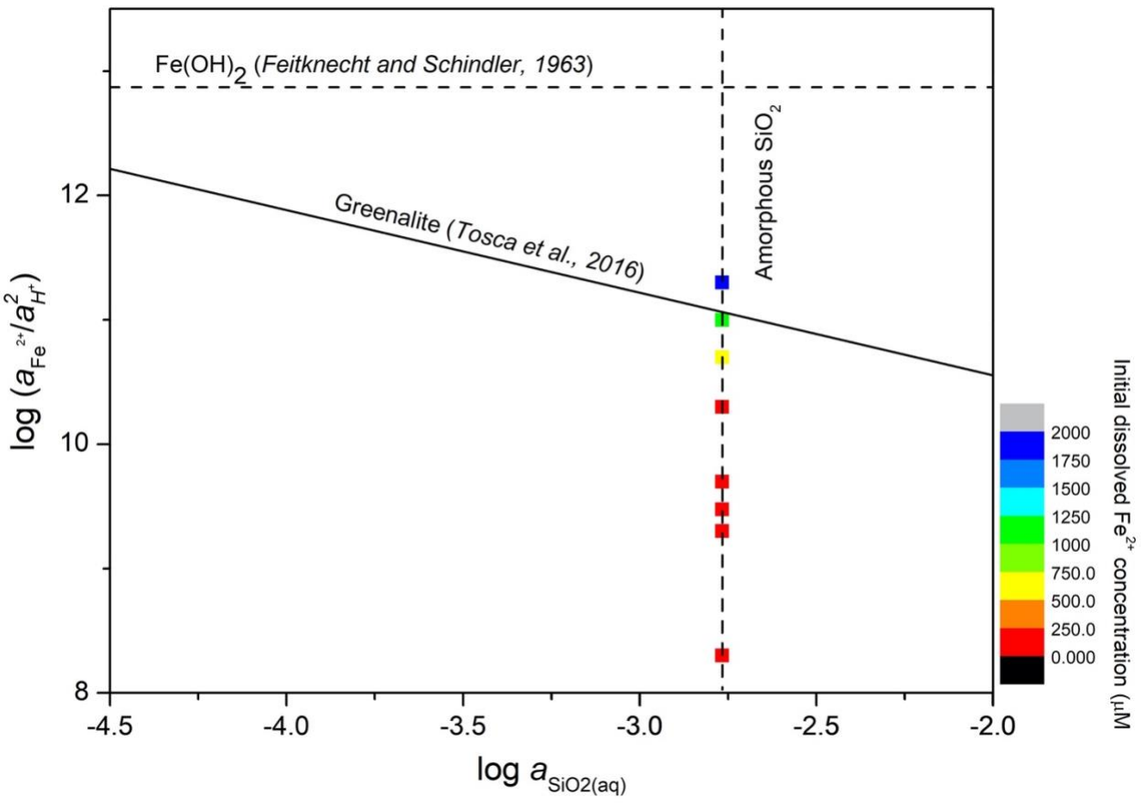

Figure B.1. Solubility diagram for the Fe^{2+}-SiO_2-H_2O system at 25 °C. Solid line correspond to previously estimated greenalite solubility (Tosca et al.,2016). Dashed lines include solubility-limiting phases: amorphous silica (this study) and freshly precipitated $Fe(OH)_2$ (Feitknecht and Schindler, 1963). Squares represent the aqueous composition of 10 g L^{-1} ASi suspensions in the presence of 0 to 2000 µM Fe^{2+}, assuming that DSi concentration is the solubility of Aerosil OX 50 at pH 7.0.

Appendix C

Supplementary information for Chapter 4

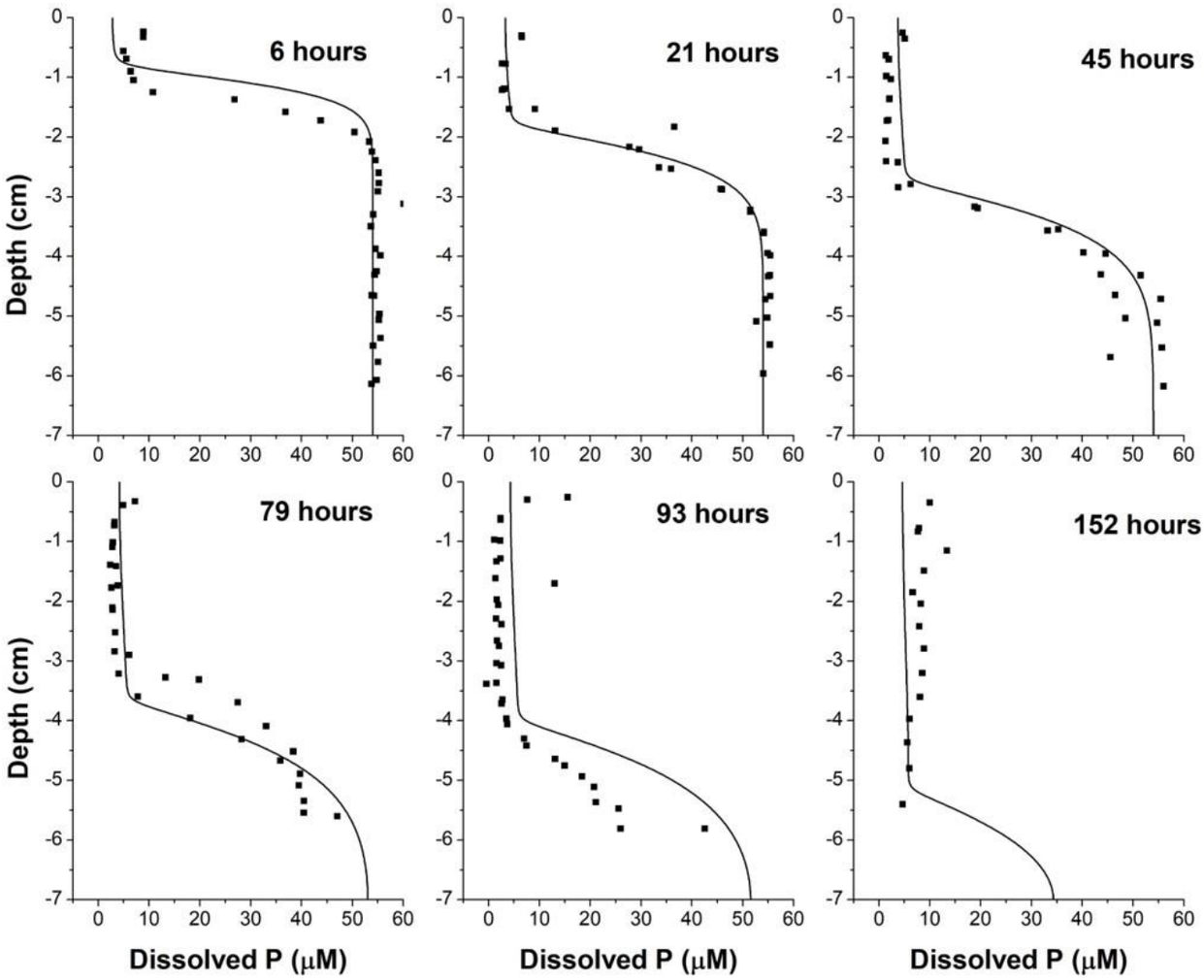

Figure C.1. The evolution of DP profiles in agar columns with time. Before exposure to air, the initial chemical composition is homogeneous throughout the agarose columns with Fe(II), P, and Si concentrations being 270, 54, and 150 μM respectively. Two agarose columns were sacrificed at 6, 21, 45, 79, 93 and 152 hours of air exposure at one end. The agarose columns were sliced into approximately 0.3 cm pieces in the anaerobic chamber, and dissolved phases were extracted with background solution and acidified before being taken out of the chamber for analysis. The initial pH is 7.0 with 20 mM HEPES as the pH buffer and the temperature of oxidation is controlled at 25±1 °C. Scattered data points represent experimental data of DP extracted, and solid lines represent model predictions (See details in Discussion).

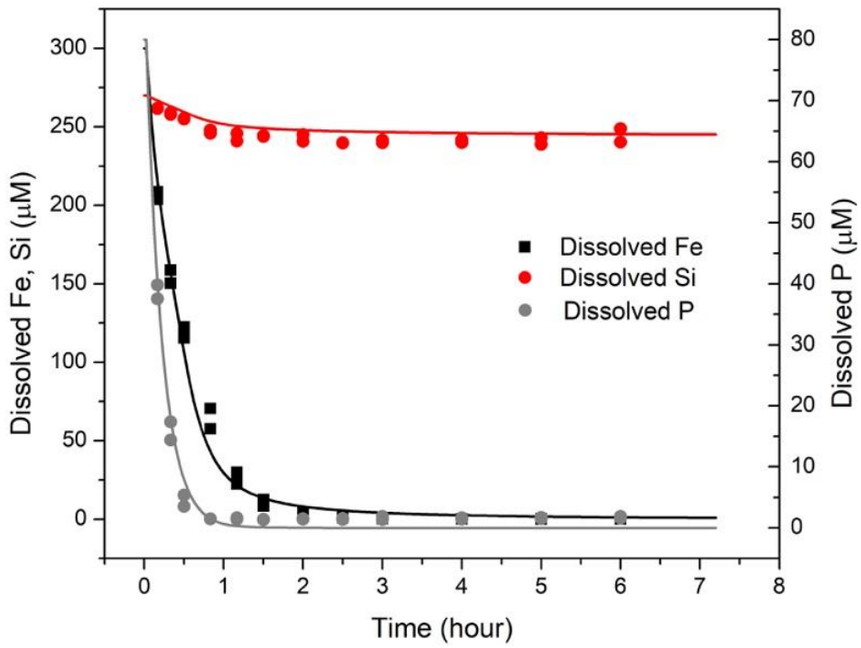

Figure C.2. Oxidation of 300 μM Fe(II) in the presence of 270 μM dissolved silicon and 80 μM dissolved phosphate at pH 7.0 (data points). Model outputs are represented by solid lines.

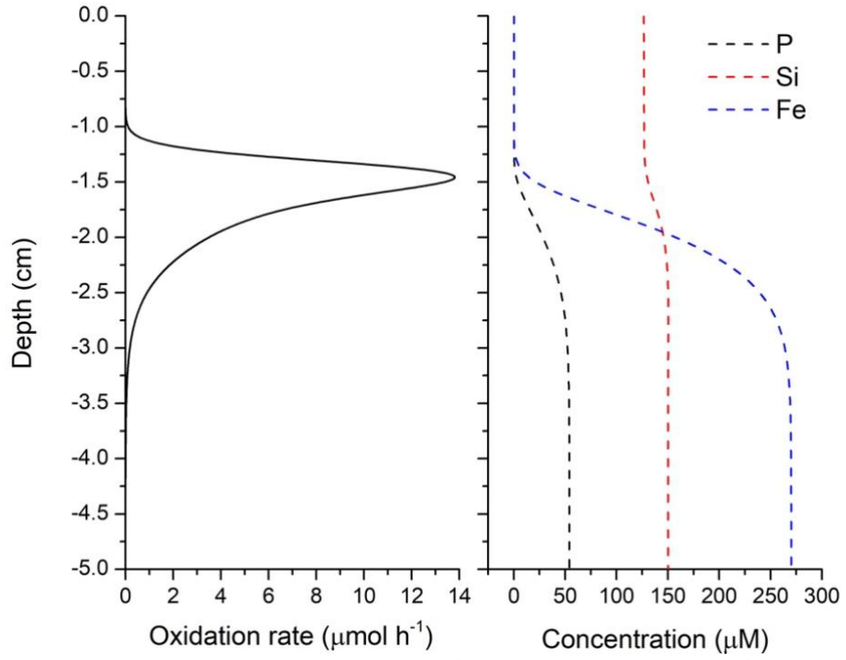

Figure C.3. Model-predicted vertical distribution of overall oxidation rate of Fe(II) and dissolved Fe, DSi and DP concentrations in the agarose column after 21 hours of air exposure.

C.1 Further information on the kinetic modeling

C.1.1 Reactions and transport

The model included the least number of reactions possible while still describing the co-precipitation processes adequately (Table 4.3). Briefly, the model includes the homogenous oxidation of Fe(II) (Reaction 1), the polymerization and condensation of Fe(III) (Reaction 2), the adsorption and desorption of Fe(II) to the surface sites of Fe(III) oxyhydroxide (Reaction 3+ and 3-), the heterogeneous oxidation of Fe(II) and surface precipitation of Fe(III) (Reaction 4), the complexation and dissociation of Fe(II) and DSi (Reaction 5+ and 5-), the oxidation of Fe(II) and DSi complexes (Reaction 6), the adsorption and desorption of DSi to the surface sites of Fe(III) oxyhydroxides (Reaction 7+ and 7-), the complexation and dissociation of Fe(II) and DP (Reaction 8+ and 8-), the oxidation of Fe(II) and DP complexes (Reaction 9), and the adsorption and desorption of DP to the surface sites of Fe(III) oxyhydroxides (Reaction 10+ and 10-). The value of *n* represents the growth of surface sites of Fe(III) oxyhydroxides during precipitation. To account for the diffusive transport of chemicals in the agarose columns, I incorporated molecular diffusion into the kinetic reaction model, herein referred to as the diffusion-reaction model.

Table C.1 Rate equations included in the model.

Reactions		**Reactions**	**Kinetic formulations**
R1	homogeneous oxidation of Fe(II)	$Fe^{II} + (1/4)O_2 \rightarrow Fe^{III}$	$k1[Fe^{II}][O2]$
R2	polymerization and condensation of Fe(III)	$Fe^{III} + Fe^{III} \rightarrow 2$ >FeOH	$k2[Fe^{III}][Fe^{III}]$
R3(+)$^{\alpha}$	adsorption of Fe(II) to the surface sites of Fe(III) oxyhydroxide	>FeOH + nFeII $\rightarrow$ >$FeO(FeII)_n$	$k3+\{>FeOH\}[Fe^{II}]$
R3(-)$^{\alpha}$	desorption of Fe(II) to the surface sites of Fe(III) oxyhydroxide	>FeOH + nFeII $\leftarrow$ >$FeO(FeII)_n$	$k3-\{>FeO(Fe)_n\}$
R4	heterogeneous oxidation of Fe(II) and surface precipitation of Fe(III)	>$FeO(FeII)_n$ + $(n/4)O_2 \rightarrow Fe(OH)_3(s)$ + n>FeOH	$k4\{>FeO(Fe)_n\}[O_2]$
R5(+)$^{\alpha}$	complexation of Fe(II) and DSi	Fe^{II} + Si $\rightarrow Fe^{II}Si$	$k5+[Fe^{II}][Si]$
R5(-)$^{\alpha}$	dissociation of Fe(II) and DSi	Fe^{II} + Si $\leftarrow Fe^{II}Si$	$k5-[Fe^{II}Si]$
R6	oxidation of Fe(II) and DSi complexes	$Fe^{II}Si + (1/4)O_2 \rightarrow$ FeOHSi(s)	$k6[Fe^{II}Si][O_2]$
R7(+)$^{\alpha}$	adsorption of DSi to the surface sites of Fe(III) oxyhydroxides	>FeOH + Si $\rightarrow$ >FeOSi	$k7+\{>FeOH\}[Si]$
R7(-)$^{\alpha}$	desorption of DSi to the surface sites of Fe(III) oxyhydroxides	>FeOH + Si $\leftarrow$ >FeOSi	$k7-\{>FeOSi\}$
R8(+)$^{\alpha}$	complexation of Fe(II) and DP	$2Fe^{II} + P \rightarrow (Fe^{II})_2P$	$k8+[Fe^{II}][P]$
R8(-)$^{\alpha}$	and dissociation of Fe(II) and DP	$2Fe^{II} + P \leftarrow (Fe^{II})_2P$	$k8-[(Fe^{II})_2P]$
R9	oxidation of Fe(II) and DP complexes	$(Fe^{II})_2P + (1/2)O_2 \rightarrow (Fe^{III})_2P(s)$	$k9[(Fe^{II})_2P][O_2]$
R10(+)$^{\alpha}$	adsorptionof DP to the surface sites of Fe(III) oxyhydroxides	>FeOH + P $\rightarrow$ >FeOP	$k10+\{>FeOH\}[P]$
R10(-)$^{\alpha}$	desorption of DP to the surface sites of Fe(III) oxyhydroxides	>FeOH + P $\leftarrow$ >FeOP	$k10-\{>FeOP\}$

Note: Fe^{II} = dissolved ferrous iron, Fe^{III} = dissolved ferric iron, Si = dissolved silicon, P = dissolved phosphate, $Fe(OH)_3$ = bulk solid Fe(III) oxyhydroxides (not surface), FeOHSi(s) = coprecipitates of Fe(III) oxyhydroxides and Si in bulk solid, $(Fe^{III})_2P$ = ferric iron phosphate, >FeOH = surface site of Fe(III) oxyhydroxides, >FeOSi = the adsorption of Si on the surface sites of Fe(III) oxyhydroxides, >FeOP = the adsorption of P on the surface sites of Fe(III) oxyhydroxides

[] = solute concentration (µmol L^{-1}), {} = solid concentration (µmol g^{-1})
R = reaction rate (µmol L^{-1} h^{-1} or µmol g^{-1} h^{-1}, k = reaction rate constant (µmol^{-1} h^{-1}),
$^{\alpha}$ Reactions (3, 5, 7, 8 and 10) where equilibrium has been assumed.

C.1.2 Implement of the model

C.1.2.1 Overview of PorousMediaLab

The toolboxes PorousMediaLab (PML) were used to model the experimental data collected, fit the kinetic parameters using an optimization procedure, and perform a sensitivity analysis.

PML is a computer program written in Python programming language that is designed to perform a wide variety of biogeochemical modelling in the aquatic environment (Markelov, 2019). The mathematical representation of the model consists of the coupled nonlinear partial differential equations representing transport and reactions processes of solid and aqueous species:

$$\frac{\partial(\theta C_i)}{\partial t} = \frac{\partial}{\partial x}\left(\theta D_i \frac{\partial C_i}{\partial x}\right) - \frac{\partial}{\partial x}(\omega \theta C_i) + \theta \sum R(x, t, C_i, \dots) \quad \text{(C.1)}$$

where C_i is concentration of i^{th} reactant; θ is the porosity φ for dissolved species and $(1 - \varphi)$ for solid species; D_i is effective diffusion constant; ω is advective term; $R(x, t, C_i, \dots)$ represents mass-conservation of the reaction term, *i.e.* sum of all sources and sinks of particular reactant. PML solves the one-dimensional advective-diffusive transport in Equation (C.1) using the transport integration of Crank-Nicolson finite difference scheme. Kinetic reactions in Equation (C.1) are solved using Butcher's Fifth-Order Runge-Kutta method.

With the operator splitting technique, PML allows for the decoupling of transport (the first and second terms on the right-hand side of Equation (C-1)) and reactive terms (the second term on the right-hand side of Equation (C-1)). Specifically, PML simulates the reactions in homogeneous systems (*e.g.*, batch reactors). While in heterogeneous systems (*e.g.*, column reactors), PML simulates one-dimensional reactions, as well as advective-diffusive transport. More details of these two cases are described in case studies bellow.

C.1.2.2 Case 1: batch experiment

The kinetic modeling aims to capture the change of measured concentrations of Fe(II), DSi and DP over time in batch reactors and evaluate the rate constants of chemical reactions listed in Table C.1 during the oxidative precipitation of Fe.

In the well-mixed batch systems, reaction rates are not affected by transport process and therefore can be described in terms of reaction term. PML was used to build a kinetic model taking reactions listed in Table C.1 into account. The code was configured to automatically estimate parameters based on measured data using different methods of optimizer. In this study, Powell's method was used to find a local minimum of normalized root mean square deviation between observed values and values predicted by the model.

The model started with the simplest scenario, i.e., the oxidation of Fe(II) in the absence of DSi and DP, the observed data and rate constants were extracted from a previous study. The complexity of the model increased gradually, with the addition of DSi, and at last DP. By doing this, the number of unknown parameters was minimized for each optimization.

C.1.2.2.1 Parameter optimizations

The kinetic model shown in Table C.1 includes not only homogeneous reaction (Reaction 1, 2, 5, 6, 8, 9) but also interactions between aqueous and solid phases (Reaction 3, 4, 7, 10). Different from that of homogeneous reactions, the kinetics of surface reactions are limited by the changing concentration of surface sites, which cannot be measured directly during precipitation. Thus, the experimental data collected does not give insight into the concentration of surface sites. To solve this problem, a surface precipitation reaction was used to distinguish surface Fe atoms (>FeOH) that are available for surface reaction and bulk Fe atoms ($Fe(OH)_3$) that are inaccessible in this study. Also, the stoichiometric coefficient, *n*, in Reaction 3 was added to reflect the growth of surface sites during precipitation. Mass balances of DO, Fe, Si and P are maintained with the stoichiometries listed in Table C.1. In reality, the stoichiometries of DSi and DP adsorption to surface sites of iron oxyhydroxides are not always equal to 1. The values are dependent on the concentration of DSi and DP relative the surface site concentrations, as well as pH of the aqueous medium (Hiemstra et al., 2007; Kanematsu et al., 2018; Sabur, 2019; Swedlund et al., 2010; Wang et al., 2017).

The kinetic data obtained from batch experiments were used to evaluate the rate constants of these processes and *n*. First, kinetic data of the oxidation of Fe(II) in the absence of complexation agents and rate constants from Kinsela et al. (Kinsela et al., 2016) were used to evaluate the value of *n*. Specifically, the rate constants of the homogeneous oxidation (Reaction 1) and the polymerization (Reaction 2) that were published in previous papers were fixed as an unchangeable values (Kinsela et al., 2016; Pham et al., 2006; Pham and Waite, 2008). The adsorption of Fe(II) to surface sites was assumed to be very fast. Therefore, when combined with reverse reactions, the adsorption effectively achieved instantaneous equilibrium (Tamura et al.,1976). As a result, the factor *n* in Reaction 3 and the rate constant of Reaction 4 are the two variables that control the ratio of surface Fe to total iron in the solid phase. According to Michel et al. (2010), the structure of ferrihydrite has two end members that are particle size-dependent. The largest particles of ferrihydrite (with a diameter of about 7-9 nm) are supposed to be defect-free and have a OH:Fe ratio of only 0.2. Based on the assumption that surface sites are single coordinated (>FeOH), 0.2 is set as the lower boundary of the ratio of surface Fe to total Fe in the largest unit cell, which corresponds to a value of $n = 1.3$. The smallest nanoparticles of ferrihydrite (2.5 nm) consist of about 200 Fe atoms, among which about 120 atoms exist on the surface (Hiemstra, 2013). Therefore, 0.6 is assumed to be the upper boundary of the surface Fe to total Fe ratio in ferrihydrite, which corresponds to a value of $n = 2.5$.

Freshly-precipitated ferrihydrite nanoparticles may aggregate and form larger particles (Li et al., 2018). According to Rzepa et al. (2016), the particle size distribution of hematite with a Fe to Si molar ratio of 1 resulting from ferrihydrite annealing centers at 200 nm, where more than 85% of the particle are between 100 and 300 nm. Therefore, the ratios of surface Fe to total Fe could be as small as 0.002. However, in this study, the aggregation effects are assumed to be minor during the co-precipitation of Fe and Si. The value of *n* was set at 2 in this kinetic model, reflecting surface site density of these freshly precipitated iron oxyhydroxides 0.5 mol per mol Fe. By fitting the

kinetic model in this model (Reaction 1-4) to their kinetic data, the rate constants of Reaction 3 and 4 were firstly optimized considering the stoichiometry of 2. The rate constants of Reaction 1 and 4 were then optimized considering the mass balance of oxygen.

The model proposed by Kinsely et al. (2016) properly describes the kinetics of dissolved Fe(II): DSi complexes with Fe(III) and precipitates as Si-ferrihydrite that inhibit the heterogeneous oxidation of Fe(II). However, it cannot be used to express the kinetics of DSi during the oxidation: much more DSi is predicted to be incorporated in solid phase than observed in this study. As discussed above, the mechanisms of DSi incorporation into Fe oxides can be separated into two regions. First, when the initial Fe(II) is high and the surface sites' concentration is low, Fe(II) and DSi form complexes that are subsequently oxidized (Reaction 5 and 6). Second, DSi adsorbs to surface sites which are mostly produced by heterogeneous Fe(II) oxidation (Reaction 7 in Table C.1). Adsorption rate constants of Reaction 5 and 7 were fixed. Kinetic data in the presence of DSi but in the absence DP were fitted to the kinetic model (Reaction 1-7) for the optimization of the rate constants of Reaction 6 and the desorption rate constants of Reaction 5 and 7.

Finally, the effects of DP on the overall oxidation rate of Fe(II) and the amount of DSi removed during co-precipitation are incorporated in the kinetic model. Adsorption rate constants of Reaction 8 and 10 were fixed. Kinetic data for Fe(II) oxidation in the presence of DSi and DP were fitted to the kinetic model (Reaction 1-10) for the optimization of the rate constants of Reaction 9 and the desorption rate constants of Reaction 8 and 10. The rate constants were further validated by varying the initial DP concentrations. Consequently, the rate constants of Reactions 1-10 at pH 6.5 and 7.0 are listed in Table C.1. The model output using rate constants at pH 7.0 are further represented by the solid lines in Table C.1, 4.9 and 4.10.

C.1.2.3 Case 2: column experiment

The kinetic modeling evaluates the rate constants of chemical reactions listed in Table C.1 describing the coprecipitation of Fe(II), DSi and DP. While in heterogeneous systems, *i.e.*, natural and near-natural systems, reaction rates are affected by not only chemical reactions but also transport processes. Therefore, the results from an experiment using agarose columns were used to develop a diffusion-reaction model to couple the effects of diffusive transport and reactions on the removal of DSi during Fe(II) oxidation.

Molecular diffusion was included in the one-dimensional mass conservation equations. To solve these differential equations, additional initial and boundary conditions are required. Initial concentrations of all chemical species were known and shown in Table C.2. Oxygen can penetrate from the top of the column via molecular diffusion. A constant dissolved O_2 concentration of 256 µM was imposed as upper boundary. With a closed bottom end of the column, the lower boundary of dissolved O_2 was set as a no-gradient boundary condition (*i.e.*, zero flux). Since there is no exchange of other chemical species between column and the environment, zero fluxes were imposed for all chemical species at both upper and lower boundary in this model.

Table C.2. The input file for the simulation of one of the column experiments.

	Description
from porousmedialab.column import Column	
L = 7	maximum length (cm)
phi = 0.98	porosity of 1% (wt.%) agarose [a]
t = 21	maximum time (hour)
dx = 0.01	space discretization
dt = 0.001	time discretization
ftc = Column(L, dx, t, dt)	
import numpy as np	
ftc.add_species(theta=phi, name='FeII', D=0.025, init_conc=270, bc_top_value=0, bc_top_type='flux', bc_bot_value=0, bc_bot_type='flux')	Add chemical species considered, and assign porosity, initial condition, diffusion coefficient and boundary condition.
ftc.add_species(theta=phi, name='FeIII', D=0.025, init_conc=0, bc_top_value=0, bc_top_type='flux', bc_bot_value=0, bc_bot_type='flux')	Porosity (phi): 0.98 (Pluen et al., 1999).
ftc.add_species(theta=1-phi, name='FeOH', D=(1e-18)/(365*24), init_conc=0, bc_top_value=0, bc_top_type='flux', bc_bot_value=0, bc_bot_type='flux')	Diffusion coefficient (D, $cm^2\ h^{-1}$): the diffusion coefficients of dissolved Fe(II), O_2, and P were sorted and calibrated for temperature using method described in Boudreau, (1997). Diffusion coefficient of dissolved Si at 25 °C was extracted from Rebreanu et al., (2008). Those of aqueous complex were set to be that of dissolved Fe(II), those of solid species were set to be much smaller than those of dissolved species, indicating the immobility of solids.
ftc.add_species(theta=1-phi, name='FeOH3', D=(1e-18)/(365*24), init_conc=0, bc_top_value=0, bc_top_type='flux', bc_bot_value=0, bc_bot_type='flux')	
ftc.add_species(theta=1-phi, name='FeOFe', D=(1e-18)/(365*24), init_conc=0, bc_top_value=0, bc_top_type='flux', bc_bot_value=0, bc_bot_type='flux')	
ftc.add_species(theta=phi, name='Si', D=0.042, init_conc=150, bc_top_value=0, bc_top_type='flux', bc_bot_value=0, bc_bot_type='flux')	Initial condition (init_conc): concentrations shown in Table 4.2, initial concentration of dissolved O_2 in agarose column is zero.
ftc.add_species(theta=phi, name='FeIISi', D=0.025 , init_conc=0, bc_top_value=0, bc_top_type='flux', bc_bot_value=0, bc_bot_type='flux')	
ftc.add_species(theta=1-phi, name='FeOHSi', D=(1e-18)/(365*24), init_conc=0, bc_top_value=0, bc_top_type='flux', bc_bot_value=0, bc_bot_type='flux')	Boundary condition of all chemical species: 'flux' = specify the flux at the boundary, 'dirichlet' = specify the concentration of unknown dependent variable at the boundary.
ftc.add_species(theta=1-phi, name='FeOSi', D=(1e-18)/(365*24), init_conc=0, bc_top_value=0, bc_top_type='flux', bc_bot_value=0, bc_bot_type='flux')	
ftc.add_species(theta=phi, name='P', D=0.028, init_conc=54, bc_top_value=0, bc_top_type='flux', bc_bot_value=0, bc_bot_type='flux')	
ftc.add_species(theta=phi, name='FeIIP', D=0.025 init_conc=0, bc_top_value=0, bc_top_type='flux', bc_bot_value=0, bc_bot_type='flux')	
ftc.add_species(theta=1-phi, name='FeIIIP', D=(1e-18)/(365*24), init_conc=0, bc_top_value=0, bc_top_type='flux', bc_bot_value=0, bc_bot_type='flux')	
ftc.add_species(theta=1-phi, name='FeOP', D=(1e-18)/(365*24), init_conc=0, bc_top_value=0, bc_top_type='flux', bc_bot_value=0, bc_bot_type='flux')	

ftc.add_species(theta=phi, name='O2', D=0.072, init_conc=0, bc_top_value=256, bc_top_type='dirichlet', bc_bot_value=0, bc_bot_type='flux')	
ftc.constants['k_1'] = 9.7e-4 ftc.constants['k_2'] = 3.6e3 ftc.constants['k_3_f'] = 3.6e5 ftc.constants['k_3_b'] = 8.3e3 ftc.constants['k_4'] = 2.5e-2 ftc.constants['k_5_f'] =3.6e5 ftc.constants['k_5_b'] = 1.3e5 ftc.constants['k_6'] =4.2e-3 ftc.constants['k_7_f'] = 3.6e5 ftc.constants['k_7_b'] = 8.7e5 ftc.constants['k_8_f'] = 3.6e6 ftc.constants['k_8_b'] =8.5e2 ftc.constants['k_9'] = 1.1e-2 ftc.constants['k_10_f'] = 3.6e6 ftc.constants['k_10_b'] = 4.3e2 ftc.constants['n'] = 2	Rate constants for chemical reactions listed in Table C.1 at pH 7 (μmol^{-1} $hour^{-1}$) 'f' = '+' in Table C.1, indicating forward reaction 'b' = '-' in Table C.1, indicating backward reaction
ftc.rates['R1'] = 'k_1*(O2)*(FeII)' ftc.rates['R_2'] = 'k_2 *(FeIII)*(FeIII)' ftc.rates['R_3_f']='k_3_f*FeOH*(FeII)' ftc.rates['R_3_b']='k_3_b*FeOFe' ftc.rates['R_4'] = 'k_4 *(O2)*FeOFe' ftc.rates['R_5_f'] ='k_5_f*(FeII)*Si ' ftc.rates['R_5_b1'] = 'k_5_b*(FeIISi)' ftc.rates['R_6'] = 'k_6*(FeIISi)*(O2)' ftc.rates['R_7_f'] = 'k_7_f*FeOH*Si' ftc.rates['R_7_b'] = 'k_7_b*FeOSi' ftc.rates['R_8_f'] = 'k_8_f*(FeII)*P' ftc.rates['R_8_b'] = 'k_8_b*(FeIIP)' ftc.rates['R_9'] = 'k_9*(FeIIP)*(O2)' ftc.rates['R_10_f'] = 'k_10_f*FeOH*P' ftc.rates['R_10_b'] = 'k_10_b*FeOP'	Kinetic formulations for chemical reactions listed in Table C.1
ftc.dcdt['FeII'] = ' - R_1 -n*(R_3_f) + n*(R_3_b) – (R_5_f) + (R_5_b) - 2*(R_8_f) + 2*(R_8_b) ' ftc.dcdt['FeIII'] = ' R_1 -2*R_2 '	Ordinary differential equations for all chemical species

ftc.dcdt['FeOH'] = '2*R_2 - R_3_f + n*R_4 + R_3_b - R_7_f + R_7_b - R_10_f + R_10_b' ftc.dcdt['FeOFe'] = '(R_3_f) - R_4 – (R_3_b)' ftc.dcdt['FeOH3'] = 'R_4' ftc.dcdt['Si'] = '-R_5_f + R_5_b - R_7_f + R_7_b' ftc.dcdt['FeIISi'] = 'R_5_f- R_5_b - R_6' ftc.dcdt['FeOSi'] = 'R_7_f - R_7_b' ftc.dcdt['FeOHSi'] = 'R_6' ftc.dcdt['P'] = '-R_8_f + R_8_b - R_10_f + R_10_b' ftc.dcdt['FeIIP'] = 'R_8_f - R_8_b - R_9' ftc.dcdt['FeOP'] = 'R_10_f - R_10_b' ftc.dcdt['FeIIIP'] = 'R_9' ftc.dcdt['O2'] = '-0.25*R_1 - (n/4)*R_4 – 0.25*R_6 - (0.5)*R_9'	
ftc.solve()	solver *FiPy* (Guyer et al., 2009) for transport step Fortran solver *LSODA* package (Jones et al., 2001) for the reaction step

The computer code for PML is divided into seven files of Python code. Each file corresponds to a different task. Main class and definitions of all shared between subclasses methods are contained in lab.py. The codes for simulation of the well-mixed reactor and 1-dimensional diffusive transport are located in batch.py and column.py, respectively. Files desolver.py and equilibriumsolver.py contain methods for computation of kinetic and equilibrium reactions. Additional calibrator.py and plotter.py files contain methods for calibration based on measured data and plotting of the modelling results (Markelov, 2019).

The kinetic data obtained from batch experiments were used to evaluate the rate constants of these processes and *n*. First, kinetic data of the oxidation of Fe(II) in the absence of complexation agents and rate constants from Kinsela et al. (Kinsela et al., 2016) were used to evaluate the value of *n*. Specifically, the rate constants of the homogeneous oxidation (Reaction 1) and the polymerization (Reaction 2) that were published in previous papers were fixed as an unchangeable values (Kinsela et al., 2016; Pham et al., 2006; Pham and Waite, 2008). The adsorption of Fe(II) to surface sites was assumed to be very fast. Therefore, when combined with reverse reactions, the adsorption effectively achieved instantaneous equilibrium (Tamura et al). As a result, the factor *n* in Reaction 3 and the rate constant of Reaction 4 are the two variables that control the ratio of surface Fe to total Fe in the solid phase. According to Michel et al. (2010), the structure of ferrihydrite has two end members that are particle size-dependent. The largest particles of ferrihydrite (with a diameter of about 7-9 nm) are supposed to be defect-free and have a OH:Fe ratio of only 0.2. Based on the assumption that surface sites are single coordinated (>FeOH), 0.2 is set as the lower boundary of the ratio of surface Fe to total Fe in the largest unit cell, which corresponds to a value of $n = 1.3$. The smallest nanoparticles of ferrihydrite (2.5 nm) consist of about 200 Fe atoms, among which about 120 atoms exist on the surface (Hiemstra, 2013). Therefore, 0.6 is assumed to be the upper boundary of the surface Fe to total Fe ratio in ferrihydrite, which corresponds to a value of $n = 2.5$.

Freshly-precipitated ferrihydrite nanoparticles may aggregate and form larger particles (Li et al., 2018). According to Rzepa et al. (2016) (Rzepa et al., 2016), the particle size distribution of hematite with a Fe to Si molar ratio of 1 resulting from ferrihydrite annealing centers at 200 nm, where more than 85% of the particle are between 100 and 300 nm. Therefore, the ratios of surface Fe to total Fe could be as small as 0.002. However, in this study, the aggregation effects are assumed to be minor during the co-precipitation of Fe and Si. The value of *n* was set at 2 in this kinetic model, reflecting surface site density of these freshly precipitated iron oxyhydroxides 0.5 mol per mol Fe. By fitting the kinetic model in this model (Reaction 1-4) to their kinetic data, the rate constants of Reaction 3 and 4 were firstly optimized considering the stoichiometry of 2. The rate constants of Reaction 1 and 4 were then optimized considering the mass balance of oxygen.

The model proposed by Kinsely et al. (2016) properly describes the kinetics of dissolved Fe(II): DSi complexes with Fe(III) and precipitates as Si-ferrihydrite that inhibit the heterogeneous oxidation of Fe(II). However, it cannot be used to express the kinetics of DSi during the oxidation:

much more DSi is predicted to be incorporated in solid phase than observed in this study. As discussed above, the mechanisms of DSi incorporation into Fe oxides can be separated into two stages. First, when the initial Fe(II) is high and the surface sites' concentration is low, Fe(II) and DSi form complexes that are subsequently oxidized (Reaction 5 and 6). Second, DSi adsorbs to surface sites which are mostly produced by heterogeneous Fe(II) oxidation (Reaction 7 in Table 4.3). Adsorption rate constants of Reaction 5 and 7 were fixed. Kinetic data in the presence of DSi but in the absence DP were fitted to the kinetic model (Reaction 1-7) for the optimization of the rate constants of Reaction 6 and the desorption rate constants of Reaction 5 and 7.

Finally, the effects of DP on the overall oxidation rate of Fe(II) and the amount of DSi removed during co-precipitation are incorporated in the kinetic model. Adsorption rate constants of Reaction 8 and 10 were fixed. Kinetic data for Fe(II) oxidation in the presence of DSi and DP were fitted to the kinetic model (Reaction 1-10) for the optimization of the rate constants of Reaction 9 and the desorption rate constants of Reaction 8 and 10. The rate constants were further validated by varying the initial DP concentrations. Consequently, the rate constants of Reactions 1-10 at pH 6.5 and 7.0 are listed in Table 4.3. The model output using rate constants at pH 7.0 are further represented by the solid lines in Figures 4.8, 4.9 and C.1.

Appendix D

Supplementary information for Chapter 5

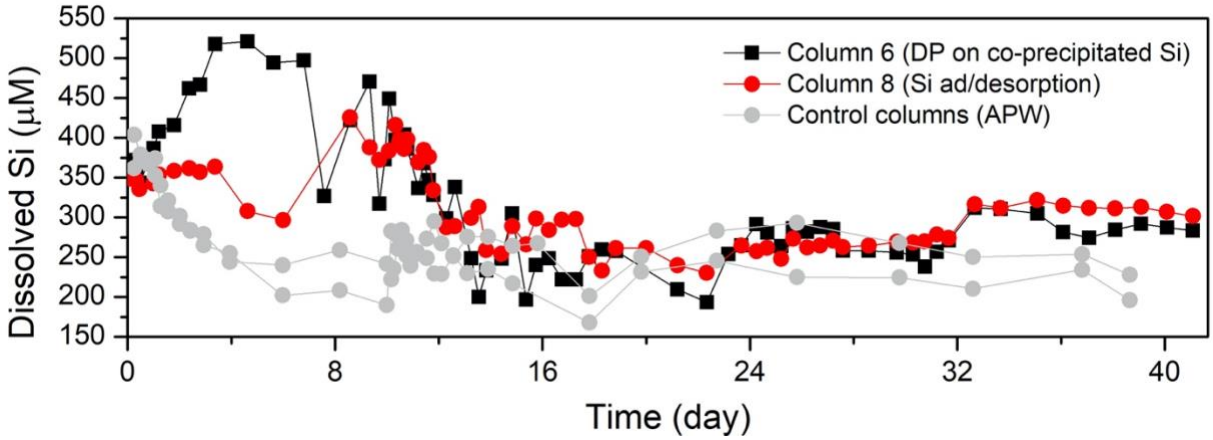

Figure D.1. Concentrations of DSi in the effluents of columns 4 and 5, and the two control columns, as a function of time. Column 4 was firstly supplied with "Fe, DSi" for 224 hours, and then with "P" for 280 hours under oxic conditions; column 5 was firstly supplied with "Fe" for 144 hours, then with "DSi" for 80 hours, and finally with "P" for 280 hours under oxic conditions. The influent to columns 4 and 5 was switched to "P" under anoxic conditions after 504 hours. Control columns were supplied with only APW throughout the incubation experiment, and the overlying water was switched to anoxic conditions after 224 hours of aeration.

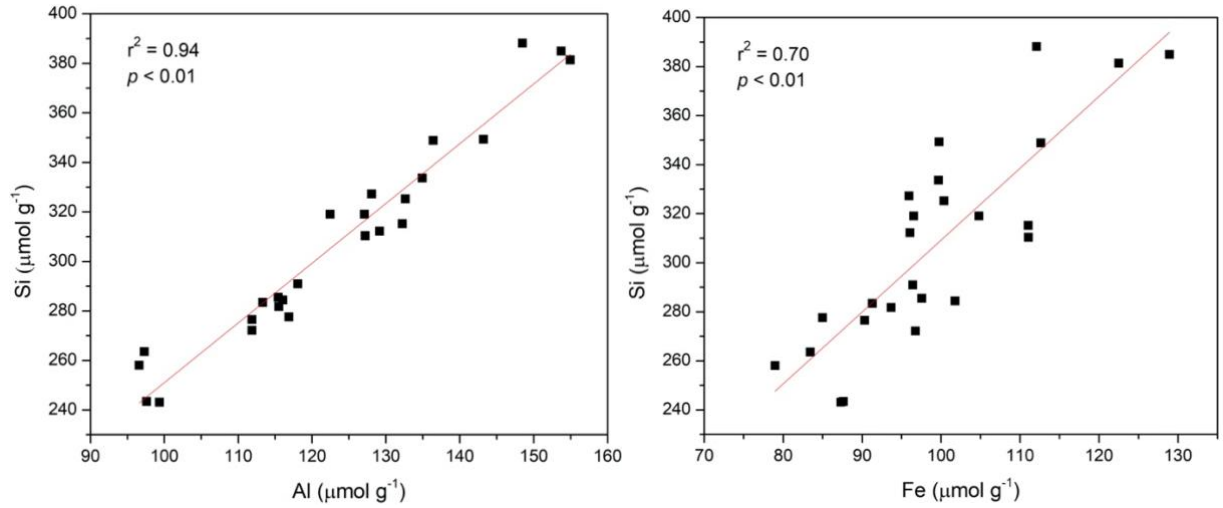

Figure D.2. Relationship between 1 M NaOH extractable Al, Fe and Si in sediments from columns 1, 2, 4 and 5. Column 1 was flushed with "DSi" for 9 days under oxic conditions, column 2 was flushed with "DSi" for 9 days under oxic conditions, and then flushed with "DSi" for 32 days under anoxic conditions. Column 5 was flushed with "Fe, DSi" for 9 days under oxic conditions, column 4 was firstly flushed with "Fe, DSi" for 9 days under oxic conditions, then with "DSi" for 32 days under anoxic conditions.